SOLAR MAXIMUM MISSION OBSERVATIONS OF SOLAR FLARES

Sri Ayilavan Thedchana Moorthy

Mullard Space Science Laboratory
Department of Physics and Astronomy
University College London
Holmbury St.Mary
Dorking
Surrey

A thesis submitted to the University of London
for the degree of Doctor of Philosophy
June 1993

Abstract

Soft X-ray observations made by instruments aboard the *Solar Maximum Mission* satellite are used to investigate the dynamics and energetics of solar flares.

The interpretation of the observations is linked to the characteristics of the instruments. The calibration of one of these instruments, the *Bent Crystal Spectrometer* (*BCS*), is described and the results of this calibration are used in the work described in the following chapters.

It is known that the width of *BCS* emission lines is affected by the spatial size of flares. This instrumental effect does not contribute much to the already broad rise phase lines, but becomes significant in the decay phase. *Flat Crystal Spectrometer* (*FCS*) images of flares are used to estimate, for the first time, the magnitude of this effect. It is found to add no more than 20% to the true non-thermal velocities in the decay phase. If the non-thermal mass motion is due to plasma being constrained to follow the transverse motion of Alfvén waves, then the amount of energy available for coronal heating via this transport mechanism can be estimated.

Another question regarding the decay phase is whether or not there is flare heating. A simplified hydrodynamical analysis of cooling coronal loops is applied to cooling flare loops seen by the *BCS* and the *FCS* to determine which of these flares show signs of decay phase heating.

The dynamics of the rise phase of flares may be studied by measuring the widths of emission lines. A novel method of doing this is introduced, and applied to a large sample of flares. It is found that the presence of a substantial amount of slow upflows is required to explain the observed trends in the data.

Contents

1 An Overview of the Solar Flare Phenomenon 15

1.1 Flare observation. 15

1.2 The observed structure of flares. 16

1.3 Flares in soft X-rays. 17

1.3.1 Classification according to soft X-ray intensity. 17

1.4 The Physics of Solar Flares 18

1.4.1 Coronal plasmas 18

1.4.2 Magnetic Diffusion in coronal plasmas 19

1.5 The energization of flares. 20

1.5.1 The initial energy release: magnetic reconnection 20

1.5.2 Continuing energy release in flares. 21

1.6 This thesis. 21

2 Basic Diagnostics of Solar Flares 23

2.1 Soft X-ray Spectroscopy of Flares. 23

2.1.1 The intensity of emission lines. 24

2.1.2 Atomic processes in flare plasma. 26

2.1.3 Nomenclature for flare emission lines. 29

2.1.4 Line Ratio Diagnostics. 32

2.2 Differential Emission Measure. 35

3 The *Bent Crystal Spectrometer* and the *Flat Crystal Spectrometer* 39

3.1 The *Solar Maximum Mission* 39

3.2 Bragg crystal spectrometers for soft X-rays. 41

3.3 *The Flat Crystal Spectrometer* 42

3.4 *The Bent Crystal Spectrometer*. 44

4 The Crystal Curvature of the Bent Crystal Spectrometer. 47

4.1 Introduction 47

4.1.1 The geometry of the *Bent Crystal Spectrometer*. 47

4.1.2 The importance of knowing the crystal curvature radius . 49

4.1.3 The aims of this chapter. 49
4.2 Prelaunch calibration. 49
4.3 Spacecraft slew measurements - 1980. 50
4.4 Spacecraft slew measurements - 1989. 51
4.4.1 Observations. 51
4.4.2 Analysis. 51
4.5 Conclusions 55
4.5.1 Further use of the results obtained here. 55

5 Turbulent Velocity During Flare Decay **61**
5.1 Introduction 61
5.1.1 Turbulent motion in coronal plasma. 61
5.1.2 The instrumental contribution to line-broadening. 61
5.1.3 Observations of flare plasma. 62
5.1.4 Observations of non-flaring plasma. 63
5.1.5 The importance of measuring the size-dependent broadening in the decay phase. 63
5.1.6 The emission line as a velocity diagnostic. 64
5.1.7 Measuring the source-size dependent effect in the *SMM-BCS*. 66
5.1.8 The aims and structure of this chapter. 67
5.2 Analysis technique 68
5.2.1 Using *FCS* images to estimate flare sizes. 68
5.2.2 Testing the method. 74
5.2.3 Comparing *BCS* Ca XIX and Fe XXV spectra. 80
5.2.4 Comparing *FCS* and *BCS* spectra. 81
5.3 Data and Results 87
5.3.1 The main sample. 87
5.3.2 Testing the extrapolation from Si XIII sizes to Ca XIX sizes. 87
5.3.3 Non-thermal broadening in the decay phase. 87
5.3.4 Comparison of turbulence measured in Ca XIX and Fe XXV spectra. 91
5.3.5 Comparing *BCS* and *FCS* spectra from the same flare. . 91
5.4 Discussion 93
5.4.1 The absence of a disc-to-limb variation. 93
5.4.2 Underlying turbulence in active regions. 93
5.4.3 Temperature dependence of plasma turbulence. 94

5.4.4 Directed motion as the cause of symmetrical broadening of emission lines. 95
5.4.5 Causes of plasma turbulence in the decay phase. 99
5.5 Summary 101

6 The cooling of flares in the decay phase. 103
6.1 Introduction 103
6.1.1 Static loops and decay phase flare loops. 103
6.1.2 The aims of this analysis. 104
6.2 Theory 105
6.2.1 The static loop: The Rosner, Tucker and Vaiana Scaling Laws. 107
6.2.2 The cooling loop. 107
6.2.3 The density-temperature diagram. 110
6.3 Analysis technique 110
6.3.1 Selection criteria for suitable flares. 112
6.3.2 The relation between the entropy decay time and the temperature decay time. 112
6.3.3 The temperature decay diagnostic diagram 113
6.3.4 Obtaining flare loop sizes from *FCS* images. 119
6.4 Results and Discussion 124
6.4.1 Comparison of Ca XIX and Fe XXV temperatures. . . . 124
6.4.2 Flares with no decay phase heating. 124
6.4.3 Flares with decay phase heating. 127
6.4.4 Comparison with analysis using density-temperature diagrams. 127
6.5 Summary 127

7 Flare Plasma Velocity 129
7.1 Introduction 129
7.1.1 Observed plasma dynamics. 130
7.1.2 The chromospheric evaporation interpretation. 130
7.1.3 Alternative interpretations 136
7.1.4 The methods and aims of this analysis. 137
7.2 Analysis technique 139
7.2.1 The measurement of directed plasma motion. 139
7.2.2 Measurement of the equivalent width. 147
7.2.3 The line-width time plot 150
7.2.4 The line-width diagnostic plot 151
7.2.5 The flare sample 151

7.2.6 Orientation of loops. 151
7.2.7 Instrument details 152
7.3 Results and Discussion 153
7.3.1 The physical meaning of the equivalent width. 153
7.3.2 Time evolution of upflows from line-width diagnostic plots. 155
7.3.3 Derivation of an upflow velocity from the equivalent widths. 161
7.3.4 Relation to component fitting methods. 161
7.3.5 Variation of maximum upflow velocity with flare position. 165
7.3.6 Temperature dependent differences 168
7.3.7 Summary of line-width diagnostic plot behaviour. 168
7.3.8 Equivalent width behaviour in the flare sample. 182
7.3.9 Transfer of energy from upflows to stationary plasma . . 183
7.3.10 Consequences for the flare models. 183
7.4 Summary 185

8 Conclusions 207

Acknowledgements 211

Appendix: ***SMM Flares*** 212

References 219

List of Figures

2.1 Emissivity functions of helium like ions. 27
2.2 Naming the lines in helium-like spectra: Ca XIX 30
2.3 Naming the lines in helium-like spectra: Fe XXV 31
2.4 Energy level diagram: the four levels of the helium-like ion. . . . 37
2.5 Energy level diagram: dielectronic recombination 38

3.1 Diagram of the *SMM* satellite 40
3.2 Principle of operation of the *FCS* and *BCS* 42

4.1 The geometry of the *BCS* 48
4.2 Crystal curvature radii for *BCS* Channel 1 53
4.3 Crystal curvature radii for other *BCS* Channels 54
4.4 Spacecraft pointing for the calibration scans of 31 August 1989 . 57
4.5 Determining crystal radius of curvature. 58
4.6 Shift of line position with flare offset shift 59
4.7 The lightcurve recorded by the *BCS* as it scanned the flare of 31 August 1989. 60

5.1 Flowchart summary of analysis 69
5.2 Flowchart of combinations of *FCS* and *BCS* data 70
5.3 Emission functions for Si XIII and Ca XIX. 73
5.4 Contour image of a flare 75
5.5 Size dependent line-broadening. 76
5.6 Comparison of Si XIII and Ca XIX images. 77
5.7 *FCS* Rastering pattern. 78
5.8 Equivalence of turbulent velocity and source size 79
5.9 Positions of flares on Sun's disc 82
5.10 Corrected turbulent velocity plots (1) 83
5.11 Corrected turbulent velocity plots (2) 84
5.12 Corrected turbulent velocity plots (3) 85
5.13 Corrected turbulent velocity plots (4) 86
5.14 Flare of 19 May 1984: *FCS* image 89

5.15 Time variation of flare east-west extent 90
5.16 Dependence of turbulent velocity on flare position 97
5.17 Tapering loop model 98

6.1 Radiative loss function for flare plasma. 106
6.2 The single loop model. 107
6.3 Density-Temperature diagram. 111
6.4 The relation between the loop top temperature and the Ca XIX temperature. 114
6.5 Exponential fitting to the temperature decay of a flare 115
6.6 An example of a decay diagnostic diagram 116
6.7 The decay diagnostic diagram of a pure exponential decay. . . . 117
6.8 The decay diagnostic diagram of a pure exponential decay with a non-zero baseline. 118
6.9 The temperature decay diagnostic diagram: the non-converging case. 118
6.10 Examples of *FCS* images. 120
6.11 Interpretation of *FCS* contour images. 121
6.12 Interpretation of *FCS* contour images. 122
6.13 Measuring flare loop lengths by taking slices of contour images. 123
6.14 The relation between the loop top temperature and the Ca XIX temperature. 126

7.1 Interpretation of flare plasma dynamics 131
7.2 Schematic of the chromospheric evaporation in flares. 133
7.3 Quasi-static electric field model. 138
7.4 Component fitting to resonance line profiles. 140
7.5 Detail of the CaXIX resonance line. 143
7.6 Summed spectrum of a flare. 144
7.7 Noisy spectra from the rise phase. 145
7.8 Method for the measurement of the flare equivalent width. . . . 146
7.9 Explanation of equivalent width 149
7.10 Testing the two band method:1 156
7.11 Testing the two band method:3 157
7.12 Evolution of upflows as seen in a line-width diagnostic plot . . . 158
7.13 Evolution of upflows as seen in a line-width diagnostic plot . . . 159
7.14 Line-width time plot: 14 October 1980 160
7.15 Deriving a mean upflow velocity. 161
7.16 Positions of flares on Sun's disc. 164
7.17 Line-width diagnostic diagram: effect of shifting the peak position. 170

7.18 Shifted synthesized resonance line profiles. 170
7.19 Frequency distribution of equivalent widths. 171
7.20 Synthesized line profiles with upflows 172
7.21 Dependence of flare upflow velocity on flare position: CaXIX . . 173
7.22 Simulated dependence of flare upflow velocity on flare position: CaXIX 174
7.23 Simulated dependence of flare upflow velocity on flare position: CaXIX 175
7.24 Dependence of flare random velocity on flare position: CaXIX . 176
7.25 Simulated dependence of flare upflow velocity on flare position: CaXIX 177
7.26 Simulated dependence of slow band equivalent width in flares with a significant contribution from slow upflows 178
7.27 Dependence of velocity upflow velocity on flare position: FeXXV 179
7.28 Dependence of flare random velocity flare position: FeXXV . . . 180
7.29 Simulated resonance line profiles: slow and fast upflows 181
7.30 Line-width time plot: 14 July 1980 186
7.31 Line-width diagnostic plot: 14 July 1980 (chan. 1) 187
7.32 Line-width diagnostic plot: 14 July 1980 (Chan. 4) 188
7.33 Velocity time plot: 8 April 1980 189
7.34 Line-width diagnostic plot: 8 April 1980 190
7.35 Line-width diagnostic plot: 8 April 1980 191
7.36 Line-width time plot: 21 May 1980 192
7.37 Line-width diagnostic plot: 21 May 1980 (Channel 1) 193
7.38 Line-width diagnostic plot: 21 May 1980 (Channel 4) 194
7.39 Line-width time plot: 5 May 1984 195
7.40 Line-width diagnostic plot: 5 May 1984 (Channel 1) 196
7.41 Line-width diagnostic plot: 5 May 1984 (Channel 4) 197
7.42 Line-width time plot: 30 April 1980 198
7.43 Line-width diagnostic plot: 30 April 1980 199
7.44 Line-width diagnostic plot: 30 April 1980 (Channel 4) 200
7.45 Velocity-time diagram: 5 July 1980 201
7.46 Line-width diagnostic diagram: 5 July 1980 (Ch 1) 202
7.47 Line-width diagnostic diagram: 5 July 1980 (Ch 4) 203
7.48 Line-width diagnostic diagram: 29 June 1980 (Ch 1) 204
7.49 Line-width diagnostic diagram: 29 June 1980 (Ch 4) 205

List of Tables

1.1 *GOES* soft X-ray classification. 18

2.1 Nomenclature for emission lines. 29

3.1 *Solar Maximum Mission* experiments 41
3.2 *FCS* Channels and data at home position. 43
3.3 *BCS* Channels and data 44

5.1 *BCS* and *FCS*: sensitivities and effective areas. 80
5.2 Flare turbulent velocity: results 82
5.3 Turbulent velocity: Abundance of data points for limb flares. . . 93

6.1 Flare cooling analysis: results. 125

7.1 Peak Equivalent Widths 163

Appendix: *SMM* Flares 212

CHAPTER 1

An Overview of the Solar Flare Phenomenon

Solar flares are very intense and quite localised bursts of energy which occur in the low density, magnetic-loop bound plasma that makes up the solar corona. Flares can last from anywhere between half an hour to several hours. Most of the life of a flare is taken up in the dissipation of the energy (up to 10^{32} erg) released during the first few minutes. It is generally held that the source of this energy is the magnetic field structure that confines the coronal plasma. This, and other issues such as the structure of flares are discussed in the sections below.

1.1 Flare observation.

The history of flare observation has been one of periods of growth which have coincided with the arrival of new and better instruments for observation. Although the first recorded observation of a solar flare was made without the help of any instruments, it was only possible because of its unusual brightness. The main growth in observational knowledge of flares is a direct consequence of more and more flares with a wider range of energies being observed in a more diverse set of wavelength bands.

The first flare to be observed and recognised as a distinct phenomenon occurred on the 1st of September 1859 (Carrington, 1860; Hodgson, 1860). This was a quite fortuitous discovery, as the flare was observed in white-light, and it must have been particularly bright to be seen against the intrinsic brightness of the photosphere. It is now known that flares stand out most against the Sun in wavelengths that are absorbed by the Earth's atmosphere, which may be unfortunate for purposes of flare observation but is fortunate in most other respects.

Thus it was not until the advent of radiation detectors that could be carried (in balloons, rockets and satellites) above the Earth's atmosphere that further advances were made in the study of solar flares. Captured *V2* rocket technology provided the vehicles for the recording of the first UV spectrum of the Sun (Baum *et al.*, 1946), and rockets continued to be the mainstay of high-altitude and space observation until satellites began to take over.

The major satellite-based solar observation programmes have been the *Orbiting Solar Observatory* (*OSO*) series of satellites, the Skylab astronaut-operated observation programme (1972-73), the *P78-1* satellite (1979-85), the *Hinotori* satellite (1984) and the *Solar Maximum Mission* (*SMM*) satellite (1980-89). It is the last of these programmes that this thesis is concerned with.

The *SMM* satellite has now been replaced by its successor *Yohkoh*, which is designed to explore further the areas of knowledge opened up by *SMM*. Such is the richness of the data gathered by *SMM*, however, that far from eclipsing the results gathered by *SMM*, any new discoveries by *Yohkoh* will always prompt re-examination and re-interpretation of *SMM* data in a search for consistency between the old and new observations.

The still unexhausted potential of *SMM*'s results reflects one of the main aspects of solar flare study - that it is heavily weighted by *observational* knowledge. That this observational knowledge has not yet been digested by *theory* is a long standing complaint which may be found in any number of reviews of the state of the science (Smith and Smith, 1963; page 447 of Sturrock, 1980; Emslie, 1992; page 1 of Tandberg-Hanssen and Emslie, 1988)

This thesis is a contribution to the effort to sift through, interpret and understand a decade of solar flare observation by *SMM*.

1.2 The observed structure of flares.

The work in this thesis is concerned with soft X-ray emission, but there is a lot more to the structure of a flare than is seen in the soft X-ray band alone. The appearance of a flare depends on the wavelength of the emission it is viewed in. Flares emit radiation of all wavelengths from radio at the lower energy end, through ultra-violet, visible, infra-red, soft and hard X-rays and right up to gamma-rays at the higher energy end. This section gives a summary of what is known about flare structure, and draws on observations of all relevant wavelengths.

Flares are associated with magnetic structures that extend from the photosphere, which lies at a depth of 10^3 km s^{-1} below the corona (Livi *et al.*, 1989). The footpoints of flare loops occur in regions of opposite magnetic polarity, with the loops themselves straddling the polarity inversion lines (neutral lines).

The two main observable features of flares in X-rays are the loop top and the loop footpoints. The footpoints are brightest in hard X-rays during the impulsive phase of the flare, and are also thought to be the source of soft X-ray emission. The loop tops are known to be stable sources of soft X-rays.

Although much modelling of flares is confined to the use of single loop models (Peres *et al.*, 1982) it is known that flares rarely occur in single isolated loops. Flares are most commonly seen to occupy one of two structural categories, in a size-based scheme devised by Pallavacini *et al.*, (1977).

(a) Compact flares
These are the smaller flares which cannot be resolved entirely. They are believed to consist of small loops which do not extend very far above the photosphere and have closely placed footpoints.

(b) Two ribbon flares
This configuration occurs only in the larger flares. The observed brightness pattern is interpreted as due to an arcade of loops which are triggered in sequence. As successive pairs of footpoints brighten, the flare takes on the appearance of a pair of parallel ribbons of brightness. To begin with, the ribbons lie very close to polarity inversion lines but are, in several cases, seen to move apart and away from the inversion line (Bhatnagar, 1986).

1.3 Flares in soft X-rays.

The work in this thesis is based on the analysis of soft X-ray emission (the 1 - 8 Å band of the electromagnetic spectrum) recorded by instruments aboard the *SMM* satellite. The energies associated with the soft X-ray waveband are high enough to distinguish a flare from it less energetic surroundings, but they are not so high that this waveband does not remain a useful diagnostic in the later, less energetic phases of the flare. Because of this, it is one of the most versatile wavebands for flare investigation.

1.3.1 Classification according to soft X-ray intensity.

The most commonly used total energy based classification of flares is the *GOES* classification. In this scheme, flares are ranked according to how bright they appeared to the soft X-ray spectrometers aboard the *Geostationary Operational Environmental Satellite* (*GOES*) series of satellites. Flares with flux rates between the limits shown in Table 1.1 are denoted by a multiplier placed after the class symbol. For example, a flare with an intensity of 1.4×10^{-3} erg cm^2 s^{-1} is a C1.4 flare. The class B is really a sub-class for very weak flares, and includes only flares with intensities less than 10^{-4} erg cm^2 s^{-1}, which are denoted by a multiplier of less than one, as in B0.7 . The figures for flare occurences are from private communications quoted in Section 1.2.1 of Tandberg-Hanssen and Emslie (1988). Of the two periods quoted, 1979-1980 was the height of the solar maximum, while 1976-1985 extends from the preceding minimum to the following one.

Table 1.1: SOFT X-RAY CLASSIFICATION OF FLARES.

GOES class	soft X-ray flux (erg cm^2 s^{-1})	Frequency of occurrence of flares above B class.	
		1979 - 1980	1976 - 1985
B	10^{-4}	-	-
C	10^{-3}	82%	74%
M	10^{-2}	16%	25%
X	10^{-1}	2%	1%
	TOTAL	100%(3447)	100% (17,986)

1.4 The Physics of Solar Flares

1.4.1 Coronal plasmas

Flares are a mainly coronal phenomenon and have many features in common with the corona. Because of this, it is worth giving a brief introduction to the corona before entering into a detailed discussion of flares themselves. Such an approach at least serves to identify which features of flares are truly peculiar to flares and which ones are common to all coronal phenomena.

The corona is the outermost layer of the Sun, lying immediately above the chromosphere, extending for a radial distance of about 10^4 km. Initially thought to be yet another layer of plasma wrapped around the layer below (the **plane-parallel model**), the ever-improving resolution of X-ray imaging instruments revealed it to have structure - it is in fact a collection of plasma bearing magnetic loops (Rosner, Tucker and Vaiana, 1978). The plane-parallel model of the corona, albeit in a diluted form, is still felt to be a valid description of the corona (Gabriel, 1992), but from the flare perspective it is the magnetic loop-bound structure that is relevant.

The main features of coronal plasmas are:

- High temperature
  The corona is the hottest region of the Sun outside the core [1], with a temperature of about 10^6 K and a low density (relative to the rest of the Sun) of about 10^8 particles cm^{-3}.

- High degree of ionization
  The bulk of the coronal mass (98.5%) is made up of hydrogen and helium, the remainder consisting of heavier elements produced by fusion in the core of the Sun. Because of the extremely high temperatures, the coronal elements are all highly ionised. This fact explains the existence of the coronal emission spectrum, which is dominated by the transitions of electrons in helium-like ions.

- Magnetically defined structure
  The solar magnetic field exerts a magnetic pressure given by $B^2/(8\pi)$, which, has a value of about 4×10^4 dynes cm^{-2} in the corona ($B = 10^3$ Gauss). The gas pressure in coronal plasmas, which is given by nk_BT, has a value of only about 1.4×10^{-2} dynes cm^{-2} ($n = 10^8$ cm^{-3}, $k_B = 1.4 \times 10^{-16}$ erg K^{-1}, $T = 10^6$ K). Because the gas pressure is so much less than the magnetic pressure, the coronal plasma is effectively contained within the coronal magnetic loop structures. The low resistivity of the coronal plasma also leads to the "frozen-in" field condition which will be discussed separately below.

1.4.2 Magnetic Diffusion in coronal plasmas

The low rate of magnetic diffusion, which is the rate at which magnetic field lines can drift through the coronal plasma, is the most important feature of coronal plasma as far as the energisation of flares is concerned. Because the coronal plasma is so highly conducting, no potential difference can be supported, which precludes the generation of an e.m.f ($= \underline{v} \wedge \underline{B}$). Thus if the plasma moves, the

[1]Solar models estimate the core temperature to be 1.5×10^7 K, a temperature which is matched by flares (Christensen-Dalsgaard, 1992).

magnetic field must move with it so that $\underline{v} = 0$ (and *vice versa*, if the magnetic field moves, the plasma moves with it).

However, for there to be any resistive dissipation (as there must be if flares do occur), there has to be a finite resistivity, which mitigates the frozen-in field condition to the extent that the magnetic field can drift, with a timescale given by $\tau_d = 4\pi L^2/\eta c^2$ (where L= flare scale length, v=plasma flow velocity and η=resistivity). The ratio between this timescale and the plasma flow timescale, $\tau_f = L/v$ is defined to be the **magnetic Reynolds number** $S = (4\pi vL)/(\eta c^2)$, which for a 10^6 K plasma in a 10^9 cm flare loop, has a value of about 10^{13}. This means that the magnetic field takes 10^{13} times as long to drift relative to the plasma as it takes it to move the same distance in tandem with the plasma.

1.5 The energization of flares.

A simple order-of-magnitude calculation shows that the only likely source of the 10^{32} erg of energy released during a flare is the coronal magnetic field. Neither the gravitational energy nor the thermal energy are sufficient.

Source	Form	Total Energy (erg s^{-1})
thermal energy	$3\,nkT\,V$	10^{28}
gravitational energy	$n\,V\,m_H\,gh$	10^{28}
magnetic energy	$(B^2/8\pi)\,V$	10^{32}

where $T = 10^6$ K, $n = 10^8$ particles cm^{-3}, $V = 10^{30}$ cm^3, $k = 1.4 \times 10^{-16}$ erg K^{-1}, $g = 2.74\times 10^4$cm s^{-2}, $h = 7 \times 10^7$ cm, $m_H = 1.7 \times 10^{-24}$ g and $B = 1000$ Gauss

1.5.1 The initial energy release: magnetic reconnection

The initial energization of flares is generally thought to be due to the release of the energy stored when magnetic field lines are twisted up by the motion of the magnetic loop footpoints (Parker, 1989).

The twisting is supposed to take place because the footpoints are anchored in the photosphere, parts of which are in motion relative to each other. When one footpoint of a loop anchored in one part of the photosphere is moved relative to the other footpoint, the loop gets twisted. The twisting can continue upto the point where it becomes energetically unstable, whereupon it takes on a less stressed loop configuration, with the excess energy being released to power the flare.

Exactly how this re-configuration takes place and how the stored energy is released is the subject of much theory and modelling. It is generally accepted that **magnetic reconnection** is the process by which field lines interact (Craig and McClymont, 1991; Démoulin *et al.*, 1993).

The reconnection process can only occur if the loops are very close together. This follows from the earlier observation that field lines are practically "frozen-in". Unless the length scale L over which the magnetic diffusion is taking place is quite small, the diffusion time scale τ_d ($\approx L^2/10^3$), will be far too long to explain the rate of energy release seen in flares. In addition to the requirement that the reconnecting loops be very close together (less than 10^9 cm apart), the plasma on opposite sides of the reconnection site is required to flow across the field lines towards the reconnection point, and in the process is accelerated so much that it is ejected violently outwards from the reconnection site. Thus in the reconnection scenario, it is the kinetic energy of this ejected plasma that serves to power the flare.

1.5.2 Continuing energy release in flares.

Although some flares do cool unhindered after the initial enery release, most flares have been seen to exhibit signs of post-flare heating (Švestka, 1989; Sylwester *et al.*, 1993). The most likely energy transport mechanism are Alfvén waves which transport mechanical energy up the flux tubes that are thought to connect the convection zone and photosphere with the corona.

1.6 This thesis.

There are two commonly recognised approaches to the analysis of flare data (Emslie, 1992). One is the **direct approach** which assumes a magnetic field structure, within which magnetohydrodynamic theory is applied to predict the magnitude and timing of energy release and its subsequent dissipation. These predictions are then compared with the observations.

The other approach is the **inverse approach** which consists of deducing the physical conditions from observations and then tailoring models to agree with the observations (for example Winglee *et al.*, 1991(a) and (b), or Antonucci *et al.*, 1987).

The second of these approaches is much more true to the data, and is a lot more useful from the point of view of the data analyst. The work in this thesis is based on data analysis, and so draws upon the results of several practitioners of the inverse approach

The work presented in this thesis is based on observations made by two of the instruments aboard the *Solar Maximum Mission* (*SMM*) satellite which flew between 1980 and 1989. The observations made by *SMM* have been the basis of most of the advances in solar flare physics seen over the last decade, and continue to be the source of new discoveries.

The two instruments in question are the *Bent Crystal Spectrometer* (*BCS*) and the *Flat Crystal Spectrometer* (*FCS*), both of which were built by a consortium led by the Mullard Space Science Laboratory.

This chapter, **Chapter 1**, has given an overview of the current state of knowledge of solar flares, and has set in context the work presented in the chapters which follow.

In **Chapter 2** the diagnostic techniques which are used in this thesis are introduced. These spectroscopic techniques are powerful probes of the physics of solar flares, and are commensurately complicated.

The *Solar Maximum Mission* is introduced in **Chapter 3**. The data used in this thesis was recorded by two of the spectrometers aboard *SMM*, the *FCS* and the *BCS*, and an outline of these instruments is given.

In **Chapter 4** the effects of the non-uniformity of the bent crystals in the *BCS* are discussed and the in-flight measurement of this non-uniformity is presented. The results obtained in this Chapter are used in Chapter 5.

In **Chapter 5**, non-thermal mass motion of flare plasma is discussed. Some of the measured non-thermal mass motion was thought to be due to an instrumental effect of the *BCS*, and this instrumental contribution has never been measured but only estimated. Using *FCS* images in conjunction with *BCS* spectra, this effect is measured in a large sample of flares, and then subtracted to yield a true value for the amount of non-thermal mass motion in flare plasmas.

In **Chapter 6**, the cooling of flares in the decay phase is examined for evidence of decay phase heating. Again, *BCS* spectra are used together with *FCS* images, this time in conjunction with a flare cooling model, to look for the presence of decay phase heating.

In **Chapter 7**, plasma velocities in the rise phase are investigated. A simple but powerful method of measuring plasma upflows is applied to *BCS* spectra, and the results compared with the predictions of various current models of the rise phase.

The various conclusions arrived at in Chapters 4, 5, 6 and 7 are brought together in **Chapter 8**, where suggestions are made as to how the work in this thesis may be extended further.

CHAPTER 2

Basic Diagnostics of Solar Flares

This thesis is based on the analysis of soft X-ray emission (1 - 8 Å) from solar flares. The chapters which follow this one each address particular questions about flares, and each one uses diagnostic techniques specifically developed to deal with these questions. But these specially developed techniques themselves are based on some fundamental soft X-ray diagnostics, and it is these fundamental diagnostics which will be discussed in this chapter.

There are two ways in which soft X-rays may be used to investigate flares. The first is to make images of the emission and use the shapes and brightness distributions so obtained to gain an idea of the *structure* of flares. The second is to redistribute the emission from flares into a spectrum and use spectroscopic analysis to find out about the *temperature, density and dynamics* of the flare plasma.

The second of these methods, spectroscopic analysis, is by far the more powerful and is commensurately complicated. For this reason this chapter will be devoted to introducing the spectroscopic techniques relevant to this thesis.

2.1 Soft X-ray Spectroscopy of Flares.

In the conditions of extreme temperature and low density that are found in flares, atoms exist in a highly ionised state. Even heavy ions such as Ca and Fe are found with all but their last remaining pair of electrons stripped off, leaving them in a **helium-like** state. [1] The soft X-ray analysis in this thesis relies exclusively on the emission from the helium-like ions in flare plasma. The

[1] **Notation for ions in solar physics:** ions are referred to by the their symbol followed by their excess positive charge (= the number of electrons that have been removed), so that helium-like calcium and helium-like iron are denoted by Ca XIX and by Fe XXV, respectively.

immediate reason for this is that the instruments being used were specifically designed to detect these emission lines, but the reason for designing the instrument around the emission lines of a helium-like ion is that the atomic physics of a simple three-body ion is much better understood than that of more complex ions. Because the atomic processes involved are already quite well understood, the spectroscopic analysis effort can concentrate on measuring physical conditions such as temperature, density and plasma velocity.

In the sections that follow, the atomic processes relevant to flare soft X-ray spectra will be introduced, and an explanation given of how they may be used directly to measure temperature, density and plasma velocity.

2.1.1 The intensity of emission lines.

In this section an expression will be derived that relates the intensity of an emission line to the temperature and density of the plasma. To begin with, an assumption may be made, that in a flare plasma all excitations are reversed by recombinations. This assumption rests on the relatively short lifetime (of the order of 10^{-3} seconds) of the transitions that occur in the helium-like ions in flare plasmas. This time is much shorter than the time it would take for any macroscopic changes to take place in the flare plasma.

It follows that the intensity of radiation absorbed by electrons being excited from the ground state to a second state, I_{g2}, is equal to that of the radiation emitted by electrons decaying from the excited state to the ground state.

$$I_{g2} = I_{2g} = N_e \, N_i \, C_{g2} \ \text{photons cm}^{-3} \tag{2.1}$$

where N_e = number density of electrons ,
N_i = number density of ions in the ground state and
C_{g2} = excitation rate coefficient from the ground state to state 2.

This expression can be considered to be the line intensity of the emission from a volume element dV. To obtain the line intensity for emission from a volume V, it has to be integrated over V.

$$I_{2g} = \int_V N_e \, N_i \, C_{g2} \, dV \tag{2.2}$$

The line intensity has so far been expressed in terms of photon flux. If E_{2g} is the energy per photon and 1.6×10^{-12} is the conversion factor to express this energy in ergs, then

$$I_{g2} = 1.6 \times 10^{-12} \int_V N_e \, N_i \, C_{g2} \, E_{2g} \, dV \ \text{ergs cm}^{-3}\text{s}^{-1} \tag{2.3}$$

On the surface of the earth, at a distance R away from the Sun, the observed intensity is a fraction of the total intensity spread over an area of $4\pi R^2$.

$$I_{2g} = \frac{1.6 \times 10^{-12}}{4\pi R^2} \int_V N_e\, N_i\, C_{g2}\, E_{2g}\, dV \tag{2.4}$$

The excitation rate coefficient, C_{g2} can be expressed in terms of the oscillator strength f_{g2} [2] , the electron temperature T_e and the integrated Gaunt factor g [3] , and the exciting photon energy E_{g2}.

$$C_{g2} = 1.7 \times 10^{-3} f_{g2}\, E_{g2}\, T_e^{-\frac{1}{2}}\, g\, e^{-\frac{E_{g2}}{kT}} \tag{2.5}$$

Expanding the expression for the line intensity:

$$I_{2g} = \frac{6.8 \times 10^{-16}}{\pi R^2} \int_V f_{g2} E_{g2}\, T_e^{-\frac{1}{2}}\, g\, e^{-\frac{E_{g2}}{kT}}\, N_e\, N_i\, C_{g2}\, E_{2g}\, dV \tag{2.6}$$

$$N_i = \frac{N_i}{N_{element}} \frac{N_{element}}{N_H} N_H \tag{2.7}$$

$$N_i = A_{zi}\, A_z\, N_H \tag{2.8}$$

where A_{zi} and A_z are respectively, the abundance of the ion with respect to the element, and the abundance of the element with respect to hydrogen.* Since most of the electrons present in the corona were stripped off hydrogen and helium atoms, the former supplying its sole electron and the latter its pair of electrons, the number of coronal electrons can be equated with the number of hydrogen and helium ions.

$$N_e = N_H + 2N_{He} = N_H \left(1 + 2\frac{N_{He}}{N_H}\right) = \frac{N_H}{0.85} \tag{2.9}$$

Thus the ground state population can be related to the total number of electrons.

$$N_i = A_{zi}\, A_z\, 0.85 N_e \tag{2.10}$$

Recalling the expression for the line intensity recorded on the Earth (Equation 2.6) and substituting for N_i:

$$I_{2g} = 7.75 \times 10^{-43} \int_V A_{zi}\, A_z\, N_e^2\, f_{g2}\, g\, T_e^{-\frac{1}{2}}\, e^{-\frac{E_{g2}}{kT}}\, dV \tag{2.11}$$

---

[2] **Oscillator strength** f_{g2} - this is a substitute for the Einstein rate coefficients A and B. The sum of the f-values for a given level is equal to the effective number of electrons. E.g.: the sum of the f-values for absorption to all levels from the ground state of hydrogen is equal to 1.

[3] **Gaunt factor** g - this is a measure of the probability that an electron goes from one energy to another, and depends on the energy change and (inversely) on the frequency. It introduces a quantum mechanical factor to this originally classical treatment of line emission. (Gaunt, 1930; van Regemorter, 1962; Billings, 1966)

* N_H = number density of hydrogen ions

$$I_{2g} = 7.75 \times 10^{-43} G(T_e)\, f_{g2} \int N_e^2\, dV \text{ erg cm}^{-3} \text{ s}^{-1} \tag{2.12}$$

The constant terms A_z, A_{zi}, g, and the temperature dependent terms T_e and $e^{-\frac{E_{g2}}{kT}}$ have been gathered together in the term $G(T_e)$, which is called the **contribution function** or the **emissivity function.** The values of the emissivity function have been determined for helium-like ions by a number of workers, (eg: Doschek and Feldman, 1987). The emissivity functions used in this thesis are shown in Figure 2.1.

Equation 2.12 is valid for an isothermal volume of plasma. The integral $\int N_e^2\, dV$ is called the **emission measure** and is a measure of number of electrons with a particular temperature (T_e) within a particular volume (or within the field-of-view).

2.1.2 Atomic processes in flare plasma.

The corona, unlike the underlying layers of the Sun, is not in a state of local thermodynamic equilibrium [4] and a detailed balance [5] does not exist between upward transtions of electrons and their reverse processes. However, because the *degree of ionization* is very closely coupled to temperature, a steady state relation between temperature and the degree of ionization can be determined for each of the various ions present. The emission spectrum of flare plasmas is dominated by contributions from two types of *spontaneous downward transitions* which reverse *collisionally induced upward transitions.* These three process are assumed to be in balance, such that:

$$\begin{array}{lcccl} \text{electron} & & \text{radiative} & & \text{dielectronic} \\ \text{collisonal} & = & \text{recombination} & + & \text{recombination} \\ \text{rate} & & \text{rate} & & \text{rate} \end{array}$$

(a) Electron collisional excitation.

Collisionally induced excitation dominates over radiatively induced events because the corona is optically thin to most of the radiation from the photosphere and the chromosphere. In other words, the chromospheric and photospheric photons have energies that are too low to excite coronal electrons.

[4] **Local thermodynamic equilibrium (LTE)** is found where the photon mean free path is much shorter than the temperature gradient. This ensures an even distribution of photon energies, and hence of temperature, at least locally. LTE is unsually accompanied by detailed balance. In the corona, the low density means that the photon mean free path is long, and a state of LTE does not exist.

[5] **Detailed balance** is the state in which every photon emission is balanced by the absorption of a photon of the same energy, and is the state in which the solar interior exists. In the corona, about half the emitted photons escape to space and this alone is enough to preclude detailed balance.

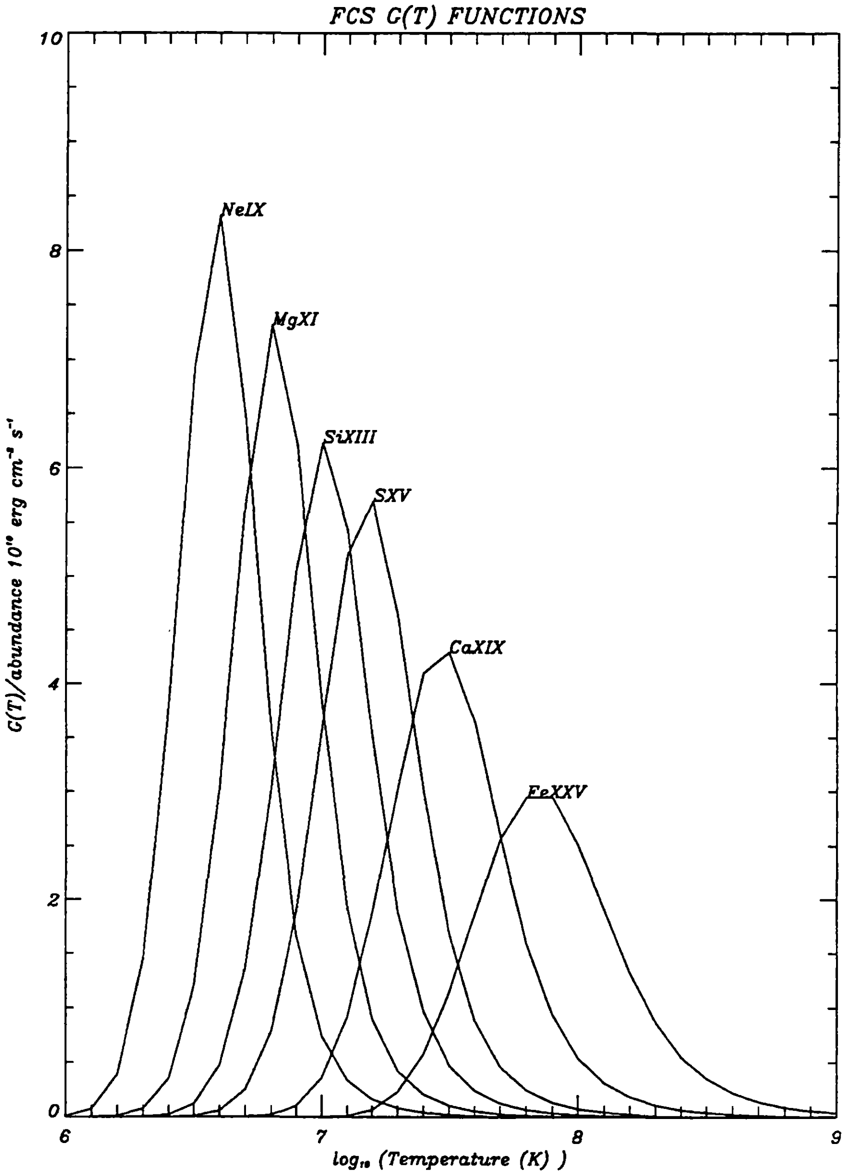

Figure 2.1: The emissivity functions of some helium-like ions. *The intensity of the resonance line transitions of the helium like ions observed by the soft X-ray spectrometers on the* Solar Maximum Mission *satellite. These calculations have assumed that* $EM = 10^{70} cm^{-3}$ *and that the ions have unit abundance (with respect to hydrogen).*

When an electron collision results in the excitation of an electron from the $1s^2$ (ground) state to the $1s2p$ state, the transition is known as a **resonance transition**.

(b) Radiative recombination

This is a *two-body* recombination process in which an excited helium-like ion returns to its ground state by the spontaneous decay of the outer of the two electrons. The spontaneous radiative decay of an electron from the $1s2p$ state to the $1s^2$ (ground) state is accompanied by the emission of a resonance-line photon.

(c) Dielectronic recombination

This is a *three-body* recombination process,† and involves the helium-like ion, one of its bound electrons and a third colliding electron. In ordinary, two-body recombination, the exciting electron does not feature, having earlier succesfully excited one of the bound electrons of the helium-like ion, and then gone on its way.

The dielectronic process takes place when the energy of the colliding electron is just below that required to excite a resonant transition. It now does two things: it excites one of the bound electrons to a non-resonant excited state, and is itself captured into an outer excited state (above the 1st ionization limit). The ion is now in a doubly excited state, and has three electrons bound to it (it is now **lithium-like** and has a charge of $Z-1$ where Z was its charge in its helium-like ionization stage).

The excited states above the 1st ionization limit of the helium-like ion are called **auto-ionization levels** and occur close to the bound states of the lithium-like ion. There are two ways in which the doubly-excited ion can de-excite. One way is to simply reverse the dielectronic capture, and for the ion to auto-ionize by spontaneously losing the previously captured electron. Because this electron is not returning to a lower energy bound state, no radiation accompanies auto-ionization.

If it does not auto-ionize, the inner excited electron in the now Li-like ion will de-excite to a lower state. The energy of this transition, which to begin with is lower than the resonance transition, is further attenuated by the presence of the colliding electron which acts against the potential of the nucleus. The result of this transition is a line that is displaced to the long wavelength side of the resonance line by a few mÅ - it is a **satellite** of the resonance line.

† Its importance as a coronal emission mechanism was established by Burgess (1964) and the theory described in detail by Gabriel (1972).

The colliding electron, then cascades to the ground state of the now lithium-like ion (which was formerly helium-like).

$$X^{+Z} + e^- \rightleftharpoons X^{+(Z-1)}_{doubly\ excited} \tag{2.13}$$

$$X^{+(Z+1)}_{doubly\ excited} \rightarrow X^{+(Z-1)}_{singly\ excited} + h\nu_{dielectronic\ satellite} \tag{2.14}$$

$$X^{+(Z-1)}_{singly\ excited} \rightarrow X^{+(Z-1)} + h\nu_1 + h\nu_2 + h\nu_3 + ... \tag{2.15}$$

It cannot escape attention that dielectronic recombination is no more or less probable a way of de-excitation than is auto-ionization. This means that the intensity of the dielectronic recombination line, as given by the expression in Equation 2.1 is true only if dielectronic recombination is the only likely de-excitation process. Because auto-ionization is also likely to happen Equation 2.1 must be modulated by the probability that dielectronic recombination will occur.†

$$I_{2g} = N_e\, N_i\, C_{g2}\, \frac{A_{DR}}{A_{auto} + A_{DR}} \tag{2.16}$$

The last term, which gives the probability of dielectronic recombination occurring after dielectronic capture, is known as the **branching ratio**. This term is included in the calculation of the $G(T_e)$ function in Equation 2.12.

2.1.3 Nomenclature for flare emission lines.

The main features of the spectra of the helium-like ions that dominate flare soft X-ray emission were classified by Gabriel (1972). The nomenclature of some of these lines, those that are used in the work presented in this thesis, are listed in Table 2.1. Figures 2.2 and 2.3 show how this labelling system corresponds to the spectra of the helium-like ions Ca XIX and Fe XXV.

TYPE	SYMBOL	TRANSITION				
resonance	w	$1s2p$	$^1P_1$	-	$1s^2$	$^1S_0$
dielectronic recombination	k	$1s2s2p$	$^2P_{1/2}$	-	$1s^22s$	$^2D_{5/2}$
dielectronic recombination	j	$1s2s2p$	$^2P_{3/2}$	-	$1s^22s$	$^2D_{5/2}$
forbidden	z	$1s2s$	$^3S_1$	-	$1s^2$	$^1S_0$
intercombination	x	$1s2p$	$^3P_2$	-	$1s^2$	$^1S_0$
intercombination	y	$1s2p$	$^3P_1$	-	$1s^2$	$^1S_0$

Table 2.1: Nomenclature for flare emission lines devised by Gabriel (1972).

† A_{auto} = probability that auto-ionization will take place.
A_{DR} = probability that dielectronic recombination will take place.

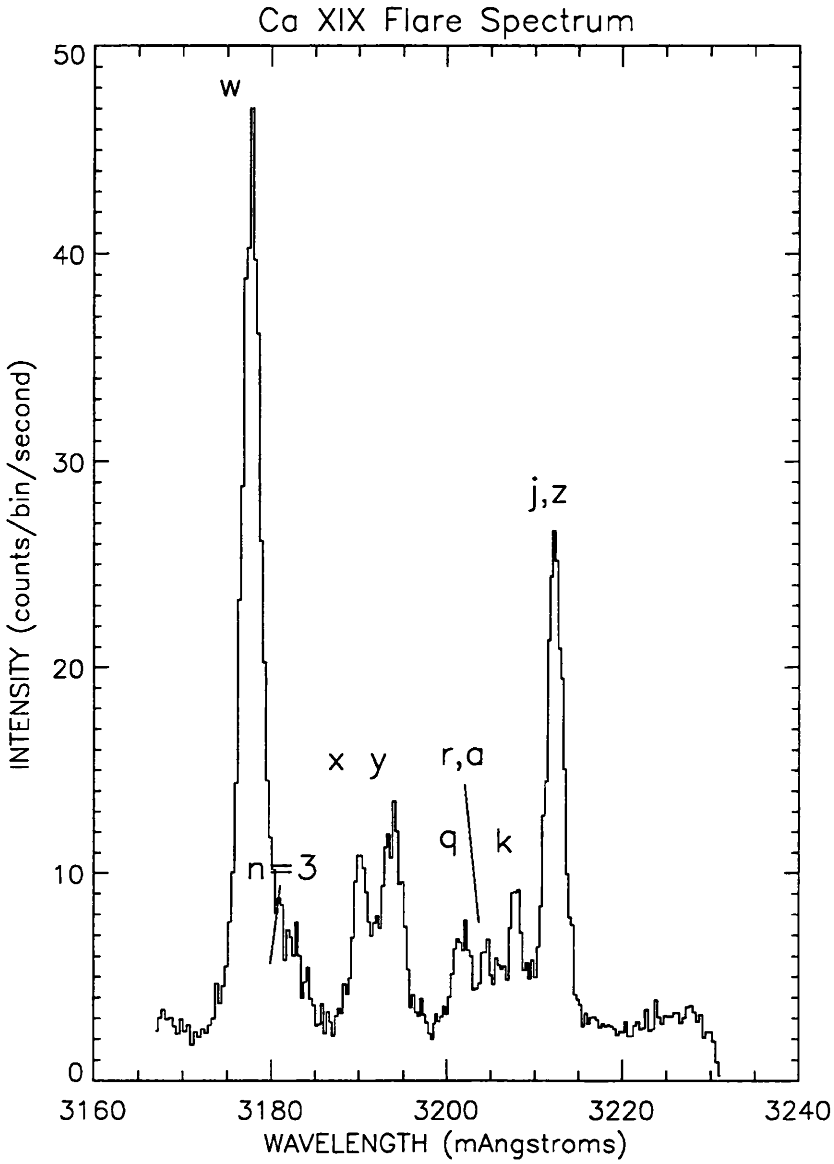

Figure 2.2: The main features of the spectrum of a helium-like ion. *This spectrum is from Ca XIX, which is Ca with 19 electrons removed from it. The nomenclature used in this figure corresponds to that given in Table 1.1, and was devised by Gabriel (1972)*

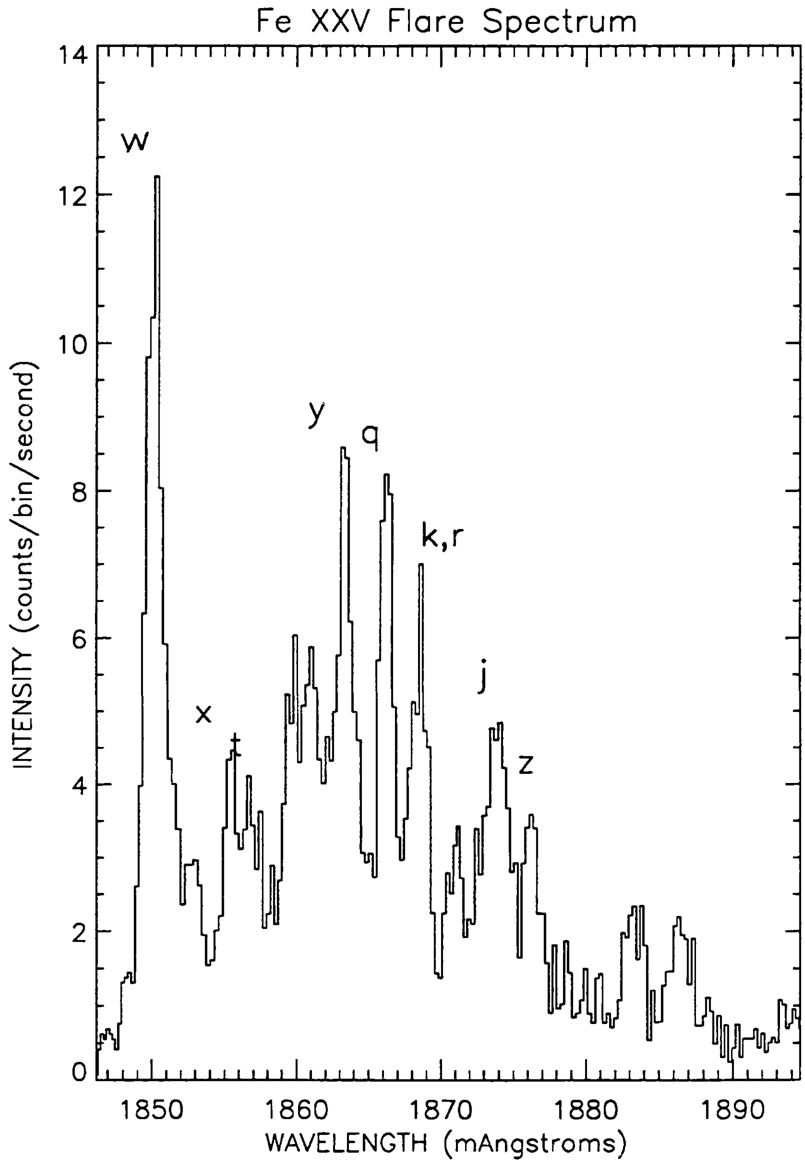

Figure 2.3: The main features of the spectrum of a helium-like ion. *This spectrum is from Fe XXV, which is Fe with 25 electrons removed from it. The nomenclature used in this figure corresponds to that given in Table 1.1, and was devised by Gabriel (1972)*

2.1.4 Line Ratio Diagnostics.

The relative intensities of the emission lines of helium-like ions may be used to determine the temperature and density of the plasma.

2.1.4(a) Determination of electron temperature.

The temperatures measured from soft X-ray emission lines are called **electron temperatures** because these emission lines are due to collisions of unbound electrons with ions, and are a measure of the thermal energies of these electrons (the thermal energy of an electron is equal to $\frac{3}{2}k_B T_e$, where T_e is the electron temperature). Electron temperatures can be determined from three different pairs of line:

1. Ratio of intensities of dielectronic recombination line to resonance line.

2. Ratio of intensities of the resonance lines of adjacent ionization stages, e.g: Ca XVIII to Ca XIX.

3. Ratio of intensities of resonance lines from the same ion, which requires at least a three-level ion.

The most commonly used method in flare physics, and the one used in this thesis, is the dielectronic satellite-to-resonance line ratio. The advantages of deriving temperatures from the intensity ratios of dielectronic recombination lines to resonance lines are threefold:

a. **The close spacing** of the dielectronic recombination line and the resonance line means that both lines can be picked up by the same detector, or the same channel of a multi-channel detector (as is the case with the *SMM-BCS*).

b. **The similar intensities** of the two lines means that the dynamic range of the detector does not have to be impractically large.

c. **Not over-extending the isothermal assumption** is a virtue that the dielectronic-to-resonance line ratio derives from drawing on emission lines from the same ion. If the line ratio was being taken between different ions, the assumption being made would be that quite widely separated ions have the same temperature. Also, the need to know relative abundances is eliminated.

The intensities of the resonance line (following the expression given in Equation 2.1) and the dielectronic recombination line (following the expression given in Equation 2.16) are:

$$I_{res} = N_e\, N_i\, C_{res} \tag{2.17}$$

$$I_{DR} = N_e\, N_i\, C_{DR} \frac{A_{DR}}{A_{auto} + A_{DR}} \tag{2.18}$$

Taking the ratio between these two lines gives:

$$\frac{I_{DR}}{I_{res}} = \frac{C_{DR}}{C_{res}} \left(\frac{A_{DR}}{A_{auto} + A_{DR}}\right) \tag{2.19}$$

The ratio $\frac{C_{DR}}{C_{res}}$ may be eliminated as follows:
The radiative recombination rate for the resonance line, C_{res}, depends on the electron temperature T_e and the energy of the transition E_{res}:

$$C_{res} \approx \frac{const.}{T_e^{1/2}}\, e^{-E_{res}/kT_e} \tag{2.20}$$

The dielectronic capture rate coefficient C_{DR} is related to the dielectronic recombination rate coefficient A_{DR} because one process is the reverse of the other. In other words they are in detailed balance, and are governed by the Boltzmann-Saha equation:

$$\frac{A_{auto}}{C_{DR}} = \frac{2(2\pi mkT)^{3/2}}{h^3} \frac{1}{g_{DR}}\, e^{-E_{DR}/kT_e} \tag{2.21}$$

Using Equation 2.21, C_{DR} can be substituted for in Equation 2.19 to give:

$$\frac{I_{DR}}{I_{res}} \approx \frac{1}{T_e}\, e^{(E_{res}-E_{DR})/kT_e} \frac{A_{auto}}{A_{auto} + A_{DR}}\, A_{DR} \tag{2.22}$$

When A_{auto} is very large (about 10^{13} s^{-1}), $\frac{A_{auto}}{(A_{auto}+A_{DR})} \approx 1$ and I_{DR}/I_{res} varies as A_{DR}. The coefficient A_{DR} itself varies as Z^4, which means that it becomes particularly strong for the heavy ions that are the sources of the spectra analysed in this thesis (10% for calcium and 50% for iron). This term is of course constant for a given ion. This leaves only the exponential term to be dealt with before the intensity ratio can be pared down to its linear temperature dependence.

The energy difference $E_{res} - E_{DR}$ between the resonance line transition and the dielectronic recombination transition is small compared with kT_e, and so permits the $\frac{1}{T_e}$ term to dominate the temperature dependence.

The use of the dielectronic recombination line and the resonance line as a temperature diagnostic has been described thus far in mainly mathematical terms. An understanding of this method would be consolidated by considering what is happening physically.

It is safe to assume that the energy (or temperature or thermal velocity) distribution of the free electrons in a flare plasma follows the Maxwell-Boltzmann law.

Dielectronic capture happens only to those electrons with energies within an auto-ionization width of the excitation energy E_{DR} of the dielectronic recombination transition. Resonance transitions are excited only by electrons with energies above the excitation energy of the resonance transition E_{res}.

Thus these two lines are sampling the population distribution of the free electrons at two different energies, which is sufficient to define a unique Maxwell-Boltzmann distribution, which in turn has a unique temperature associated with it. It is this temperature which is being measured when the dielectronic-to-resonance line ratio is measured.

The spectra of the helium-like ions Ca XIX and Fe XXV (shown in Figures 2.2 and 2.3) offer the choice of the resonance (w) line and several dielectronic recombination lines. A glance at the Ca XIX spectrum, however, will show that the j and z lines are so close in wavelength that it would not be possible to extract the intenisty of the j line alone. For this reason the w/k line ratio is used to determine temperature from Ca XIX spectra. The problem of a blended j line does not occur in Fe XXV spectra, and the w/j line ratio is used to determine temperature.

2.1.4(b) Electron density.

In the energy level diagram for a helium-like ion (Figure 2.4), the curved arrows connecting the four excited states represent the jumps that occur at different densities.

At low densities ($\sim 10^8$ cm^{-3} for O VIII) all four energy levels decay to the ground state. As the density increases, however, the increasing number of collisions by exciting electrons prevents bound electrons from remaining in the lower energy levels, and the higher energy levels begin to fill up at the expense of the lower energy levels. The first energy level to be depopulated is the 1s2s ^{3}S, from which electrons move up to the 1s2p ^{3}P level. This depopulation is marked with the symbol (i) on Figure 2.4. It is followed by the depopulations marked (ii) and (iii), ending up with all electrons in the 1s2p ^{1}P level.

Thus as the density increases, the z, 2-photon and y lines successively decrease in intensity and eventually disappear, while the w line increases in intensity. This property may be exploited by using the intensity ratios of different pairs of lines for different density ranges.

2.2 Differential Emission Measure.

The concept of the emission measure of a plasma was introduced in the derivation of an expression for the intensity of an emission line (see Equation 2.12). To recapitulate, the emission measure is defined to be:

$$\int_V N_e^2 \, dV = N_e^2 \, V \tag{2.23}$$

where N_e is the electron density. This expression is only valid in a volume V where all volume elements dV are at the same temperature.

Because in fact flares are *not* isothermal, and have a distinct temperature structure, it would be useful to define some quantity which expressed this variation. The integral quantity of the emission measure can be re-expressed as a differential quantity, which is called the **differential emission measure (DEM)**.

Various definitions of the DEM have been given, and the most rigorous is that given in Craig and Brown (1976), but a good working definition would be as follows:

$$DEM(T_e) = n_e^2(T_e) \, \frac{dV}{dT_e} \tag{2.24}$$

It is the measure of the number of electrons with a particular temperature located within a given (or unit) volume of plasma.

A full exposition of the use of the differential emission measure to analyse X-ray spectra has been given by Withbroe (1975). Sylwester, Schrijver and Mewe (1980) have adapted Withbroe's method specifically for use with *SMM-BCS* and *FCS* data, and appraisals of this adaptation have been made by Fludra and Sylwester (1986).

The basic principle of the use of the differential emission measure is that each emission line gives one value of $DEM(T_e)$ for a particular temperature range. In other words, there exist a series of expressions,

$$I_1 = \int G_1(T_e) \, DEM(T_e) \, dT_e \, , \tag{2.25}$$

$$I_2 = \int G_2(T_e) \, DEM(T_e) \, dT_e \, , \tag{2.26}$$

$$I_3 = \int G_3(T_e) \, DEM(T_e) \, dT_e \, , \tag{2.27}$$

$$\ldots \quad . \quad \ldots\ldots\ldots\ldots \quad , \tag{2.28}$$

$$\ldots \quad . \quad \ldots\ldots\ldots\ldots \quad , \tag{2.29}$$

$$\ldots \quad . \quad \ldots\ldots\ldots\ldots \quad . \tag{2.30}$$

which can be solved simultaneously to yield $DEM(T_e)$.

The differential emission measure so obtained can be compared with that calculated from flare models, and is a powerful test of the validity of such models.

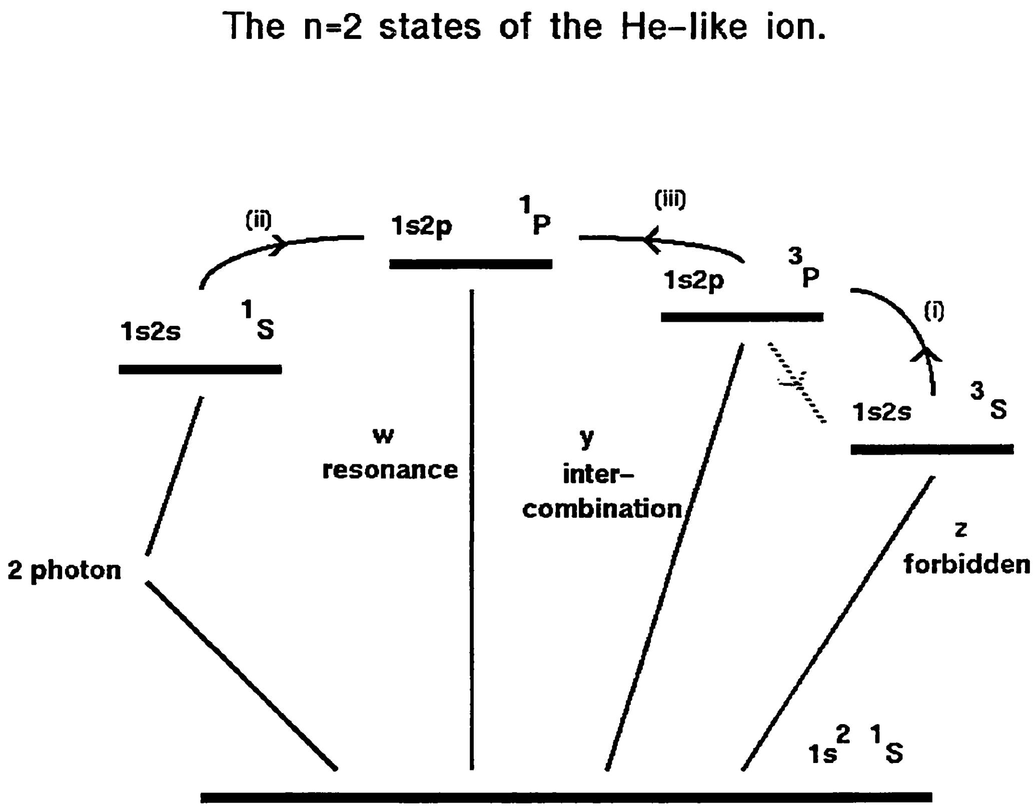

Figure 2.4: The energy level diagram for a helium-like ion. *Population interchange between the ^1S,^3P and ^3S levels to the ^1P level is a function of density. At high densities, all electrons occupy the ^1P state, augmenting the* w*-line intensity and diminishing the intensities of the* y*- and* z*- lines*

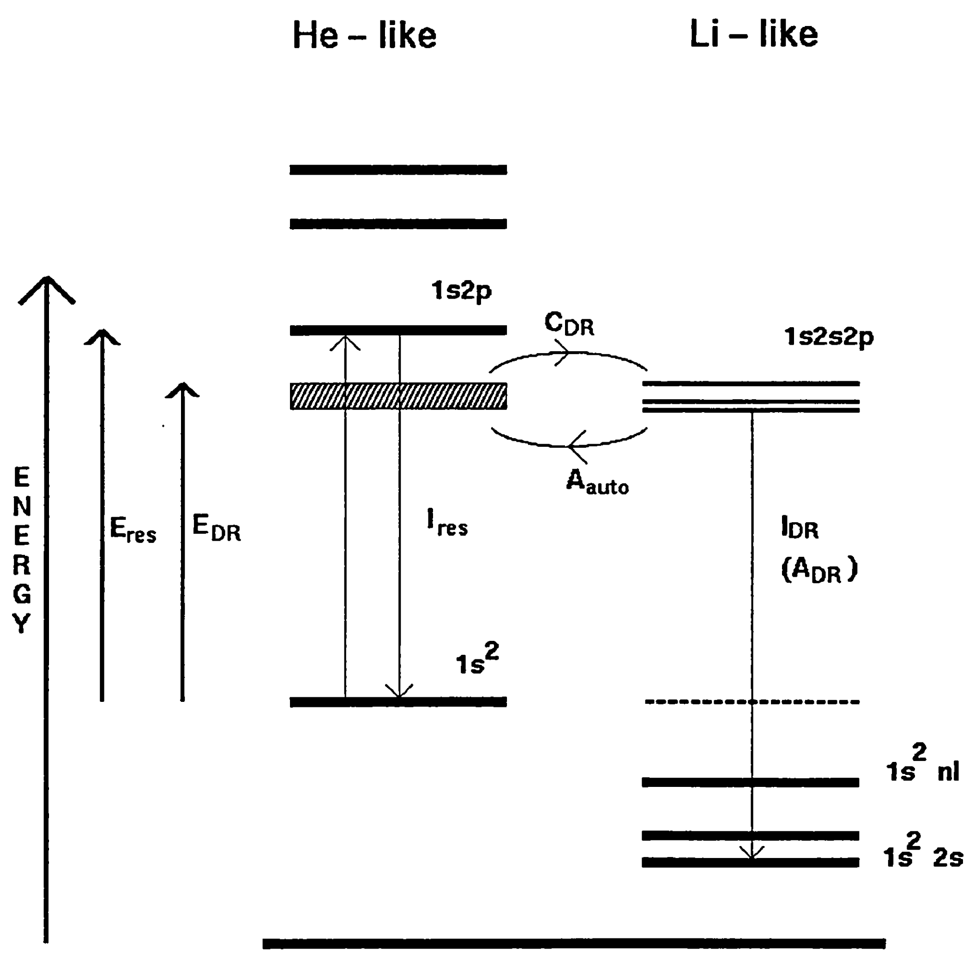

Figure 2.5: The energy level diagram for dielectronic recombination. *C_{DR}, A_{DR}, I_{DR} are respectively the capture coefficent, the auto-ionization rate and the line intensity for dielectronic recombination, A_{auto} is the auto-ionization rate, and E_{res} and E_{DR} are the energies that correspond to the resonance transition and the dielectronic transition respectively.*

CHAPTER 3

The *Bent Crystal Spectrometer* and the *Flat Crystal Spectrometer*

3.1 The *Solar Maximum Mission*

The object of the *Solar Maximum Mission* (*SMM*) was to obtain interrelated information about different aspects of the solar flare phenomenon. (Bohlin *et al.*, 1980).

To this effect, a satellite-borne experiment was prepared by a consortium of twelve institutions [1] to observe the Sun during the maximum activity year, 1979-1980. The result of this endeavour, the 2360 kg, 4.0 m long, cylindrically-shaped *SMM* satellite was launched on 14 February 1980 into an almost perfectly circular orbit with an altitude of 574 km and an inclination of 28° to the equator, which took 96 minutes to traverse. The *SMM* satellite had been designed with a minimum lifetime of 1 year, and was provided with an attachment to allow its retrieval by one of the Space Shuttles (Chipman, 1981).

In the event, it turned out that the *SMM* satellite had considerably more life in it than was expected. The in-orbit retrieval facility was actually put to use in April 1984, but only for a quick repair on board the Space Shuttle *Challenger*, after which the satellite was re-launched to continue observing the Sun.

The *SMM* statellite remained in orbit until 1989, by which time the next solar maximum was beginning to gather pace. Ironically, the very longevity which allowed it to witness its second solar maximum was also the cause of

[1] Appleton Laboratory, Astronomical Institute at Utrecht, High Altitude Observatory, Jet Propulsion Laboratory, Lockheed Palo Alto Research Laboratories, Max Planck Institute for Physics and Astrophysics, Mullard Space Science Laboratory, NASA-Goddard Space Flight Center, NASA-Marshall Space Flight Center, Naval Research Laboratory, University of Birmingham and University of New Hampshire.

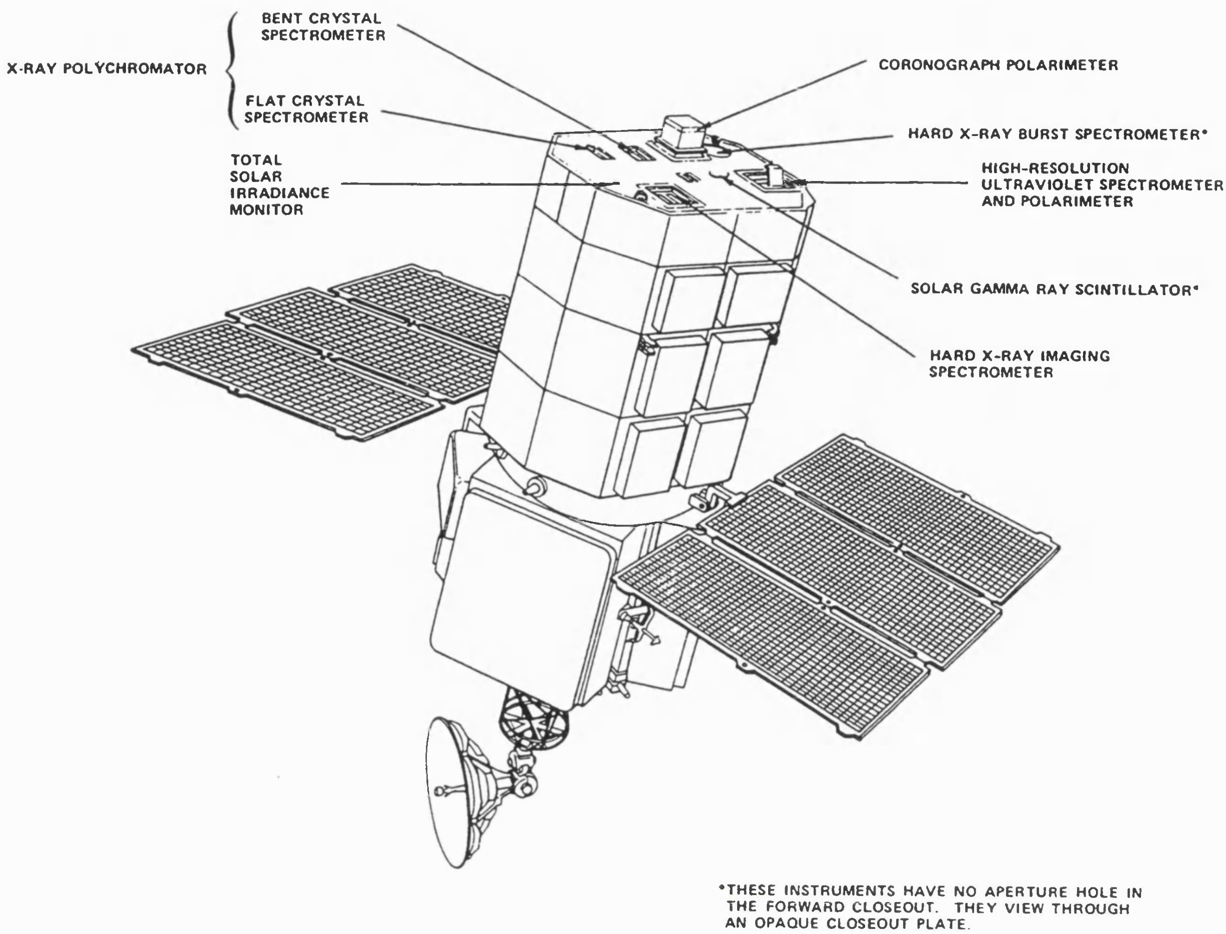

Figure 3.1: The *Solar Maximum Mission* satellite

its downfall. The heating of the upper part of the Earth's atmosphere by the approaching solar maximum resulted in it expanding sufficiently to impinge on the *SMM* satellite orbit and increase its atmospheric drag. Unable to maintain its altitude, the satellite began to spiral Earth-wards and finally disintegrated over the Indian Ocean in December 1989.

The payload of the *SMM* satellite consisted of 8 individual experiments, each one covering a different spectral range. Together, they were intended to produce spectra and images of the Sun in the wavelength ranges that were known to be crucial for the investigation of solar activity.

The work in this thesis is based on data taken with the *X-ray Polychromator*, which is the collective name for the *Bent Crystal Spectrometer* (*BCS*) and the *Flat Crystal Spectrometer* (*FCS*). These two instruments will be described in the detail necessary for this thesis in Sections 3.2 and 3.3. A fuller description may be found in Acton *et al.*, 1980 and Rapley *et al.*, 1977.

Instrument		Data type	Spectral range	Target
Gamma-ray Spectrometer		spectra	0.3-10.7 MeV	flare onset
Hard X-ray Burst Spectrometer		spectra	20-300 keV	flare onset
Hard X-ray Imaging Spectrometer		images	3.5-30 keV	flare onset
Soft X-ray Polychromator:	*BCS*	spectra	1.7-3.23 Å	full flare
	FCS	spectra+images	1.4-22.4 Å	flare decay
Ultra-violet Spectrometer and Polarimeter		images	1100-3000 Å	flare decay,active region
Coronograph/Polarimeter		images	4435-6583 Å	flare decay,active region
Active Cavity Radiometer		spectra	UV - IR	total irradiance

Table 3.1: The *Solar Maximum Mission* Experiments

3.2 Bragg crystal spectrometers for soft X-rays.

The *Flat Crystal Spectrometer* (*FCS*) and the *Bent Crystal Spectrometer* (*BCS*) exploited the Bragg diffraction property of certain types of crystals to disperse radiation with X-ray wavelengths. The Bragg diffraction condition is given by

$$n\,\lambda = 2d\,sin\Theta_B \tag{3.1}$$

where λ is the wavelength of the incident radiation, n is the order of diffraction [2], d is the crystal lattice spacing and Θ_B is the Bragg angle (the angle between the plane of the diffracting surface and the incident radiation) The type of crystals used in the *FCS* and the *BCS* have a lattice spacing of between about 1 mÅ and 15 mÅ , which means that (from Equation 3.1) the wavelengths which will be diffracted will be between about 1 mÅ and 25 mÅ , and these wavelengths fall in the soft X-ray waveband.

For any given crystal, the crystal lattice spacing d is fixed. Thus, if a beam of parallel, polychromatic X-rays is shone on a crystal, at a Bragg angle Θ_B, a unique wavelength λ will be picked out of the polychromatic X-ray beam and constructively diffracted. To produce a *wavelength spectrum*, the Bragg angle Θ_B must be varied. The conventional way of doing this is to rotate the crystal with respect to the incident X-ray beam. The different wavelengths thus selected will be diffracted to different parts of the detector plane (see Figure 3.2). This is the principle that the *FCS* was based on.

The *BCS*, however, actually used a *bent crystal* to vary Θ_B. The advantage of this type of spectrometer is that *all parts of the available spectrum are observed simultaneously*, whereas rotating spectrometers *scan the spectrum over a period of several seconds* (the scanning speed constraint is a consequence of detector

[2] $n = 1, 2, 3, ...$ Bragg crystal spectrometers are designed to record only the 1st order diffracted radiation ($n = 1$).

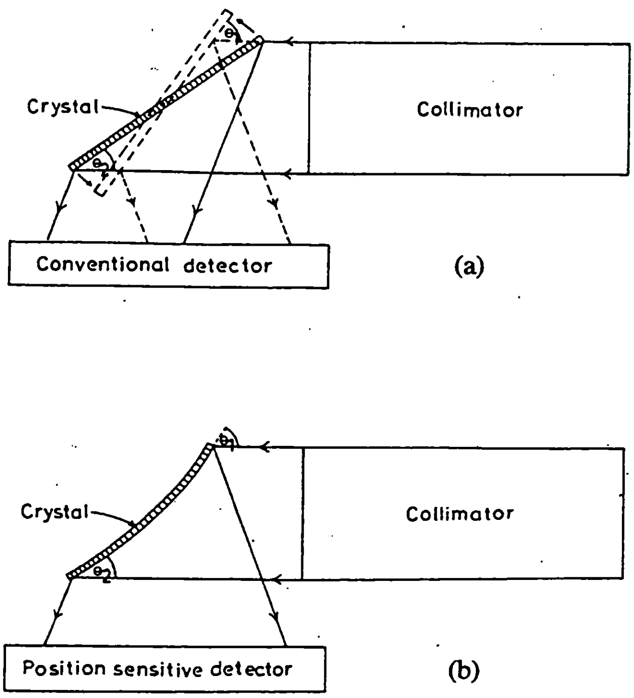

Figure 3.2: The principle of operation of (a) the *Flat Crystal Spectrometer*. and (b) the *Bent Crystal Spectrometer*

sensitivity limitations - if the crystal does not dwell long enough in a given position, the number of photons diffracted will be insufficient to form a decent spectral feature).

The *XRP* combined these two principles of Bragg crystal spectroscopy in such a way as to complement each other. The *FCS* was equipped with a fine collimator that enabled it to achieve fairly high spatial resolution ($\sim$ 15 arcseconds), and would concentrate on producing monochromatic images of flares. The *BCS* was only provided with coarse collimation that allowed it to observe a 6 $\times$ 6 arcminute area, so that it could monitor all the flares that occured within the same active region.

3.3 *The Flat Crystal Spectrometer*

The *FCS* was an example of the conventional type of crystal-spectrometer of which the *BCS* was a variation. Its working principle is illustrated by the part (*a*) of Figure 3.2.

The *FCS* had seven data channels. Each channel was served by a flat crystal, and these crystals were mounted on a common spindle. When the *FCS* was scanned, each of the seven channels simultaneously scanned their respective

Channel No.	Spectral range (Å)	Ion	Home position wavelength (Å)	Collimator response function width (arcseconds)	Effective area (mm^2)	Crystal lattice spacing $2d$ at 15° C (Å)
1	13.10-22.43	O VIII	18.969	16	55	26.622
2	10.56-14.94	Ne XIX	13.447	15	91	15.962
3	7.33-10.09	Mg XI	9.169	14	108	10.641
4	4.93- 7.61	Si XIII	6.649	14	110	8.509
5	3.63- 5.84	S XV	5.039	13	41	6.686
6	2.38- 3.61	Ca XIX	3.173	12	85	4.000
7	1.40- 2.10	Fe XXV	1.850	14	109	2.310

Table 3.2: Properties of the ***Flat Crystal Spectrometer***

wavebands. When in its so-called "home-position" each *FCS* channel would record the resonance line of one of the helium-like ions which feature most strongly in flare spectra. The channels and their wavelength ranges are listed in Table 3.2

The *FCS* had two principal modes of operation.

(a) Raster scanning mode:
In this mode the *FCS* would step across the region of interest in the pattern of a boustrophedon - moving in a series of vertical steps, alternately north-to-south and then south-to-north, with a single sideways (west-to-east) step between each change of vertical sweep direction. The *FCS* raster pattern is illustrated in Figure 5.7 (in Chapter 5: Turbulent Velocity During Flare Decay). The *FCS* would pause at each step for 1.024 seconds, and could complete a 16 $\times$ 16 pixel image in 5 minutes 8 seconds.

(b) Spectral scanning mode:
In this mode the *FCS* would first perform a raster scan across the region of interest to locate the position of peak brightness. It would then point at this position and rotate the crystal spindle to scan the seven wavebands and produce a set of seven spectra.

The *FCS* could actually combine its own two modes of operation, by rastering across an area of the Sun, pausing at each raster position to perform a spectral scan. In this way a spectral map of a particular region could be produced. This combined mode was so slow, however, that it was only of use for observing quiescent active regions but not flares, which evolve somewhat more quickly.

In each of the seven *FCS* channels, the intensity of the diffracted x-rays was recorded by a gas-filled proportional counter [3]. This would record the total

[3]**Proportional counters** are devices which respond to the entry of photons into a de -

Channel No.	Principal contributing ion	Spectral range (mÅ)	Spectral resolution (FWHM) (mÅ)	Sensitivity
1	Ca XIX	3165-3231	0.62	0.020
2	Fe(*innershell*)	1928-1945	0.14	0.019
3	Fe(*innershell*)	1893-1947	0.42	0.006
4	Fe XXV	1840-1984	0.42	0.006
5	Fe XXV	1866-1879	0.18	0.025
6	Fe XXV	1854-1867	0.18	0.026
7	Fe XXV	1842-1855	0.18	0.026
8	Fe XXVI	1869-1796	0.22	0.013

Table 3.3: Properties of the ***Bent Crystal Spectrometer***

number of photons diffracted by the flat crystal at a certain position. The crystal position could be translated directly into a wavelength and a spectrum was obtained by plotting the wavelength against count rate.

3.4 *The Bent Crystal Spectrometer*

The *BCS* differs from conventional types of Bragg crystal spectrometer, of which the *FCS* is an example, in that it dispenses with the need to *scan* a spectral range. Instead the crystal is bent so that, at one time, it offers to the incident X-rays a range of differently angled diffracting planes.

The performance of the *BCS* depends crucially on the accuracy to which the geometry of the spectrometer setup is known. Of particular importance is the radius of curvature of the bent crystal. This aspect of the *BCS* is investigated in greater detail in Chapter 4 of this thesis.

In the case of the *FCS*, the wavelength information was obtained from the crystal drive position. In the *BCS*, the wavelength information is obtained from the position of the diffracted radiation along the length of the detector. This is why the *BCS* radiation detector had to be both intensity sensitive *and* position sensitive whereas the *FCS* detector had only to be intensity sensitive. It was for this reason that the *BCS* employed a proportional counter with an anode aligned with the dispersion axis (along the length of which, events of different wavelengths were recorded, allowing event positions to be deduced from current pulse arrival times) while the *FCS* employed a proportional detector that only

tection chamber by producing an electrical current which is proportional to the number of photons. This happens because the detection chamber contains a gas that is held in a partly ionized state by an electric field. The entry of an X-ray photon (an event) sets off a chain of further ionizations, which is sufficient to allow a significant enough separation of ions and electrons in the gas to be measured as a current pulse.

recorded the number of events.

The *BCS* had eight separate position sensitive proportional counters, one for each of the channels listed in Table 3.3. Of these, Channel 1 (Ca XVIII-XIX) and Channel 4 (Fe XXIV - XXV) have proved to be the most productive, and are the ones which are used in this thesis.

CHAPTER 4

The Crystal Curvature of the Bent Crystal Spectrometer.

4.1 Introduction

4.1.1 The geometry of the *Bent Crystal Spectrometer.*

The *Bent Crystal Spectrometer (BCS)* consists of two main parts: the crystals and the detectors. There are eight fixed bent crystals which act as the wavelength selectors and a corresponding set of position sensitive detectors which record the intensity and spatial distribution of the selected wavelengths. This chapter is concerned mainly with the performance of the bent crystals.

The concept and principles of operation of bent crystal spectrometers have already been introduced in Chapter 3 but a more detailed description of the *SMM-BCS*, based on Rapley *et al.*(1977) and Parmar (1981), is given here.

Incoming radiation, after passing through a collimator which ensures that the entry of stray radiation is minimised, strikes the surfaces of the bent crystals. At different points along a crystal, the angle between the crystal surface and the incoming ray varies, and the Bragg angle varies correspondingly. Different wavelengths, therefore, will be diffracted at different points along the crystal. The geometry of the *BCS* for a crystal with a radius of curvature R is shown in Figure 4.1. Using this diagram, the position z of the diffracted ray on the detector can be derived in terms of the angle χ between the diffracted ray and the instrument axis.

The position z of the diffracted ray on the detector is given by

$$z = \frac{\sin\chi}{\sin\chi + \phi}(y_1 - y_0) \tag{4.1}$$

where

$$\chi = 2\Theta_B + \alpha \,, \tag{4.2}$$

$$y_0 = R\sin\theta_0 - x\cos\theta_0 \,, \tag{4.3}$$

and

$$y_1 = R\sin(\theta_0 + \theta) - (R(\cos\theta_0 - cos(\theta_0 + \theta)) + x)\cot\chi) \,. \tag{4.4}$$

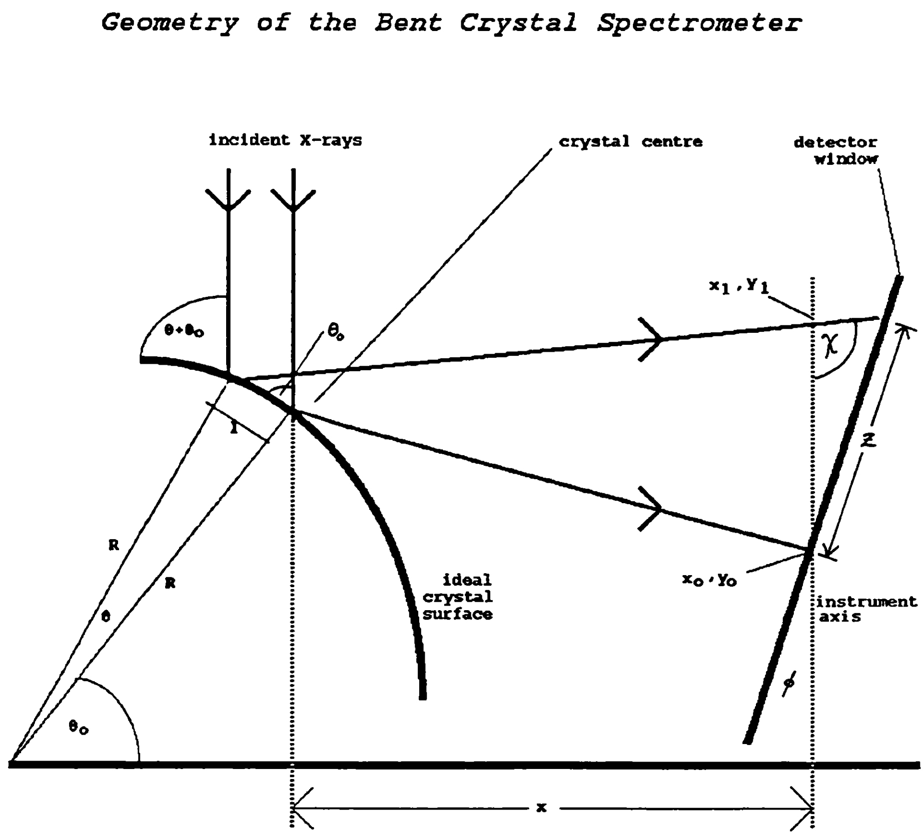

Figure 4.1: The geometry of the *BCS*.

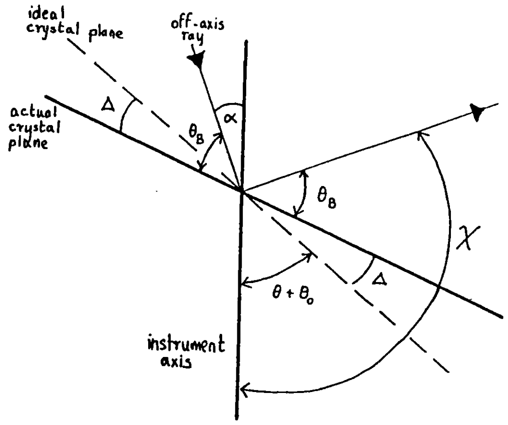

4.1.2 The importance of knowing the crystal curvature radius

The rate at which z varies for a given change in wavelength is known as the **dispersion measure**, and is denoted by the symbol dW (with units of Å/cm).

For a perfectly cylindrically curved crystal (one which has a constant radius of curvature), equally spaced wavelengths are diffracted at equally spaced points along the crystal face, and the position of the lines on the detector will vary uniformly according to Equation 4.1. The dispersion measure dW, therefore, is constant along the whole length of a cylindrically curved crystal face.

Should the radius of curvature of the crystal depart from this ideal cylindricity, the positions of the lines on the detector would change accordingly. Local decreases in the radius of curvature (bumps on the crystal face) will cause closely spaced line positions on the detector to bunch even further together, while local increases in radius of curvature (flattening of the crystal face) will cause the line positions to spread apart. A combination of increases and decreases in local radius of curvature would thus result in a distorted spectrum in which certain groups of lines were narrower and more closely spaced and other groups of lines were broader and more spread out.

It is therefore of fundamental importance to know accurately the value of the radius of curvature of the crystal at every point along the length of its useful surface.

4.1.3 The aims of this chapter.

In this chapter, data from the in-orbit scans carried out in August 1989 are used to determine the radius of curvature of the crystal in Channel 1 of the *BCS* (the Ca XIX channel), which is then compared with the pre-launch calibration carried out in 1979 and the in-orbit scans carried out in November 1980. The method for the in-orbit calibration of the *BCS* employs the idealised spectrometer geometry to predict the line positions that would be expected for a given crystal curvature radius. These predicted variations are matched to the observed variation and the crystal curvature radius taken to be the one which gives the best fitting prediction.

4.2 Prelaunch calibration.

The bent crystals, which were originally flat, were pressed into shape with curved mandrils.

The crystals used in Channels 1 and 4 have the smallest radii of curvature and were therefore deformed the most, the crystals in Channels 5, 6 and 7 being bent much less severely. As a result of the stresses they were subject to, the Channel 1 and Channel 4 crystals have been found to have the greatest non-uniformities.

However the calibration of these crystals that were carried out in the laboratory do not indicate the presence of these irregularities, indicating that the effects of the stresses manifested themselves with the passage of time. The pre-launch calibrations were carried out by Dr. A. Burek at the National Bureau of Standards in Washington, D. C. Using a narrow collimated X-ray source of a known wavelength, the position of the rocking curve of the diffracted beam was measured every 0.5 cm along the length of the crystal faces. This was done in four parallel tracks, equally spaced across the 2.5 cm widths of the crystals. The two central tracks were summed and this data used for further analysis. The results of this calibration is shown in Figure 4.2

However, after the spacecraft was launched and data began to be analysed, it became clear that the crystal radii measured prior to launch were inadequate for the purpose of interpreting the new data.

4.3 Spacecraft slew measurements - 1980.

To check that the radius of curvature of the crystals had remained constant, a method was devised to measure the radius of curvature while the spacecraft remained in orbit. When a flare occurred on 6 November 1980, the spacecraft was swung so that it scanned the Sun in the east-west direction, which is parallel to the crystal dispersion plane. The purpose of the scans was to move the point of diffraction of a particular wavelength across a portion of the crystal, and thus obtain an idea of the local radius of curvature.

The scans were repeated until the flare had died down. The time taken to complete each scan is small compared to the duration of the flare (particularly during the decay phase), so that the flare does not change significantly over the period of one scan. A spectrum integrated over this period can be regarded as a reasonably good snapshot of the flare at that time.

The results of this scan were analysed by Dr. A. Parmar in his PhD thesis (Parmar, 1981). His results are shown in Figures 4.2 and Figure 4.3, where they are compared with the pre-launch calibration carried out by Dr. A. Burek. In figure 4.2 the variation of the crystal radius of curvature for one of the seven *BCS* crystal (corresponding to Channel 1 which recorded the Ca XIX spectrum) is plotted against distance along the crystal. The continuous line shows the pre-launch measurements, and it appears that between the time those measurements were made and November 1980, the crystal had already lost some of its curvature.

This deterioration appears to have continued, is evident from the August 1989 calibrations which are presented here. These measurements show that the radius of curvature at the w-line position and at the k-line positions have increased.

The crystals of Channels 1 and 4 show the largest deviation from their pre-launch values, with the remaining channels having survived in better shape. The reason for this is that the mean radius of curvature of the crystals in Channels 1 and 4 is at least half that of the other channels. Because the crystals were formed by being pressed against a curved mandril, the crystals with the smallest radii of curvature underwent the greatest deformation, which caused the stresses which revealed themselves with time.

4.4 Spacecraft slew measurements - 1989.

4.4.1 Observations.

The spacecraft slews that were performed in 1980 were repeated in 1989, shortly before the *SMM* satellite came to the end of its working life. A flare which occurred around 1600 UT on the 31st of August 1989 was observed by the *BCS.* The flare was kept in the *BCS*'s field of view while the entire satellite was manouevered so that it scanned the Sun through an 8 arcminute east-west sweep in steps of 0.5 arcminutes, which were held for 35 seconds each (see Figure 4.4). This data has not been analysed before, and the results of the experiment are being published for the first time in this thesis.

4.4.2 Analysis.

4.4.2(a) Obtaining and matching spacecraft pointing data and spectral data.

The raw, unformatted *SMM-XRP* data is downloaded from data tape onto disc by using the reformatting program REF. The reformatted data are stored in files with the prefix BCSDA, BCSIX and SPSUB (for *BCS* data).

The reformatted data files are further processed by integrating spectra over the desired time intervals. Fits to these spectra give the positions of the principal emission lines (the w-line and the k-line), which are stored in files with the prefix CAL (for the 31 August 1989 flare, the CAL files were called CAL890831.1530 and CAL890831.1608).

At the same processing stage, the spacecraft pointing data are exracted from the SPSUB files, using the program DVE, and written to the DVE.OUT data file.

For the purpose of this analysis, the start and end times of each spectrum must match the start and end times of each of the pointing stages shown in Figure 4.4. The spacecraft pointing information, which consists of the pointing angles and the times at which the information was recorded is plotted in Figure 4.4. This plot shows how the spacecraft pointing angle was changed in 0.5 arcminute steps, and held at each step for 35 seconds. Using the times given in the pointing file, a set of spectra were created such that each spectrum was integrated over the period of time that the spacecraft was in one stable pointing position.

The positions of the centres of the main emission lines were measured by fitting Voigt profiles [1] to the real data. Individual spectra were also inspected visually to ensure that they were statistically acceptable and had no obvious irregularities.

4.4.2(b) Deducing the offset angle of the flare.

In order to determine the offset angle of the flare) it was necessary to determine its position in terms of the spacecraft pointing angle.

This was done by looking at the way the light curve has been modulated by the movement of the spacecraft. The lightcurve shown in Figure 4.7 distinctly shows the three scans that were made across the flare of 31 August 1989. The peaks indicate when the spacecraft was pointing directly at the flare. The position of the flare was obtained by matching the time measured on the light curve with the times recorded in the pointing file. The pointing angle found in this way can be confirmed by looking at the variation with time of the pointing angle itself. The difference between the spacecraft pointing angle and the flare position is equal to the offset of the flare with respect to the spacecraft instrument axis.

4.4.2(c) Finding the crystal curvature radius that best fits the observed data.

Figure 4.5 summarises the procedure for determining the crystal curvature radius from the observed line position shift. The offset angles, which were obtained using the method described in the previous section, were fed into the program WLC which uses the idealised geometry of the *BCS* (as shown in Figure 4.1) to predict the bin number of the w- and k-lines. These predicted line positions are shown plotted alongside the measured line positions in Figure 4.6.

[1]**Voigt profiles** represent the convolution of the Lorentzian crystal rocking curve of the *BCS* with the emitted Gaussian spectral line profile.

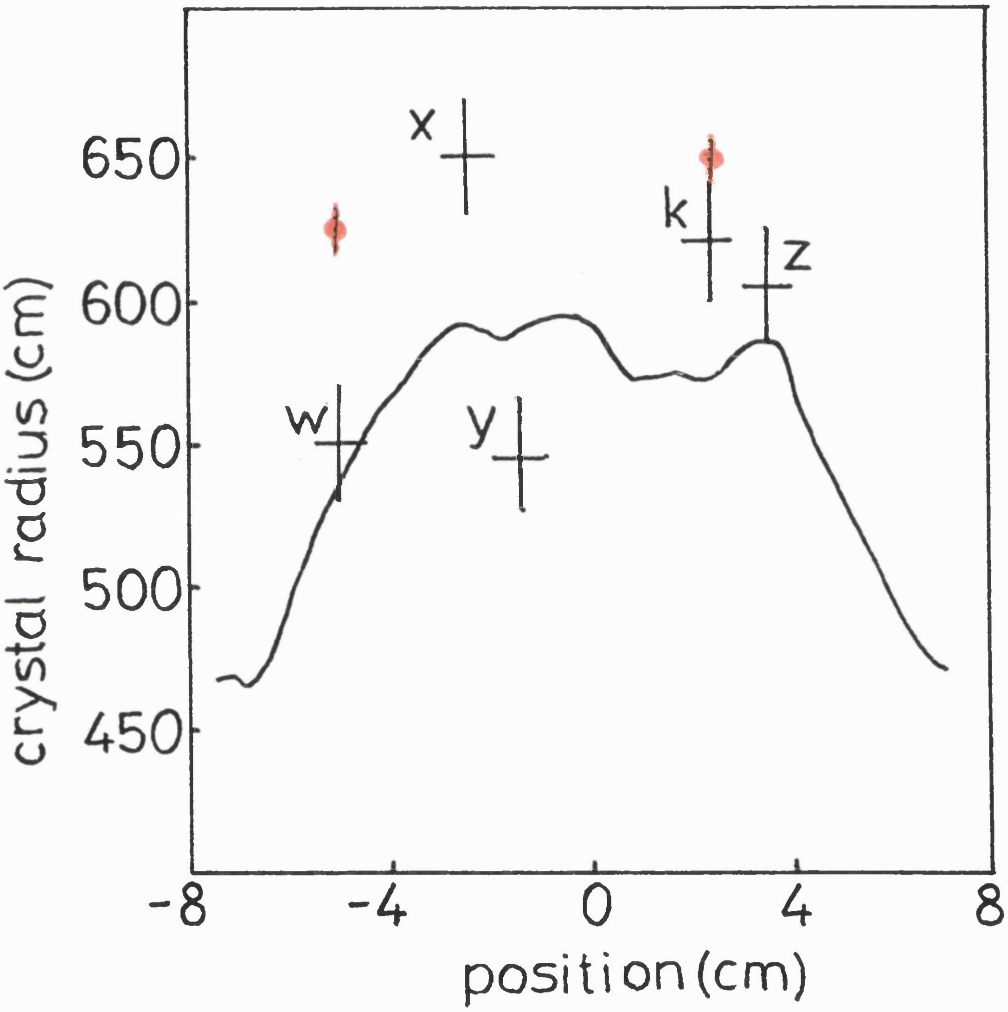

Figure 4.2: Crystal curvature radii for *BCS* Channel 1.
The continuous line represents the radii of curvature measured prior to launch by Dr. A. Burek. The crosses represent the measurements made by Dr. A. Parmar in 1980, based on the shift of the w,x,y,k and z-lines in the Ca XIX spectrum. The analysis of the 1989 scans yielded crystal curvature values at the w- and k-line positions, which are marked in red ink. It appears that the crystal curvature radius has increased gradually, over a period of a decade.

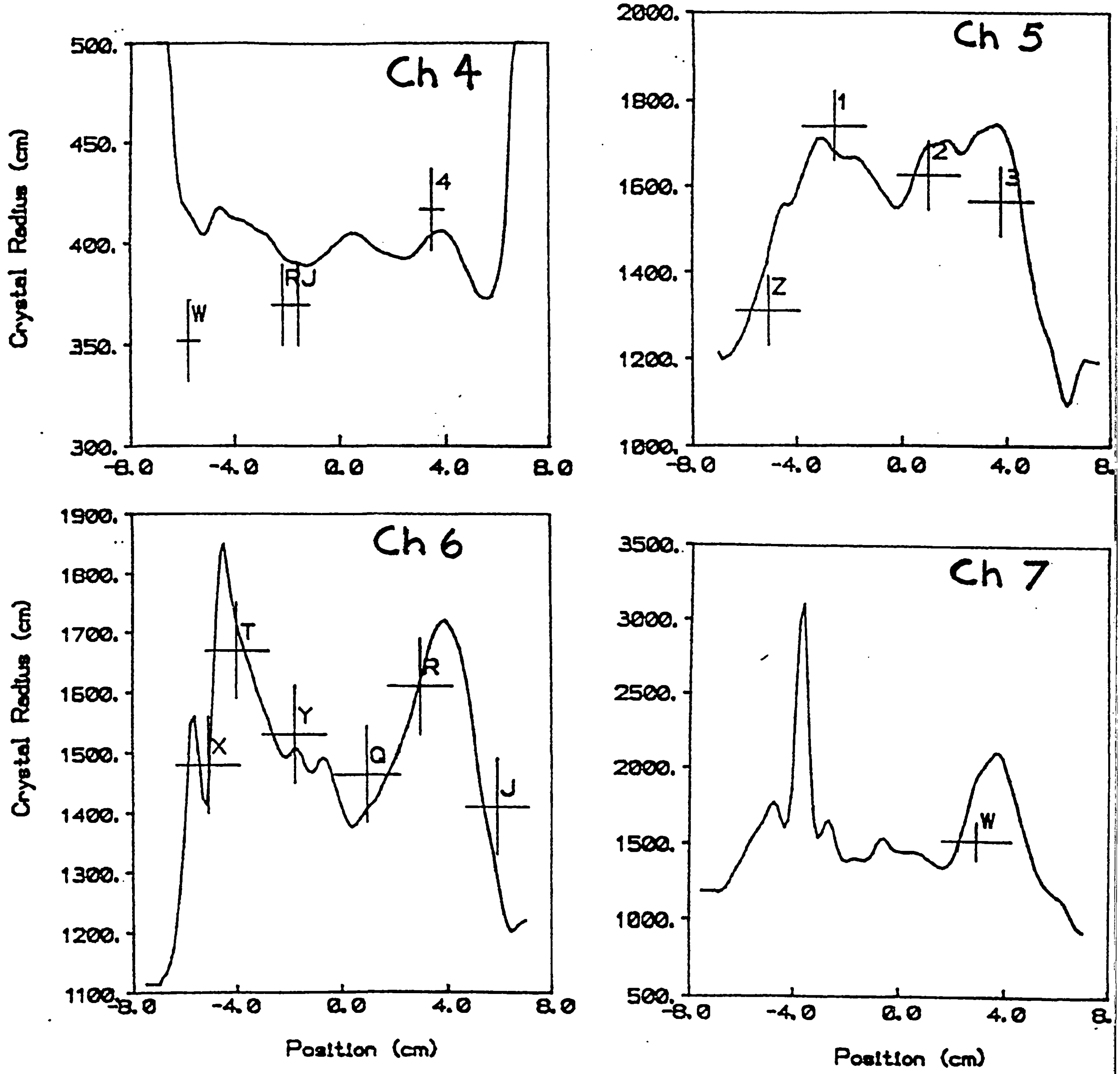

Figure 4.3: Crystal curvature radii for other *BCS* Channels.
The continuous lines represent Dr. A. Burek's pre-launch measurements and the crosses represent Dr. A. Parmar's 1980 measurements. These plots show that the crystals for Channels 5,6 and 7 are not bent as much as those for Channels 1 and 4.

In order to determine the actual crystal curvature radius over the relevant range, this calculation was repeated for a range of values of R, varying the offset θ for each value of R.

Thus the R for the predicted line position variation which best matches the observed variation is the best measure of the crystal curvature radius at that point of the crystal.

4.5 Conclusions

The 31 August 1989 scans were used to measure the radius of curvature of the Channel 1 crystal for the regions of the crystal that diffract the w- and k-lines.

The radius of curvature at the w-line section of the crystal is between 620 cm and 630 cm, which is 13 % greater than radius measured in 1980 (Parmar, 1981). The 10 cm range of the crystal curvature radius values from the 31 August 198 scan represent local variations in the radius of curvature.

The radius of curvature at the part of the crystal that diffracts the k-line is between 640 cm and 650 cm, an increase of only 4 % over the 1980 measurement.

The w-line is diffracted from a point which is nearer to one of the ends of the crystal than it is to the crystal centre, while the k-line is diffracted from a region nearer to the centre. This is consistent with the measured "uncurling" of the crystal, as it was the ends of the crystal that were subjected to the greatest deformation, and will therefore exhibit the greatest restitutive movement.

4.5.1 Further use of the results obtained here.

In order to obtain the radius of curvature of the *BCS* Channel 1 crystal, the rate at which line position (bin number) changes with source offset (arcminutes) was measured.

The shift of the w-line is found to be 3.3 wavelength bins per arcminute of source offset, and for the k-line it is found to be equal to 2.75 bins per arcminute. This information can be used to help measure the broadening of *BCS* emission lines that is caused by spatially extended sources, and that forms the subject of Chapter 5.

If a point source is offset from the *BCS* instrument axis, the peak of its w-line will be shifted by an amount equal to the offset multiplied by the bin per arcminute rate.

This principle can be applied to a source that is extended in the east-west direction, by considering it to be made up of a number of points. Then the w-lines due to each of these points will be shifted by a different amounts, so that instead of all overlaying perfectly to form a fairly sharp line profile, each contributory w-line is slightly shifted, and the summed effect is a broadened line profile.

The shift of each contributory w-line is given by the bin per arcminute rate. Thus if this rate is known, and the east-west size of the source is known too, the magnitude of the line-broadening effect can be calculated.

4.6 Correction: Changes in the *SMM-BCS* detector which could appear as a change in crystal curvature.

In the spacecraft scan experiment described in this Chapter, the source offset is varied so that the CaXIX spectrum in Channel 1 slides along the length of the detector anode. For a given source offset, the amount by which the spectrum shifts depends on the radius of curvature of the crystal. The greater the radius of curvature of the crystal, the greater is the shift of the spectrum. The length of the detector anode is divided into bin numbers, and the spectral shift in this experiment is expressed as bin no.'s per arcminute of source offset.

When it was found that the bin no., per arcminute rate had increased over the period 1980 to 1989, it was concluded that the radius of curvature of the crystal had increased with time.

There is another possibility: *that the ruler for measuring distance along the detector anode itself had shrunk.* This ruler is of course the bin no., scale which (in 1980) divided up the Channel 1 anode into about 230 bins. If this scale had somehow become compressed so that the anode was divided into more than 230 bins, then the same actual spectral shift would appear greater (in terms of bin no.'s) in 1989 than it did in 1980.

There are two additional facts to support this possibility:
(i) The position of the Ca XIX resonance line had drifted from bin no. 190 to bin no. 205 over the period 1980-1989. This is to be expected if the bin no., scale had become compressed.
(ii) It was learned, through a private communication with Dr. B. J. Kent [1] who worked on the *SMM-BCS* (Acton *et al.*1980), that the crystal holders were too robust to have allowed the 13 % change in radius of curvature that is required by the bin no., per unit source offset measured in 1989.

When these two facts are taken into consideration, it appears that the increased bin no., per arcminute rate measured in 1989 was due to the compression of the bin no., scale which was used to measure distance along the length of the Channel 1 anode.

[1] now at the Rutherford Appleton Laboratory, Chilton, Didcot, Oxfordshire OX11 0QX.

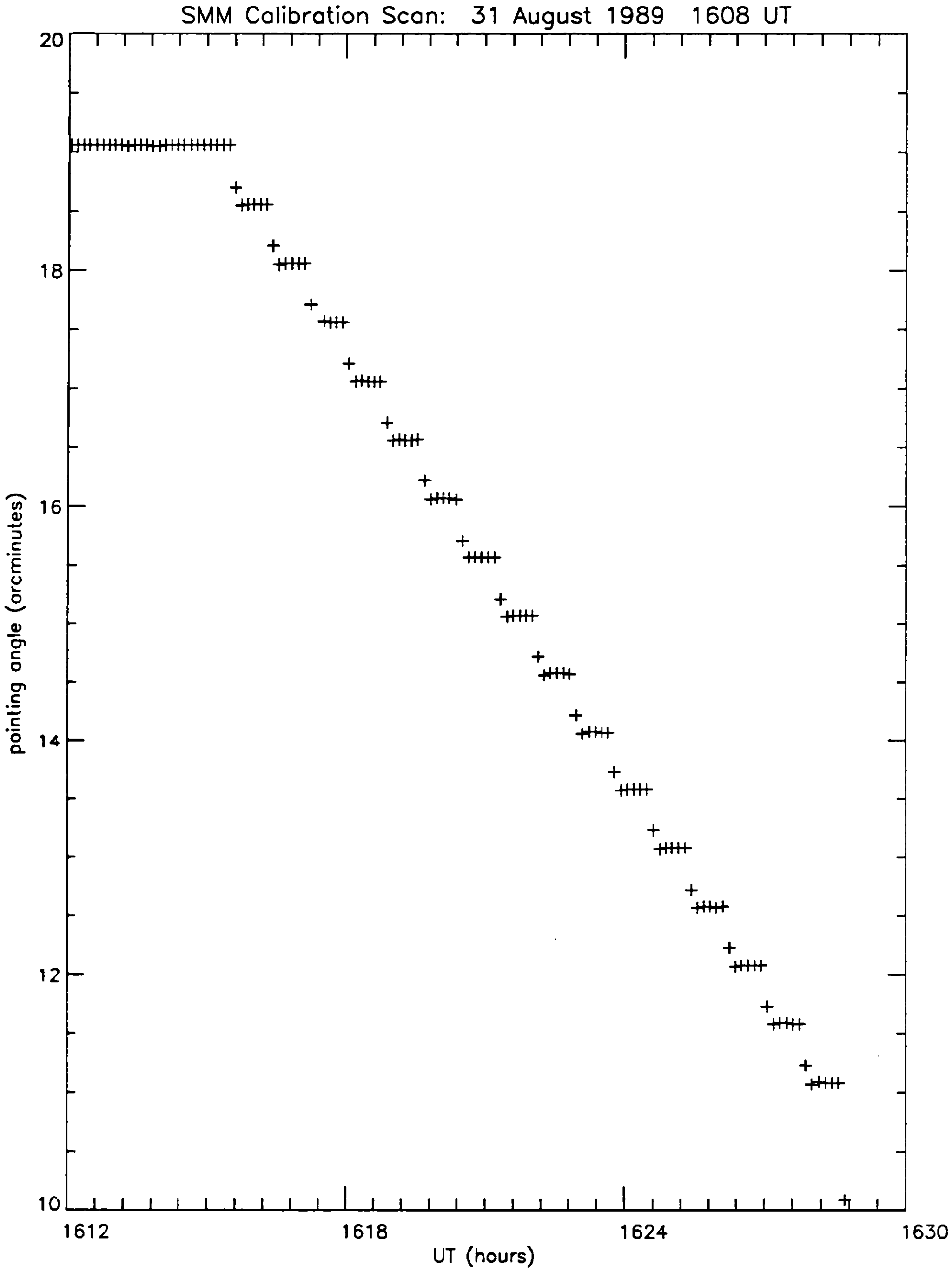

Figure 4.4: Spacecraft pointing for the calibration scans of 31 August 1989
The spacecraft was held at each of the pointing stages shown for approx 35 seconds. The spacecraft position was recorded every 7 seconds. One spectrum was integrated for each 35 second pointing stage to obtain the most reliable measure of the line positions for each offset angle.

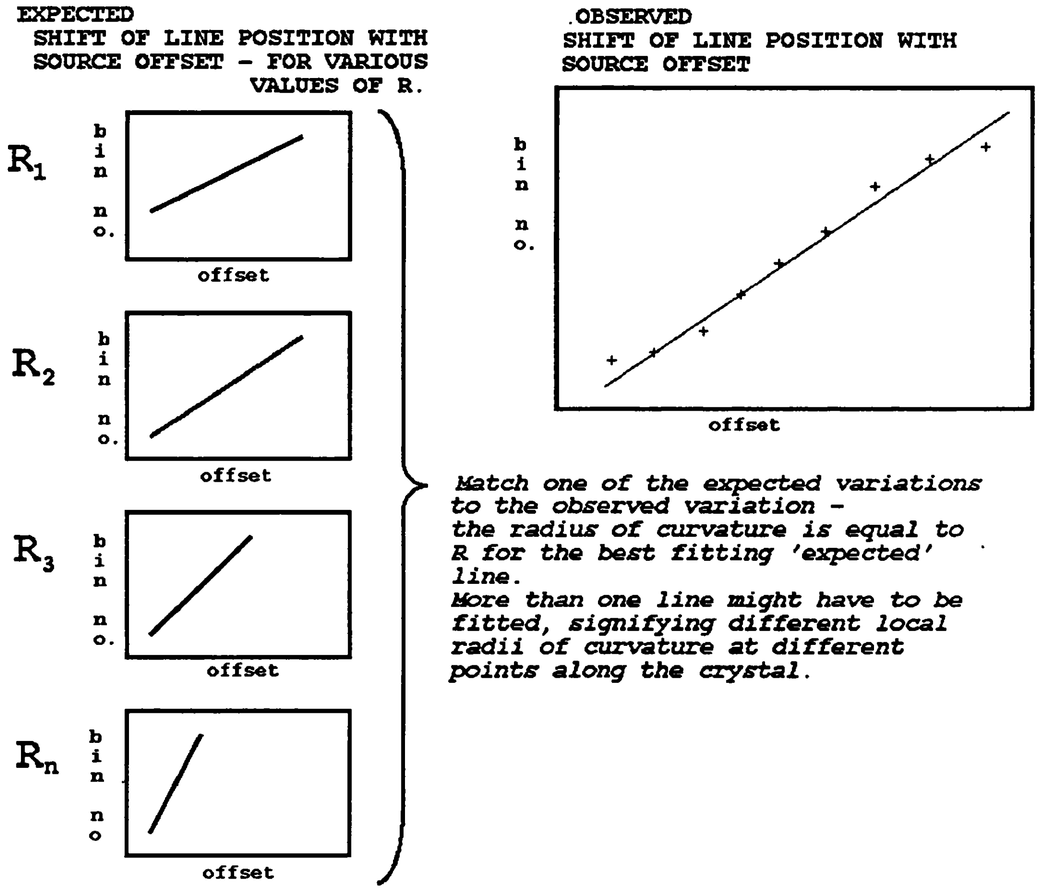

Figure 4.5: Fitting an expected line position shift to the observed data.
The expected line position shifts are calculated for fixed values of R (radius of curvature), and the actual crystal curvature radius can be determined by matching one (or more) of the expected variations with the observed variation.

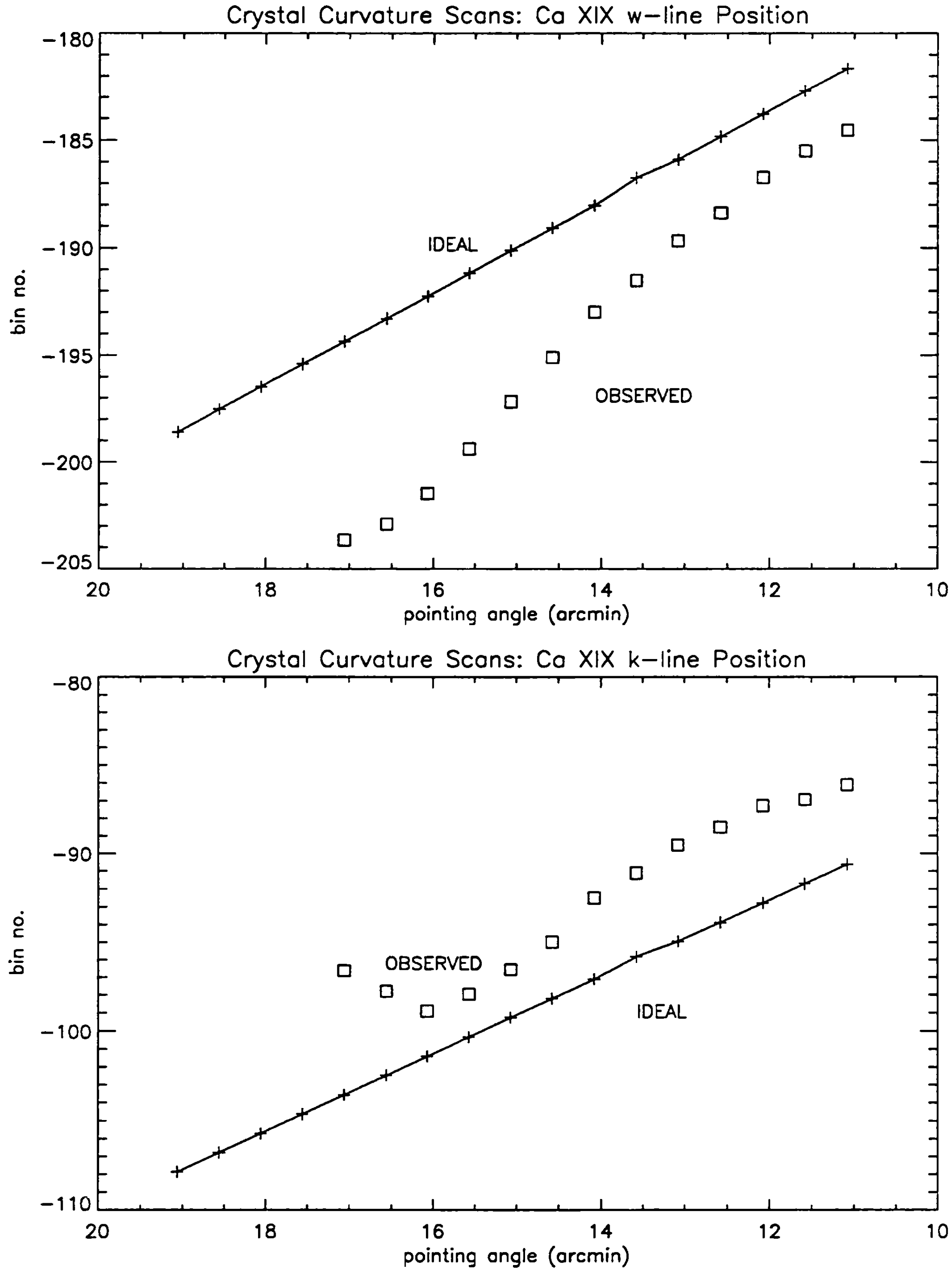

Figure 4.6: Shift of (a) the w-line position, and (b) the k-line position, with shift in flare offset.
The crosses mark the line position shift predicted for a perfectly cylindrically curved crystal with a curvature radius of 625 cm at the w-line position and 645 cm at the k-line position. The square symbols mark the observed line position shift, measured during the spacecraft scans.

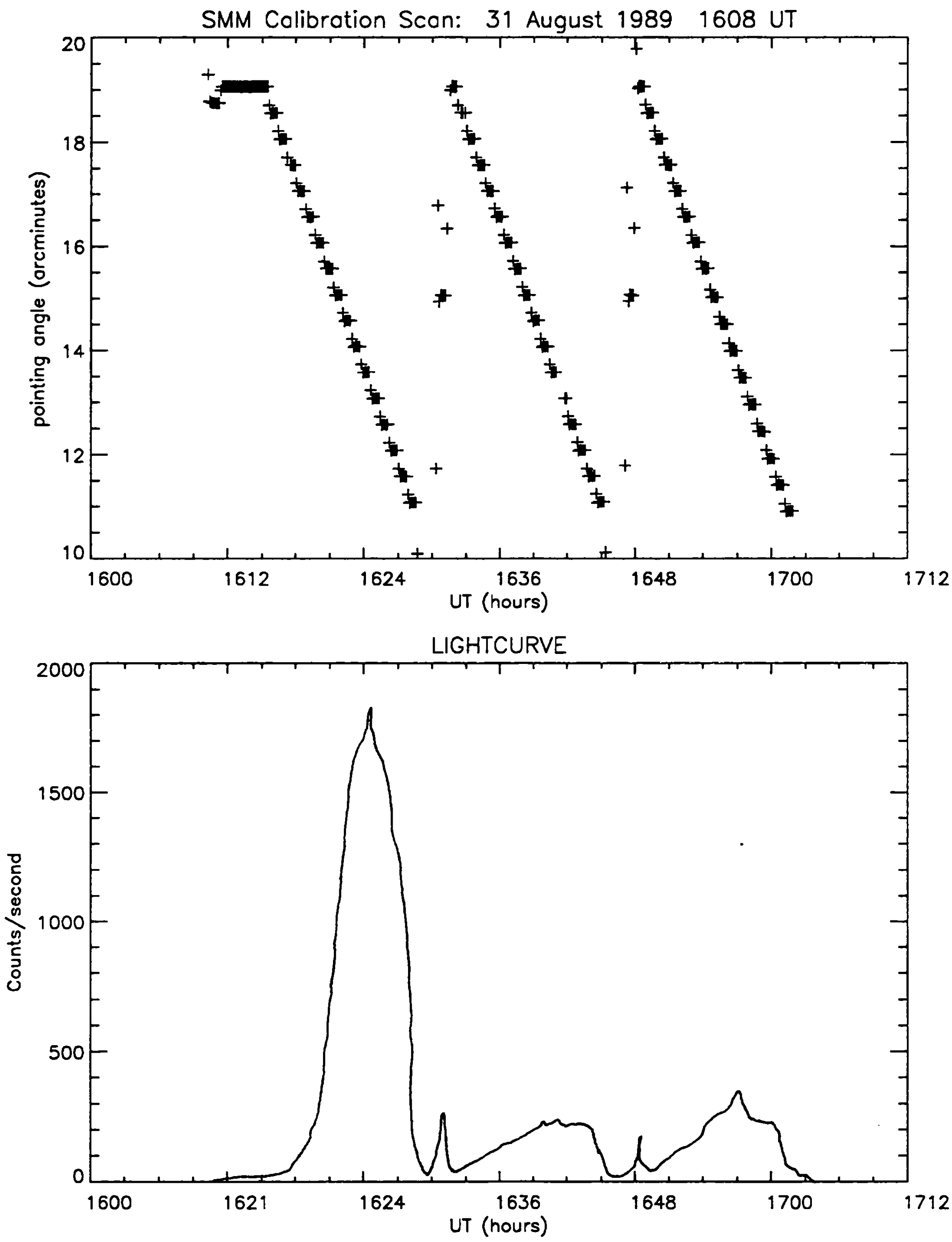

Figure 4.7: The lightcurve recorded by the *BCS* as it scanned the flare of 31 August 1989. *This observed lightcurve is the result of the modulation imposed on the ususal monotonic flare lightcurve by the spacecaraft scanning.*

CHAPTER 5

Turbulent Velocity During Flare Decay

5.1 Introduction

5.1.1 Turbulent motion in coronal plasma.

Non-thermal mass motion, sometimes referred to as **turbulent motion**, is observed in all coronal plasmas, whether it be in active region loops or in flaring loops. Its presence is indicated by the broadening of emission lines in excess of the Doppler broadening due to thermal motion (of the plasma ions).

The importance of non-thermal mass motion is that it requires an energy input in *excess of that required to maintain the observed temperature.* The aim of most studies of non-thermal broadening is to find out where the energy is supplied from, and how it is converted into the kinetic energy of plasma mass motion, which broadens the emission lines.

5.1.2 The instrumental contribution to line-broadening.

The majority of the spectrometers used to record ultra-violet and soft X-ray emission from the Sun are of the bent-crystal type. Spectrometers of this type have the property of spreading out the wavelengths of the emission from anything larger than a point source. Thus the spectrum of an extended source (which most flares are), will be broadened by an amount which is proportional to its spatial extent.

This is why the non-thermal line broadening observed in bent-crystal spectrometers have been approached with some caution and even scepticism. Watanabe (1989) was able to account for *all* of the non-thermal broadening seen in Hinotori flare spectra by measuring the size-dependent broadening effect for that particular spectrometer. Though it is believed that the *SMM-BCS* does show true non-thermal broadening, the only way to lay to rest fears about the extent of the size-dependent contribution is to actually measure it.

5.1.3 Observations of flare plasma.

That turbulent mass motion is present in the rise phase of flares and in non-flaring active regions is a generally accepted fact based on the findings of authors such as Cheng, Doschek and Feldman (1979), Doschek, Kreplin and Feldman (1979), Antonucci *et al.*, (1982), Tanaka *et al.*, (1982), Antonucci *et al.*, (1987), Fludra *et al.*, (1989), Watanabe (1989) and Saba and Strong (1991).

Antonucci *et al.*, (1982, 1987) and Fludra *et al.*, (1989) analysed flare X-ray spectra recorded by the *SMM-BCS.* Antonucci *et al.*, (1982) studied line widths in the rise phase and measured upflow velocities and turbulent velocities. Antonucci *et al.*, (1987) analysed over a hundred spectra from the *BCS* and the *SOLFLEX* spectrometer aboard the *P-78* spacecraft with the object of determining the calcium ionization balance in Solar flares.

Fludra *et al.*, (1989) analysed the spectra from 40 flares that occurred in 1980 and 1984-5. Their principal aim was to study the rise phase, for which purpose they devised a two-component fitting method (described in greater detail in Chapter 7, Section 7.2.1) to reproduce the observed emission lines. Two possibilities emerge from their results, concerning the nature of the stationary component and its relation to the upflowing component, which are that they are both broadened, the upflowing component at least as much as the stationary component and usually more so, and that there is a correlation between the turbulent velocity of the stationary component and the directed velocity of the upflowing component.

However, this is during the rise phase, when it is quite clear that energy is being dissipated in the flare, as indicated by the rising electron temperature, and some of this energy manifests itself as turbulent mass motion, while another part of it fuels the upflows.

Although Fludra *et al.*, (1989) did study the decay phase as well, for which they used a single component, (which is justified both empirically, by the quality of the fit, and theoretically, because no upflows are expected) their main area of interest was the rise phase.

Other instruments too have observed an excess of non-thermal line broadening in the rise phase of flares. Spectra from the *SOLFLEX* spectrometer have been mentioned above, and Watanabe (1990) describes the non-thermal line broadening in the large flare of 6 June 1982 which was observed by the spectrometers aboard the *Hinotori* spacecraft (Tanaka *et al.*, 1982). However Watanabe concludes that there is no excess broadening left after instrumental effects have been taken into account.

Thus there is general agreement about the presence of a significant excess of line width over the thermal width in the rise phase of all flares seen by the *BCS*, equivalent to turbulent velocities of up to 150 to 200 km s^{-1} .

But so far, there have been no conclusive studies on line broadening during flare decay, and it is not known with certainty whether line widths become purely thermal during the decay phase of flares.

This chapter concentrates on turbulence in the *decay phase.* The decay phase is intermediate both in time and in energy to the well studied rise phase and post-flare phase, and it is hoped that by studying the decay phase, some light will be shed on the connection between the (relatively) stable and long-lived active region environment and the short-lived flare.

5.1.4 Observations of non-flaring plasma.

There also exists a body of work on line broadening in non-flaring regions. The study of soft X-ray lines in active regions (Saba and Strong, 1991, 1992) shows the presence of excess line widths in non-flaring plasma, raising the question of whether flare line broadening and non-flare line broadening have the same origin.

Whether or not there is additional line broadening during flare decay has implications for discussions of possible flare heating mechanisms, the connection between turbulence and heating and the nature of the broadening itself (whether it is directed mass motion or random mass motion).

5.1.5 The importance of measuring the size-dependent broadening in the decay phase.

Given the importance of accurate measurements of decay phase line broadening, it follows that if there are any *significant* instrumental contributions to this measurement, they must be removed. Spectra from the *SMM-BCS* are known to suffer from a line broadening effect that depends on the size of the observed flare. Though the presence of this contribution is well known, no concerted effort has ever been made to measure it. This is because most previous work on turbulent broadening has been more concerned with the rise phase, during which turbulent velocities have values in the range 100 to 200 km s^{-1} . The size-dependent broadening effect, though not entirely ignored, has generally been assumed to be negligible during the rise phase (eg: McClements and Alexander, 1989).

During the decay phase, however, turbulent velocities have values in the range 30 to 100 km s^{-1} and it is at this stage that the size dependent broadening effect becomes significant. This analysis is concerned with the decay phase, which is why it is important to measure the instrumental broadening effect accurately.

Since the basis of this work is the use of the emission line as a velocity diganostic, the next section contains a brief discussion of the interpretation of emission lines as a velocity diagnostic.

5.1.6 The emission line as a velocity diagnostic.

The emission line used as the velocity diagnostic in this study is the one due to the transition of the electron from the $1P_1$ to the $1S_0$ state in the helium-like Ca XIX ion (which has nineteen electrons stripped off, leaving an ion with two bound electrons).

The total width, usually referred to as the **Doppler width**, is made up of three contributions:

$$(\Delta\Lambda_{Doppler})^2 = (\Delta\Lambda_{thermal})^2 + (\Delta\Lambda_{non-thermal})^2 + (\Delta\Lambda_{spatial})^2 \tag{5.1}$$

The first two terms on the right hand side are due to physical conditions in the plasma, and the third term represents the size dependent broadening effect that needs to be removed. Each of these terms shall be considered in turn below. [1]

(a) The thermal width ($\Delta\Lambda_{thermal}$)

The first term in Equation 5.1 represents the broadening due to the thermal motion of the plasma ions. The Ca XIX resonance line has an intrinsic width that is due to the uncertainty in the energy difference between the $1S_0$ and $1P_1$ states, given by $\Delta E \Delta t \sim h$ (where Δt is the time spent in the higher energy state). This is the least width that the line can have, and lines are never observed with pure intrinsic widths, but are observed Doppler broadened by the thermal motion of the emitting ions.

Thermal motion is *random*, and acts to broaden the emission line *symmetrically* in the following way. Motion of ions towards the observer results in a shift to a shorter wavelength and motion in the opposite direction results in a shift to a longer wavelength. Random velocity distributions result in symmetrically broadened lines because at any given instant in time most of the ions have a

[1] It is useful to keep in mind the equivalence of wavelength and velocity. They are related by the factor c/Λ, which will transform Equation 5.1 into $v^2_{Doppler} = v^2_{thermal} + v^2_{non-thermal} + v^2_{spatial}$

negligible line-of-sight velocity component and contribute to the central portion of the emission line, while the minority of the ions with a significant line-of-sight velocity component contribute to the wings of the line profile.

The thermal motion of the ions thus results in the symmetrically broadened emission lines which are commonly observed in coronal spectra, and which shall be referred to as the **thermal profile**. The width of a thermal profile is given by:

$$\Delta\Lambda_{thermal} = \frac{2k_BT}{cM_i}\Lambda_i \tag{5.2}$$

where T is the plasma electron temperature, Λ_i is the rest wavelength of the emission line, M_i is the atomic mass of the ion, c is the speed of light and k_B is Boltzmann's constant.

The thermal profile is the fundamental line profile unit, and (except when the instrumental response dominates, which fortunately is not the case with the *SMM-BCS*) all observed line profiles may be considered to be made up of these fundamental units.

(b) The non-thermal width ($\Delta\Lambda_{non-thermal}$)

The second term in Equation 5.1 represents the broadening due to the non-thermal motion of the plasma ions. If a volume element in the total body of plasma is moving with respect to the observer, there will be an additional shift in the wavelengths of the photons emitted from this volume element.

If there is *random mass motion* within the plasma, the line-of-sight velocities of every one of the volume elements will be in a different direction at any given moment, and each one will give rise to a Doppler shifted thermally-broadened line profile.

In line profile terms, the sum over the whole flare volume of these volume elements is equivalent to the sum of a set of slightly Doppler shifted thermally-broadened line profiles, which results in a single line profile which is wider than the individual thermally broadened profiles. It is the difference between these widths that is referred to as the non-thermal width.

Because temperatures can be determined independently of line widths (from line intensity ratios) an *expected* thermal width can be calculated and removed from the *observed* line width. This leaves the line width due to non-thermal mass motion and the size-dependent broadening effect. Therfore, to determine the true non-thermal broadening contribution, the size-dependent broadening has to be calculated and subtracted from the observed line width:

$$\Delta\Lambda_{non_thermal} = \sqrt{(\Delta\Lambda_{Doppler})^2 - (\Delta\Lambda_{thermal})^2 - (\Delta\Lambda_{spatial})^2} \tag{5.3}$$

(c) The size-dependent width ($\Delta\Lambda_{spatial}$)

The third term in Equation 5.1 represents instrumental broadening effects. The *SMM-BCS* suffers from such an instrumental effect, which directly affects the measurement of line widths. This effect is related to the apparent size L by the relation

$$\Delta\Lambda_{spatial} = \frac{LdWdB}{2\sqrt{ln2}}, \tag{5.4}$$

where dW=dispersion of crystal ($\sim$ 3mÅ/bin) and dB= offset dependent spectral shift ($\sim$ 2 bins/arcmin). Thus if the size of the flare and can be measured, the magnitude of the size dependent effect can be determined.

This, however, has hitherto not been done, and the magnitude of the effect has remained the subject of speculation, with some workers (McClements and Alexander, 1989) neglecting it all together, while others (Watanabe 1989) attribute all of the excess width to it. Exactly how the instrumental broadening effect works and how it may be compensated for is discussed in the next section.

5.1.7 Measuring the source-size dependent effect in the *SMM-BCS.*

In the *SMM-BCS* instrument, which employs a curved crystal, some proportion of the broadening may be caused by the spatial extent of the flare. This is a property of bent-crystal spectrometer design: an extended source which has a finite size in the direction parallel to the dispersion plane of the spectrometer produces additional line broadening. So far most analyses of *BCS* spectra have assumed that the contribution of this effect is negligible. What is needed is some way of knowing what the sizes of the flares were, and how large they would have appeared to the *BCS.* Knowing the size, and knowing the relation between the size and the line broadening effect, the exact proportion of the line width that is due to size dependent broadening may be determined.

In this analysis, it is proposed that this effect be measured with the help of flare images recorded by the *FCS*, and that were contemporaneous with *BCS* flare spectra. This would decide whether the increase in line widths observed late in the decay phase is real, or is merely due to an increase in the flare size.

The *FCS* also recorded spectra and for a few flares there exist simultaneous *FCS* and *BCS* spectra. The differences in the way the two instruments operate is reflected in the differences between spectra drawn from the same source. The smaller field of view of the *FCS* means that its information is more specific as regards temperatures, densities and velocities. The *BCS* averages over a larger range of these quantities and its information gives more weight to the more abundant plasma which is also less energetic. In this chapter a comparison is made between the *BCS* and *FCS* spectra for one flare, which is followed by a discussion of whether the measured differences can be explained in terms of different volumes of plasma.

A comparison of *BCS* spectra from two different channels (Ca XIX with FeXXV) shows that more non-thermal line broadening is seen in Fe XXV spectra. This too, like the difference between *FCS* and *BCS* spectra mentioned above, is thought to reflect the spatial distribution of turbulence. Jakimiec and Fludra (1991) suggest that energy release occurs in hot turbulent kernels which dominate the FeXXV emission and which thus gives rise to more line broadening in the Fe XXV spectra than in the Ca XIX spectra, which have a bigger contribution from the surrounding cooler regions.

5.1.8 The aims and structure of this chapter.

This analysis aims to use *FCS* images to estimate flare sizes and thus measure the size-dependent broadening effect in *BCS* spectra. It also aims to identify the energy source which drives turbulent mass motion.

The non-thermal broadening of flare emission lines has been outlined and its implications for flare plasma dynamics were discussed in Section 5.1. Also introduced was the problem of instrumental broadening which is present in *BCS* spectra and which is caused by the east-west size of the flares.

A method to measure this instrumental broadening effect is described in Section 5.2. This method involves the use of *FCS* images to derive flare sizes.

It is tested and applied to a sample of flares, and the results are presented in Section 5.3. These corrected line-width data are discussed alongside related observations of the same flares. The observations of an extreme limb flare help test the hypothesis that directed flows rather than turbulent motion are responsible for non-thermal line broadening. It is also instructive to compare *FCS* spectra, where it is available, with contemporaneous *BCS* spectra, as the two instruments provide different perspectives on the same source.

Section 5.4 considers the impact that the correction of the instrumental effect has on the observed behaviour of non-thermal line broadening and whether the data supports the view that it is caused by turbulent mass motion rather than by directed flows. Also addressed is the question of the extent to which non-thermal broadening in flares differs from that seen in the active regions sites which surround the flares. The most important question to be answered is, if it is true that turbulent mass motion gives rise to non-thermal line broadening, what the nature of the mechanism that sustains it is, and whether the energy that it carries will cause flare heating in the decay phase. This question is also discussed in Section 5.4, where some likely sources of energy and dissipation mechanisms are identified and evaluated, using quantities measured in some of the flares in the sample.

It is concluded in the summary in Section 5.5 that the non-thermal line broadening is real enough and cannot be dismissed as an instrumental artefact. It is also found that it cannot be due to a superposition of the directed motion that is expected during the rise phase of flares, and that furthermore, its persistence late in the decay phase demands the presence of some energy deposition mechanism that is not associated with the flare rise phase.

5.2 Analysis technique

5.2.1 Using *FCS* images to estimate flare sizes.

The flowchart in Figure 5.1 summarises the procedure described in this section. In essence it consists of reducing an *FCS* image to an east-west intensity profile, which is convolved with the thermal line profile expected from a point source. The result of this convolution is a *thermally and spatially broadened line* which is compared with the *observed* line profile which is *thermally, spatially and non-thermally* broadened. The difference between the (squares of the) widths of the observed line and the convolved line is a measure of the non-thermal broadening in the observed line.

The various steps in this procedure are discussed more fully in Sections 5.2.1(a) to (d).

5.2.1(a) How an extended source causes line broadening.

The *SMM-BCS* uses a set of curved crystals, each of which simultaneously reflects a range of wavelengths. An ideal spectrum is one which would be produced by a point source on the Sun's disk. If such a point source is displaced parallel to the dispersion plane of the spectrometer, its spectrum shifts along the length of the detector.

A *spatially extended* source can be thought of as a collection of point sources, each having an offset with respect to the instrument axis that is slightly different to the offset of its neighbours. Radiation from each offset point contributes to the cumulative spectrum by producing an individual spectrum which is shifted relative to its neighbours, but only slightly, and thus they overlap. The total spectrum is thus broadened, and the extent of this broadening depends on the spatial extent L of the source, as given in Equation 5.4. Because the *BCS*

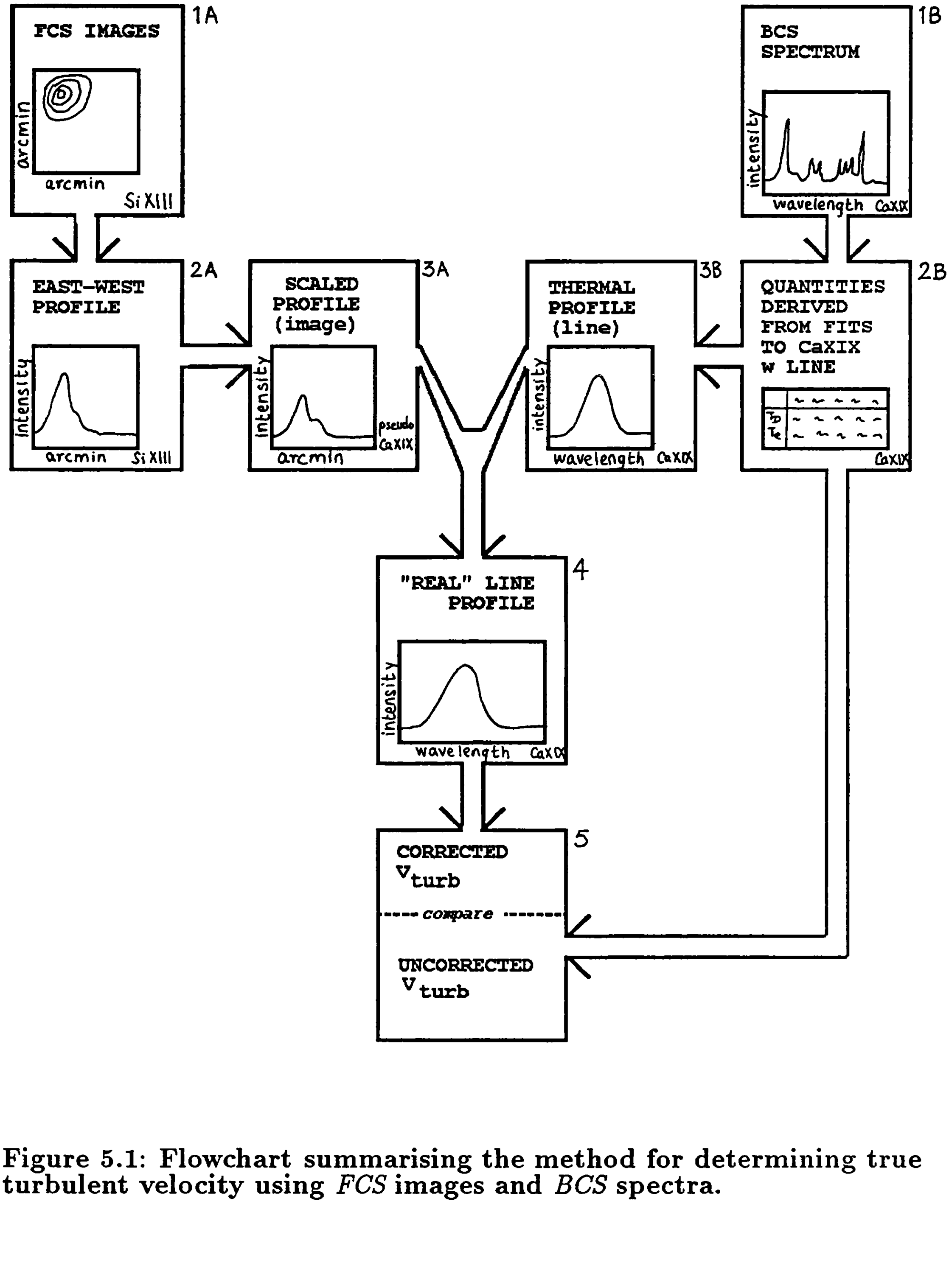

Figure 5.1: Flowchart summarising the method for determining true turbulent velocity using *FCS* images and *BCS* spectra.

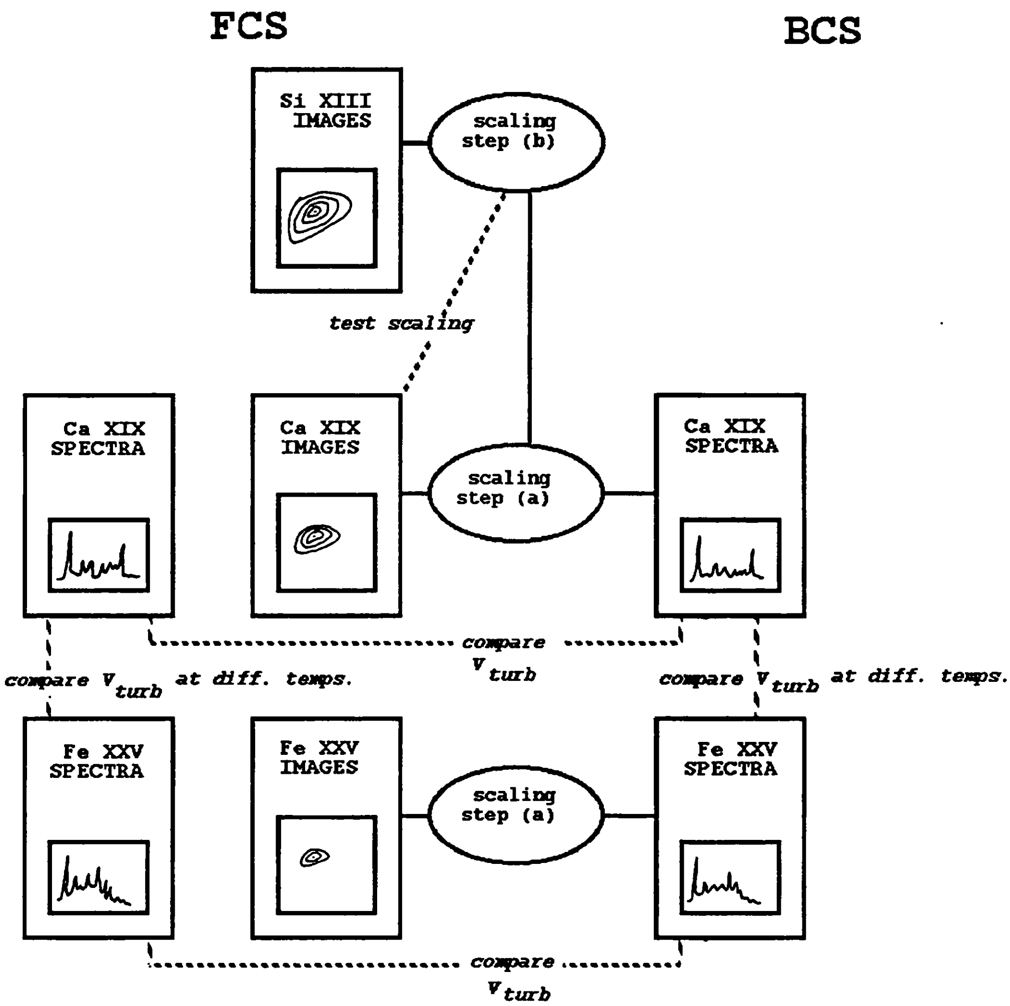

Figure 5.2: The possible combinations of *FCS* and *BCS* data. *The solid lines connecting the boxes represent the matching of data prior to processing. The broken lines represent the comparison of results after processing.*

dispersion axis was held in an east-west attitude, the spectrometer was not sensitive to north-south intensity distributions. Therefore it is the east-west extent of the source which determines the amount of line broadening. The *BCS* recorded spectra only, making it necessary to use coincident *FCS* images to determine the source size. This is the main criterion for selecting suitable flares: that there should exist simultaneously observed *FCS* images and *BCS* spectra. As it is the east-west distribution that is of interest, each image was reduced to an east-west intensity profile. An example of a contour image of a flare and the corresponding intensity projection along the east-west axis is shown in Figure 5.4.

The *SMM-FCS* uses a set of seven flat crystals each of which is so positioned as to diffract one of the resonance lines of seven helium-like ions. These seven channels are ranked in order of increasing energy. For most of the flares that were observed by the *FCS*, images were recorded only in Channels 1 to 5, the highest of which records the Si XIII resonance line. Channels 6 and 7 recorded the Ca XIX and Fe XXV resonance lines respectively, which would have been ideal, but in lieu of this the next highest line, Si XIII, is used. However for one flare, which occurred on 29 June 1980 at 0230 UT, there do exist *FCS* images of the Ca XIX and Fe XXV resonance line emission. This flare can then be used as a test of the extrapolation method that has been developed for the other flares.

5.2.1(b) Estimating the Ca XIX flare size from Si XIII images.

It is not possible to compare the intensity of Si XIII resonance line emission directly with that of Ca XIX resonance line emission, even if they have a common source. The intensity of a line is a function of temperature and volume:

$$I_\Lambda = A \int_{t1}^{t2} G(T_e)\, DEM(Te)\, dT_e \tag{5.5}$$

The emission function $G(T_e)$ is calculated from laboratory atomic physics data and is known to represent accurately the emission from highly ionised plasma (Bely-Dubau *et al.*1982). The differential emission measure $DEM(T_e)$ gives the number of electrons with temperatures in the range T_e to T_e+dT_e. The measured intensity of the Si XIII resonance line is equal to the integral of Equation 5.5 over the appropriate temperature range. Similarly the intensity of the Ca XIX resonance line, had it been measured by the *FCS*, is equal to the integral of its $G(T_e)$ function over the same temperature range:

Therefore the ratio of Si XIII resonance line intensity to Ca XIX resonance line intensity is equal to the ratio of the integrals of their emission functions:

$$\frac{I_{SiXIII}}{I_{CaXIX}} = \frac{\int_{t1}^{t2} G_{SiXIII}(T_e)\, DEM(T_e)\, dT_e}{\int_{t1}^{t2} G_{CaXIX}(T_e)\, DEM(T_e)\, dT_e} \tag{5.6}$$

The ratio on the right hand side of Equation 5.6 can be approximated by measuring the areas under the respective $G(T_e)$ curves. Having obtained the value of this ratio, dividing it by the measured Si XIII resonance line intensity gives the expected Ca XIX resonance line intensity. It is necessary to check that the $G(T_e)$ curves for Ca XIX and Si XIII do share a common temperature range, and that this range is relevant to the flare temperature. It is necessary to check this because the temperature profile of the flare is derived from the Si XIII emission, and if this profile does not apply equally well to the Ca XIX emission function there is a risk of obtaining a false picture of the Ca XIX emission. In the case of the resonance lines of Si XIII and Ca XIX, Figure 5.3 shows that there is a large overlap between the two functions. An important assumption being made here is that $DEM(T_e)$ over this temperature range is constant. For the temperature range that is of concern here, the distribution is more or less flat. The validity of this assumption is tested in Section 5.2.2 using the rare occurrence of *FCS* Ca XIX images .

So far the procedure has reached the stage illustrated in box number *3A* on the flowchart. Starting from an east-west profile of the flare in Si XIII resonance line emission, an adjustment has been made to compensate for the differences in sensitivity between the *FCS* and the *BCS*, the intensity has been scaled down to the level expected for Ca XIX resonance line emission to obtain a one-dimensional, east-west oriented, intensity profile of the flare in Ca XIX.

5.2.1(c) Convolution of the spatial intensity profile with the thermal line profile.

The spatial intensity profile can be considered to be a collection of point sources, each of which produces a thermally broadened line profile. Thus the convolution of the spatial intensity profile with a thermally broadened line profile will result in the thermally broadened profile for a spatially extended source (Box 4 on the flowchart in Figure 5.1).

By comparing this simulated thermal profile with a real profile and measuring the excess width that the latter has over the former, the amount of true non-thermal broadening may be measured. If it is assumed that turbulent mass motion is the cause of the non-thermal broadening, the broadened line width may be expressed in terms of a *turbulent velocity* given by:

$$v_{turb} = \frac{c}{\Lambda_i}\sqrt{\Delta\Lambda^2_{Doppler} - \Delta\Lambda^2_{spatial} - \Delta\Lambda^2_{thermal}} \tag{5.7}$$

where Λ_i = wavelength of line, c = speed of light and $\Delta\Lambda_{thermal}$ is the thermal width. $\Delta\Lambda_{spatial}$ is the width of the Gaussian intensity profile that is equivalent to the *real* intensity profile. If the real intensity profile *was* Gaussian shaped, then it would save the effort of having to convolve it with the thermal line

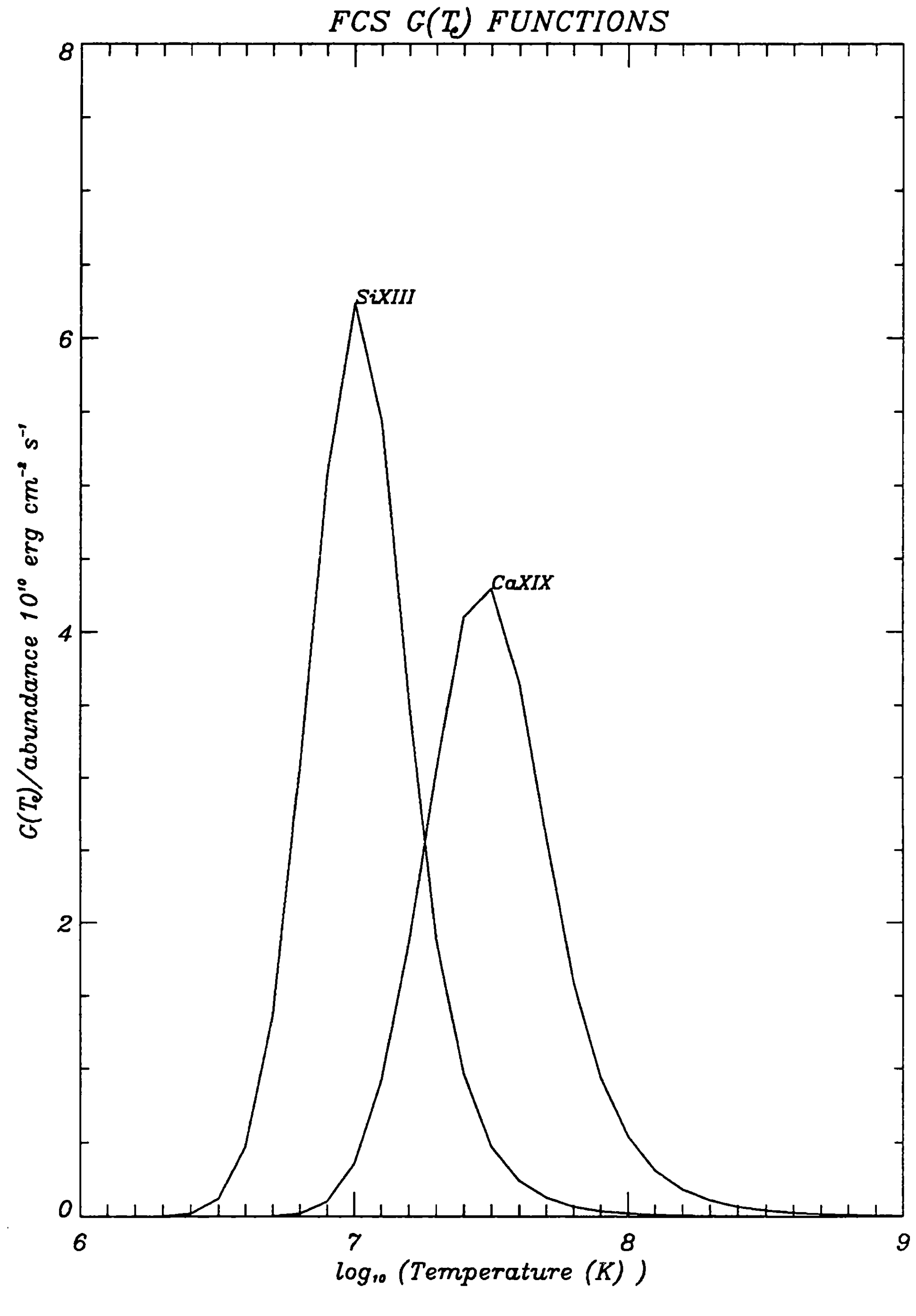

Figure 5.3: Overlap of the emission functions of the Si XIII and Ca XIX resonance lines.

These curves represent the function $G(T_e)$ from Equation 5.5. The ratio of the areas under the curves ($= \int G(T_e)$) is equal to the ratio between the corresponding line intensities, if $DEM(T_e)$ is constant. If $DEM(T_e)$ varies, and is say, equal to 2 from $10^6 MK$ to $10^7 MK$ and is equal to 1 for higher temepratures, the area under the Si XIII curve will be doubled while that under the Ca XIX curve will remain the same. The temperature range shown is typical of the flare decay phase.

profile - all that would have to be done in that case would be to measure the width of the Gaussian intensity profile and use it as the value for $\Delta\Lambda_{spatial}$ in Equation 5.7.

Figure 5.8 shows the predicted dependence of turbulent velocity on source size for different pairs of values of Doppler temperature and electron temperature. Thus in a flare which, for example, has a Doppler temperature [2] of 20 MK and an electron temperature of 10 MK, a 1.9 arcmin east-west size would account for all the excess line width. A 1.0 arcmin size would leave it with about 55 km s^{-1} of turbulent velocity.

5.2.2 Testing the method.

The extrapolation method described in Section 5.2.1(b) was used to derive Ca XIX images sizes from Si XIII images. The efficacy of this method can be put to the test with the help of real Ca XIX images. There is such a rare sequence of *FCS* Ca XIX images of the flare of 29 June 1980 (at 0230 UT) that exists in addition to the usual Si XIII images.

Although most flares observed by *SMM* lack *FCS* images of Ca XIX w-line emission (*FCS* Channel 5), the 0230 UT flare of 29 June 1980 does have *FCS* Ca XIX images, in addition to *BCS* Ca XIX spectra.

The extrapolation process, already described in detail above, consists of scaling down an *FCS* Si XIII image to mimic the flare as it would have been seen by the Ca XIX channel of the *BCS*. This involved two scaling steps:

> **Scaling step (a): To compensate for the different sensitivities of the two instruments.** This is a scaling factor that is derived from known instrument performance factors and there is not much uncertainty about its value.
>
> **Scaling step (b): To compensate for the difference in temperature ranges.** Si XIII corresponds to a slightly lower temperature range than Ca XIX, and if the electron density in these two temperature ranges is different, the amount of emission will also differ. The measure of how the electron density varies across the temperature range is the DEM. This scaling step was dealt with by making the assumption that the DEM distribution is uniform between and across the Si XIII and Ca XIX temperature ranges. The scale factor was thus assumed to be equal to 1.

---

[2] The *Doppler temperature* is the temperature equivalent of the Doppler width, and is given by $T_D = \frac{\Delta\Lambda_{Doppler}}{\Delta\Lambda_i}\frac{cM_i}{2k_B})$

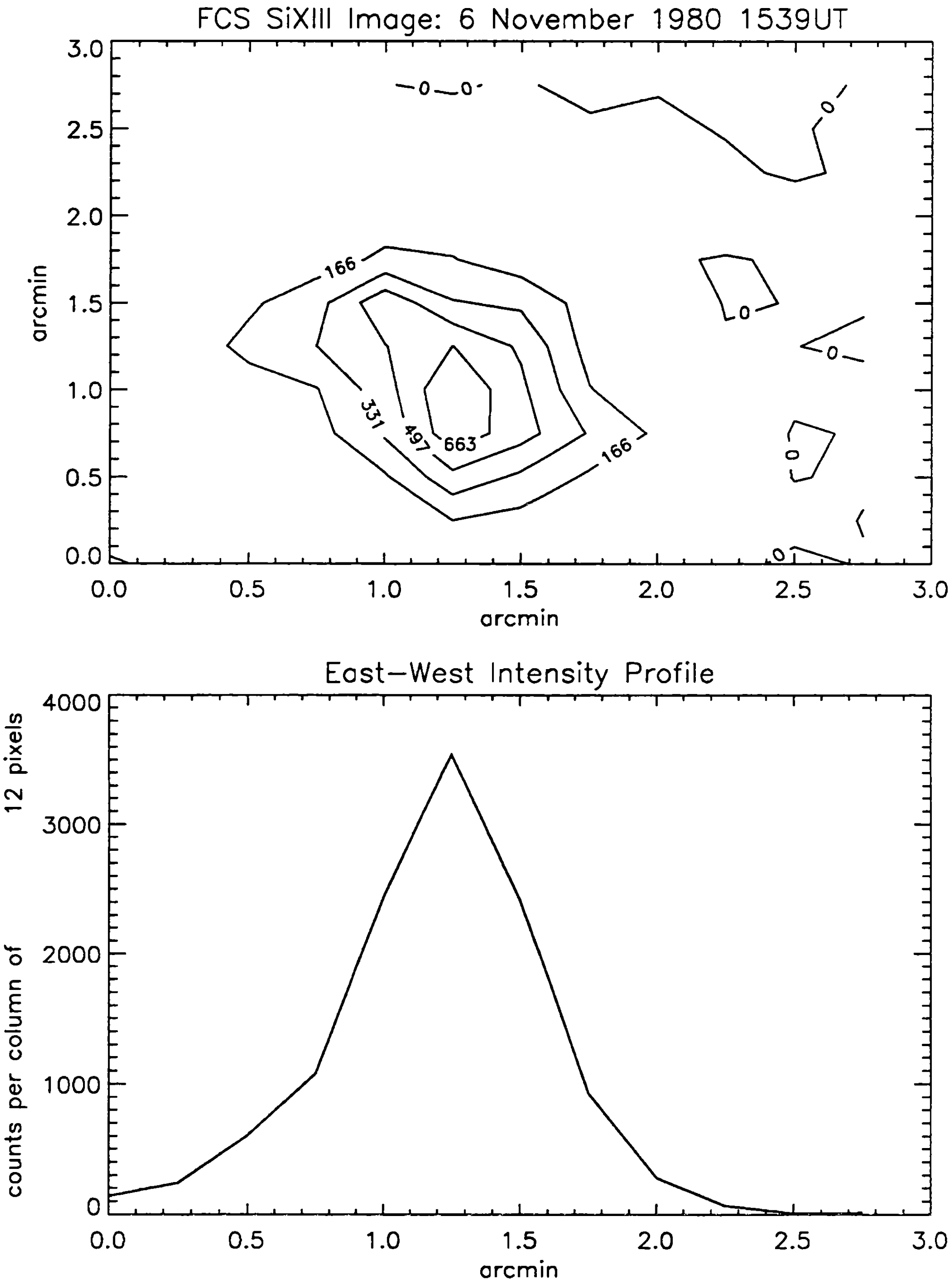

Figure 5.4: Contour image of a flare (upper) and its east-west intensity projection (lower).
The intensity projection, which is obtained by summing the intensity values in each north-south column of pixels in the flare image, is a simulation of the intensity distribution seen by the BCS, *which is not sensitive to intensity variations in the north-south direction.*

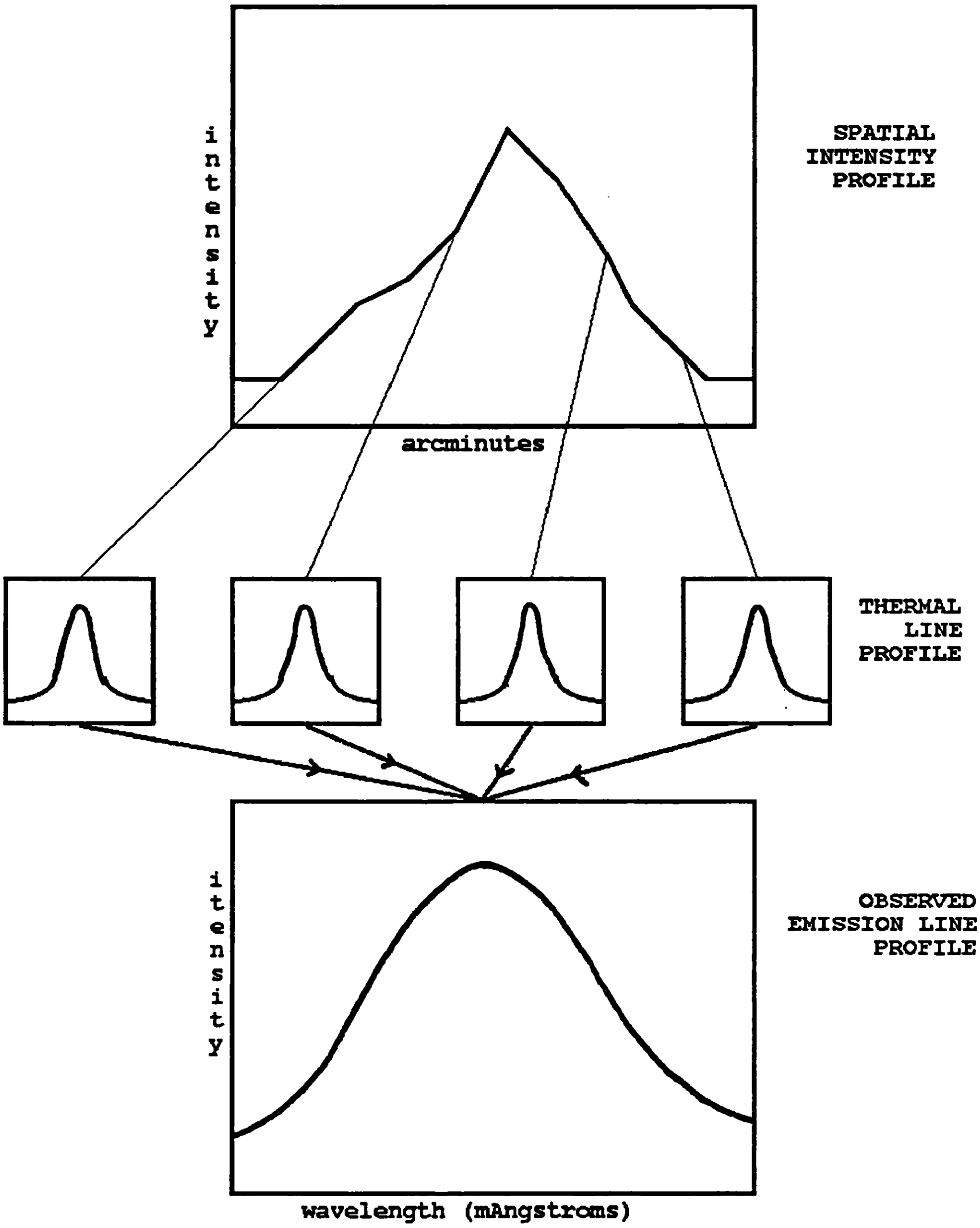

Figure 5.5: How an extended source causes line broadening.
Each point on the spatial intensity profile is the source of a thermally broadened line profile. The convolution of the spatial intensity profile with the thermal line profile results in a size-broadened line profile. If this profile is still not as wide as the observed line profile, it means that the thermally broadened profile was too narrow, and that some extra broadening, probably due to turbulent motion, must be added to the thermal profile.

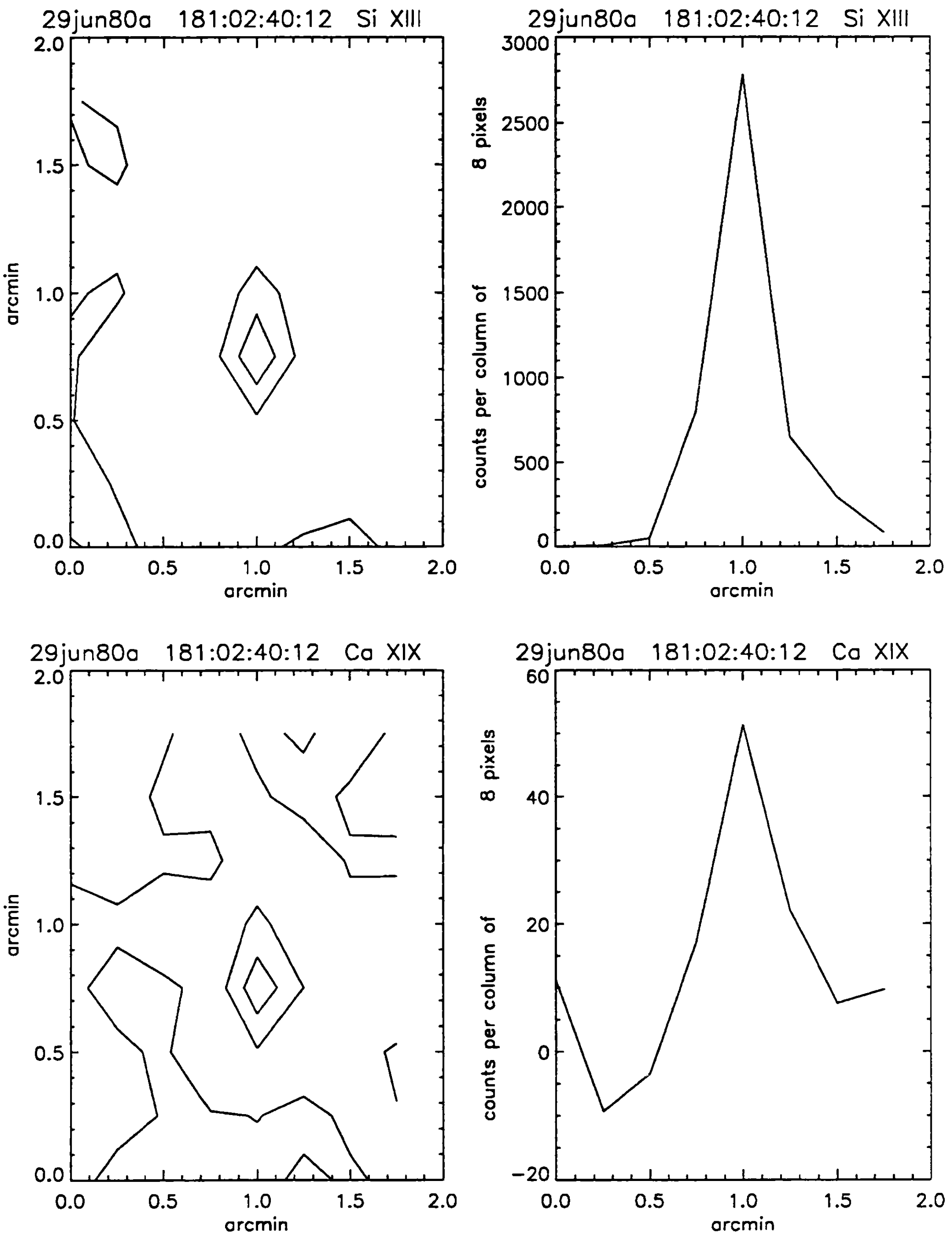

Figure 5.6: Simultaneous Si XIII and Ca XIX images.

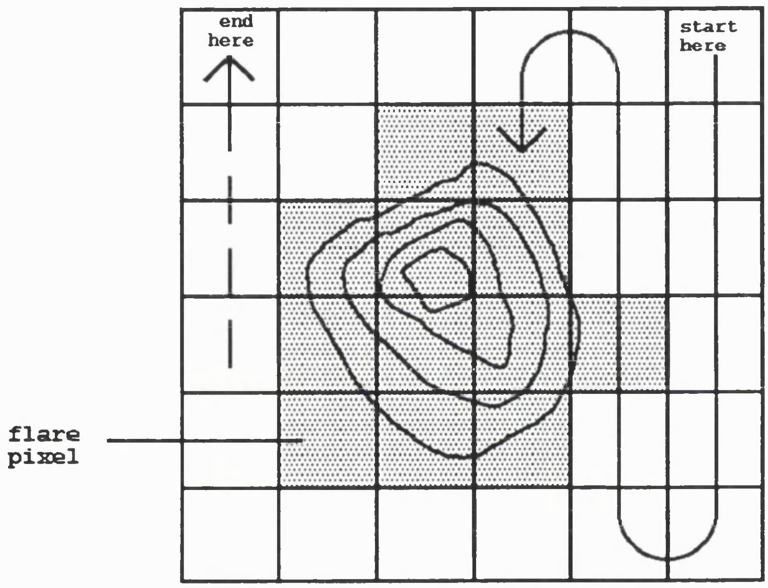

Figure 5.7: How the *FCS* in its imaging mode scans a flare. *Each pixel is observed for 1.024 seconds, and the 6×6 pixel image shown above would take take 0.6 minutes to scan. More typical images are 16 ×16 pixels and would take 4.4 minutes to scan. The flare itself is being scanned for only a part of this time, and it is important to select* BCS *spectra which correspond to the relevant time interval.*

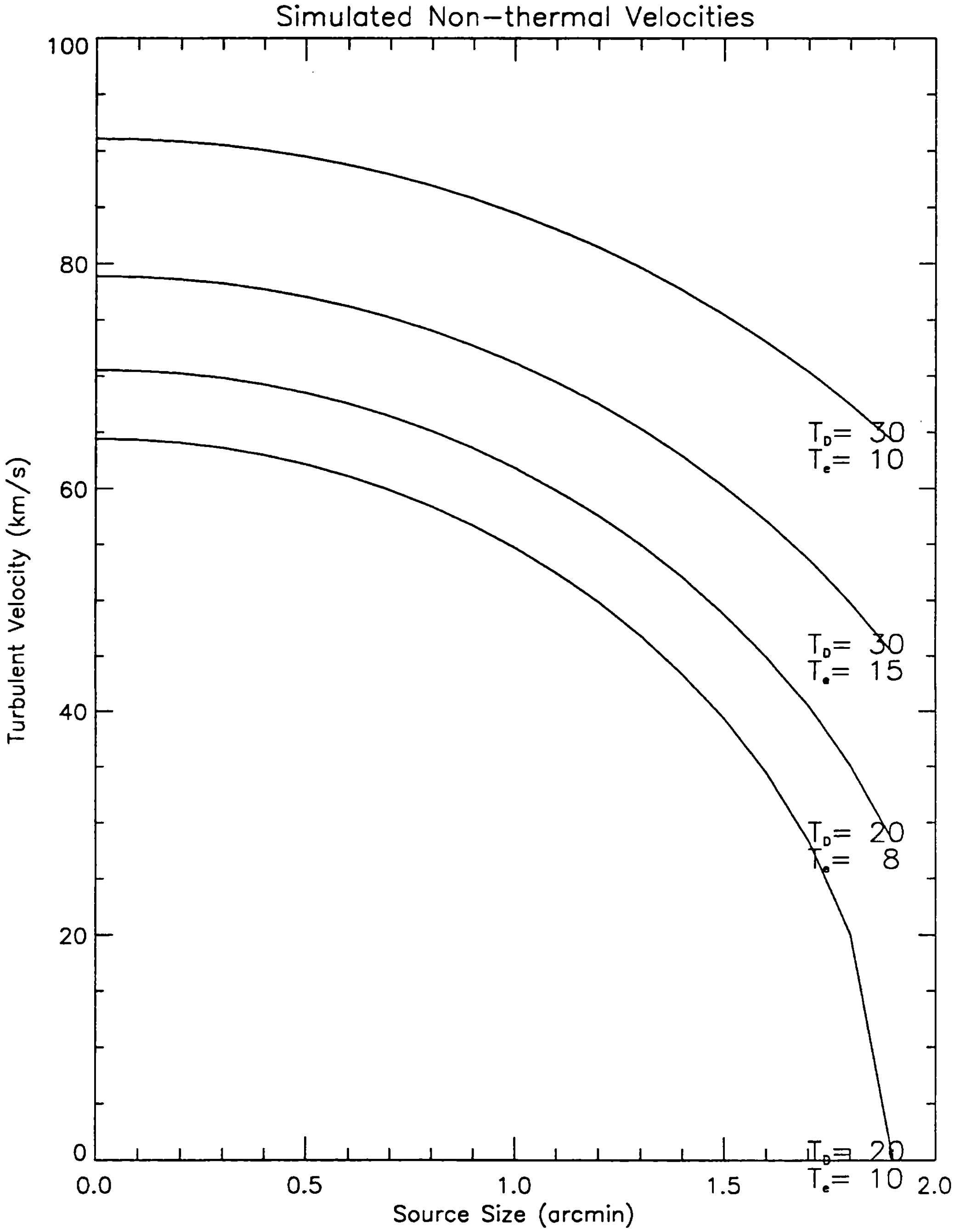

Figure 5.8: Equivalence of turbulent velocity and source size.
For given pairs of values of Doppler temperature (T_D)and electron temperature(T_e), the non-thermal line width may be interpreted as a combination of the effect of turbulent motion and of the effect of flare size.

Quantity	*FCS* Channel 1 (Si XIII)	*BCS* Channel 4 (Ca XIX)
Ion abundance	$(5.36 \pm 2.96)10^{-5}$	$(3.19 \pm 1.28)10^{-6}$
Effective area cm^3	-	0.024
Sensitivity $counts/photon/cm^2$	0.0053	-
$\int G(T_e)$ $erg/cm^2/s$	5.24×10^{11}	1.67×10^{11}

Table 5.1: Instrument parameters for the *FCS* and *BCS*.
The scaling factors (a) and (b) are calculated from the instrument parameters given in this table.

When using *FCS* Ca XIX images, however, the second scaling step is avoided altogether. Thus the Ca XIX size obtained from the *FCS* Ca XIX images that exist for this particular flare can be compared with the size extrapolated from *FCS* Si XIII images to test the validity of the uniform DEM assumption.

5.2.3 Comparing *BCS* Ca XIX and Fe XXV spectra.

The purpose of this comparison is to look for differences between the non-thermal broadening/turbulence from plasma of different temperatures. For most flares observed with the *BCS*, both Ca XIX and Fe XXV spectra are available. The method adopted in this analysis is to match the available *BCS* spectra with *FCS* images that are closest in temperature to the spectra (See Figure 5.2). If the instruments had worked as intended, it would have been straightforward to match *FCS* Ca XIX w-line images to *BCS* Ca XIX w-line profiles. Because of the failure of various channels, it so happens that the highest temperature *FCS* channel that is commonly available is the Si XIII channel. The Si XIII temperature range lies below the Ca XIX temperature range, but there is still a sufficient amount of overlap between their emission functions (as can be seen in Figure 5.3) to permit the extrapolation from Si XIII emission levels to Ca XIX emission levels.

There is in fact a sole flare (29 June 1980, 0230 UT) for which there are not only *FCS* Ca XIX images, but Fe XXV images as well. Thus a direct match can be made between (*FCS*) Ca XIX images and (*BCS*) Ca XIX spectra *and* between (*FCS*) Fe XXV images and (*BCS*) Fe XXV spectra. This also means that a comparison can be made between the non-thermal broadening from two different plasma temperature ranges and thus test the existing notion that hotter plasma is more turbulent. (Jakimiec and Fludra, 1991)

5.2.4 Comparing *FCS* and *BCS* spectra.

The purpose of this comparison is to look for differences in the spatial distribution of non-thermal broadening/turbulence, by exploiting the differences in the fields-of-view of the *FCS* and *BCS*.

The *FCS* was capable of being used not only as a monochromatic imaging device, but also as a spectrometer. Some joint spectral observations were made with the *FCS* and the *BCS*, with the *FCS* in its spectral scanning mode. In one of these modes the *FCS* would initially raster across the flaring region, (in the manner shown in Figure 5.7) select the brightest pixel in the scan, point the instrument at this region of peak brightness and then record its emission spectrum. Because *like* spectra (Ca XIX) are being compared, only the differences in instrument sensitivity and spectrum integration times have to be compensated for. The remaining instrument differences can then be used as flare diagnostics, as follows:

(a) The *FCS* has a much smaller field of view than the *BCS*. The smaller the observed volume of plasma, the smaller will be the range of temperatures and mass velocities seen. Thus the *FCS* will be averaging over a more specific range of temperatures and velocities than the *BCS*

(b) The *FCS* does not suffer from the flare size-dependent line broadening that the *BCS* suffers from, and line widths derived from *FCS* spectra can be taken to reflect purely physical effects

BCS spectra from the main sample of flares were fitted to using line fitting programs written for the *SMM-BCS*.† Less sophisticated programs to fit *FCS* spectra also exist. Recently, the line fitting programs written for the new *Yohkoh Bragg Crystal Spectrometer* (*Yohkoh BCS*) have become available and they have been used to fit lines to both *FCS* and *BCS* spectra. This is a more consistent approach than using different fitting programs for spectra from the different instruments, and is quite important when different spectra from the same source are being compared directly with each other.

---

† *Yohkoh-BCS* spectral fitting routines were used only for the purpose of comparing *SMM-BCS* spectra with *FCS* spectra from the 5 November 1980 flare.

Table 5.2: The main sample of flares.

Flare index no.	Date	Data between (UT)	Solar coords. (arcmin)		No. of pnts	Av.E-W FWHM (arcmin)	Corrected V_t			Uncorrected V_t		
			N	E			Av km/s	Max km/s	Min km/s	Av km/s	Max km/s	Min km/s
2	8 Apr 80	0308-0312	-4.9	-3.4	4	1.04	71.7	89.9	59.7	80.97	97.27	64.22
3	10 Apr 80	0920-0929	-4.6	10.3	3	0.75	71.8	89.9	55.7	78.72	93.51	66.49
8	21 May 80	2115-2126	3.3	-3.5	3	1.08	58.2	60.4	56.5	68.71	70.98	66.99
14	29 Jun 80	0234-0302	7.6	-13.2	25	0.55	67.2	87.6	53.8	70.05	88.56	57.85
16	29 Jun 80	1814-1829	7.5	-13.7	2	0.43	53.3	58.5	48.1	56.22	62.05	50.39
54	6 Nov 80	1539-1635	4.3	14.4	14	0.83	35.7	55.3	22.2	47.18	55.56	38.16
55	6 Nov 80	1720-1738	4.2	14.3	7	1.49	85.7	104.0	64.0	97.95	115.94	80.58
56	7 Nov 80	0440-0520	4.4	13.5	17	0.88	56.6	72.2	38.5	66.38	78.42	48.85
82	13 Nov 80	0059-0137	4.2	-4.9	10	1.41	45.2	52.0	35.3	61.92	70.74	50.35
85	22 Nov 80	0540-0603	-2.5	0.7	10	0.98	84.8	101.8	69.6	90.51	102.22	78.34
96	2 May 84	1924-1940	3.5	-12.9	3	0.48	55.1	65.2	45.1	59.5	68.34	50.67
101	5 May 84	1814-1829	4.1	-15.3	2	0.43	52.1	58.3	45.9	55.03	61.78	48.29
106	19 May 84	2144	3.5	15.4	1	0.38	85.1	85.1	85.1	87.85	87.85	87.85
114	21 May 84	1749	3.4	10.1	1	1.21	64.0	64.0	64.0	88.48	88.48	88.48
116	22 May 84	1453-1551	3.4	7.7	3	0.61	77.7	103.7	47.5	88.26	109.44	49.81
133	7 Feb 86	1040	1.3	-5.3	1	1.05	83.9	83.9	83.9	92.72	92.72	92.72
134	11 Feb 86	2311	-0.3	-11.0	1	0.63	58.0	58.0	58.0	73.57	73.57	73.57

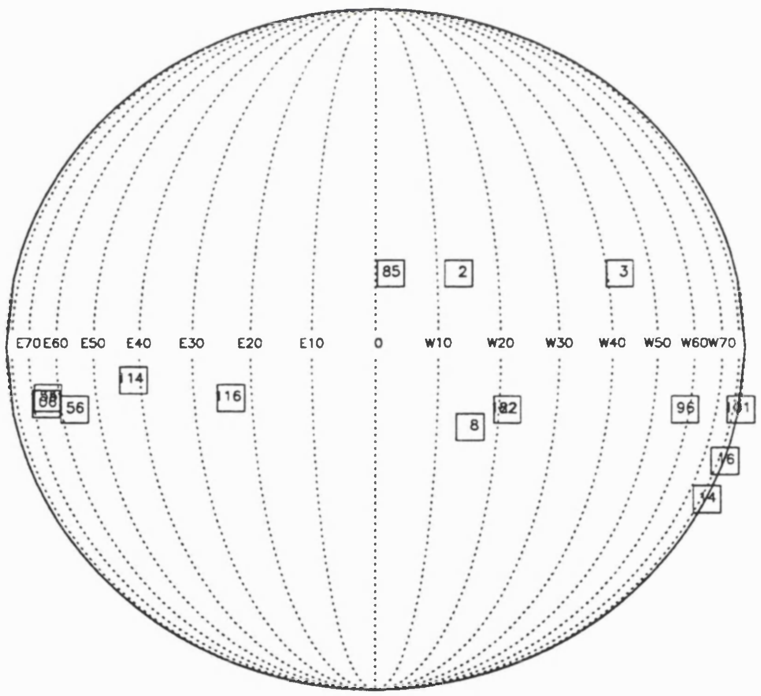

Figure 5.9: The positions on the Sun's disc of the flares listed in Table 5.2 .

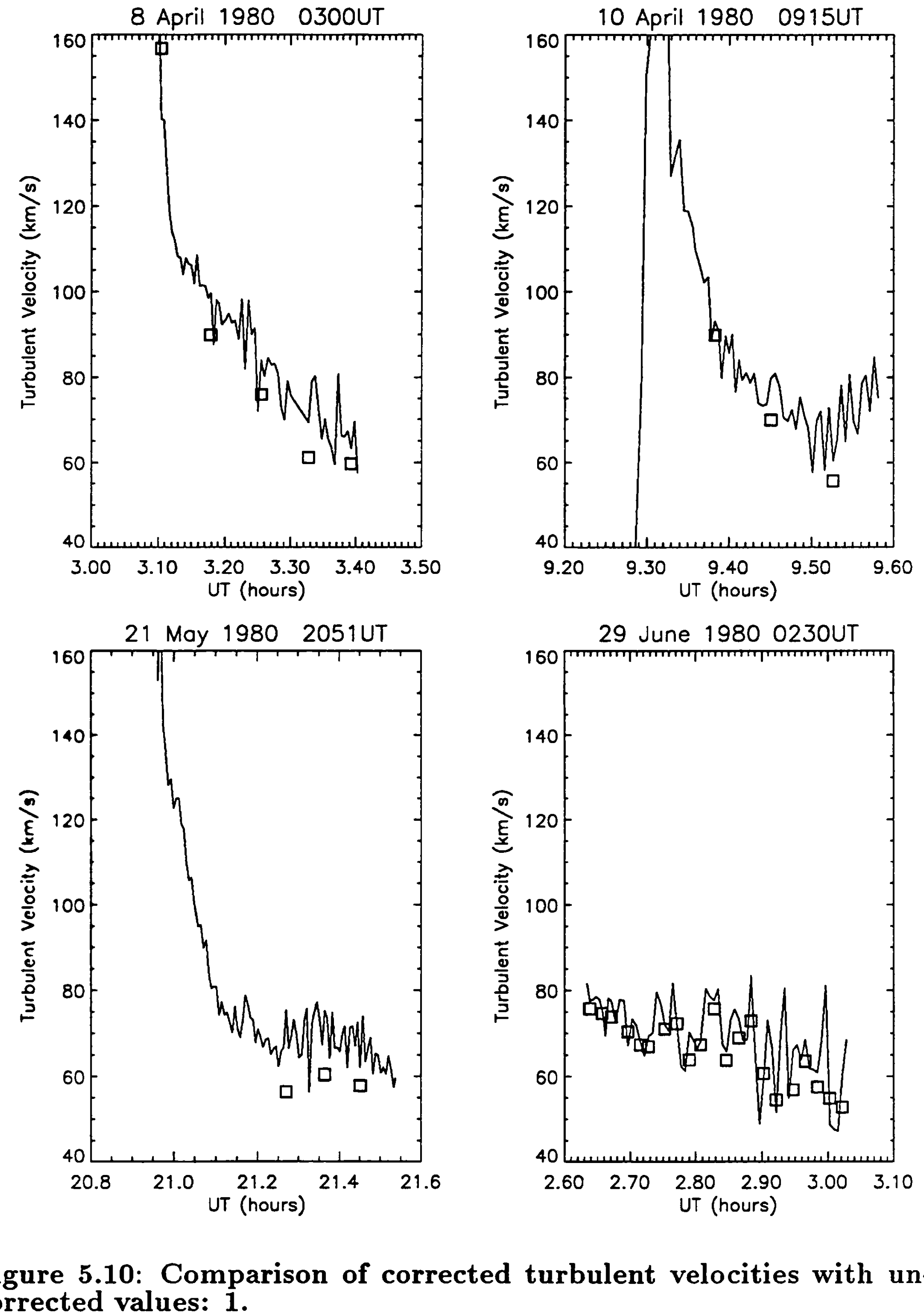

Figure 5.10: Comparison of corrected turbulent velocities with uncorrected values: 1.
The continuous line represents the uncorrected turbulent velocities and the square symbols represent corrected values.

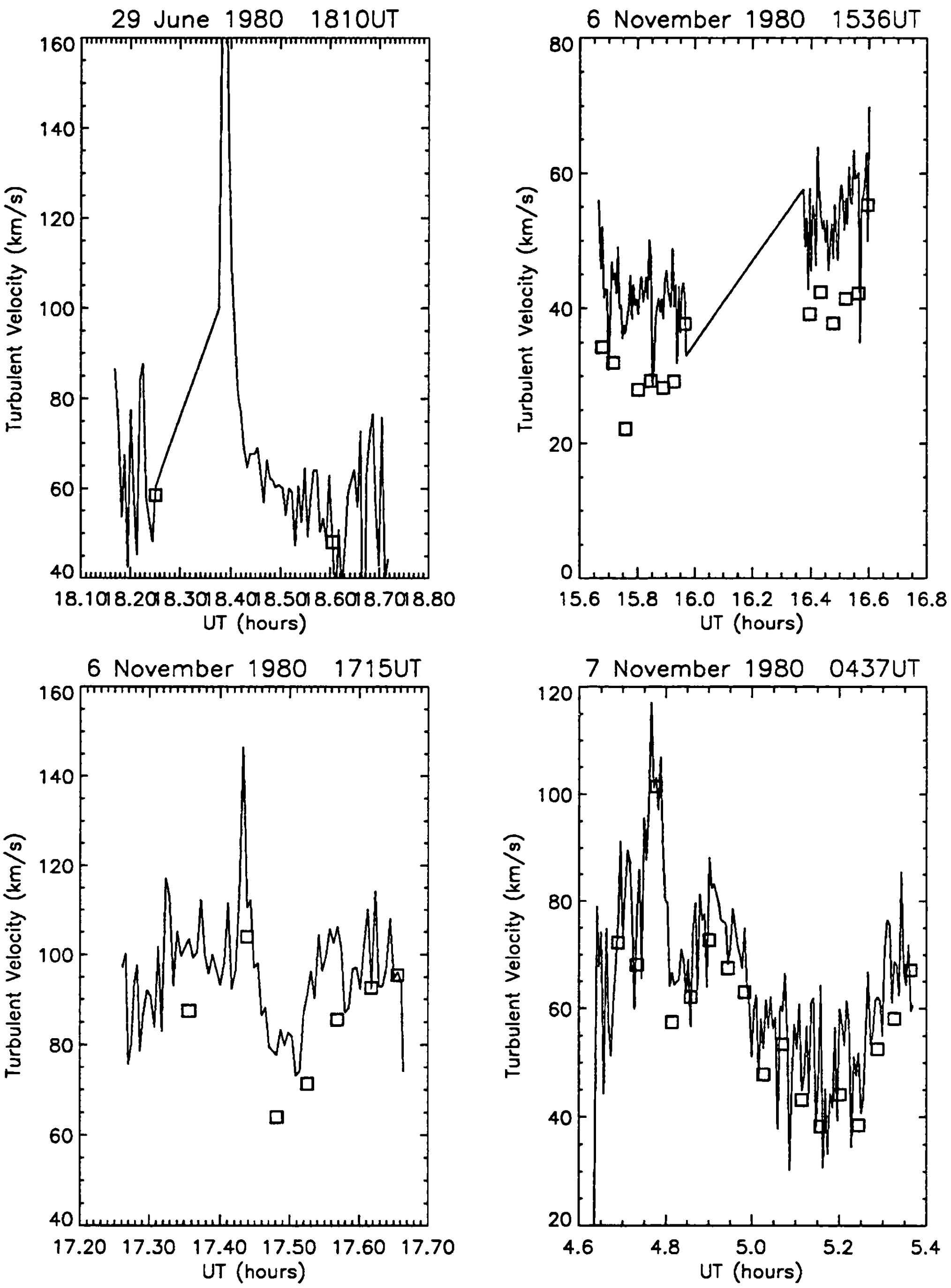

Figure 5.11: Comparison of corrected turbulent velocities with uncorrected values: 2.
The continuous line represents the uncorrected turbulent velocities and the square symbols represent corrected values.

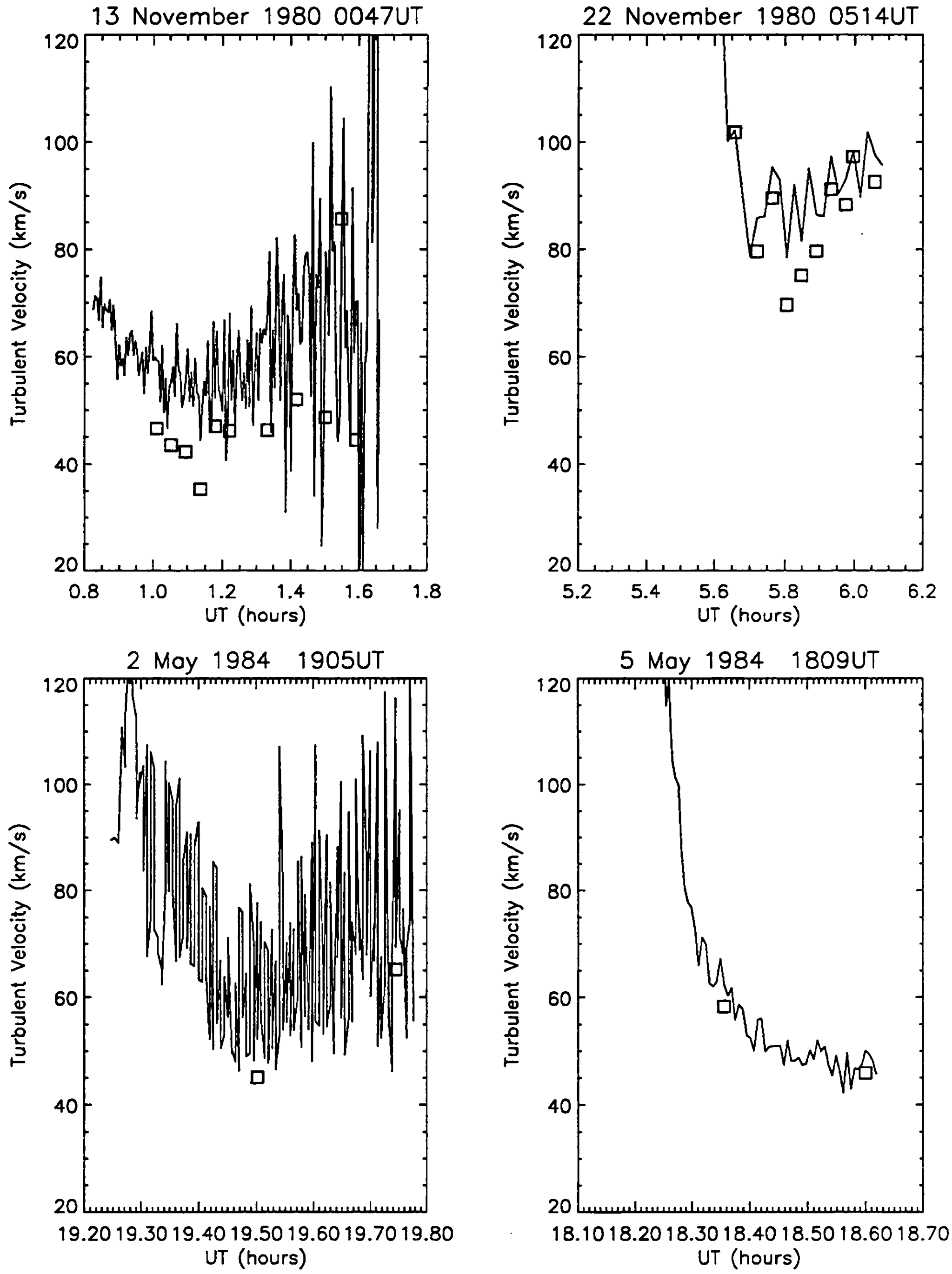

Figure 5.12: Comparison of corrected turbulent velocities with uncorrected values: 3.
The continuous line represents the uncorrected turbulent velocities and the square symbols represent corrected values.

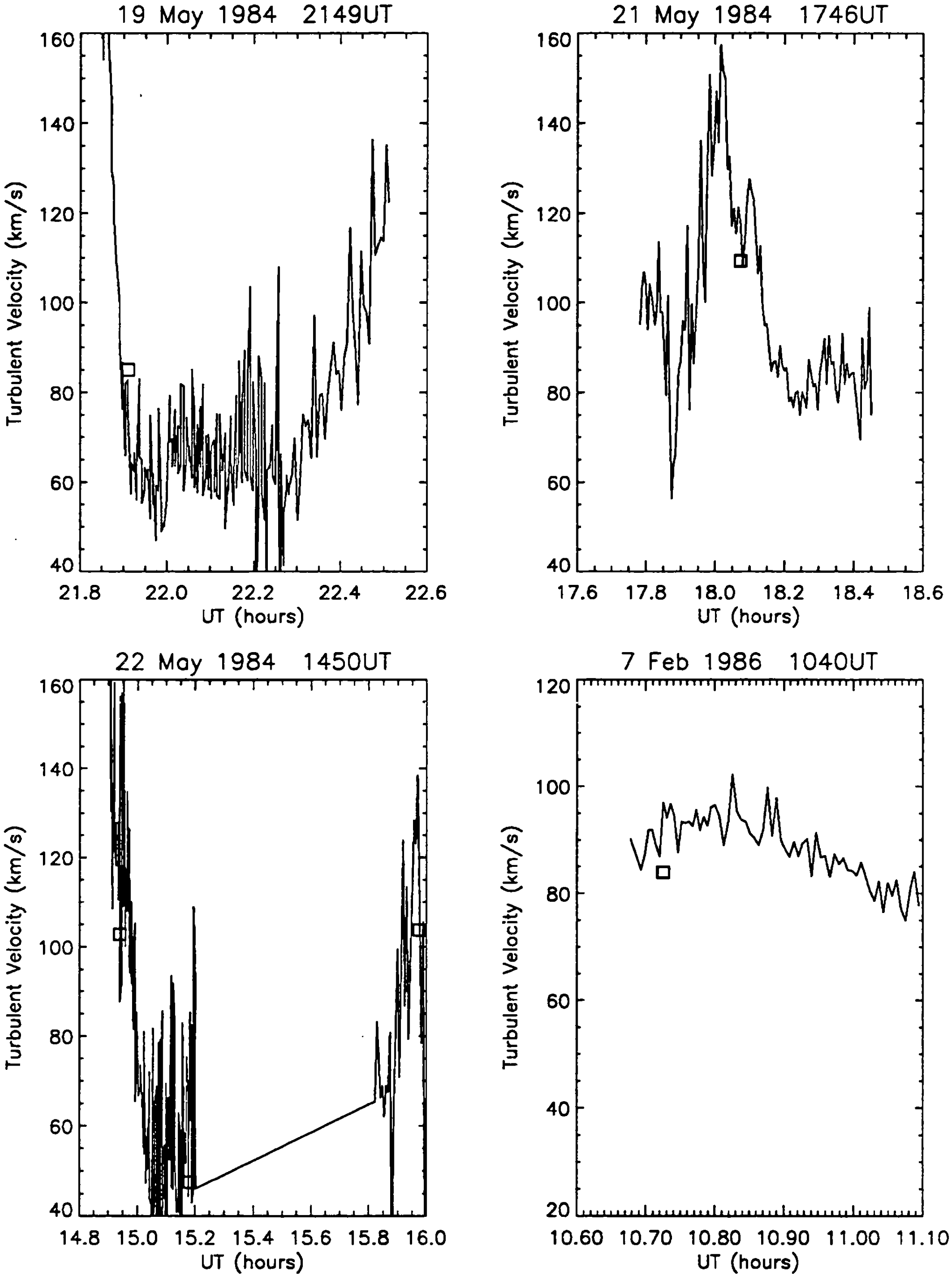

Figure 5.13: Comparison of corrected turbulent velocities with uncorrected values: 4.
The continuous line represents the uncorrected turbulent velocities and the square symbols represent corrected values.

5.3 Data and Results

5.3.1 The main sample.

The choice of flares to be included in the main sample presented here is restricted by the number of occasions on which both the *BCS* and *FCS* successfully observed the same event. Though the *BCS* observed more than 150 flares, which are listed in the table in the Appendix, far fewer of these events were recorded by the *FCS* in its imaging mode. Seventeen flares which have good quality *FCS* images and *BCS* spectra of their decay phase are listed in Table 7.1. The distribution of these flares on the Sun's disc is shown in Figure 5.9.

5.3.2 Testing the extrapolation from Si XIII sizes to Ca XIX sizes.

The 0230 UT flare of 29 June 1980 has, in addition to *FCS* Si XIII images, a sequence of Ca XIX and Fe XXV images.

The Ca XIX images of this flare are used to check the extrapolation method for deriving Ca XIX flare sizes from Si XIII images. Scaling the Si XIII profile down by the factor of 44.3 (combining the values of the relevant scaling factors given in Table 5.1) produces a simulated Ca XIX profile size that is quite close to the actual Ca XIX size, if a little bigger. This means that the size dependent effect that is being estimated will be an upper limit.

5.3.3 Non-thermal broadening in the decay phase.

The results of applying the correction for the size-dependent broadening to the Ca XIX resonance line are presented here. The series of plots shown in Figure 5.10, 5.11, 5.12 and 5.13 show the effect of the correction made to the size-dependent broadening. The continuous lines in these plots represent uncorrected turbulent velocities. The points marked with boxes represent corrected values, wherever *FCS* images were available to estimate the flare size.

Turbulent velocities have to be corrected by 20% on average, this correction being greatest when the turbulent velocity reaches a minimum during the decay phase. Having corrected for the size-dependent effect, the remaining non-thermal line width can be justifiably described as turbulent broadening and its behaviour studied in terms of turbulent velocities with greater confidence than previously.

Turbulence in flares reaches high figures (upto 200 km s^{-1}) during the rise phase and begins a rapid decrease soon after the flare reaches its soft X-ray peak.

In the flares in this sample, it reaches a minimum about 20-30 minutes after the flare has peaked and then begins to increase. This behaviour is observed in ten out of the sample of seventeen flares, and is illustrated most clearly by the 1715 UT flare of 6 November 1980 (Figure 5.11). In these instances, the post-peak minimum reached has values of between 30 and 60 km s^{-1} .

The post-peak minimum is strongly correlated with the emission measure peak, being coincident in three cases (02 May 1984 at 1905 UT, 05 May 1984 at 1810 UT and 21 May 1984 at 1746 UT), and occurring not later than 12 minutes after the emission measure peak in the other flares.

The post-peak minimum is not sustained for longer than 5 minutes, and the turbulent velocity increases once again. The magnitude of the rise varies between 50% of the minimum value (6 November 1980 at 0103 UT) and over 100% (19 May 1984 at 2149 UT). In all the flares this rise in the late phase was apparent even before the correction for the effect of the flare size was made. The difference between corrected and uncorrected values is greatest when the turbulent velocity is at its post-peak minimum and decreases as the turbulent velocity increases towards the late phase. This has the effect of emphasising the minimum and the steepness of the subsequent rise.

Of all the flares, the flare of 19 May 1984 shows the most distinctive late phase turbulent velocity increase. Figure 5.13 shows the uncorrected turbulent velocity reach a minimum of about 60 km s^{-1} at 2210 UT and then increase by almost 60 km s^{-1} over a period of 20 minutes. However, this is the uncorrected turbulent velocity and the behaviour of the turbulent velocity cannot be deduced with much certainty until it has been corrected for the size-dependent effect. It is unfortunate that no *FCS* image of the flare during its decay phase exists, but the single image shown in Figure 5.14, which was recorded as the flare reached its peak, permits an estimate to be made of the size that it could have had during the decay phase. Figure 5.15 shows how the east-west extents of the flares in the sample vary with time during their decay phases. In all but two flares, 21 May 1980 (Index No. 8) and 6 November 1980 (Index No. 55), their sizes either increase or remain constant, but never decrease.

So taking the rise phase size of the 19 May 84 flare to be about 0.4 arcminutes, out of a total line width equivalent to 87.9 km s^{-1} only 13.5 km s^{-1} may be attributed to the size effect. Thus at least 70% of the decay phase turbulent velocity cannot be accounted for by the size of the flare without requiring it to grow from being 0.4 arcminutes across at the flare peak to being 3.7 arcminutes just 40 minutes later. If on the other hand, the flare size does decrease, it cannot be expected to do so by more than a factor of 2.0, which is the largest drop seen in this flare sample (for flare no. 55, 1720 UT on 6 November 1980). This

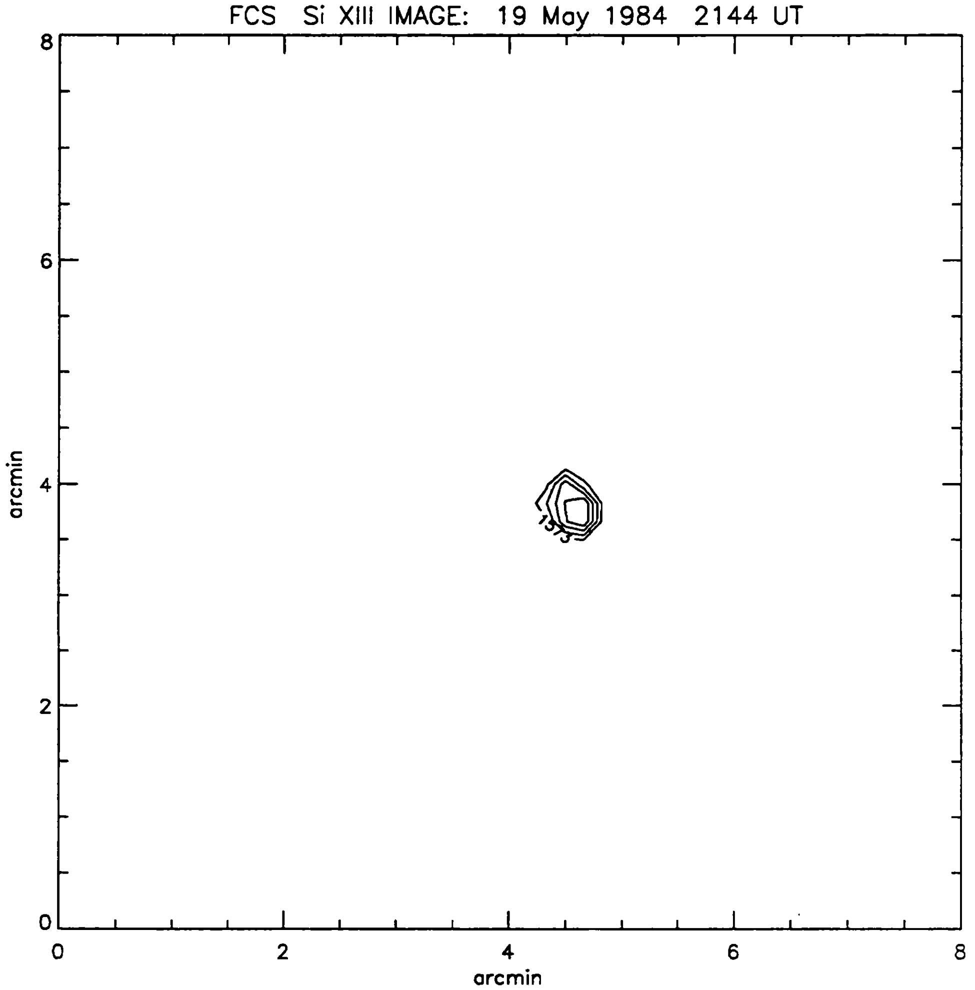

Figure 5.14: ***FCS* image of the 19 May 1984 flare.**
This is the sole image that exists of this flare in Channel 4 (Si XIII). If it behaves as do most flares, its size should increase in the decay phase, giving a true turbulent velocity of 70 % of the observed value. If on the other hand, its size decreases, the maximum true turbulent velcocity will be 85 % of the observed value.

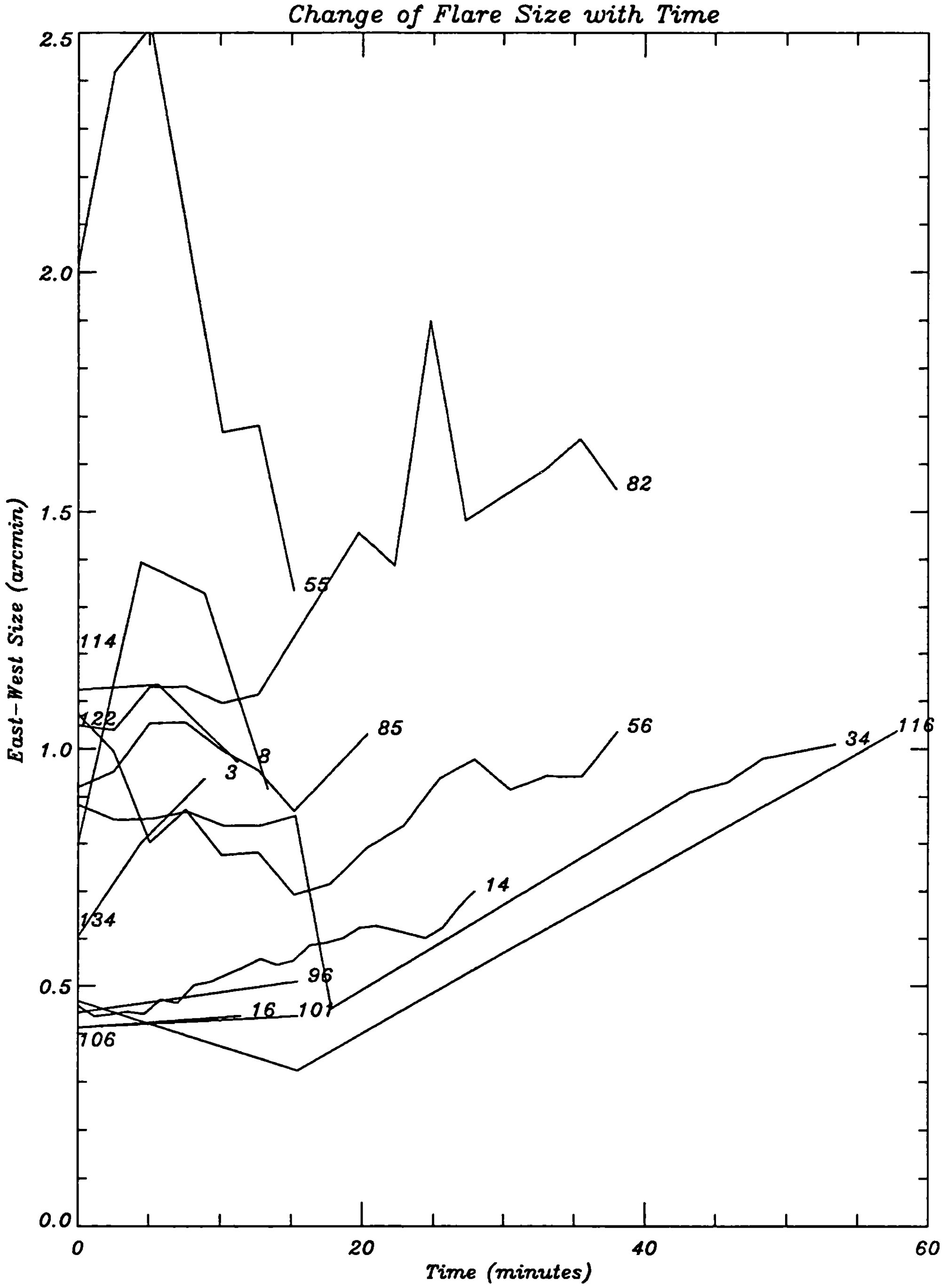

Figure 5.15: Change with time of east-west size of flares. *The east-west sizes of flares remain constant or increase with time, but never decrease. This observation is used to define an early east-west size as the minimum flare size for the 19 May 1984 flare (symbol 106).*

would make the minimum size that it could have had 0.2 arcminutes, which will account for only 15% of the decay phase non-thermal excess width.

Thus between 70% and 85% of the turbulent velocity measured in the 19 May 1984 flare is truly due to non-thermal mass motion.

5.3.4 Comparison of turbulence measured in Ca XIX and Fe XXV spectra.

The 0230 UT flare of 29 June 1980 is the only flare for which there are *FCS* images from both Ca XIX and Fe XXV channels, and these images were used (Section 5.3.2) to check the size extrapolation procedure. These images were also used *in place* of the Si XIII images, and directly matched to *BCS* Ca XIX spectra and Fe XXV spectra to obtain corrected turbulent velocity values for the two corresponding temperature regimes. The *FCS* images were scaled down only to take into account the difference in sensitivity between the *FCS* and *BCS* (*Scaling step (a)*), and directly used to correct the turbulent velocities derived from *BCS* Fe XXV spectra. The difference in the temperature ranges to which Ca XIX spectra and Fe XXV spectra respond, may be exploited in this one flare to study the differences between the turbulent velocity across a temperature divide.

5.3.5 Comparing *BCS* and *FCS* spectra from the same flare.

Spectra from the flares of 5 November 1980 (2235 UT) and 25 August 1980 were recorded by both *FCS* and *BCS*, enabling a direct comparison to be made. These spectra include the only Ca XIX flare spectra recorded by the *FCS* throughout the *SMM* mission. The *FCS* recorded spectra from a region 15 $\times$ 15 arcsecond, while the *BCS* observed a 6 $\times$ 6 arcminute region. The total intensity recorded by the *FCS* over the Ca XIX emission spectrum between 3.16 and 3.24 Å is less than that recorded by the *BCS* over the same range. However, when the intensities of the resonance line are compared, they are found to be more or less equal (*FCS* - 1161 counts/s and *BCS* - 1188 counts/s).

5.3.5(a) Differences between the instruments.

Fits were made to both *FCS* and *BCS* spectra, to obtain line intensities and widths. There are some important differences between *FCS* and *BCS* spectra that must be taken into account: because *BCS* spectra are integrated over intervals of typically 25 seconds and *FCS* spectra are scanned over periods of minutes, several consecutive *BCS* spectra can be obtained in the time that it takes to produce a single *FCS* spectrum. Also, all parts of a *BCS* spectrum are recorded simultaneously, while the wavelength scale of an *FCS* spectrum is scanned in time - so that different parts of an *FCS* spectrum are recorded at different times. This has an effect on the measured electron temperature, which is derived from the intensity ratio of the w-line to the k-line. The time that elapses between the *FCS* recording the w-line and recording the k-line is sufficiently large for a new *BCS* spectrum to have been recorded.

5.3.5(b) Differences between the spectra.

The Doppler width of the *BCS* resonance line is more than twice as great as that of the *FCS* resonance line. Thus even a 15% correction for flare size effects would leave the *BCS* turbulent velocity higher than that derived from the *FCS*. The electron temperature that has been derived from the w/k line intensity ratio in the *FCS* spectrum is 14.5 MK which is only 70% of the *BCS* electron temperature of 21.1 MK. Because of the time lag that exists between the k-line and the w-line being recorded by the *FCS*, it could be argued that the k-line intensity increased relative to the w-line in the time that it took the *FCS* to scan the region between the two lines, thus reducing the w/k line intensity ratio from its true value. However the actual time difference is under 21 seconds, and it is not likely that the DEM distribution could have changed quickly enough for this to happen (i.e: neither the temperature itself could have changed nor could there have been an increase in the amount of plasma at the temperature corresponding to maximum k-line emission. The other factor that points towards a stable temperature is the level of the thermal continuum, which is constant throughout the time that the spectrum was being recorded.

The third explanation is that the *FCS*, with its smaller field of view, happened to pick out a less turbulent volume of plasma and excluded the rest of the flare, which was more turbulent and was seen by the *BCS*. This explanation is explored further in Section 5.4.3.

Flare date	Peak time (UT)	No. of pnts.	Comments
29 Jun 80	0234	25	representative
29 Jun 80	1814	2	
6 Nov 80	1539	14	representative
6 Nov 80	1720	7	representative
7 Nov 80	0440	17	representative
22 Nov 80	0500	10	representative
2 May 84	1924	3	
5 May 84	1814	2	

Table 5.3: The abundance of data points for limb flares.
The flares on the edge of the Sun's disc have the largest scatter of average decay-phase turbulent velocities. To show that this is not due to unrepresentative averaging, this table gives the number of points over which the averages were taken.

5.4 Discussion

5.4.1 The absence of a disc-to-limb variation.

By plotting the corrected turbulent velocities against flare position, it has been established that there is no variation of turbulent velocity across the Sun's disc. In fact, contrary to the general pattern exhibited by the velocities of directed flows, the average turbulent velocities exhibited by limb flares have the highest scatter of any group of flares anywhere on the Sun's disk, having a range of average velocities that extends from 125 km s^{-1} to 50 km s^{-1} . This could be due to the unequal way in which averages have been obtained for the corrected turbulent velocities in different flares. This is determined by the number of *FCS* images available, which for some flares is just one, while other flares have as many as twenty five. The list of limb flares given in Table 5.3 shows that 5 out of 8 flares have a representative number of points. For the three flares which have only three points or fewer, an examination of their turbulent velocity curves shows that the points that are available do represent the true average fairly accurately, and that it is safe to conclude that there is no position dependence in *BCS* turbulent velocities.

5.4.2 Underlying turbulence in active regions.

On separating out the instrumental broadening component from *BCS* spectral line widths, it is found that the remaining excess non-thermal broadening never actually reaches a zero value. On the contrary it dips to a minimum value before rising again and levelling out at about 40 - 70 km s^{-1} , at least for those flares in which asymptotic values were reached while they were being observed. This is a not unexpected result since Saba and Strong (1991), looking at a selection of eleven active regions, (six on the limb and five on the disc) found that they all had non-zero turbulent velocities. These velocities ranged between 20 km s^{-1} and 60 km s^{-1} , which corresponds very well with the range of 40 - 70 km s^{-1} that the asymptotic flare turbulent velocities lie in. This continuity between the late decay phase and the active region is to be expected because flares always occur in active regions, and the brighter flare dominates over the active region emission, which comes into its own again only after the flare has subsided. There is a less simple explanation: that the late decay phase turbulence is an enhancement of the existing active region turbulence. In other words, whatever mechanism exists to sustain active region turbulence could convert enough thermal flare energy into plasma turbulence to explain the measured turbulent velocities. This possibility is discussed in Section 5.4.4 below, as one of the mechanisms which could cause turbulence in flare plasma.

5.4.3 Temperature dependence of plasma turbulence.

Comparison of *BCS* and *FCS* spectra from the flare of 5 November 1980 showed that the width of *BCS* lines is more than twice as large as that of *FCS* lines. This means that plasma seen by the *FCS* is less turbulent than the plasma seen by the *BCS*.

The original intention in making this comparison was to exploit the differences in spatial discrimination between the two instruments to detect spatial variations in plasma turbulence. But it was found that the *FCS* spectra, in addition to having narrower line profiles than *BCS* spectra, also indicated (via the w-line to k-line ratio) a plasma temperature that was only 70% of the *BCS* temperature. These two findings are entirely consistent with each other because hotter plasma is expected to be more turbulent.

It is not , however, consistent with the general assumption that the *FCS* was looking at the hottest part of the flare. In its spectral scanning mode, the *FCS* would generally raster across the flare, note the position of the brightest pixel and then perform a spectral scan across that pixel. This must mean that the *FCS* neglected to pick the brightest pixel in this instance, or it could be that the flare brightness configuration had changed in the time that it took the *FCS* to complete the initial exploratory raster.

But the primary finding still stands: that hotter plasma is more turbulent. This is consistent with the findings of Jakimiec and Fludra (1991) who studied the non-thermal line broadening of the *BCS* Fe XXV resonance line in the flares of 21 May 1980 and 14 October 1980. They found that the turbulent velocities derived from Fe XXV spectra are consistently higher than those derived from Ca XIX spectra. Because Fe XXV spectra are produced by plasma that is hotter than the plasma which produces Ca XIX spectra, it would appear that hotter plasma is more turbulent.

In order to be consistent with the aims of this analysis, which was to account for the size-dependent broadening effect in *BCS* spectra, one point has to be addressed before the temperature dependence can be accepted as conclusive. It is that the analysis of Jakimiec and Fludra did not take into account the effect of the source size on the non-thermal line width.

It is known, from *FCS* images of flares, that the Fe XXV emitting area is less than the Ca XIX emitting area. Thus if the size-dependent broadening of the Ca XIX plasma is only 15%, the broadening due to the size of the Fe XXV plasma area would be even less. This means that more of the turbulent broadening seen in Fe XXV spectra is real.

Therefore Fe XXV turbulent velocities would continue to be consistently larger than Ca XIX turbulent velocities even after correction for the size effect.

5.4.4 Directed motion as the cause of symmetrical broadening of emission lines.

By plotting the average turbulent velocity in flares against their displacement from the centre of the Sun's disc, it was shown that there is no relationship between the two. Any such relationship would point to directed motion rather than to turbulent motion as the cause of the non-thermal broadening, because only if motion is directed would there be a change in its observed velocity when the viewing angle is changed

The simplest such variation would be a $cos\theta$ dependence (where θ is the angle between the line of sight and the Sun's radial vector at the flare site). In Figure 5.16 a series of $cos\theta$ curves (where θ is the angle between the line of sight and the Sun's radial vector at the flare site) have been overlaid on a plot of turbulent velocity against distance from disc centre. Each curve corresponds to a different (radial) upflow velocity, since there is no reason to assume that all the flares should have the same upflow velocity.

What these curves show is that for some limb flares, if the observed turbulent velocities are to be explained as a superposition of projected upflow velocities, the unprojected upflow velocities would have to have values of several hundreds of kilometres per second. Given that the suggestion that upflows exist in the decay phase does not have much basis either in other observations or in flare theory, the suggestion that there are upflows in the decay phase with velocities of *several hundreds of kilometres per second* is simply unsupportable.

The reason that the possibility of a centre-to-limb effect is being discussed at all is to eliminate it from further discussion. The idea that non-thermal broadening is a superposition of directed motion has certainly been floated by a few authors (Emslie and Alexander, 1990; Alexander 1990), but it is has always been in the context of the *rise phase.* So, whatever its validity as an explanation of rise phase non-thermal broadening, it is difficult to see how it could be appropriate to the decay phase.

The explanation proposed by Alexander (1990) is based around a highly tapered magnetic loop, (shown in Figure 5.17), in which plasma moving upwards along the expanding field lines will have transverse velocity components. The idea of a tapered magnetic loop was developed by LaRosa and Emslie (1988) to explain how the large areas of coronal hard X-ray emission could be related to the much smaller areas of chromospheric EUV emission, both of which are observed simultaneously during the rise phase. Alexander (1990) extended the application of this loop configuration. This hypothesis was formulated to explain how the extreme limb flares studied by Fludra *et al.*(1989) could exhibit non-thermal line broadening without invoking turbulent plasma motion. In this model, the field lines at the chromosphere are bunched together, and diverge strongly as they extend through the photosphere and into the corona. When plasma at the footpoint expands into the loop, it follows the field lines, moving upwards and sideways. In a limb flare with radially directed loops, the sideways velocity component would be parallel to the line of sight, and integrating over all such line-of-sight velocities in the optically thin flare plasma would result in symmetrical line broadening. Because the bulk of the plasma has no line-of-sight velocity component, the emission line centre remains at the rest wavelength. The expression for the turbulent velocity that would be seen in such a loop configuration is derived, quite simply, from the geometry of a diverging loop. As the detailed derivation may be found in Alexander (1990), it is merely outlined here. Beginning with the expressions which define a dipole magnetic field in Cartesian coordinates, an expression for the radius of cross-section of the loop as a function of distance along its length is derived. As the flare plasma moves along the length of the loop, its cross-sectional area increases accordingly, and the rate at which it expands (the line of sight velocity) is proportional to the rate at which it moves along the loop length (the upflow velocity). If L is the half-length of the loop, A_{chromo} and A_{corona} are the cross sectional areas of the loop at the chromosphere and the corona respectively, the average line-of-sight

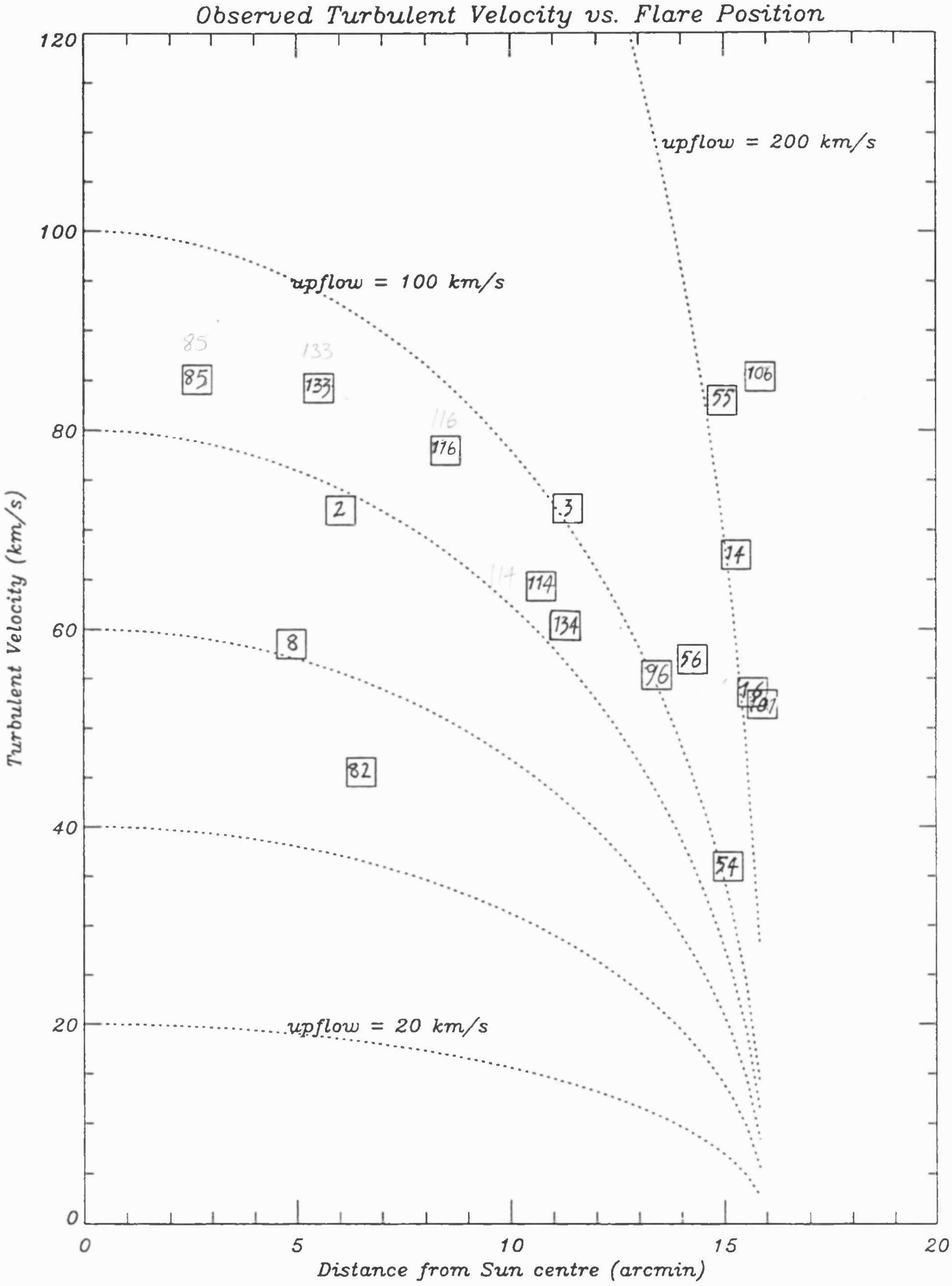

Figure 5.16: The predicted variation of radial velocity compared with observed variation of turbulent velocity across the Sun's disk.
The dotted lines show how the observed magnitude of radially directed upflow velocities will vary with flare position. If the measured turbulent velocities are due to a superposition of upflow velocities, then some of the flares on the limb (No.'s 114, 55, 14, 16, 106) would require intrinsic upflow velocities of more than 200 km s^{-1} *, which is excessive in the decay phase.*

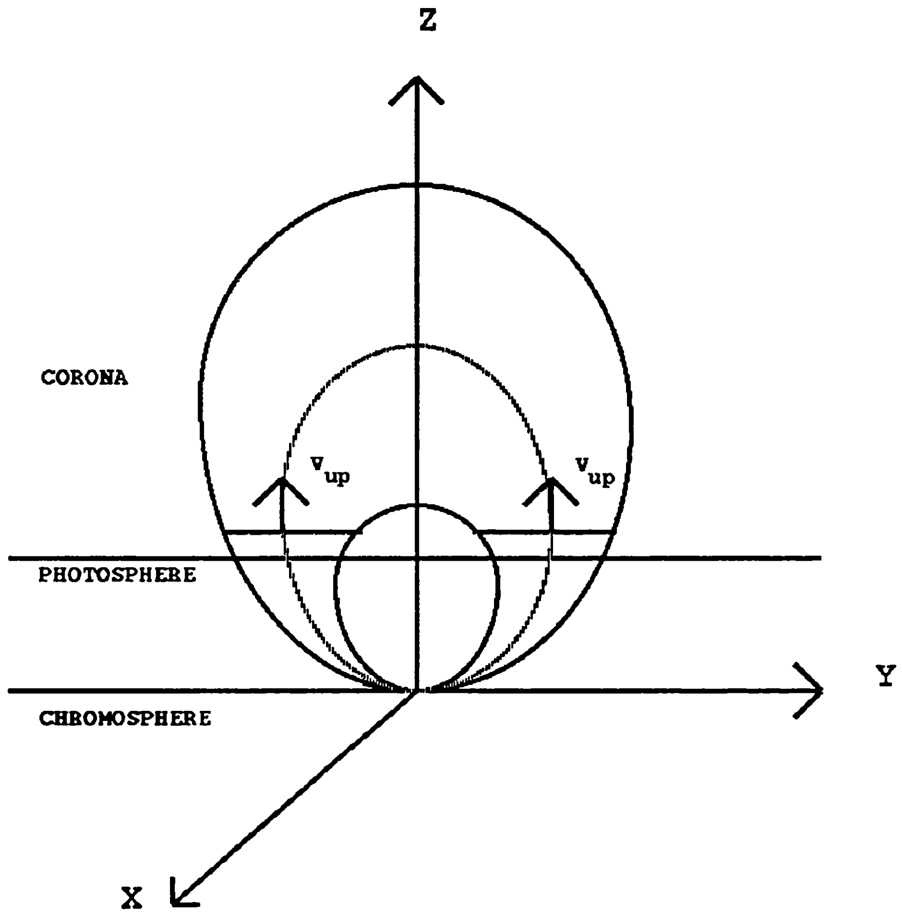

Figure 5.17: The highly-divergent loop configuration. *This loop configuration was suggested by Alexander (1990) to explain how plasma upflows could result in symmetrical line broadening.*

velocity will be given by:

$$V_{turb} = \frac{(A^{1/2}_{corona} - A^{1/2}_{chromo})}{\pi^{1/2} L} V_{up} \tag{5.8}$$

This is a linear relationship, and for the typical values quoted by Alexander ($A_{corona} = 10^{18}$ cm^2, $A_{chromo} = 10^{17}$ cm^2, $L = 10^9$ cm), the constant of proportionality is approximately 0.4. Therefore the range of turbulent velocities observed in the sample of flares analysed here would require average upflow velocities of between 100 and 225 km s^{-1} . This is not very different from the range of upflow velocities that were arrived at using the simple $cos\theta$ variation, and these velocities exceed those that could reasonably be expected during the decay phase.

Another way in which symmetrical broadening could be produced is if there is a symmetrical distribution of either upflows or of downflows. The net effect of this would be a symmetrically broadened line, but in this case the whole line would be shifted bodily to a shorter wavelength (upflows) or to a longer wavelength (downflows). The displacement of the shifted line peak from the rest line position would be proportional to the peak of the up/downflow velocity distribution. Limb flares would not only have lines with less broadening, but their centres would be closer to the rest position. Unfortunately the absolute calibration of *BCS* spectra and limits on spectral resolution prevent this hypothesis from being tested. But the absolute calibration of the *FCS* spectrum *can* be determined, and where *FCS* spectra are available (for the 5 November 1980 and 25 August 1980 flares), this possibility has been eliminated.

5.4.5 Causes of plasma turbulence in the decay phase.

There is no evidence for the existence of a centre-limb variation and it has to be concluded that random mass motion is the cause of non-thermal line broadening. The non-thermal line broadening is seen to reach a minimum that in many cases coincides with the peak emission measure, and then increases slightly. In some flares, the increase in non-thermal broadening is accompanied by brief rises in the electron temperature. Jakimiec and Fludra (1991) use this evidence to suggest the existence of compact energy release sites (turbulent kernels).

Saba and Strong (1990) considered whether sustained non-equilibrium conditions can be maintained for long enough without further energy injections. They estimated the times for which an inequality in electron temperature and ion temperature (or a non-equilibrium ionization state, or a non-equilibrium velocity distribution) can exist, and found them to be of the order of seconds. Therefore repeated energy injection on this time scale would be required to sustain non-equilibrium conditions over the lifetime of the flare. However the radiative and conductive cooling times for flare plasma are of the order of 10^3 seconds. This would mean that the repeated energy injection required to maintain a non-equilibrium situation would raise the temperature of the flare and this was not observed in Saba and Strong's active regions. Nor is this evident in the sample of flares analysed here. There are some flares in which the electron temperature rises briefly and by a small amount, but these amount to no more than small spikes in the temperature decay curve. The sustained rise in electron temperature that would indicate continuous energy injection is not seen.

The only form of wave propagation that is not refracted or dissipated before it can penetrate the corona is Alfvén wave propagation (Parker, 1987). Alfvén waves are transverse perturbations of the magnetic field lines, rather like those produced by plucking a taut string. They propagate along the direction of the field, though their effect is seen only in the transverse direction. Because the magnetic pressure is so much greater than the gas pressure of the flare plasma, the plasma will be constrained to follow the motion of the Alfvén waves, and this mass motion will result in the observed non-thermal line broadening. A derivation of the relation between the energy carried by an Alfvén wave and the turbulent velocity it causes may be found in McClements, Harrison and Alexander (1990). The tension in a magnetic field line is $\frac{B^2}{4\pi}$, and the speed v_A with which an Alfvén wave propagates along it is given by:

$$v_A = \frac{B}{\sqrt{4\pi\rho}} \tag{5.9}$$

where B is the magnetic field strength and ρ is the plasma mass density. The electronic mass of a plasma is negligible, so the plasma density can be approximated by $\rho = nm_p$ where n is the plasma number density and m_p is the proton mass.

The energy flux density Φ_A (erg cm^{-2} s^{-1}) for an Alfvén wave is given by

$$\Phi_A = n\, m_p\, v_t^2\, v_A \tag{5.10}$$

where v_t is the observed turbulent velocity in cm s^{-1}.

Taking $B = 1000$ Gauss, $nm_p = 2 \times 10^{-15}$ g cm^{-3} and $v_t = 5 \times 10^6$ cm s^{-1}, an energy flux of 3.2×10^8 erg cm^{-2} s^{-1}is obtained.

This is the energy carried by an Alfvén wave with an amplitude large enough to explain the non-thermal mass motion observed in the decay phase of flares. This figure can be compared with the energy requirements of flares in which there is evidence of decay-phase heating, and if found sufficient could help answer the question of how decaying flares and post-flare loops are heated. It must be pointed out that the figure calculated above is the maximum energy borne by an Alfvén wave in the specified conditions, and the amount of energy available for heating depends very much on the efficiency with which the Alfvén wave energy is dissipated in the coronal plasma (how exactly the dissipation occurs is not known (Hollweg, 1984).

5.5 Summary

Taking into account the broadening caused by the extended size of the flares does not remove all of the excess line broadening seen in *BCS* flare spectra in the decay phase. Having considered all known instrumental effects which could be responsible for the remaining excess width and having eliminated the possibility of spurious size dependent effects, it must be concluded that this broadening is physically real and is caused by motion of the flare plasma.

Subtracting the effect of the flare size on the line width reveals a pattern in the behaviour of non-thermal line broadening/turbulent velocity. The peak values reached during the rise phase (100 - 200 km s^{-1}) rapidly decrease and reach a minimum point (30 - 50 km s^{-1}), after which there is a gradual increase to a more or less constant level (40 - 70 km s^{-1}).

The possibility that non-thermal line broadening is due to the superposition of upflows has been considered and found not to stand up to the observations.

The constant background of turbulent velocity that remains in the active region after the flare has decayed is consistent with the findings of Saba and Strong (1991) that turbulent velocities between 20 km s^{-1} and 60 km s^{-1} exist in non-flaring active regions.

The broadening is different in two different channels of the instrument: the higher temperature iron spectra have an excess width greater than the calcium spectra which originate in plasma cooler by 3 - 5 MK. Comparison of *BCS* and *FCS* spectra (from the only two flares for which the *FCS* Ca XIX spectra were recorded) suggests that the mass motions are greater in the hotter parts of the flare. As pointed out by Jakimiec and Fludra (1991), this is consistent with the suggestion that the broadening mechanism is spatially non-homogeneous and concentrated in hotter plasma.

If the non-thermal broadening is due to the displacement of plasma by the transverse component of Alfvén waves, then the maximum amount of energy that is available for flare heating from this source can be calculated. For a typical turbulent velocity of 50 km s^{-1} , the available Alfvén wave energy is equal to 3.2×10^8 erg cm^{-2} s^{-1}, though what proportion of this is can be converted to thermal energy depends on the dissipation mechanism.

5.6 Correction: Possible causes of the non-thermal line width minimum at the beginning of the decay phase.

The flares analysed in this chapter show that the corrected non-thermal line width reaches a minimum soon after the flare reaches its soft X-ray peak. This minimum also coincides with the emission measure peak (to within about 12 minutes). There are two possible causes of this effect, both of which have been observed in *Yohkoh-BCS* data.

(i) Fitting of two-component spectra to decay phase spectra could result in the blue-shifted component "robbing" the stationary component of some of its width. In *Yohkoh-BCS* line-width vs. time plots this effect is evident from the discontinuity in the line-width curve, which occurs when the switch-over is made from two-component fitting to single-component fitting. Such a discontinuity could be present in the *SMM-BCS* line-width curves shown in Figures 5.10 to 5.13, but the statistical uncertainty present in the data is too great to allow an immediate conclusion to be drawn.

(ii) A count-rate dependent line narrowing effect would explain the coincidence of the line-width minimum with the peak emission measure. The magnitude of this effect is related to the depth of the detection chamber (to be exact, the distance between the cathode and the anode). This effect is very evident in *Yohkoh-BCS* spectra, but the magnitude of the effect is exaggerated by the depth of the detection chamber. However, the *SMM-BCS* had shallower detection chambers, and the effect of count-rate dependent line narrowing would have been much less than in *Yohkoh-BCS* spectra.

It could be that both these effects are combining in some unknown ratio to create the overall line-width minimum effect. Of course there remains the possibility that the line width minimum is real and that non-thermal mass motion actually does reach a minimum in the early part of the decay phase. This could only happen if there was a time lag between the switching-off of one energising mechanism and the emergence of a subsequent energising mechanism.

CHAPTER 6

The cooling of flares in the decay phase.

6.1 Introduction

6.1.1 Static loops and decay phase flare loops.

In trying to answer the question of what powers flares, it is as instructive to study the decay phase of a flare as it is to study the rise phase. Because of the very high rate of energy release ($\sim 10^{30}$erg s^{-1}) that occurs during it, the rise phase is the obvious choice of study when seeking to identify the energy source of a flare. But though there are events which happen only during the rise phase, such as hard x-ray bursts, radio and microwave emission and particle ejection, there are other observational features of the rise phase, such as plasma mass motion, that are continuous with the events that take place in the active region before the flare occurs, and with the events that follow it or occur during its decay. This points to the possibility that the same processes which exist before and after a flare are also responsible for the flare itself. In short, the sudden energy release of the rise phase could be an extreme enhancement of the pre-existing mechanisms which power quiescent coronal loops.

Observations of some coronal loops over several days have shown that they can be assumed to be static over a period of that length. The assumption that such loops are static was used as the basis for of the analysis of quiescent coronal loops by Craig, McClymont and Underwood (1978) and by Rosner, Tucker and Vaiana (1978). The latter authors established the well known pair of scaling laws which relate the temperature, loop base pressure, heating flux and loop length.

Later workers have studied the cooling of flares in their decay phase and tried to establish a ratio of radiative cooling to conductive cooling which would fit the observed flare cooling characteristics (Bornmann and Strong 1988, van den

Oord and Mewe 1988). The most recent treatment of the flare cooling problem has returned, however, to the analysis of Rosner, Tucker and Vaiana (1978). In the first of three papers dealing with the dynamics of static loops, Serio *et al.*, (1991) adapt the hydrostatic loop treatment to address the cooling of the plasma in *flare* loops. By attributing the heat loss to conduction and radiation, they derive a relation between observable quantities: $\tau \sim 120(L_9/T_7^{1/2})$ where τ = entropy decay time, T_7 = maximum temperature at loop top at beginning of decay phase in units of 10^7K, and L_9 = loop half-length in units of 10^9cm. This relation is very similar to that derived by Craig, McClymont and Underwood (1978) who found that the ratio $T^{9/4}/nL$ was a constant for a given loop (T = temperature, L = loop length and n = density).

Given that the chief means of heat loss is conduction, it becomes clear why there is an inverse dependence on the loop length. The loop can lose heat by conduction only through its footpoints, where it is in contact with the chromosphere. In a longer loop, more of the plasma is further from the footpoints, decreasing the conductive loss rate.

Because numerical models do not have to skirt round certain features of a complex physical problem in the way that a realistic analytical treatment has to, it is possible to use such a numerical model to validate the simplifications made in the analytical treatment. Serio *et al.*, use the Palermo-Harvard Model (described in Peres *et al.*, 1982) to confirm the validity of their analytical treatment.

The flare loop length is a primary observable quantity, and because it can be measured independently, it can be used to test the relations between the other quantities.

6.1.2 The aims of this analysis.

In this chapter the analytical treatment of Serio *et al.*, (1992), which was outlined above, is applied to data derived from *BCS* spectra and is used to predict flare loop lengths. It must be noted that two basic assumptions are being made: the first and most important is that the flare takes place in a *single* loop. A further assumption is that there is no heating of the flare plasma following the cessation of the rise phase heating.

The predicted loop lengths can then be compared with loop lengths measured from the soft X-ray images recorded by the *FCS*. The *FCS* was sensitive to plasma of the same temperature range as the *BCS* was sensitive to, and its images can be relied upon to represent the same plasma that the *BCS* detected. In the instances where the predicted loop lengths are found to be quite different from the observed loop lengths it has to be concluded that the assumptions made in the hydrodynamic analysis are invalid. That is to say, either the flare had a structure that was complicated enough to render the simple loop approximation just too crude, or there was in fact heating in the loop during the decay phase. The first explanation may be ruled out by excluding those flares which are thought to have complex structures or consist of "arcades " (a row of parallel loops, stacked side-by-side along a common axis). This leaves the second explanation, that there is heating in the decay phase, and it is the aim of this analysis to identify the flares for which this is true.

6.2 Theory

The theory used to investigate decaying flare loops is adapted from the theory which deals with static coronal loops. A flare loop which is just about to enter its cooling phase is likened to a static loop at the moment at which the heat input to the loop is "switched of". Such a loop is considered to have been initially in a static state during which heat input was exactly balanced by heat losses. This state lasts until the heat source is "switched off". At this point stability is replaced by decay and the temperature, pressure and density (which quantities are interrelated by the quantity **entropy**) begin to decrease.

Though the decay of the observable quantities becomes apparent only when the heat source is switched off, the underlying heat loss rate in the period immediately following the switch-off is the same as during the static phase. This is because it depends on the initial temperature of the loop plasma and geometry of the loop, both of which have the same value before and just after the switch from the static phase to the decay phase.

Knowing this, it becomes possible to substitute the heat loss terms in the heat balance equation for the decay phase with the heat input term from the static phase. Thus a relation is established between a quantity that is measured during the static phase (the heat input rate), and a quantity that is measured during the initial part of the decay phase (the entropy decay rate).

The final step in the analysis is to draw on a well established relation between the heat input rate and the flare loop geometry, and use it to relate the entropy decay rate to the flare loop geometry. Both these quantities can be measured directly (entropy in flare loops is proportional to temperature, and temperature can be measured directly) which means that the validity of the relation (and

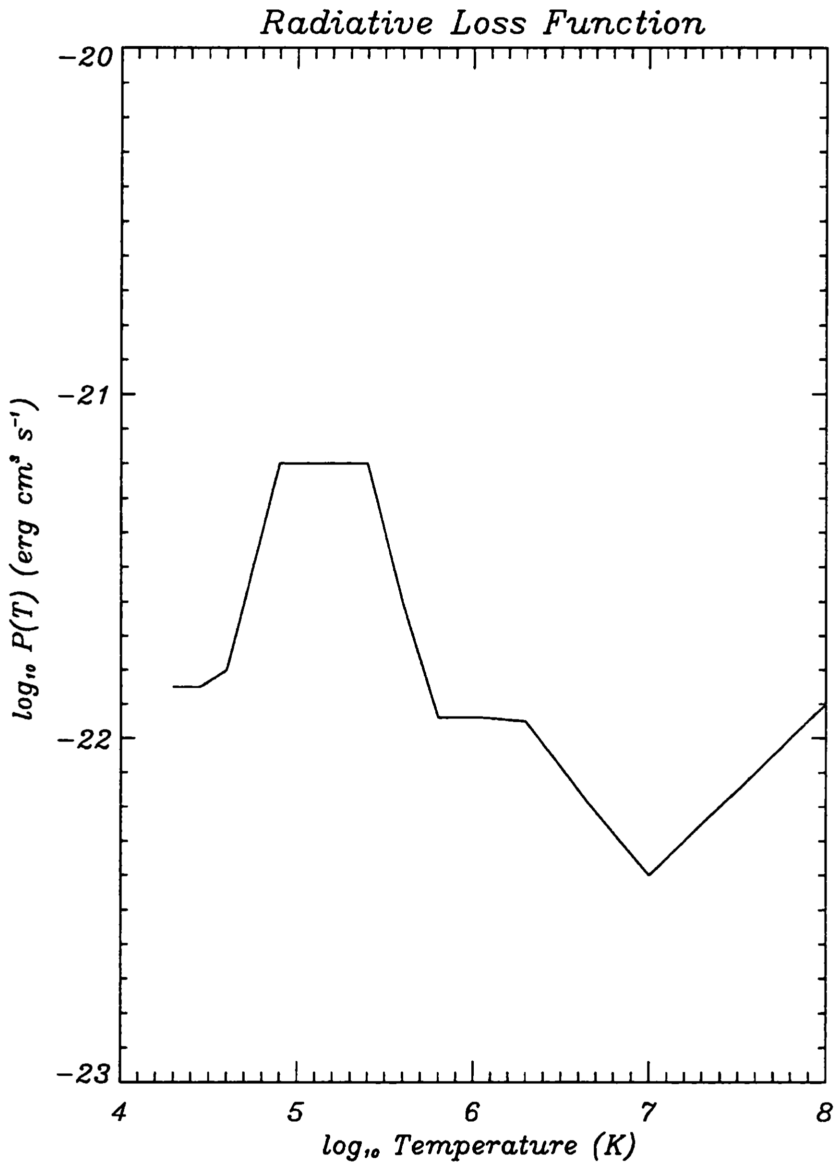

Figure 6.1: The Radiative Loss Function for a flare plasma.
The radiative loss function shows how the amount of energy lost through radiation varies with the plasma temperature. In a decaying flare loop, with temperatures ranging between 10 MK and 20 MK, the radiative loss increases as temperature decreases. This is vital for maintaining a loop structure in which the maximum temperature occurs at the highest point in the loop. The data plotted in this figure was obtained from Serio et al., (1992).

by extension, the validity of the whole analytical treatment) can be tested on observational data.

6.2.1 The static loop: The Rosner, Tucker and Vaiana Scaling Laws.

The pair of laws which relate the heating rate, temperature, pressure, and loop length in *static* loops were originally derived by Rosner, Tucker and Vaiana (1978). The assumption of a static state is important, because it reduces the variable quantities involved to just four, the loop length L, the base pressure p, the maximum temperature T_{max} and the energy input E_H, of which only two vary independently. Within a pressure scale height of the loop base, the base pressure may be considered to apply right through the loop. In addition, if the heating rate is constant, it is found that:

$$T_{max}^3 \propto pL, \tag{6.1}$$

and that

$$E_H \propto p^{7/6}L^{-5/6} \tag{6.2}$$

It is argued that the conditions under which these laws are valid *are* found in flare loops which have reached their soft X-ray peaks and are just about to enter their decay phases (Serio *et al.*, 1991). In Section 6.2.2, below, such cooling loops are considered.

6.2.2 The cooling loop.

In this section is considered the hydrodynamics of a plasma contained in a single semi-circular loop of uniform cross-section, as shown in Figure 6.2. The object is to obtain a relation that expresses the dependence of the energy loss rate on the

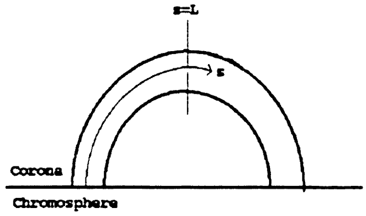

Figure 6.2: The geometry of the single loop model
The coordinate system used in the derivation outlined in this section has its origin at the base of the loop, with distance along the loop axis defined as s. In this semi-circular loop of uniform cross-section, hydrodynamical stability requires that the maximum temperature can only exist at the loop top (at s=L).

size of the loop. Starting with the three basic hydrodynamic equations expressing continuity of mass flux, momentum balance and energy balance, approximations appropriate to a static loop are made. The principal approximations are that the plasma consists of mostly hydrogen, and that the coronal heating source can be considered to have an instantaneous and uniformly distributed effect due to the high thermal conductivity of the flare plasma.

In a coordinate system with its origin at the base of the tube, in which the distance along the tube axis is defined as s, the equation of **continuity of matter** for plasma moving at a velocity v is :

$$\frac{dn}{dt} = -n\frac{\partial v}{\partial s}. \tag{6.3}$$

Considering the **balance of forces** on this plasma, which is assumed to consist of mainly hydrogen (atomic mass = m_H), we have :

$$nm_H\frac{dv}{dt} = -\frac{\partial p}{\partial s} + nm_H g_s + \frac{\partial}{\partial s}(\mu\frac{\partial v}{\partial s}) \tag{6.4}$$

And considering the **heat balance** in the loop

$$\frac{d\varepsilon}{dt} + (p+\varepsilon)\frac{\partial v}{\partial s} = E_H(s,t) - n^2\beta P(T) + \mu(\frac{\partial v}{\partial s})^2 - \frac{\partial}{\partial s}F_c. \tag{6.5}$$

The term $E_H(s,t)$ represents the coronal heating source and the conductive flux $F_c = -\kappa_0 T^{5/2}(\partial T/\partial s)$. Even though the coronal heating source term is expressed as a function of position and time, the high thermal conductivity of the flare plasma makes this dependence unimportant. The radiative loss term $P(T)$ has a power law dependence on temperature and varies as shown in Figure 6.1. The temperature range relevant to decay phase flare plasmas is 10 MK to 20 MK, which as Figure 6.1 shows, is a range in which the radiative loss increases with decreasing temperature. The heating due to the viscosity of the plasma is negligible and can be ignored.

If the plasma has a number density n, and an ionization fraction β (the ratio of the number of ions to the number of electrons), the equation of state (as for an ideal gas) is

$$p = (1+\beta)nk_BT = 2nk_BT, \tag{6.6}$$

because $\beta = 1$ for a fully ionized plasma. The internal energy density ε is given by

$$\varepsilon = \frac{3}{2}p + n\beta\chi \sim 3nk_BT, \tag{6.7}$$

because in the corona k_BT is very much greater than the hydrogen ionization potential χ.

In addition, if the **entropy per particle** S is defined to be

$$S = k_B ln\left(\frac{T^{5/2}}{p}\right), \tag{6.8}$$

the heating equation (Equation 6.5) reduces to:

$$p\frac{d}{dt}S/k_B = E_H(s,t) - n^2P(T) - \frac{\partial}{\partial s}F_c. \tag{6.9}$$

Whilst the loop is in a static state, $v = 0$ and $d/dt = 0$ and so:

$$E_H(s,t) = +\left(n^2P(T) + \frac{\partial}{\partial s}F_c\right). \tag{6.10}$$

This last equation says that the coronal heating source exactly balances the heat lost from the loop due to conduction and radiation.

When at the beginning of the decay phase, the heating is switched off, E_H becomes zero and is removed from Equation 6.5 leaving only the two heat loss terms:

$$p\frac{d}{dt}S/k_B = -n^2\beta P(T) - \frac{\partial}{\partial s}F_c. \tag{6.11}$$

But from the steady state situation which existed until just before the heating was switched off, it is known that E_H was equal to the heat loss terms (Equation 6.10). So the two heat loss terms can be substituted for thus:

$$p\frac{d}{dt}S/k_B = -E_H(s,t). \tag{6.12}$$

Rearranging it into an integrable form:

$$dS = -k_B\frac{E_H}{p}dt. \tag{6.13}$$

Which, when integrated gives

$$S = S_0 - \frac{k_Bt}{\tau}. \tag{6.14}$$

where τ is the characteristic decay time and is defined as

$$\tau = \frac{p_0}{E_H}, \tag{6.15}$$

From the definition of the entropy per particle S given in Equation 6.8, S and S_0 can be expressed in terms of T and P, the temperature and pressure and in terms of their initial values T_0 and P_0,

$$+ k_B ln\left(\frac{T^{5/2}}{p}\right) = +k_B ln\left(\frac{T_0^{5/2}}{p_0}\right) - \frac{k_Bt}{\tau} \tag{6.16}$$

$$\frac{T^{5/2}}{p} = \frac{T_0^{5/2}}{p_0} e^{-t/\tau} \tag{6.17}$$

Recalling the loop scaling laws of Rosner, Tucker and Vaiana (1978) given in Equations 6.1 and 6.2, the characteristic decay time τ can be related to the loop length L :

$$\tau = \frac{10^{-5} L^{5/6}}{p_0^{1/6}} = \frac{3.7.10^{-4} L}{T_0^{1/2}} \sim 120 \frac{L_9}{T_7^{1/2}} \tag{6.18}$$

where T_7 is the initial loop-top temperature in units of 10^7 K and L_9 is the length of the loop in units of 10^9 cm.

The characteristic decay time τ derived above is associated with the entropy S. In Section 6.3.2 it is shown how the entropy decay time is related to the **temperature decay time**, a quantity which is more easily and more directly measured from the observational data.

6.2.3 The density-temperature diagram.

The density-temperature diagram devised by Jakimiec (1986) is a sensitive indicator of decay phase flare heating. The principle underlying the density-temperature diagram is that the temperature and density in a flare loop have a constant relationship for a given heating rate. Figure 6.3 shows the relation between density and temperature in a freely cooling loop. The slope of the curve marked d-e is more steep in this freely cooling case than if the loop was being heated. The detailed interpretation of this diagram is described in Jakimiec *et al.*, (1992). It is introduced here for the purpose of comparing the results of its use (presented in Sylwester *et al.*, 1993) with the results presented here.

6.3 Analysis technique

The main aim of the procedure described below is to match the entropy decay time of a flare with its loop length. Entropy is not a quantity that can be measured directly - it depends on temperature and pressure. An assumption of constant pressure, therefore, permits the measurement of temperature to stand in for entropy (Section 6.3.2). Temperatures are measured from *BCS* spectra, and the decay time is measured using a novel method described in Section 6.3.3. Loop sizes are measured from *FCS* images contemporaneous to the *BCS* spectra (Section 6.3.4).

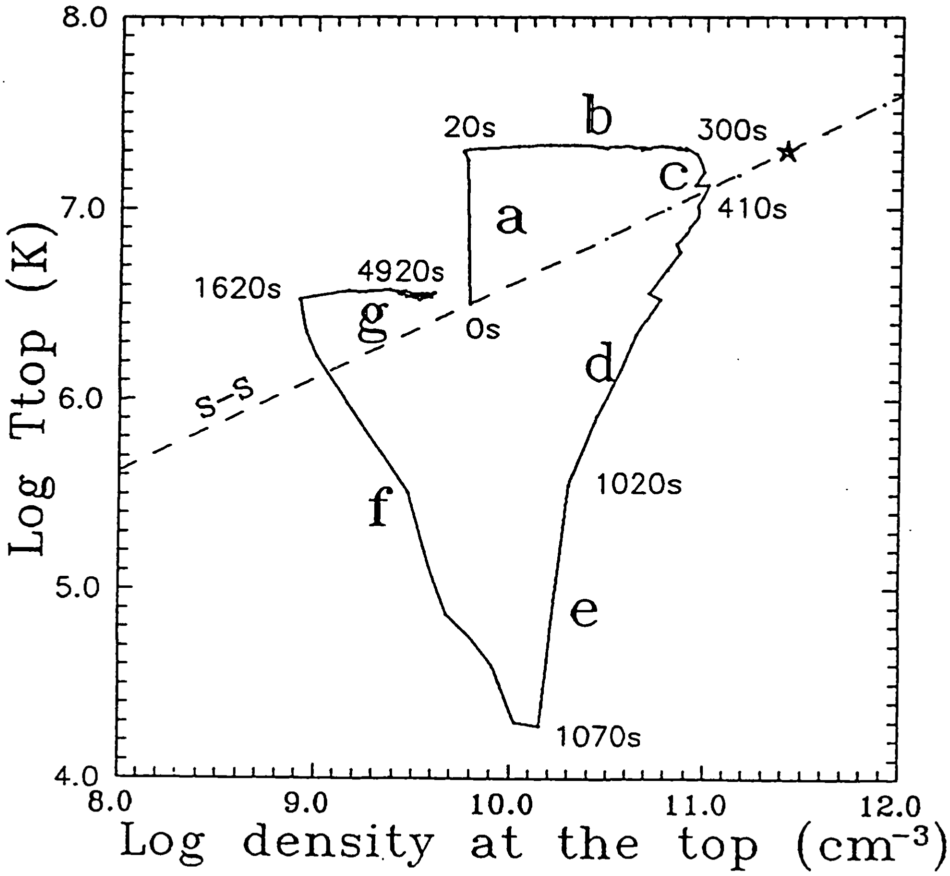

Figure 6.3: The density-temperature diagram of Jakimiec (1986). *For a given heating/cooling rate, the temperature and density in a quasi-static loop have a constant relationship. The dotted line marks the density-temperature relationship for a steady-state loop. The part of the curve marked d-e represents the free cooling of a formerly steady-state loop.*

6.3.1 Selection criteria for suitable flares.

There are about 140 flares which were observed by the *BCS* during the period 1980 to 1987. Any flares for which the spectra are of good enough quality for a long enough period of time are suitable. The spectra have to be of good enough quality for line intensities and widths to be measured from them, and this quality needs to be sustained over a long enough period to permit the measurement of the characteristic decay time. As has been explained in Chapter 2, Section 2.1.4(a), electron temperatures can be measured from the ratio of the intensity of the resonance line to that of the dielectronic satellite line. The plasma temperature derived from the plasma emission spectrum reflects the temperature of the electrons and is refered to as the electron temperature. The intensities of these lines were measured by fitting synthesized spectra (in which the line intensities were known) to the observed *BCS* spectra and these data were stored in *BCS* FIT files [1]. The temperature is derived from the intensity ratio of the resonance line to a dielectronic satellite line: w/k line for Ca XIX and w/j line for Fe XXV. Most of the flares in the sample have Ca XIX data available, but only a few have Fe XXV data. An example of an electron temperature curve from a FIT file is shown in the top left hand frame of Figure 6.5.

6.3.2 The relation between the entropy decay time and the temperature decay time.

This analysis is based on the assumption that the entropy decay time (defined in Equation 6.18) is approximately equal to the temperature decay time. This has been shown to be true by the hydrodynamical model, the results of which are presented in Sylwester *et al.*, (1993).

Although it is the ratio derived from the hydrodynamical model that is used in this analysis, its validity can be confirmed quite simply by inspecting the definition of entropy that is given in Equation 6.8. Differentiating that expression with respect to time:

$$\frac{dS}{dt} = \frac{k_B}{(T^{5/2}/p)} \frac{d}{dt} \left(\frac{T^{5/2}}{p} \right) \tag{6.19}$$

$$\frac{dS}{dt} = \frac{k_B p}{T^{5/2}} \left(\frac{5}{2} \frac{T^{3/2}}{p} \frac{dT}{dt} - \frac{T^{5/2}}{p^2} \frac{dp}{dt} \right) \tag{6.20}$$

[1] FIT files contain data from spectral fits to BCS spectra, and include the positions, widths, and intensities of the principal lines

$$\frac{dS}{dt} = k_B \left(\frac{5}{2T}\frac{dT}{dt} - \frac{1}{p}\frac{dp}{dt} \right) \tag{6.21}$$

Now if T is varying exponentially, then $T = T_0 e^{-\frac{t}{\tau_T}}$ and $p = p_0 e^{\frac{-t}{\tau_p}}$, which gives $\frac{dT}{dt} = -\frac{T}{\tau_T}$ and $\frac{dp}{dt} = -\frac{p}{\tau_p}$ and $\frac{dS}{dt} = -\frac{S}{\tau_S}$.
Therefore,

$$\frac{dS}{dt} = k_B \left(-\frac{5}{2\tau_T} + \frac{1}{\tau_p} \right) \tag{6.22}$$

If τ_p is very much greater than τ_T (that is, the temperature decay time is much less than the pressure disssipation time), then $\frac{1}{\tau_p}$ tends to zero, leaving:

$$-\frac{dS}{dt} = -\frac{5}{2\tau_T} \tag{6.23}$$

The other conditions limiting these approximations are that only the maximum temperature at the top of the loop should be considered in this approximation. Also, the time period for which the approximation applies begins immediately after the rise phase heating has been switched off and ends when heating (from whatever source) is switched on. In practice this restriction is observed by initially fitting an exponential to the earliest part of the temperature decay, and then gradually increasing the time period being fitted to until a significant change in the decay time τ is encountered.

The maxiumum temperature for soft X-ray emitting plasma will be that derived from Fe XXV w/k line ratio (Doschek 1990). It is also safe to assume that this temperature represents the loop top, from the evidence of *FCS* images of the Fe XXV resonance line. These show that the area of emission at this wavelength is considerably smaller than that of lower temperature emission lines. But Sylwester *et al.*, (1993) find that the loop top temperature varies more or less linearly with Ca XIX temperature, in the range 0 - 20 MK, and in the range above this deviates only slightly with the loop top temperature increasing slightly more quickly than the Ca XIX temperature. This finding justifies the use of Ca XIX temperatures in lieu of Fe XVV temperatures.

6.3.3 The temperature decay diagnostic diagram

In order to determine which flares are suitable for the analysis outlined in the introduction to this chapter, a temperature decay diagnostic diagram has been devised. This diagram indicates whether or not the temperature decay of a flare is exponential, and when it is exponential, it indicates the period of time over which it remains exponential.

The diagram consists of the characteristic exponential decay time τ plotted along the x-axis, and plotted along the y-axis is the time interval over which

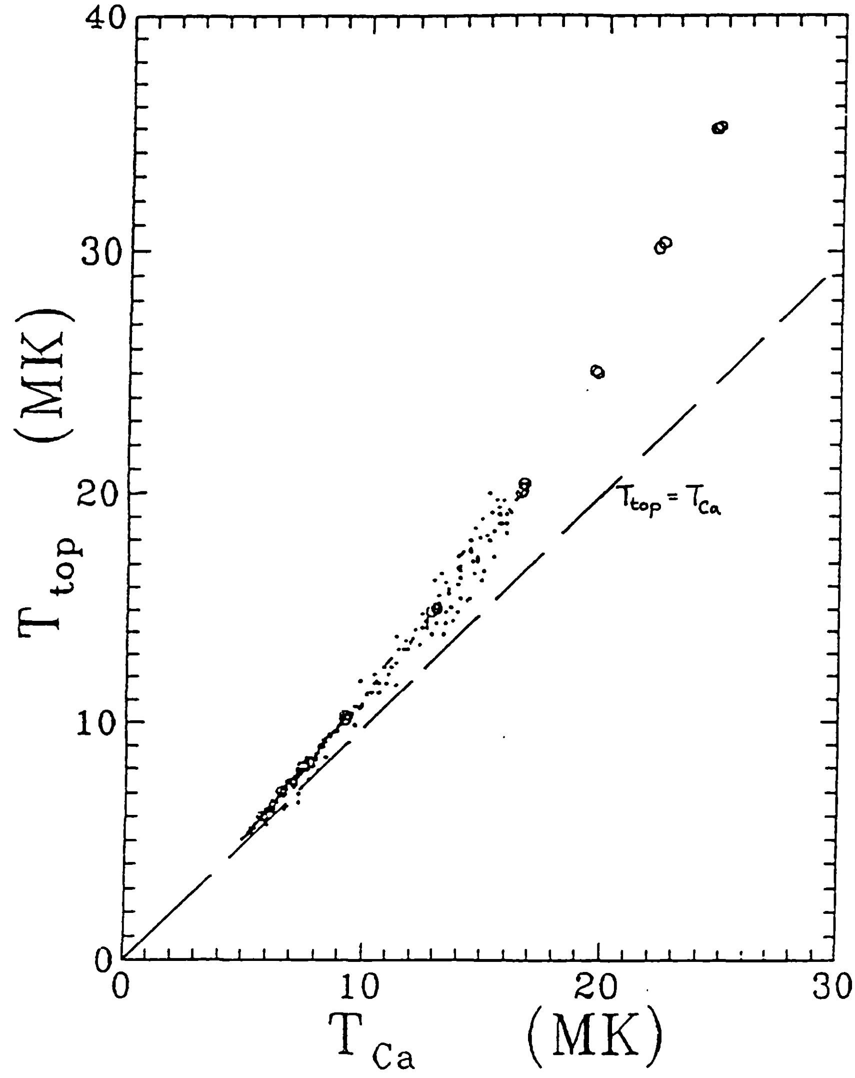

Figure 6.4: The relation betwen the temperature at the loop top and that derived from Ca XIX spectra, as synthesized in a hydrodynamic loop model.
The temperatures plotted here were obtained by Sylwester et al. (1993) from their version of the Palermo-Harvard hydrodynamic loop model, and show that temperature derived from Ca XIX spectra are an accurate representation of the loop top temperatures.

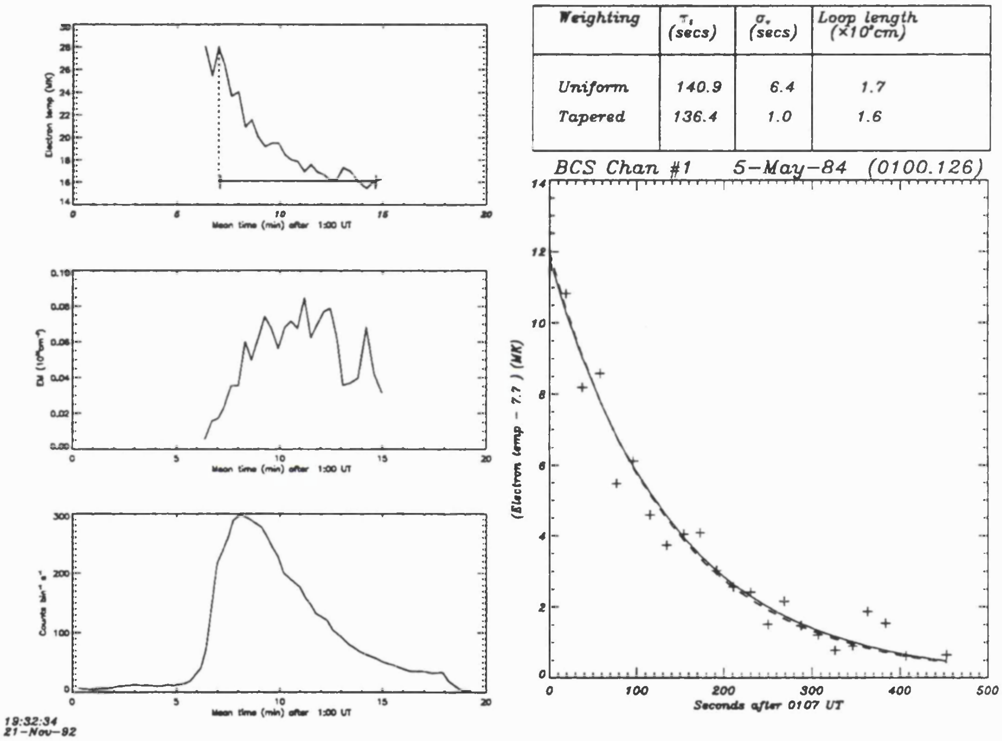

Weighting	τ_1 (secs)	$\sigma_\bullet$ (secs)	Loop length ($\times 10^9$cm)
Uniform	140.9	6.4	1.7
Tapered	136.4	1.0	1.6

Figure 6.5: Exponential fitting to the temperature decay of a flare. *The three sub-plots on the left show the change of temperature, emission measure and total intensity in Channel 1 of the* BCS. *The main plot shows the temperature decay curve again, but with the observed data plotted as crosses and a fitted exponential curve as a solid line. The dotted line is an exponential that has been weighted to take greater account of the earlier data points. The results of both exponential fits are given in the box above the main plot.*

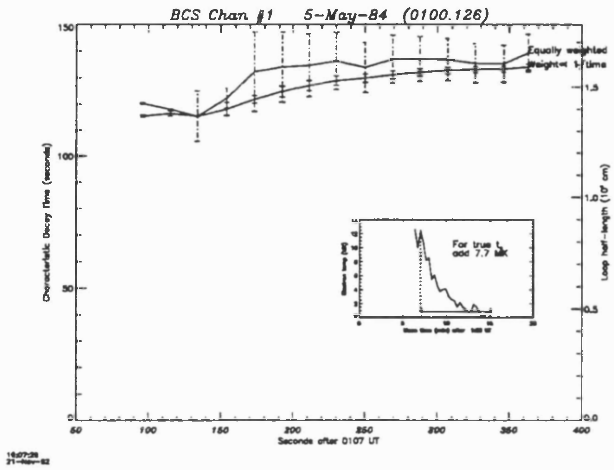

Figure 6.6: The decay diagnostic diagram of the flare of 5 May 1984. *The almost flat curve shows how consistently exponential the temperature decay of this flare is.*

the decay is being analysed. An example of the diagnostic diagram is shown in Figure 6.6 The range of values plotted along the ordinate is obtained by varying the length of the time interval over which the exponential is fitted. To determine the characteristic decay time τ of the electron temperature, a short period of time immediately after the temperature begins to decrease (indicated by the vertical line in the top left hand frame of Figure 6.5) is selected, and a uniformly weighted exponential fitted to the temperature decay curve. Figure 6.5 shows the observed data points overlaid with the exponential fit. This fitting procedure was repeated, using a sample with slightly longer time period every time.

The theory of quasi-static cooling is strictly true only for a very short time after the heating is "switched-off". In practice, this period can be extended until the pressure begins to change appreciably. The purpose of incrementally extending the time period of the data sample is to determine the maximum period over which the "post-switch off state" can be said to exist. Maximising the number of useful data points in this way helps to constrain the fit as much as possible (the fewer the observed data points there are to constrain the fit, the less likely it is that a good fit can be obtained).

The application of this diagram to idealised cases is the best way to illustrate how it is to be used and interpreted. In Figure 6.7 is shown an artificially generated expoential decay curve to which this analysis has been applied, and alongside it is the corresponding temperature decay diagnostic diagram. Be-

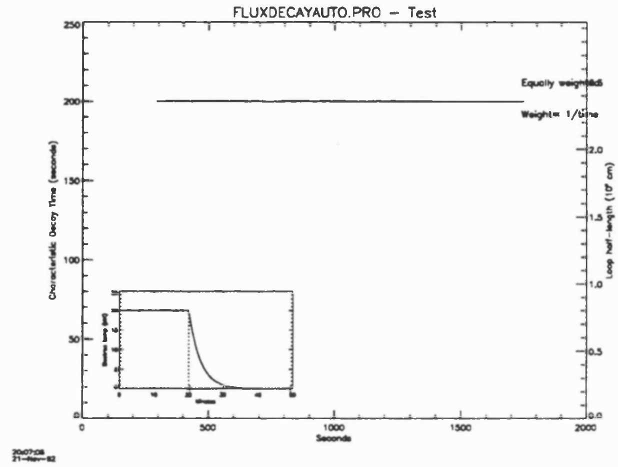

Figure 6.7: The decay diagnostic diagram of a pure exponential temperature decay: *the characteristic decay time of this artificially generated exponential decay curve is the same irrespective of the position or length of the time interval considered.*

cause the curve is a pure exponential, the characteristic decay time remains constant irrespective of either the length or the starting position of the time interval.

It is important to note that the exponential in the ideal case illustrated in Figure 6.7 approaches zero as it decays. The effect of trying to fit an exponential to a curve that has a non-zero asymptote is illustrated in Figure 6.8. In fact, the diagnostic diagram, rather than show the expected convergence to a single value of τ, shows a steady increase with the length of the time interval. The characteristic decay time thus obtained is quite wrong. The implication of this result for real data is that, before attempting to fit an exponential to an observed decay curve, a baseline must be subtracted from the temperature decay curve, so that it decays to zero.

The characteristic decay time can be read off most diagnostic diagrams to an accuracy of about 10 %, and Equation 6.18 can then be used to derive the loop half-length.

In those cases where the diagnostic diagram curve does not converge readily on a characteristic decay time, the shape of the curve can be used to determine whether it is the presence of heating or whether it is an enhanced cooling rate that is the cause of the deviation. A decay diagnostic curve with a positive slope indicates that the temperature decay is faster than an exponential decay, and that the assumed cooling rate is an underestimate. A curve with a negative

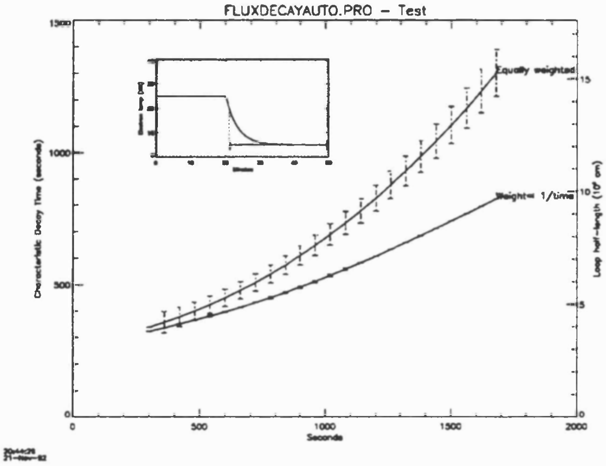

Figure 6.8: The decay diagnostic diagram of a pure exponential decay with a non-zero baseline. *The characteristic decay time obtained by fitting to this exponential curve, which decays to a non-zero value, is found to be not the true value. It is necessary to subtract the the baseline value, which is 5 MK in this example, before the diagram will converge to the actual value of 200 seconds.*

slope, on the other hand, indicates that the temperature decay is slower than an exponential decay and that the assumed cooling rate is an overestimate, or that the decay phase flare is still being heated.

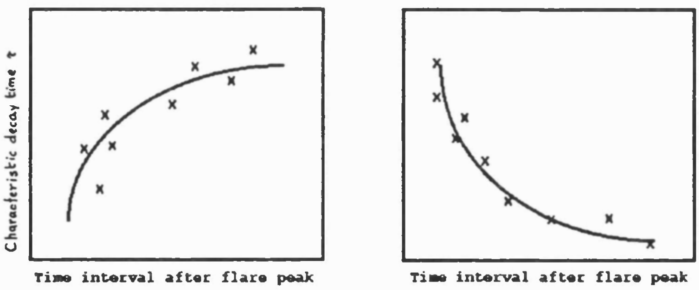

Figure 6.9: Interpretation of a non-converging temperature decay diagnostic diagram.
The curve in these plots represent the second differential of theflare electron tmepreature (d^2T_e/dt^2). The curve on the left is from a flare loop whose temperature decay curve is steeper than an exponential. The curve on the right is from a flare loop whose temperature decay curve is flatter than in the exponential case, i.e: being heated.

6.3.4 Obtaining flare loop sizes from *FCS* images.

The *FCS* was used to scan regions of upto 8 arcminutes square with steps as small as 15 arcseconds. In effect an *FCS* images is made up of "pixels" which could be as small as 15 $\times$ 15 arcseconds. Examples of *FCS* images in different scanning modes are shown in Figure 6.10.

Another property of rastered images is that they are not uniformly integrated over time. Pixels which occur early in the *FCS*'s raster path reflect the state of the flare as it was upto several minutes before the last image pixel is recorded. This time lag can be as long as 5 minutes. For the purposes of this analysis, and because it is the size of a stable flare loop that is being sought, images which are integrated over 4-5 minutes intervals are perfectly adequate.

To obtain *loop lengths* from *FCS* images, it is necessary to reconstruct the three-dimensional structure of the flare loop from a two-dimensional image. It is possible to do this if the position of the flare on the Sun's disc is known, and if some assumptions are made. The first assumption concerns the intensity distribution through the loop: it is that the brightest part of the soft X-ray emitting structure occurs at the loop top, because it is the hottest part of the loop (as reasoned in Rosner, Tucker and Vaiana, 1978). The second assumption concerns the orientation of the flare loop, and is that they are mostly radially pointing, and deviate by only about 30° (this assumption is justified by the work done in Chapter 7).

The projection of a flare loop onto a plane, for different orientations and positions on the Sun, are shown in Figure 6.11 and Figure 6.12. Using the projections in these figures as a guide, and knowing the flare position, the dimensions measured off *FCS* images can be transformed into loop lengths.

For flare loops which appear to be side-on to the line-of-sight, the loop length can be measured directly off the contour image. In reality, however, loops are rarely seen side-on. By using the projections shown in Figures 6.11 and 6.12 as a guide, the dimension which best represents the loop diameter or the loop height is decided upon. This is then measured by taking a "slice" across the contour image, and plotting the intensity profile along this slice. This procedure is illustrated in Figure 6.13. The width of the intensity profile along a correctly positioned slice corresponds to the diameter of the loop (if the loop is not being viewed end on) or to the height of the loop (in the case of a loop which is being viewed end-on). The loop length is then equal to either $((\pi/2) \times \mathit{diameter})$ or to $(\pi \times \mathit{height})$.

Where loops *are* seen side on, the loop length can be measured directly from the image without taking slices.

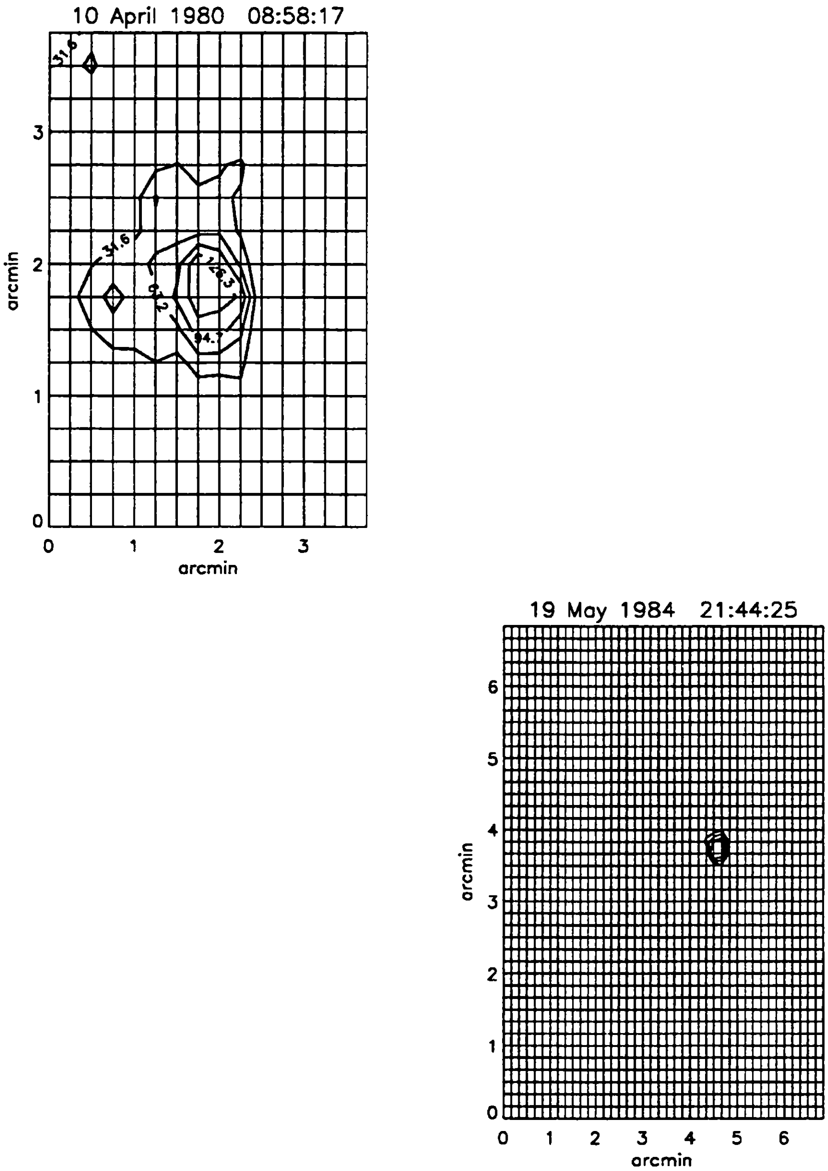

Figure 6.10: Examples of *FCS* images obtained using different rastering modes. *The* FCS *was used to scan an area on the Sun in vertical columns, with 10 arsecond steps over a 16 arcminute² area (image on L/HS), and with 15 arcsecond steps over a 49 arcminute² area (image on R/HS).*

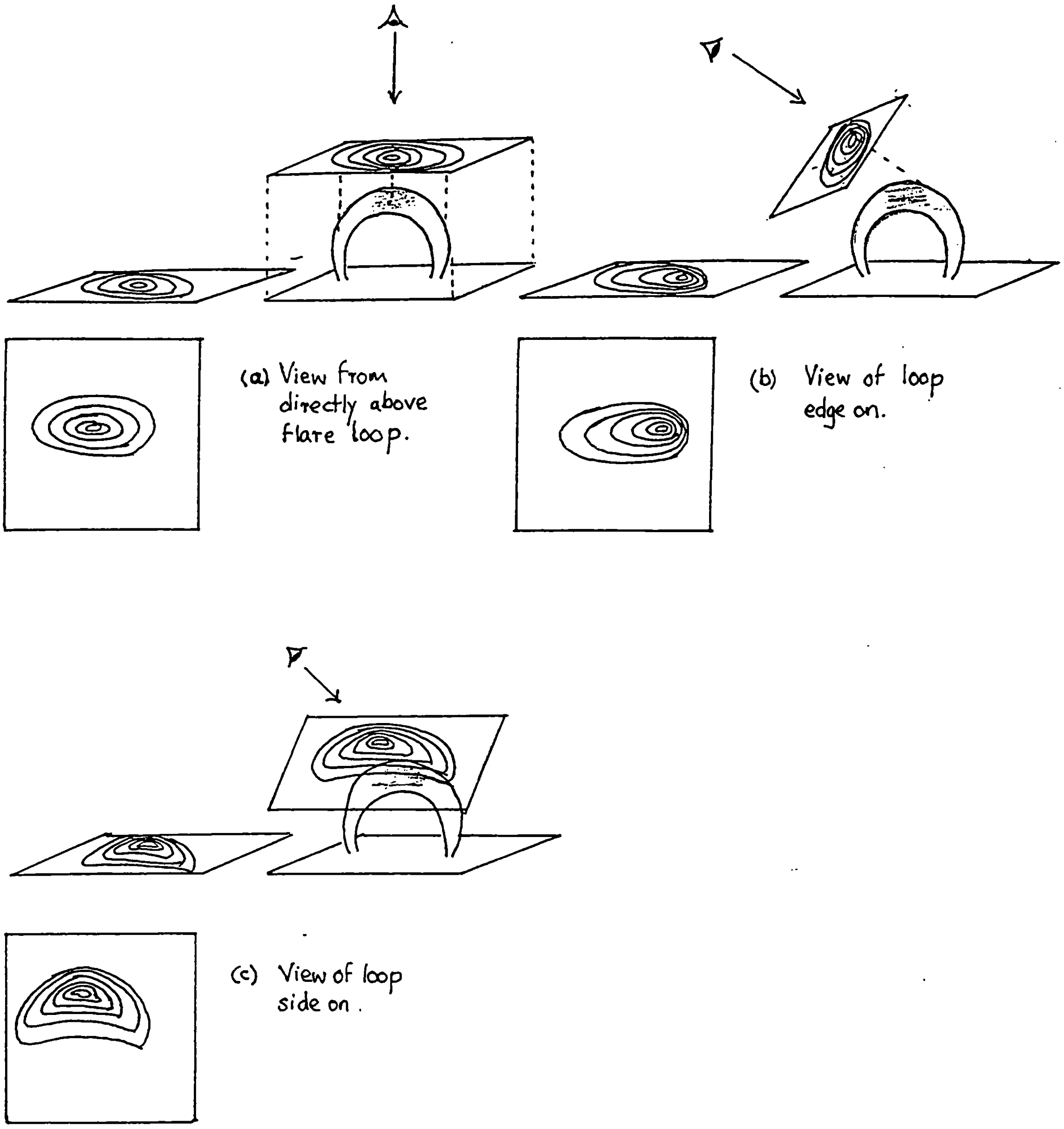

Figure 6.11: The projection of a flare loop onto a plane. *Studying the projections of flare loop shapes onto the plane normal to the line-of-sight is necessary for the correct interpretation of* FCS *contour images. Loops viewed from above, or pointing along the line of sight generally have symmetrical contours. Loops viewed end on, or side on, will have contours bunched up to one side of the contour map.*

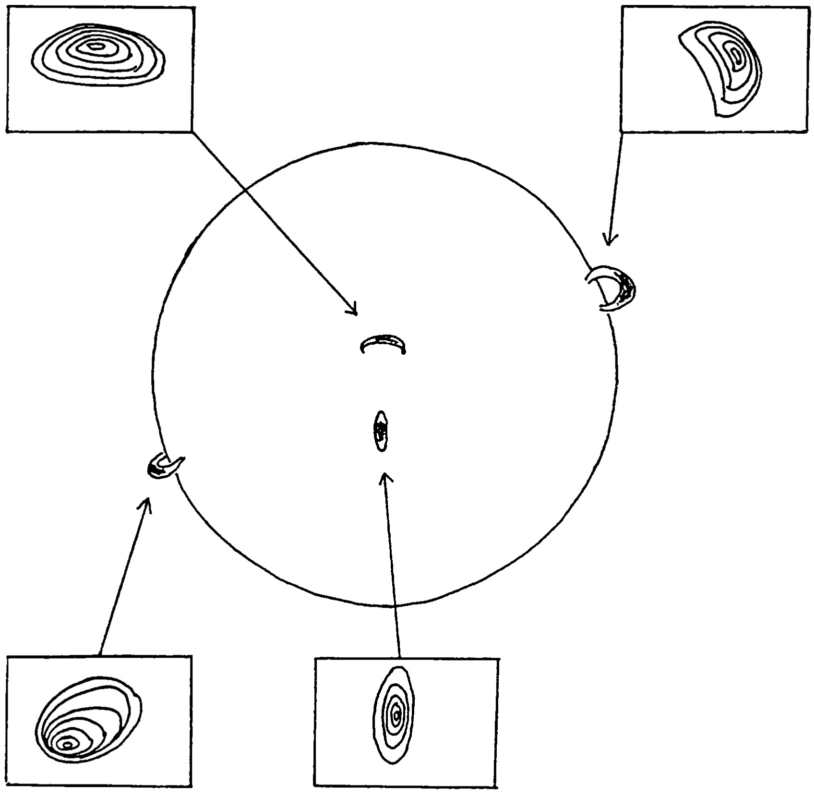

Figure 6.12: How to deduce the flare loop structure from an *FCS* contour image. *Given the position of the flare on the Sun's disc, it is possible to deduce the orientation of the flare loop in the manner shown in this figure.*

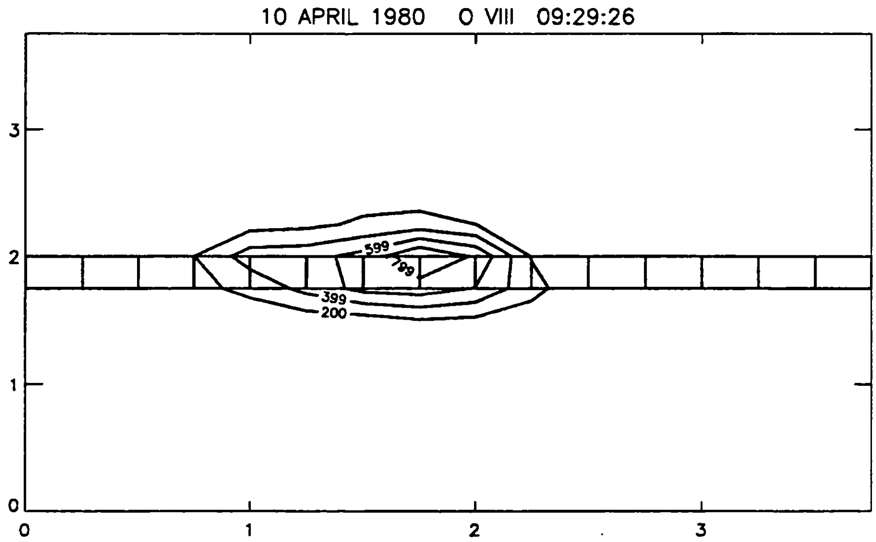

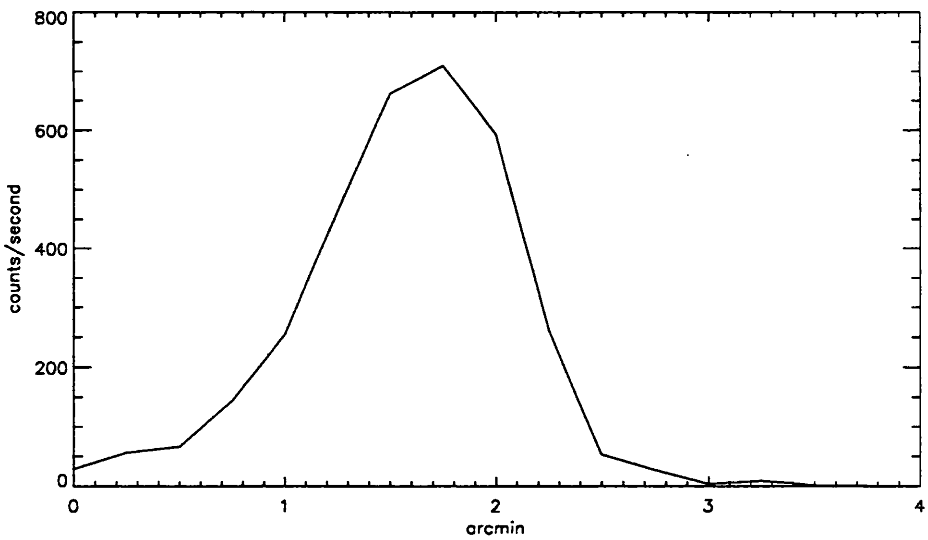

Figure 6.13: How to measure the size of a flare loop by taking a slice across a contour image. *An intensity slice has been taken across the contour image, in the position which is most likely to correspond to the top ridge of the loop. The intensity distribution along this slice is shown in the lower figure. The width of this intensity distribution corresponds to the diameter of a semi-circular loop, from which the loop length is obtained.*

6.4 Results and Discussion

The results of this analysis are presented in Table 6.1. The entropy decay time was determined for all the flares, and the predicted loop lengths are listed in the table. Only some of these flares, however, had *FCS* images from which loop lengths could be measured. This subset is divided into two groups according to how the predicted loop lengths compare with the observed lengths, and these two groups are dicussed in Sections 6.4.2 and 6.4.3.

6.4.1 Comparison of Ca XIX and Fe XXV temperatures.

All the flares had good quality Ca XIX spectra, but very few of them had Fe XXV spectra of a similar quality. Where Fe XXV spectra are available, it is found that Fe XXV emitting plasma is consistently hotter than Ca XIX emitting plasma by an average amount of 3 MK. At first sight this appears to undermine the assumption made in Section 6.3.2 that the loop top temperature is well represented by the Ca XIX temperature. But when these two sets of temperatures are plotted against each other in Figure 6.14, the relation between them is found to be identical to that of the hydrodynamic loop model shown in Figure 6.4. This is taken to be confirmation of the validity of using Ca XIX temperatures to represent loop-top temperatures.

The results in the table also show that except for the flares of 13 April 1980, 25 August 1980 and 7 July 1980, the characteristic decay time of the Fe XXV temperature is shorter than that of the Ca XIX temperature.
As expected from the theory, the characteristic decay time for a given loop length is shorter for hotter plasma.

6.4.2 Flares with no decay phase heating.

For only one of the six flares for which *FCS* images were available (10 April 1980) was the measured loop length found to be equal to the length predicted by the temperature decay diagnostic diagram. Thus for this flare, the assumptions that were made about the flare decay cooling mechanism are justified - that the only source of heating available to this flare was the rise phase heating source, and that this ceased to heat the flare just as abruptly as it started up.

Date	Observing times (UT)	ENTROPY DECAY DATA τ_T(s) Ca	τ_T(s) Fe	L_9 (10^9cm) Ca	L_9 (10^9cm) Fe	T_{max}(MK) Ca	T_{max}(MK) Fe	LOOP SIZE DATA Measured loop half-length (10^9cm)	Source	Comments
7 Apr 80	0049	900	-	8.5	-	-	-	-	-	-,H
7 Apr 80	0537	954	-	9.3	-	-	-	-	-	-,NH
10 Apr 80	0915	340	-	3.4	-	-	-	3.3 ± 0.9	*FCS*	NH,H
13 Apr 80	0400	725	456	6.9	5.1	13.5	17.6	-	-	-,H
4 Jun 80	0917	-	1726	10.9	20.6	16.3	17.0	-	-	-,NH
13 Jun 80	2230	785	-	7.8	-	13.1	16.3	-	-	-
24 Jun 80	1520	209	-	2.0	-	-	-	-	-	-,H
29 Jun 80	0230	732	-	7.1	-	-	-	3.4 ± 0.9	*FCS*	H,SH
29 Jun 80	1040	625	-	6.9	-	-	-	-	-	-,SH
29 Jun 80	1810	430	-	5.1	-	-	-	2.7 ± 0.9	*FCS*	H,SH
1 Jul 80	1622	421	-	4.6	-	-	-	-	-	-,H
5 Jul 80	2237	1349	-	13.8	-	-	-	-	-	-,H
7 Jul 80	1140	252	160	2.6	1.9	16.2	20.0	-	-	-
11 Jul 80	2223	1080	-	9.6	-	-	-	-	-	-,H
12 Jul 80	1109	806	-	7.7	-	-	-	-	-	-,H
12 Jul 80	1558	390	-	3.2	-	-	-	-	-	-
12 Jul 80	1733	333	-	3.2	-	-	-	-	-	-
12 Jul 80	0628	695	-	6.7	-	-	-	-	-	-
13 Jul 80	1432	179	-	1.8	-	-	-	-	-	-
13 Jul 80	1730	576	-	5.0	-	-	-	-	-	-
24 Aug 80	1601	409	43	3.9	0.5	12.7	15.8	-	-	-,NH
25 Aug 80	1250	-	433	-	4.9	12.5	16.1	-	-	-,NH
7 Nov 80	1129	264	-	3.0	-	-	-	-	-	-
8 Nov 80	1120	43	-	0.5	-	-	-	-	-	-
9 Nov 80	1705	262	-	2.3	-	-	-	-	-	-
11 Nov 80	0620	381	-	4.3	-	-	-	-	-	-
12 Nov 80	1057	688	-	8.0	-	-	-	-	-	-,H
13 Nov 80	0047	1183	-	12.7	-	-		6.8 ± 0.6	*FCS*	H,H
26 Apr 84	0857	259	-	3.0	-	-	-	-	-	-,NH
27 Apr 84	0537	88	-	0.9	-	-	-	-	-	-,NH
2 May 84	1614	660	-	6.2	-	-	-	-	-	-
2 May 84	1915	417	-	4.3	-	-	-	-	-	-,H
5 May 84	0100	145	-	1.6	-	-	-	-	-	-
5 May 84	1809	377	-	5.9	-	-	-	-	-	-
6 May 84	0140	317	-	3.2	-	-	-	-	-	-
6 May 84	1620	171	-	1.7	-	-	-	-	-	-
19 May 84	2141	949	-	11.4	-	-	-	2.5 ± 0.9	*FCS*	H,H
20 May 84	0109	612	-	6.0	-	-	-	-	-	-,NH
20 May 84	0245	~600		~6.5	-	-	-	-	-	-,H
20 May 84	0536	830	-	8.7	-	-	-	-	-	-,H
20 May 84	2252	730		6.8	-	-	-	4.0 ± 0.6	*FCS*	SH,SH
21 May 84	1746	739	-	7.2	-	-	-	-	-	-,H
22 May 84	1445	1257	-	8.5	-	-	-	-	-	-

Table 6.1: Predicted and observed loop lengths.
τ_T is the characteristic decay time of the electron temperature, measured using the temperature decay diagnostic diagram. Derived from this is L_9, the loop half-length (in units of 10^9 cm) and T_{max} is the maximum measured temperature. If the measured loop half-length is less than the predicted half-length, the loop is probably being heated in the decay phase. The last column compares the results of this analysis (entry before comma) with that of Jakimiec et al., 1993 (entry after comma). The symbols used are: H = heating, SH = some heating, NH = no heating.

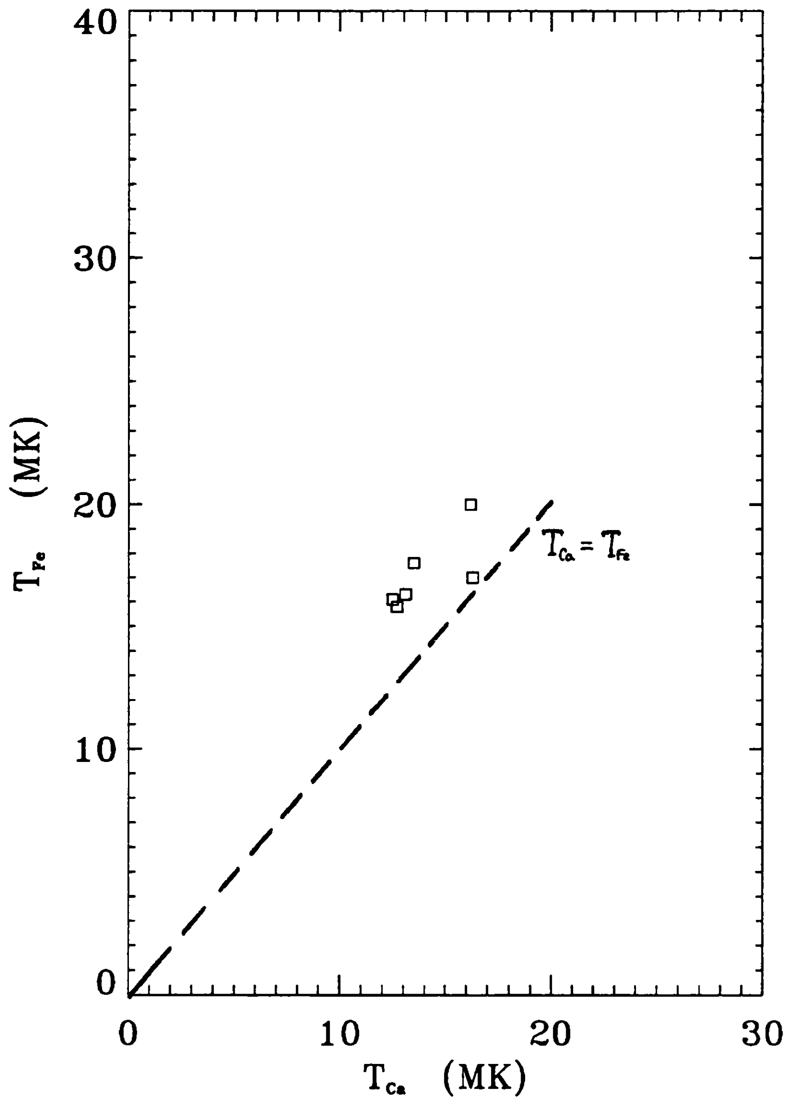

Figure 6.14: The relation betwen the temperature derived from Fe XXV spectra and that derived from Ca XIX spectra.
The relation between Fe XXV temperatures and Ca XIX temperatures is identical to that between the synthesized loop-top temperature and Ca XIX temperature obtained from the Palermo-Harvard model.

6.4.3 Flares with decay phase heating.

For five out of the six flares for which *FCS* images were available (0230 UT and 1810 UT on 29 June 1980, 13 November 1980, 19 May 1984 and 20 May 1984) the measured loop sizes are less than that predicted by the temperature decay diagnostic diagrams.

This means that there must be heating present in the decay phase of these flares. This heating would cause the temperature in these flares to decay more slowly than they otherwise would. So if this temperature decay time were then used to calculate the loop length, on the basis that longer loops cool more slowly, the length obtained would be an overestimate.

6.4.4 Comparison with analysis using density-temperature diagrams.

Jakimiec *et al.*, (1993) have used the density-temperature (N-T) diagrams of Jakimiec (1986) to analyse the decay phase heating of several flares. N-T diagrams are plots of flare plasma temperature against density, and it has been shown that the slope of the plot during the decay phase is a sensitive indicator of the presence of heating.

The results of their analysis is shown alongside the results of this work in the last column of Table 6.1. They are in agreement except for one case: that of the 10 April 1980 flare. This flare is described as having a complex heating history by Sylwester *et al.*, (1993). The analysis presented here depends on the accuracy to which flare sizes can be measured from *FCS* images. To that extent the results presented here are less easily defended against the results of the N-T analysis, and it must be concluded that the flare size measurements for the 10 April 1980 flare has been overestimated.

6.5 Summary

The theory of static coronal loops can be extended to investigate the cooling of flares, provided that it is only the very early part of the flare decay that is studied. This allows a relation to be derived between the temperature decay time and the flare loop length. This relation is valid only in the instance where no heating is present.

By measuring the temperature decay time and flare loop length independently, the validity of this assumption can be tested for a flare. Temperatures measured from *BCS* spectra and loop lengths measured from *FCS* images were obtained for several flares, and it was found that all but one of the flares was being heated in the decay phase.

The method presented in this Chapter is potentially a powerful one with which to test for the presence of heating in the decay phase of flares. It is held back by two factors: the lack of spatial resolution of images, and the lack of information about loop orientations.

The lack of spatial resolution means that the presence of several loops in a flaring structure cannot be detected with certainty, and the lack of information about orientations introduces ambiguity to the interpretation of two-dimensional images.

CHAPTER 7

Flare Plasma Velocity

7.1 Introduction

Well before upflows were ever seen in the soft X-ray spectra of flares, it was suggested by Neupert (1968) that the deposition of energy in the chromosphere by energetic electrons would cause the ablation of plasma from the chromosphere and into the coronal loop and thus enhance the soft X-ray emission. The electrons in question are those that are responsible for the microwave and radio emission seen early in the life of a flare, and Neupert observed a correlation between the amount of energy seen in the microwave emission and the amount of energy associated with the soft x-ray emission which appears minutes later. The time lag and the energy balance seemed to point to a transfer of energy from the microwave electrons to the soft X-ray plasma, and it was suggested that the conversion took place when electrons, which spiral down the magnetic field lines in the loop emitting radio and microwave radiation (via the synchrotron process), encounter the denser plasma of the chromosphere and lose their energy to it (via the Coulomb collision process). The response of the chromosphere to the deposition of this energy would be to eject heated plasma into the less dense coronal part of the loop. This upflowing plasma would emit soft X-rays itself as well as heat the ambient plasma so that it too would emit soft X-rays.

It was not until the advent of spectrometers of high enough resolution and sensitivity to detect line broadening during the rise phase of the soft X-ray flare (when emission at these energies is still quite weak) that possible confirmation of these upflows was obtained. The Bragg crystal spectrometers on the *P-78* spacecraft (which were very similar to the *SMM-FCS)* recorded Fe XXV and CaXIX spectra in which blueshifts were seen and reported by Doschek *et al.*, (1980). Since then the spectrometers aboard *SMM* and *Hinotori* have consistently observed blueshifts and line broadening and the main points which emerge from these data are discussed in Section 7.1.1.

7.1.1 Observed plasma dynamics.

The main features of CaXIX and FeXXV spectra recorded during the rise phase of flares are

(a) the high velocity blueshifted line emission in the rise phase,

(b) the non-thermal broadening which peaks in the rise phase and persists into the decay phase, and

(c) the dominant stationary emission which appears before the impulsive energy release and (of course) persists for the duration of the flare.

There is, as yet, no satisfactory unified explanation for all of these aspects of the dynamics of the flare plasma.

The **chromospheric evaporation** interpretation, which is discussed below, mainly addresses the blue shifted emission, going some way towards explaining the presence of the non-thermal broadening, but failing completely to account for the early appearance of the dominant stationary component.

There are **alternative interpretations**, which are discussed in Section 7.1.3.

7.1.2 The chromospheric evaporation interpretation.

The process in which thermalised plasma [1] flows up into the flare loop came to be called chromospheric evaporation (Antonucci and Dennis, 1983). It must be pointed out that *evaporation* is a misnomer, as it implies a change of state, which, by definition, cannot occur in a plasma. It was perhaps introduced to evoke a picture of heated material rising up off the surface of a reservoir of cooler, denser material.

The three questions at the heart of this interpretation are

1. What is the nature of the energy release ?

2. Where is the energy release site ?

3. How is the released energy transported from the release site to the site of chromospheric evaporation?

In the attempt to answer these questions, several workers have developed fairly detailed models of the chromospheric evaporation process, which are of two

[1]**thermalised plasma** - this term is used to describe plasma which has been heated sufficiently to make it dynamically active.

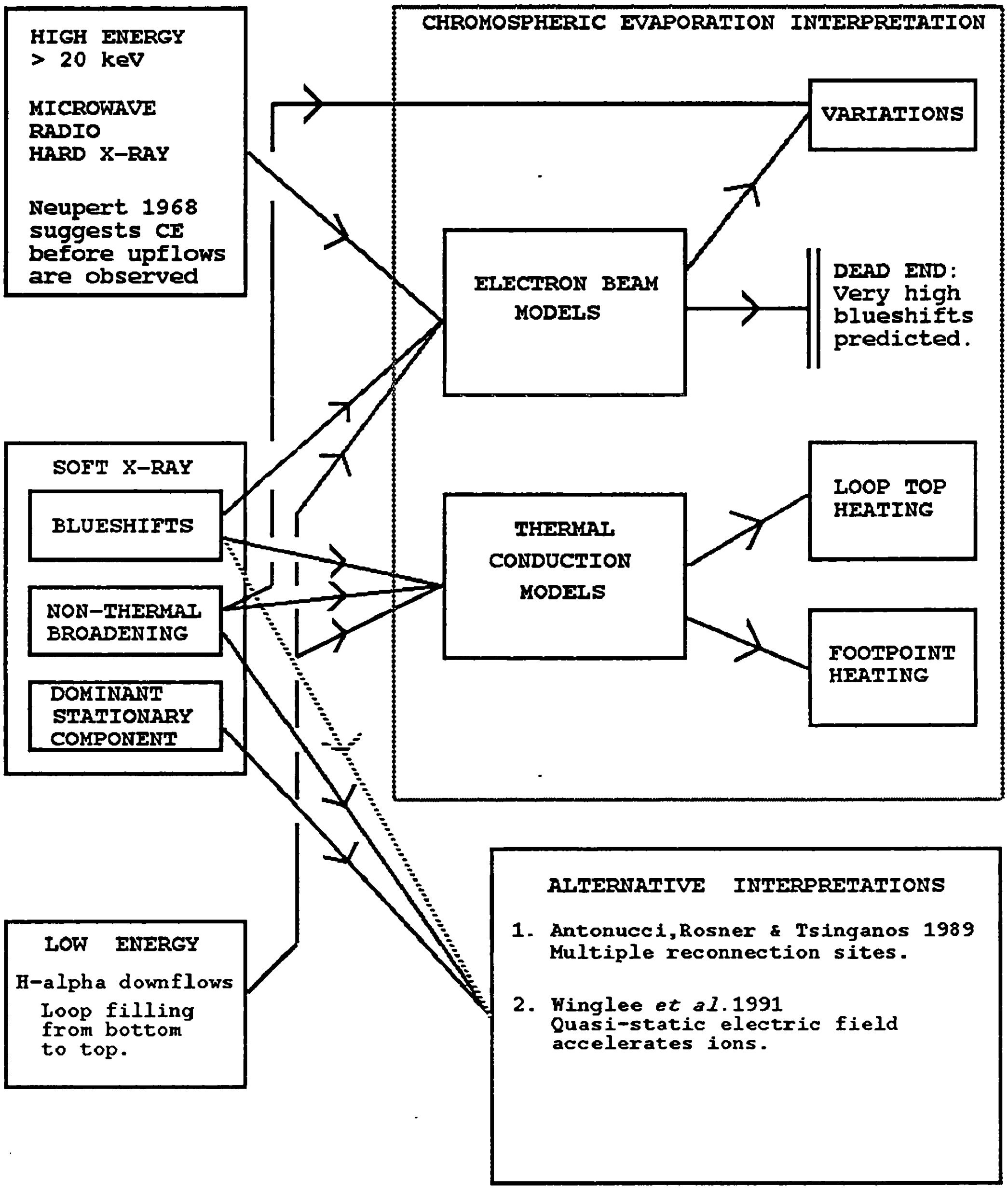

Figure 7.1: The current state of the interpretation of flare plasma dynamics.

types: those that invoke a stream of energetic electrons which are accelerated by an as yet undefined mechanism in the loop top (electron beam models: the left hand side of the schematic in Figure 7.2) and those that rely on the thermal conduction from local energy release sites which could be either in the loop top (thermal conduction models: the right hand side of the schematic in Figure 7.2) or at the footpoints themselves.

7.1.2(a) Electron beam models

There are several versions of the electron beam model, most of which explain observed rise phase spectra with varying degrees of success (Nagai and Emslie, 1984; MacNeice *et al.*, 1984; Fisher, Canfield and McClymont, 1985(a),(b),(c); Li, Emslie and Mariska, 1989).

In essence, electron beam models consist of a beam of electrons, usually with a power law spectrum of energies, being accelerated from the loop tops. They follow the magnetic field lines of the loop legs, emitting radio and microwave radiation as they go. Because the density of the coronal part of the loop is so low, there is negligible interaction with the ambient plasma. Close to the bottom of the coronal loop, however, the electrons encounter the denser plasma of the chromosphere where the probability of Coulomb interaction becomes significant. The deceleration of electrons in this manner usually causes bremsstrahlung radiation at hard X-ray wavelengths and indeed this is one of the observed features during the first minute of a flare.

With respect to the interaction of the electron beam with the chromosphere, the generic electron beam model divides into the thin target model, thick target model and the thermal model. The efficiency of conversion of electron energy to observed photon energy is least in the thin target model, more so in the thick target model and is very much more in the thermal model. Because electron beam models require that microwave, radio and hard X-ray emission from the primary electrons *precedes* thermalisation of the loop plasma, they cannot account for the existence of the dominant stationary component that is seen in advance of both microwave and radio emission and soft X-ray upflows. It was suggested by Emslie and Alexander (1987) that the dominant stationary component of the *BCS* CaXIX resonance line reported by Antonucci *et al.*,(1982) was itself wholly blueshifted and that Antonucci *et al.*, had mis-calibrated their spectra. However, the latter authors were vindicated by McClements and Alexander (1989) who confirmed that there was no shift of the main component of the CaXIX resonance line , and by K. J. H. Phillips (in a private communication to Li, Emslie and Mariska (1989)) who used absolutely calibrated *FCS* spectra to check the *BCS* calibration of Antonucci *et al.*, and found it to be correct.

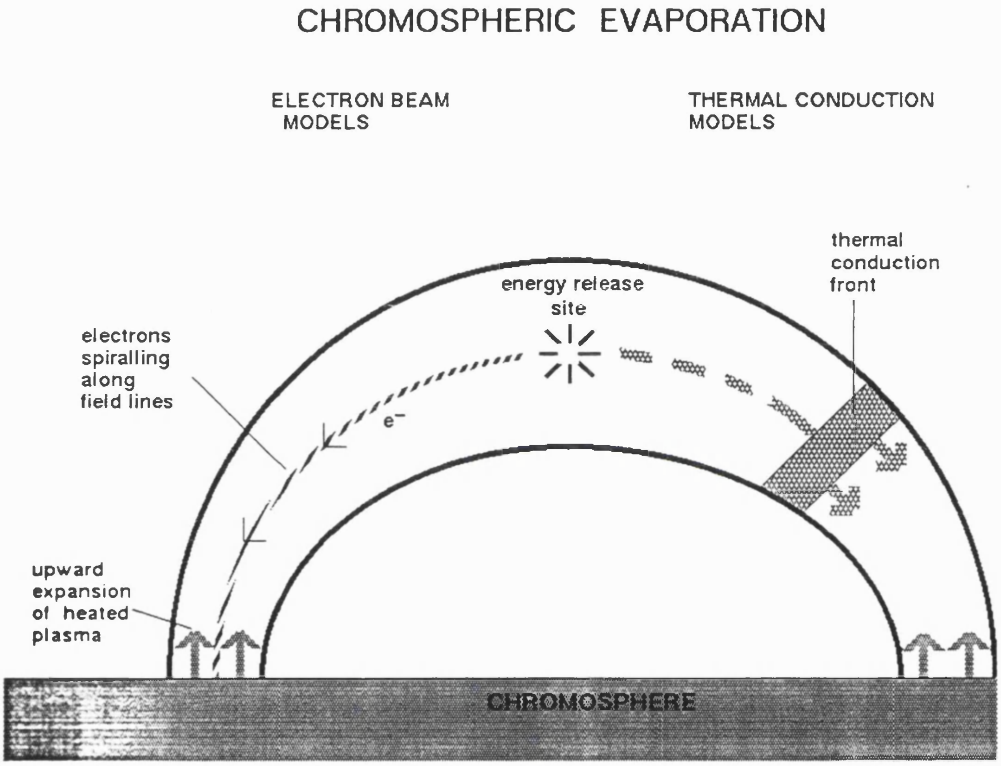

Figure 7.2: The main features of chromospheric evaporation models of flares.
Different chromospheric evaporation models invoke different energy transport mechanisms to link the energy release site (at the loop top) with the evaporation site (at the loop foot points). On the left of this schematic is the electron beam model in which electrons with a certain energy distribution are acclerated along the loop field lines. On the right is the thermal conduction model in which a conduction front moves down the loop legs. Both mechanisms transfer energy to the chromospheric plasma which can neither dissipate the heat quickly enough nor expand downwards, and so surges upwards into the corona.

The main point about electron beam models is that no mechanism for the acceleration of the electrons has ever been agreed upon, and that the prime justification for all the work that has been put into electron beam modelling has been that it should correctly reproduce the dynamics of the soft X-ray plasma. As one of the effects that it predicts (a bright, fast component, blueshifted by 3 to 4 mÅ) has not been observed, and a major observed feature (the dominant stationary component) is not predicted at all, to continue to work with this model would require some other justification.

7.1.2(b) Thermal conduction models

In thermal conduction models, a thermal conduction front is substituted for the electron beam as the mechanism via which energy is transported from the energy release site to the footpoints. In those models in which the energy release happens at the loop top, the dynamical response of the plasma is very similar to that predicted by the electron beam model. In other thermal conduction models, the energy release site is in the loop footpoints. Antonucci *et al.*, 1987 modelled heating of the chromosphere by thermal conduction for both cases. They concluded that 40% of the flares they studied were heated at the loop footpoints. They could not, however, rule out loop top heating, because some of the predicted dynamical effects would be too weak or too shortlived to be detected by the *SMM-BCS.*

7.1.2(c) Evidence in support of the chromospheric evaporation interpretation.

Whether heated by an electron beam or by a thermal conduction front, the predicted effect of chromospheric evaporation models is the ablation of hot plasma from the chromosphere. Antonucci *et al.*, (1982) showed that the estimated energy borne by the upflowing plasma in the 10 April 1980 flare was more than adequate to account for the energy seen in the coronal plasma. The excess energy accounted for the energy lost from the coronal plasma by conduction and radiation. A similar calculation was done for the 6 June 1982 flare by Tanaka and Zirin (1985). Thus there appears to be support for the chromospheric evaporation interpretation in as far as it explains the energization of the post-rise phase flare.

There have also been studies of some effects on the chromosphere itself which could be interpreted as a consequence of chromospheric evaporation. Zarro *et al.*, (1988) and Canfield *et al.*, (1990) used H_α spectra to estimate the momentum of the downward moving chromospheric plasma, which ought to be equal in magnitude to the momentum of the chromospheric evaporation plasma moving in the opposite direction. This was found to be so, but these calculations have been criticised as subject to uncertainties so large as to render them inconclusive (Doschek, 1990).

The spatial coincidence of soft X-ray emission and hard X-ray emission from loop footpoints (Antonucci *et al.*, 1985) is evidence of a common site for the transfer of energy between the two bands of emission.

Lower energy soft X-ray images of the rise phase of flare loops show the progressive brightening of loops from footpoints to their apex (Hiei and Widing, 1979; Bruner *et al.*, 1988) which is commensurate with the initial transfer of energy to the plasma at the footpoints.

7.1.2(d)Evidence against the chromospheric evaporation interpretation

The chromospheric evaporation scenario is, however, far from being a complete explanation of the dynamics of the rise phase of flares. There are several well documented observational features which do not concur with the predictions of models.

The large blueshifts predicted in the first few seconds of the rise phase are not seen in real soft X-ray spectra. In fact, observed spectra are dominated by lines centered around the rest wavelength, and this is observed before the appearance of the blue asymmetries associated with upflows.

It is argued that the density of this stationary plasma is already quite high, thus reducing the potential of the density gradient that must exist between the chromosphere and the corona for chromospheric evaporation to occur.

Even if the loop density was sufficiently low that a steep enough gradient did exist between the two regions, the loop filling times of about 10 seconds predicted by chromospheric evaporation models are too long to fit in with observed patterns of soft X-ray emission. The loop filling time is the product of the maximum plasma velocity and the loop length, and obviously if the estimate of the length were revised downwards the loop filling time could be shortened.

Karpen, Doschek and Seely (1986) showed that in the 7 November 1980 flare, the upflows actually lacked the pressure needed to force their way up into coronal part of the loop.

7.1.2(e) Resolution of contested issues by improved instrumentation

The argument that chromospheric evaporation predicts large blueshifts which have not yet been seen could be resolved if spectra could be integrated over a period of seconds, during the rise phase. If there were highly blue-shifted upflows they ought to appear in the edge of the blue wing, and be resolved without much ambiguity.

The sensitivity of a spectrometer capable of performing this task would make it suitable to measure the density in the pre-flare loop. Thus a true idea of the density increase during the rise phase could be obtained, which could be compared with the predicted increase due to the entry of chromospheric plasma into the coronal part of the loop.

If improved image resolution leads to a downward revision of estimated loop lengths, predicted loop filling times might shorten enough to agree with observed flare evolution.

7.1.3 Alternative interpretations

7.1.3(a) Multiple local reconnection sites.

Antonucci, Rosner and Tsinganos (1986) suggested that in fact there were multiple local reconnection sites distributed along the loop, each producing local, directed plasma flows, the cumulative effect of which would be a symmetrically broadened emission line. This explanation can be extended to cover non-flaring activity seen in quiescent loops, and in fact would unify the solutions to the release of energy in coronal loops, both flaring and non-flaring, if it could be extended to cover upflows.

7.1.3(b) Quasi-static electric fields.

Winglee *et al.*, (1991a,b) offer the only explanation to cover the high energy impulsive emission (hard X-ray, microwave and radio) *and* the soft X-ray blueshifts and turbulence. They invoke quasi-static electric fields [2] that would serve both to accelerate electrons down to the chromosphere and to accelerate ions in the opposite direction. The schematic of their model, reproduced in Figure 7.3 shows the configuration of the electric field relative to the flare loop. Because the ions make up the bulk of the plasma, their motion parallel to the field will constitute the upflowing motion required by the soft X-ray blueshifts seen in the rise phase. Winglee *et al.*, (1991a) further propose that the electric fields are "filamented" into small-scale structures, and that there would be a perpendicular acceleration of ions between these filaments. This would of course be over scale lengths which are much smaller than the scale lengths along the electric field, and would result in small scale mass motion, which would appear as random mass motion when integrated over the loop. Thus they explain both the

[2] A **quasi-static electric field** does change, but only on a time scale which is much longer than the time taken by energetic electrons to travel from the loop top to a footpoint.

hard X-ray, microwave and radio emission, the broadened soft X-ray emission from the stationary plasma, and the soft X-ray emission from the upflowing plasma. Above all, the crucial feature of the model is that the *timing* of these flare onset events agree with observations.

7.1.4 The methods and aims of this analysis.

In this analysis, data obtained with the *SMM-BCS* have been used to investigate the dynamics of the flare plasma. Spectra from two of the *BCS*'s channels (Channel 1, for CaXIX spectra, and Channel 4, for Fe XXV spectra) are available for most of SMM's observing life (from 1980 to 1989) and the consistent quality of this data has made it the foundation of many of the advances made in flare physics over the last decade (see reviews by Antonucci, 1990 and Doschek, 1990). Here, the same data is used, but a new approach to the analysis of spectral line profiles is taken.

Because the method introduced here is quite a novel one, some space is devoted to explaining the concepts involved and testing it on simulated data. Following this exploration of the method, examples of its application to *SMM* data are presented.

This analysis differs from other work on measuring plasma velocities in that it does not assume velocity distributions. Instead it makes a rough division between two velocity regimes - a division which, though it might be rough, is found to be quite adequate for the purpose.

The existence of data from two channels of the *BCS*, each of which responded to a different temperature range, permits the comparison of the dynamics of plasma of two different temperature ranges.

Because of the limitations imposed by the sensitivity of the *BCS*, this analysis cannot deal with the more rapid changes that are thought to occur in the rise phase, except in a very few cases (for example, the 14 October 1980 flare). The limited sensitivity forces the exclusion of spectra recorded during the very early part of the flare when its soft X-ray brightness is so low that the registered count rate is lost in the instrument's intrinsic noise. Even when the soft X-ray brightness is above the instrument noise level, in order to obtain a decent spectrum, the integration interval has to be about 10 seconds or longer. This makes it difficult to detect the more rapid changes that could be occurring.

The aims of this analysis are, then,

(a) to develop a simple alternative method of analysing line-widths in soft X-ray spectra,

(b) to explore ways of using it to detect the presence of upflows in *SMM-BCS*

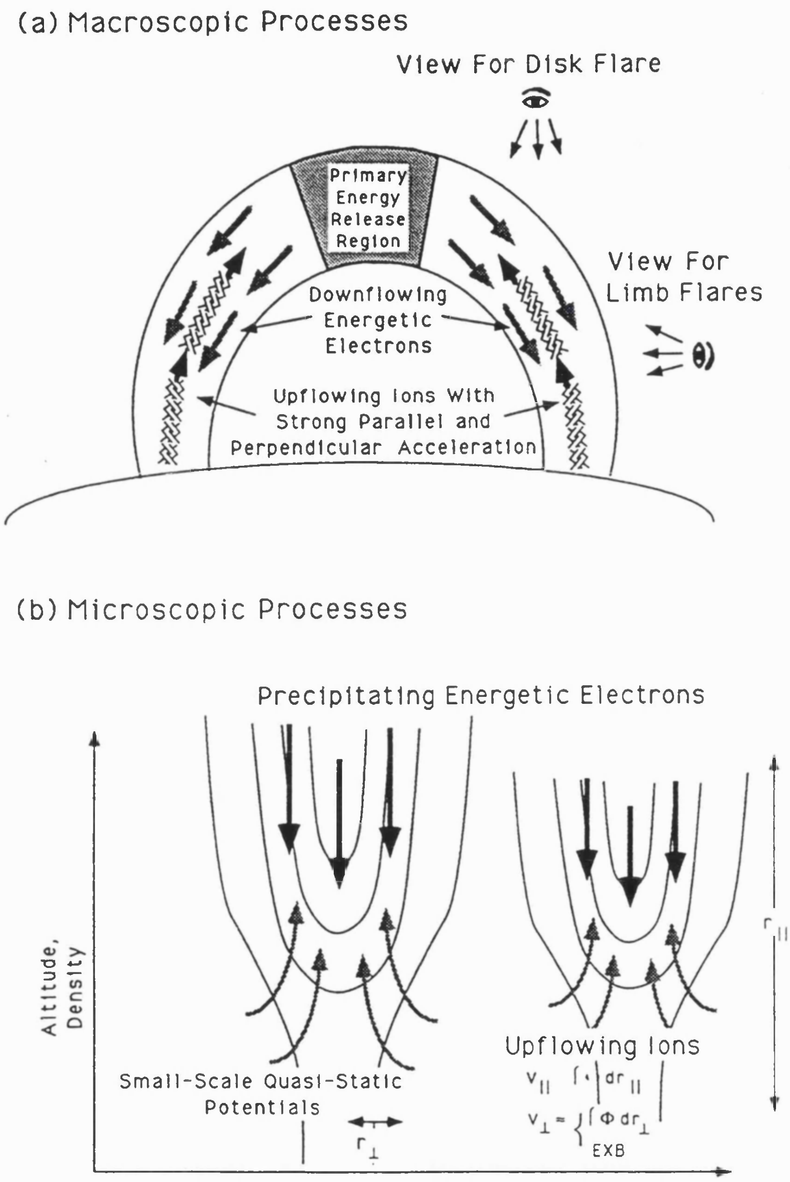

Figure 7.3: Schematic of the quasi-static electric field model proposed by Winglee *et al.*, (1991a,b).
Electrons are accelerated down towards the chromosphere, and ions are accelerated in the opposite direction. The perpendicular velocity of the ions causes the non-thermal broadening, while their parallel velocity causes the rise-phase blueshifts. Reproduced from Winglee et al., (1991a).

flare data and,

(c) thus identify some of the characteristic features of flare plasma dynamics which may then be compared with the features predicted by the models which were introduced earlier.

7.2 Analysis technique

7.2.1 The measurement of directed plasma motion.

7.2.1(a) Component fitting.

Information about the motion of flare plasma can be derived in quite a simple manner from the shape and width of flare emission lines. Up until now the study of flare line widths and shapes has been based on the rather complicated procedure of breaking down an emission line into *line components*, each of which is held to represent a mean upflow velocity about which are distributed velocities due to thermal motion and random mass motion. This method is applied prinicipally to the resonance line of helium-like ions, which is the most prominent line in the spectra of such ions, and has been used by Fludra *et al.*, (1989) and Antonucci, Dodero and Martin (1990). Figure 7.4 illustrates the component fitting methods used by these authors. Fludra *et al.*, fitted a pair of Gaussian shaped components, one to represent the stationary plasma and another the moving (upflowing) plasma. Each line component represents a range of velocities distributed around a mean value: the peak of the line component corresponds to the Doppler shift due to a unique upflow velocity and the wings of the component correspond to the deviations from this peak due to thermal and random mass-motion. The component representing the stationary plasma therefore has a centre with zero Doppler shift while the component representing the upflowing plasma has a Doppler shift of several mÅ towards the blue (shorter) end of the wavelength scale.

The physical significance of this must be pointed out: the use of a single Gaussian component to represent upflows means that the upflows are actually expected to have a unique value, which just happens to be blurred out by thermal motion and random mass-motion.

Of course it is difficult to justify the imposition of a unique upflow velocity such as the one derived from two-component fits. The use of just a pair of components is only the simplest convenient approximation that may be made. Even the workers who use such approximations recognise that two-component or even three-component fits are not often satisfactory and never unique (for example, Antonucci, Dodero and Martin 1990). Chromospheric evaporation itself might

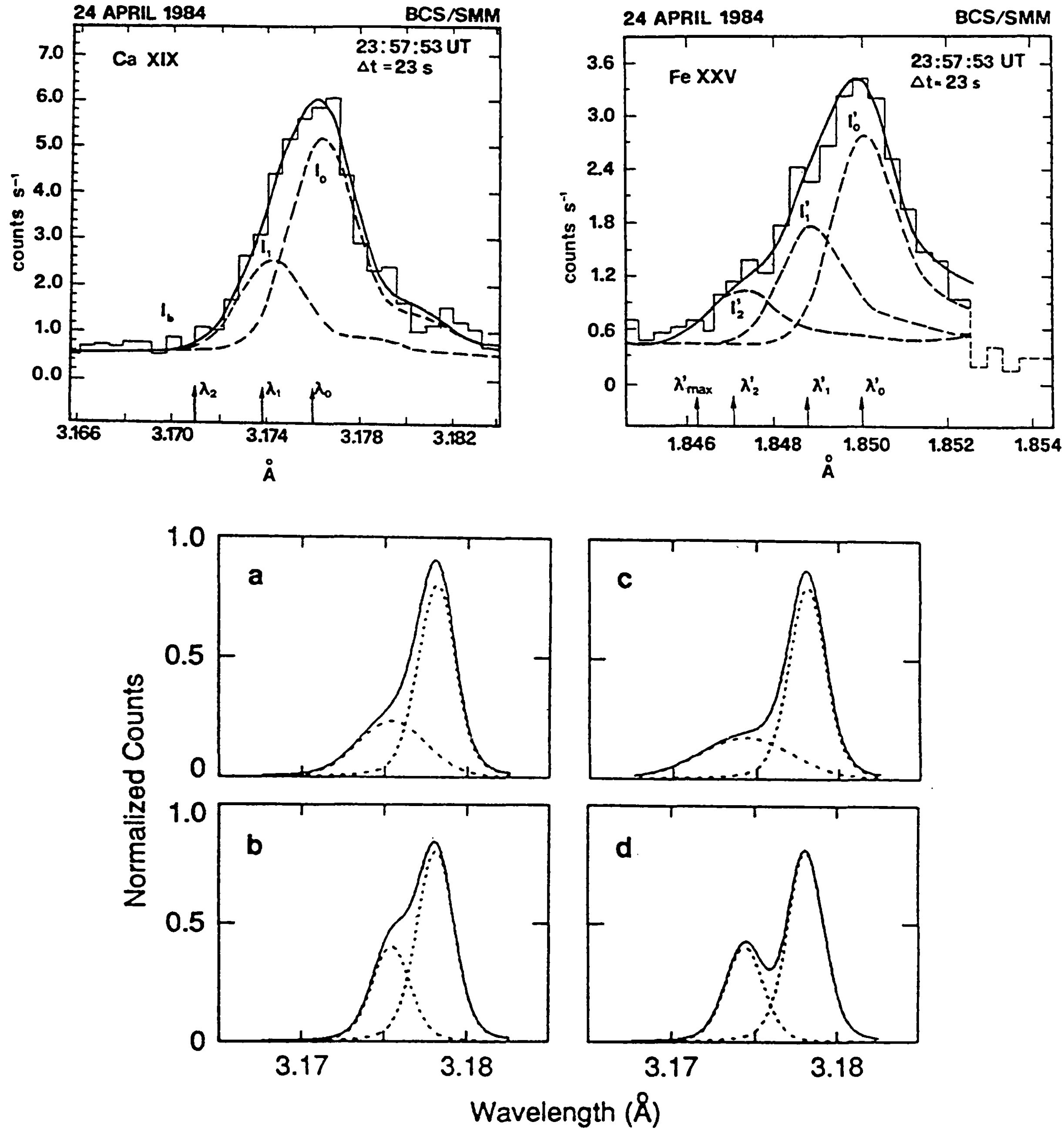

Figure 7.4: Component-fitting to resonance line profiles.
In the upper two panels are shown the two- and three-component line profile models used by Antonucci, Dodero and Martin (1990) to reproduce the CaXIX and FeXXV resonance line profiles. The lower four panels show examples of the synthetic line profiles generated by Fludra et al., (1989). In panels a *and* c *the width of the blueshifted component is proportional to the blueshift of its centre (peak velocity). In panels* b *and* d *both line components have the same width. The area under the blueshifted component is half that under the stationary component. Observed spectra resemble more the line profiles in* a *and* c*. Reproduced from Fludra et al., (1989) and Antonucci, Dodero and Martin (1990).*

not take place in one sustained upsurge, but could well be taking place in discrete bursts at different sites at the footpoints (Doyle and Bentley 1986; Emslie and Alexander 1987).

Theoretical models, too, predict continuous distributions of velocities (Pallavacini *et al.*, 1983 among others, as well as most of the electron beam models mentioned in Section 7.1.2(a)).

A more accurate representation of a continuous distribution of velocities would be a line profile model made up of *several* components to represent the upflowing plasma. Even for the simplest case of two components, however, there is a large number of ways in which they can be combined to represent a broadened emission line. Determining the width, heights *and* positions of several components is bound to be even more difficult and is not likely to yield an any more satisfactory answer.

In short, despite the effort to measure some representative "upflow velocity", by the above-mentioned authors, all that is being measured is a *convenient index* of the level of upflow activity. Such an index may not even be a totally accurate representation of the upflow velocity distribution. There are alternative ways of using line profiles to probe upflow activity. One such alternative method is introduced in the next section.

7.2.1(b) A simpler method: estimating the area in the blue wing.

In the analysis presented here, a different approach is being taken, which does not involve fitting Gaussian components. Instead, the area (integrated intensity) under the blue wing is compared with the height (intensity) of the centre of the line. This normalisation against the height of the line compensates for the changing total intensity of the flare, and permits the comparison of spectra recorded at different times during the life of a flare. It also permits comparisons to be made *between* flares.

The count rate per bin in the blue wing of the flare, however, will be composed of emission from both upflowing plasma and randomly moving plasma. One way of distinguishing between them, or at least of determining the proportion of each contribution, would be to compare the count rate per bin in the red wing with that in the blue wing (because emission from upflowing plasma is wavelength-shifted into the blue wing only). The difficulty in doing this is that the red wing of the CaXIX resonance line is contaminated by contributions from nearby low-intensity lines (the n=3 satellites) that blend into the base of the resonance line on the red side. This effect can be seen in the detail of the spectrum around the resonance line in Figure 7.5.

What this seems to suggest is that if the effect of the n=3 satellite line were accounted for somehow, a very reliable measure of the amount of upflows could be obtained, and indeed this is true. Taking account of the effect of the n=3 satellite line, however, is a task in itself, and one which could draw this work away from its main purpose, which is to investigate the rise phase dynamics of flares.

Instead, the analysis presented here uses the *blue wing alone* as the source of information about directed motion. The blue wing is first divided into the two bands marked on the resonance line profile in Figure 7.5. The band which extends from the peak position to the division is called the **slow band** and should contain most of the emission from the main stationary mass of plasma. The band which extends from the other side of the division to the edge of the spectrum is called the **fast band** and should contain mainly emission from plasma moving at velocities of several hundreds of kilometres per second.

The position of the division between these two bands reflects the diminishing contribution of emission from the main stationary plasma mass to the bins in the ends of the blue wing. The stationary plasma has a spread of velocities due to the thermal motion and the random mass motion of its ions. The further away from the peak of the line, the less is the contribution from the stationary plasma, and the greater is the contribution from upflowing plasma. The division between the velocity bands is chosen so that, on its short wavelength side, the dominant influence is upflowing plasma, while on the long wavelength side, the dominant influence is the stationary plasma.

As is clear from this description, this is not a perfect division, but, allowing for these imperfections, the counts in the fast band represent reliably the emission from fast plasma upflows with some contribution from the stationary plasma, while the counts in the slow band represents the emission from stationary plasma, with a small contribution from slow plasma upflows. This non-negligible contribution from slow upflows is expected to arise from the continuous distribution of upflow velocities which is believed to exist (this has been discussed earlier, in Section 7.2.1(a)), the lower velocity end of which will fall into the slow band.

What has been introduced in this section is the *principle* of an alternative way of measuring upflow activity. It is developed further on being put into practice, when a quantity called the **equivalent width** is defined. It will be shown that the equivalent width for a particular velocity band is a measure of the mean velocity in that band. How it is defined and measured is described in detail in Section 7.2.2.

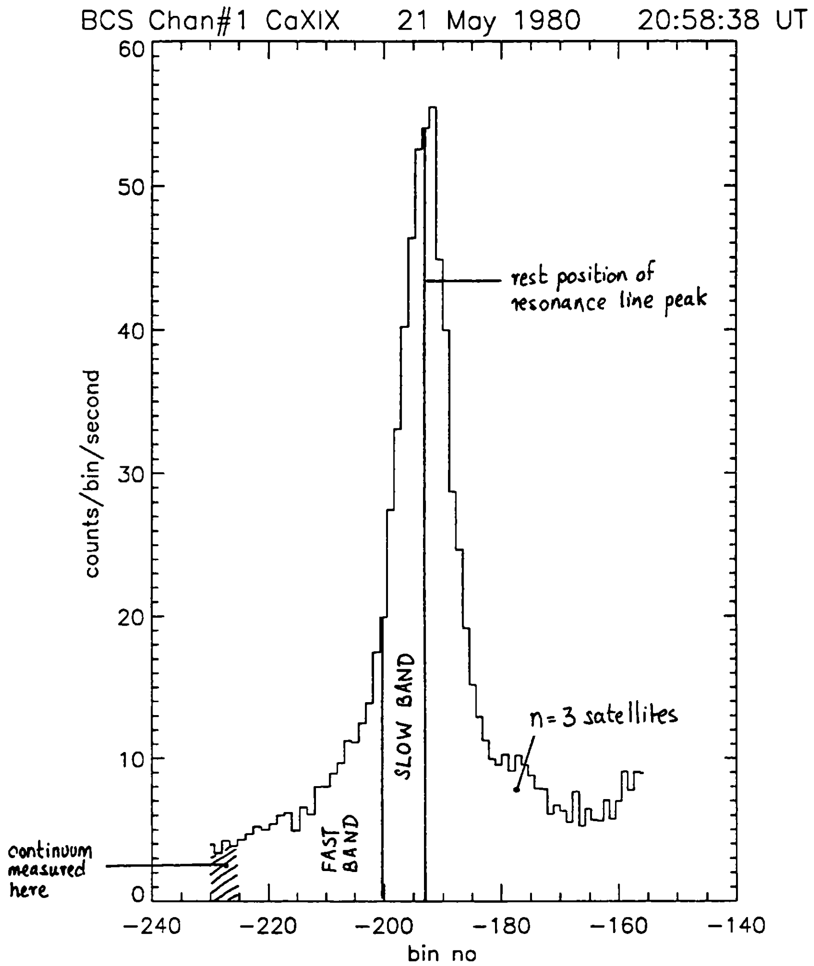

Figure 7.5: Detail of the CaXIX spectrum around the resonance line. *This spectrum is from the rise phase of a flare, and shows the broadening of the blue wing. The difficulty of estimating the asymmetry of the line is apparent from the level of contamination of the line on its red side. The blue wing has been divided into two regions at the sixth bin from the rest peak position. The continuum level is measured in the shaded region on the left hand side.*

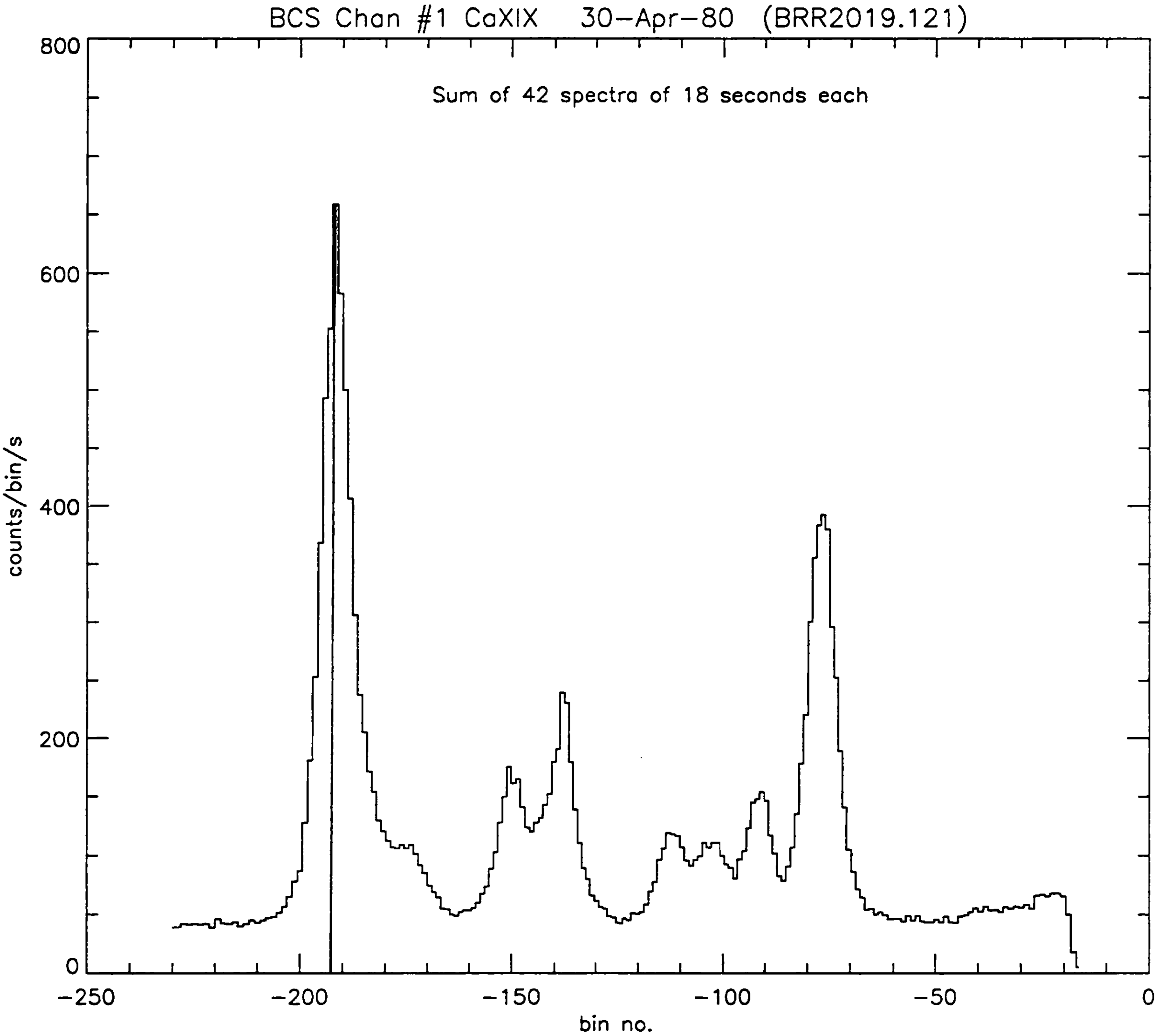

Figure 7.6: The summed spectrum of a flare.
This spectrum was obtained by summing together the individual spectra over the whole duration of the flare. The position of the resonance line is determined from this summed spectrum, and for the particular case shown in this figure, has been marked with the tall vertical line at bin no. -193.

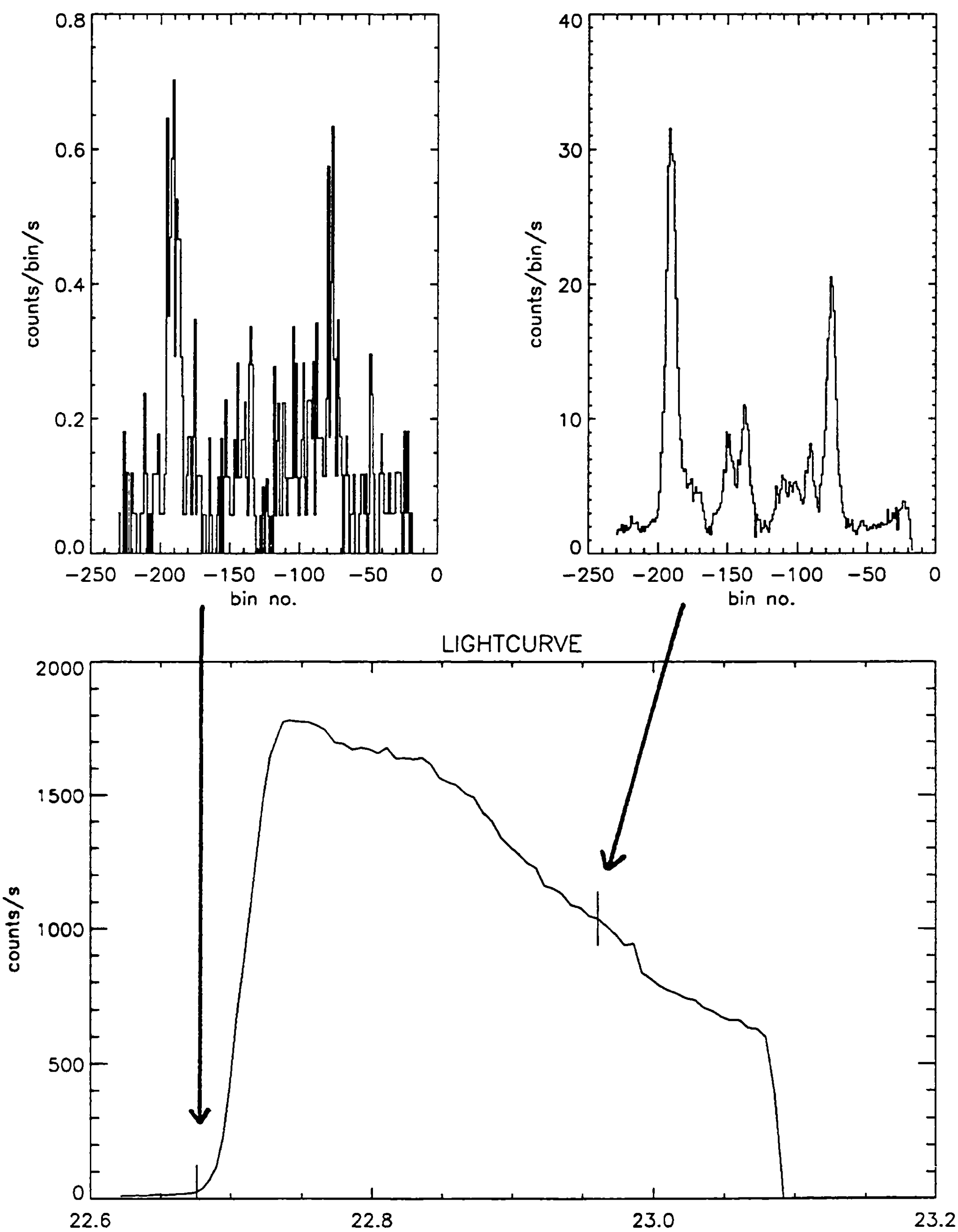

Figure 7.7: Comparison of spectra from early in the rise phase with spectra from the decay phase.
The low count rate early in the rise phase means that spectra which are integrated over as short a time interval as is possible are very noisy in comparison to decay phase spectra integrated over the same time interval.

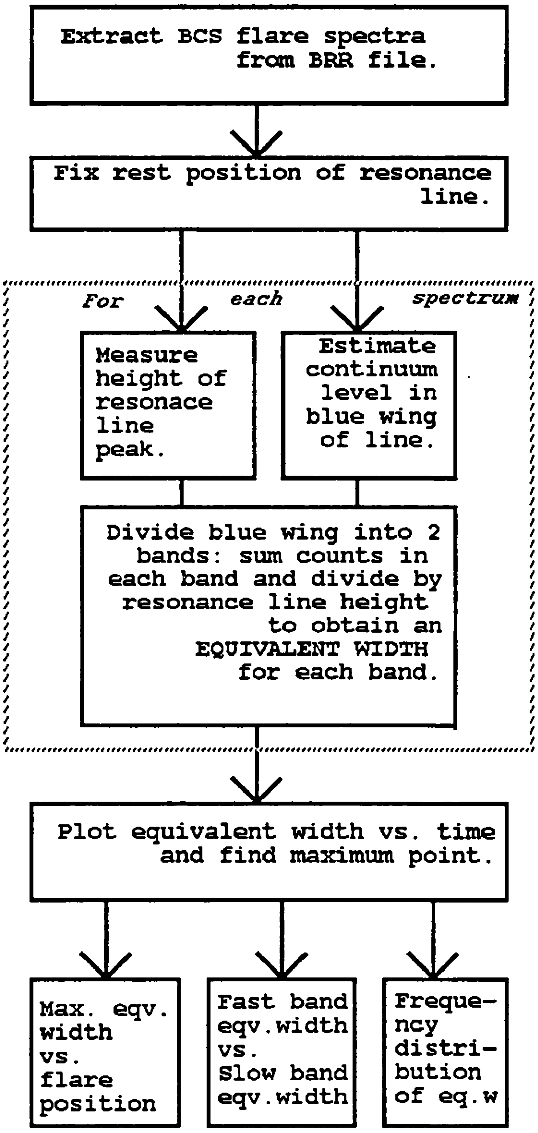

Figure 7.8: Derivation of the flare equivalent width from *BCS* spectra. *This flowchart shows the main steps involved in deriving equivalent widths from* BCS *spectra stored in BRR files. These steps are described in greater detail in Section 7.2.2.*

7.2.2 Measurement of the equivalent width.

To express the intensity distribution of the emission line between the two velocity bands as a single number, a quantity called the **equivalent width** is defined. That it is a *width*, with units of bins (or bin equivalent units such as wavelength or velocity), becomes apparent when the procedure for deriving it is explained.

The procedure for deriving the equivalent width is summarised in the flowchart in Figure 7.8. In essence, it consists of finding the position that the line ought to have if the plasma were at rest, and then comparing the spectra at different times during the flare with this ideal stationary line, and thus determine the amount of blueshifted emission. Absolute calibration of the spectrum is not required in this analysis: the limits of the wings of the resonance line are measured relative to the position of the peak of the line. The main steps of the process are expanded upon in subsections *(a)* to *(d)* below. The ever-present problem of bad data is addressed in subsection *(e)*, along with a method for screening the flare spectra to which this analysis is applied.

7.2.2(a) Fixing the rest position of the resonance line.

To obtain the best estimate of the rest position of the resonance line, all spectra recorded during the decay phase are summed together to give a single spectrum. This summed spectrum is equivalent to a spectrum that has been integrated over the entire duration of the decay phase, and the length of the integration period averages out the temporal changes in the spectrum. It can then be used to identify those features which should be constant over the duration of the flare, such as the rest position of the resonance line.

The summed spectrum from the flare at 2019UT on 30 April 1980 is shown in Figure 7.6 and on it are marked the resonance line peak position and the boundaries of the selected continuum region. Because it has been summed over the *decay* phase, the resonance line position should be at the rest wavelength. Once the position of the resonance line has been fixed using the *summed spectrum*, the count rate at this position can be obtained from *individual spectra.*

7.2.2(b) Measuring the continuum level and the peak count rate.

The continuum level, too, is measured from individual spectra. It is measured in a region of the spectrum that is undisturbed by emission lines and so should provide a measure of the background thermal emission . The average continuum count rate is obtained by adding up all the counts in the continuum window and dividing by the number of bins. The peak count rate per bin is obtained by averaging the counts per bin over the central bin and the two bins on either side of it.

So far two numbers that describe the spectrum have been obtained: the average count rate per bin at the peak and the average count rate per bin in the continuum. The third number that is required is the average count rate per bin in the blue wing.

7.2.2(b) Division of the wing into two velocity bands.

The point at which to divide the blue wing into two velocity bands was fixed on the basis of the maximum rise phase line broadening seen in the three limb flares of 29 June 1980. Voigt profiles fitted to the resonance line profiles of these flares yield Doppler widths of between 6 and 7 bins (in Channel 1).

Because these flares occurred on the limb (and assuming that their loops were radially directed) the widths of their rise phase emission lines should have a minimal contribution from (radially directed) upflows, and these widths can be taken to be an upper limit of the amount of mass-motion line broadening.

The blue wing is defined here to be the region which lies between the peak of the resonance line and the point at which the count rate per bin reaches the continuum level. There is no contamination from other emission lines in this wavelength band and it can be taken to represent reliably the thermal emission level. The shaded region of the spectral region around the Ca XIX resonance line shown in Figure 7.5 marks the continuum region used here.

Total count rates for the shorter-wavelength band (the fast band) and for the longer-wavelength band (the slow band) are obtained by summing the counts across each band. The total count rate from the fast band is a measure of the amount of *fast moving upflowing plasma and the more energetic stationary plasma.* The total count rate from the slow band is a measure of the amount of *moderately energetic stationary plasma and slower upflows.*

7.2.2(c) Derivation of an equivalent width by normalisation of the count rate.

The total count rates in each of the two bands have to be normalised in some way which will take into account the changing *total* soft X-ray output during a flare as well as to permit comparisons between different flares. Taking the *ratio* of this number to the average peak count rate per bin satisfies both requirements.

A consequence of performing this normalisation is that a summed count rate is turned into an equivalent width. This conversion may be understood by considering the units involved: the summed count rate from either of the velocity bands has units of *counts per second*, while the average count rate per

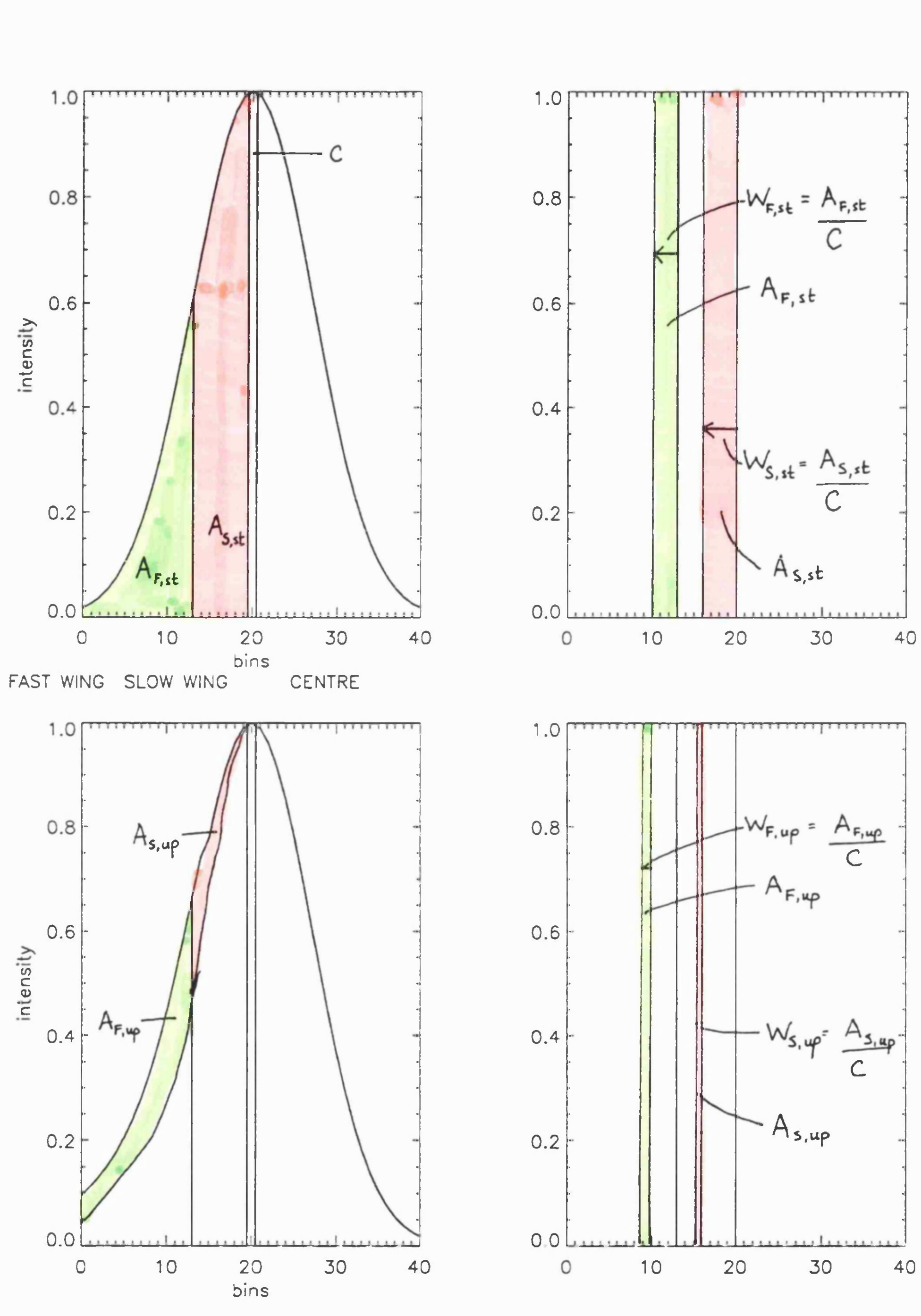

Figure 7.9: How observed line profiles translate into equivalent widths.
The upper two frames show a symmetrical line profile (no upflows) and the corresponding equivalent widths. The lower two frames show a line profile asymmetrically broadened by upflows, and its corresponding equivalent widths. The difference between the equivalent widths in each band is equal to the mean upflow velocity in those bands.

bin at the line peak has units of *counts per second per bin.* So, dividing the first quantity by the second yields a quantity with units of *bins*, which in turn may be expressed as a wavelength or as a *velocity.*

Thus a complementary pair of equivalent widths is obtained for each spectrum, and it is these equivalent widths that are plotted against time in the line-width time plot described in Section 7.2.3, and against each other in the line-width diagnostic plot described in Section 7.2.4.

7.2.2(e) Screening of data points.

Early in the flare, when the count rate per bin is very low, the amount of noise in the signal received by the detector is comparable to the intensity of the the resonance line itself. This has been illustrated in Figure 7.7 where a spectrum from the impulsive phase is shown alongside a spectrum from the decay phase. It is a problem that becomes particularly acute when the quantity in question is a ratio because a small negative deviation from the true value of the denominator which coincides with a small positive deviation from the true value of the numerator results in a large deviation from the true value of the ratio. So, much as it is desirable to have information from all phases of a flare, particularly from the rise phase, the inclusion in the line-width time plot of the data points which represent these weak spectra would simply mislead and confuse.

To avoid having to sift out the true data points from a jumble of false ones at the output end of the analysis, a preliminary screening of the spectra is carried out at the input end. All spectra in which the continuum level is greater than 10% of the peak resonance line intensity are excluded.

Bad data is somewhat less of a problem in the line-width diagnostic plot, which is a more robust way of representing the behaviour of the equivalent widths, because good data points form a quite well defined and easily recognisable group or pattern.

7.2.3 The line-width time plot

The line-width time plot shown in Figure 7.14 shows how the equivalent width in each velocity band is related to the total soft X-ray flux (the **lightcurve**), for both Channel 1 (Ca XIX spectra) and Channel 4 (Fe XXV spectra) of the *BCS.*†

The equivalent width in the fast band reaches a peak and begins to decline while the lightcurve is still rising, and has almost reached its minimum level by the time the lightcurve peaks. The *maximum level* of the equivalent widths

† It must be noted, however, that the line-width time plot is not the best way to compare the behaviour of the fast band and slow band equivalent widths, and can sometimes be quite misleading. For this reason, it has been used in this analysis only as a complement to the more useful line-width diagnostic plot which is described in Section 7.2.4.

reflects the dynamic state of the flare during its *rise phase*, and the *minimum level* reflects its dynamic state during the *decay phase*. This analysis is mainly concerned with the rise phase, and it is the maximum level that has been focussed on. The last four columns of Table 7.1 show the maximum value attained by the equivalent widths in each of velocity bands in each *BCS* Channel.

7.2.4 The line-width diagnostic plot

The line-width time plot showed how the equivalent widths in the fast and slow bands varied with time, and to a limited extent, showed how they are related to each other. The **line-width diagnostic plot** has been devised to give a true idea of their inter-relation. It consists of the fast band equivalent width plotted directly against the slow band equivalent width, as has been done in Figures 7.12 and 7.13 for the 14 October 1980 flare.

The line-width diagnostic plot does make it possible to determine a mean upflow velocity for the flare plasma, although this cannot be done without first adopting, *a priori*, distribution of upflow velocities. Section 7.3.3 explains at greater length how this is done.

7.2.5 The flare sample

All the flares that were observed by the *SMM-BCS* between 1980 and 1987 were considered. A complete list of these flares is given in the Appendix. The distribution of the flares across the Sun's disc, in even this, the most complete sample available, is not entirely uniform. Activity appears to be greater in the southern hemisphere, but this north-south asymmetry does not matter as much as it would have had there been a similar east-west asymmetry. What matters is that the data should cover the full range of possible flare loop orientations and positions.

The sample of 143 flares was whittled down to 40 flares after the rejection of those which had incomplete coverage or low count rates (and hence poor quality spectra). The subset of the flares which were selected is listed in Table 7.1, and their positions on the Sun's disc are indicated in Figure 7.16.

7.2.6 Orientation of loops.

Because this analysis is concerned with differentiating between fast directed motion and random motion, and because directed motion is expected to follow the direction of flare loop field lines, it is important to clarify the situation regarding the orientation of flare loops. It is not known for certain whether flare loops are always directed radially or whether they deviate from the normal to the Solar surface. If all flare loops are radially directed, those that lie on the limb would point at right angles to the observer and no directed motion would be visible. Random mass motion, however, would be seen irrespective of whether the flare were at the disc centre or on the limb. On the other hand, if flare loops could be tilted at any angle to the radial vector, upflows in flares on the limb would be seen with the same frequency as upflows in flares close to the disc centre.

Therefore, to make any sense of the observed variation of plasma upflow, one *has* to assume a preponderance of upright flare loops, and moderate this assumption by allowing some deviation of inclinations from the vertical position. Some information about the distribution of flare loop inclinations can be obtained from the large number of soft X-ray images of flaring loops that exist, but for a more quantitative answer, work along the lines of Berton and Sakurai (1985) is more useful. They tracked the progress of stable coronal loops which moved across the line of sight with the rotation of the Sun, and by using a stereoscopic method, deduced that the loops were inclined by up to 24 ° . This figure, approximated to 30 ° , is used later in this chapter as the upper limit of the deviation of flare loops from the normal.

7.2.7 Instrument details

The analysis described below has been applied to spectra from Channels 1 and 4 of the *BCS*. Channel 1 covered the spectral range 3.16 to 3.23 Å which includes the resonance line of the helium-like CaXIX ion and its satellites. Channel 4 covered the spectral range 1.84 to 1.90 Å and the resonance line of the helium-like FeXXV ion and its satellites. Channel 1 has a lower spectral resolution but is more sensitive and also responds to a lower temperature plasma, which is more plentiful: this Channel thus enjoys an altogether higher count rate and more trustworthy statistics. This is why this analysis rests more heavily on CaXIX spectra than it does on FeXXV spectra.

7.3 Results and Discussion

7.3.1 The physical meaning of the equivalent width.

The equivalent width is a measure of the distribution of velocities within a given velocity band. Its physical meaning is best understood by considering how it applies to the different cases of a symmetrically broadened line (which *has no upflows*) and an asymmetrically broadened line (which *does have upflows*).

An example of each of these two types of line profile is shown in the frames on the left hand side of Figure 7.9. The division between the fast and slow bands are marked on the profiles. In the frames to the right is illustrated the effect of dividing the count rate in the velocity bands by the height of the line profile. The counts which were distributed across the band as shown in the left hand side frames have been redistributed into a rectangle of the same height as the line peak. *The width of this rectangle is the equivalent width.*

Another way of understanding this redistribution is to consider the following: by adding up all the counts in a particular velocity band, a total count is obtained for that band. Also at hand is the number of counts in the central bin of the line profile. Dividing the first number (total counts in a given velocity band) by the second number (counts in the central bin) then becomes a way of finding out how many such central bins it takes to add up to the total count rate in that velocity band. Thus the number obtained is a *number of bins.*

For a line enclosing an area A_T (units of counts) and a height h (units of counts per bin), a total equivalent width W_{TOTAL} (units of bins) may be defined.

$$W_{TOTAL} = \frac{A_T}{h} \tag{7.1}$$

By dividing the line into two velocity bands, the total equivalent width splits into a pair of equivalent widths:

$$W_{TOTAL} = \frac{A_T}{h} = \frac{A_F + A_S}{h} = \frac{A_F}{h} + \frac{A_S}{h} = W_F + W_S \tag{7.2}$$

where A_F and A_S are the areas in the fast and slow bands respectively, and W_F and W_S are the corresponding equivalent widths. Using the knowledge that the counts in each band have contributions from both stationary and upflowing plasma, the equivalent widths can be further broken down into their stationary and upflowing components:

$$W_{TOTAL} = W_{F,up} + W_{F,st} + W_{S,up} + W_{S,st} \tag{7.3}$$

where the subscripts $_{up}$ and $_{st}$ denote "upflow" and "stationary" respectively.

If it were possible to measure the values of $W_{F,st}$ and $W_{S,st}$ in Equation 7.3, it is easy to see that the equivalent widths of both fast and slow upflows may be obtained.

To do this, what is required is a line profile in which $W_{F,up}$ and $W_{S,up}$ are known to be equal to zero. Such a line is of course a symmetrically broadened, Gaussian line profile. A symmetrical profile is one which would be produced by flare plasma with no upflows at all. Its width is entirely due to the random thermal motion of the ions and the random mass motion of the plasma.

A series of such profiles is shown in Figure 7.10. These profiles have been generated to match the resonance line profile in Channel 1 of the *BCS*. All the known instrumental effects in Channel 1 (the crystal rocking curve, uneven bin widths etc.,) are taken into account when generating these profiles [3]. Each profile has a different width, and on each is marked the fast band and the slow band. The equivalent widths in these two bands are plotted against each other in Figure 7.11. *This is the variation expected from flares with no upflows.*

The curve that has been plotted represents synthesized line profiles. Though it terminates at a point corresponding to $W_F + W_S \approx 8$, in real life, symmetrical resonance lines with total equivalent widths greater than about 7 bins are never seen [4]. Thus any data points which lie in the region to the right and above the point at which $W_F + W_S \approx 7$ *must* owe their position on the plot to the presence of upflows. The *vertical displacement* of points from the bottom edge of the region increases with *mean upflow velocity in the slow band.* The *horizontal displacement* of these points from the left hand edge of the region increases with mean *upflow velocity in the fast band.*

The following two sections describe how the line-width diagnostic diagram may be used to follow the time evolution of upflows, and how it may be used to derive a mean upflow velocity. The first of these uses is an extension of the essentially *qualitative* interpretation of the line-width diagnostic diagram that has already been described in this section. The second use, which is to obtain a single number to represent the strength of upflows (similar to the mean upflow velocity obtained via component-fitting methods), requires that a *distribution of upflow velocities* be assumed. Why this is so is explained in Section 7.3.2.

[3] These profiles were generated by the FORTRAN program SIMTWO, written by Dr. A. Fludra.

[4] 7 bins in *BCS*'s Channel 1 is equivalent to 2.1mÅ or 200km s^{-1}

7.3.2 Time evolution of upflows from line-width diagnostic plots.

Some examples of the line-width diagnostic plots of observed data are shown in Figures 7.12, and 7.13, and amongst Figures 7.31 to 7.49. The synthesized curve from Figure 7.11 has been plotted over the real data points from Channel 1 of the *BCS* to illustrate the extent to which upflows make the diagnostic plot deviate from the "no upflows" case.

In this way the presence of both slow upflows and fast upflows are determined without involving either the red wing of the line profile or the complicated and uncertain process of component fitting.

Because it was not possible to simulate the same symmetrical line profiles for Channel 4 as was done for Channel 1, it was not possible to generate a "no upflows" curve for Channel 4 for comparison against the observed data.

Line-width diagnostic plots can be used to follow the evolution of upflows in a flare. The line-width diagnostic plot for the flare of 14 October 1980 is shown in Figures 7.12 and 7.13. In following the line-width diagnostic plot, it must be remembered that displacement along the x-axis scales with magnitude of upflow velocity. To begin with, the upflows seen in Channel 1 (Ca XIX) are not very strong, but begin to pull away to the right of the plot (indicating faster upflows) at 0600 UT (data point no. 40). For the next $6\frac{1}{2}$ minutes the upflows switch on and off intermittently. The upflows then start to decrease, and the line-width diagnostic plot begins its decay phase evolution (point no. 65 onwards).

The line-width diagnostic plots for the 14 October 1980 flare (Figure 7.12 and 7.13) and the 5 May 1984 flare (Figure 7.40 and 7.41) show that after the upflows cease, the total line width does not decrease immmediately, but remains constant for quite a long period (for several minutes in the 14 October 1980 flare, and for about a minute in the 5 May 1984 flare). During this period of conservation of total line width, the fast band equivalent width is transferred to the slow band.

This example has demonstrated how the line-width diagnostic plot may be used to follow the evolution of the upflow velocity in a flare. Its main advantage lies in the fact that no assumptions are made about the distribution of upflow velocities, but, far from precluding the use of assumed distributions, it lends itself perfectly to the fitting of hypothesised distributions of upflow velocities to real data.

It is also an ideal way of comparing the predictions of hydrodynamic flare models with real data. All that has to be done is to apply the two-band division to synthesized spectra, measure the equivalent widths for the bands and plot the line-width diagnostic diagrams.

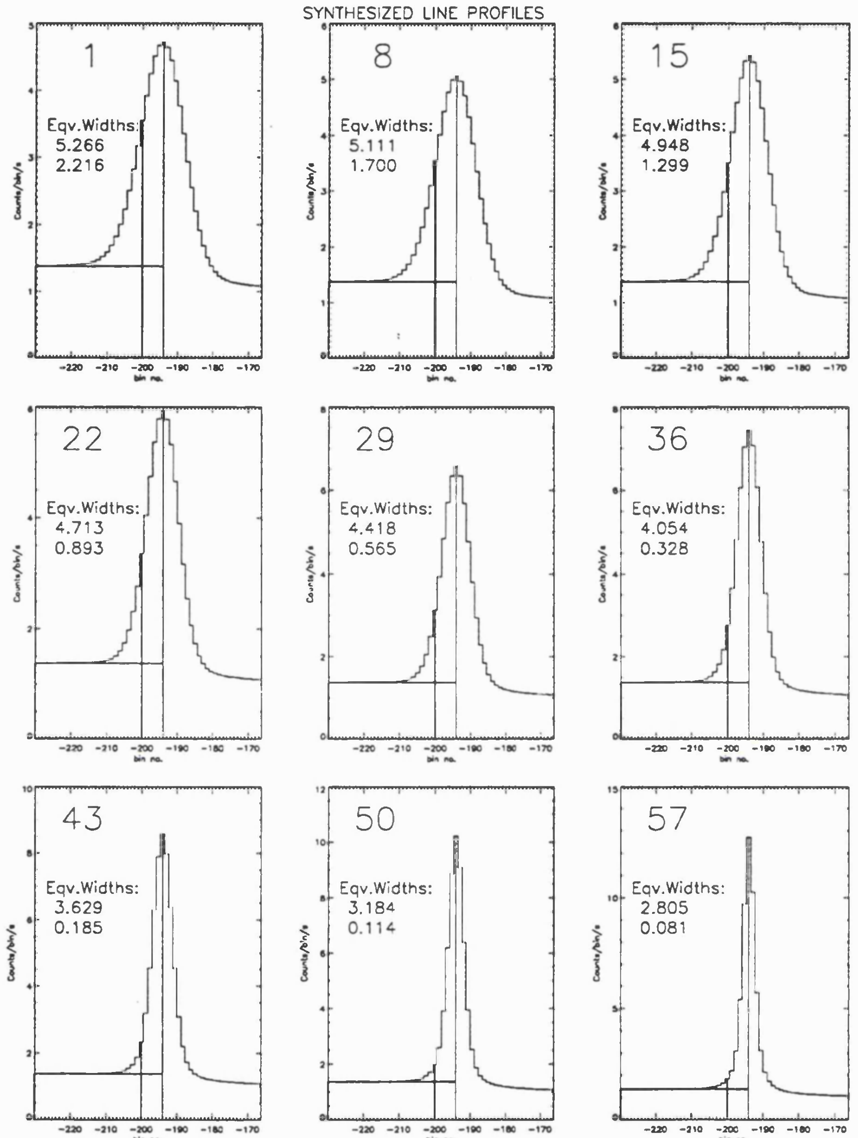

Figure 7.10: Synthesized line profile with no upflows.
These line profiles represent what would be seen by the BCS *when observing a flare with no upflows, and were generated by assuming that the intrinsic distribution would be a Gaussian and convolving it with the instrumental response (using a program written by Dr. A. Fludra). The integer numbers in the top left hand corner of each frame is an arbitrary unit of time starting at 1 (flare peak) and ending at 50. The pair of numbers below it are the equivalent widths in the slow and fast bands respectively. The vertical line running at the centre of each of the line profiles marks the line-peak rest position, and the shorter vertical line to its left marks the division between the slow and fast bands.*

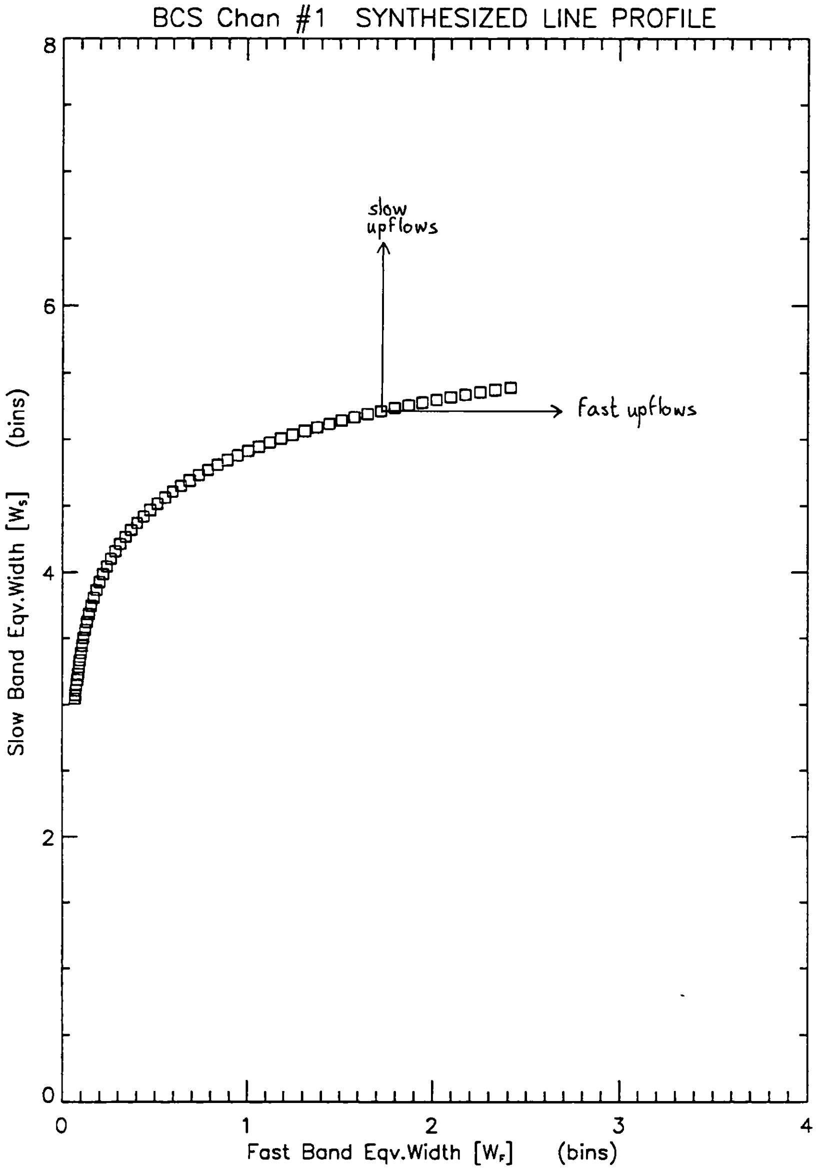

Figure 7.11: The equivalent widths for synthesized Ca XIX resonance lines.

The points plotted in this figure are derived from the synthesized line profiles shown in Figure 7.10. In real life, the maximum W_{TOTAL} *of symmetrical Ca XIX resonace lines is 7 bins. If the point at which* $W_F + W_S \approx 7$ *defines the bottom left hand corner of a region on the diagram, then: (i) the vertical displacement of points from the bottom edge of this region increases with slow band mean upflow velocity; (ii) the horizontal displacement of these points from the left hand edge of the region increases with mean fast band upflow velocity.*

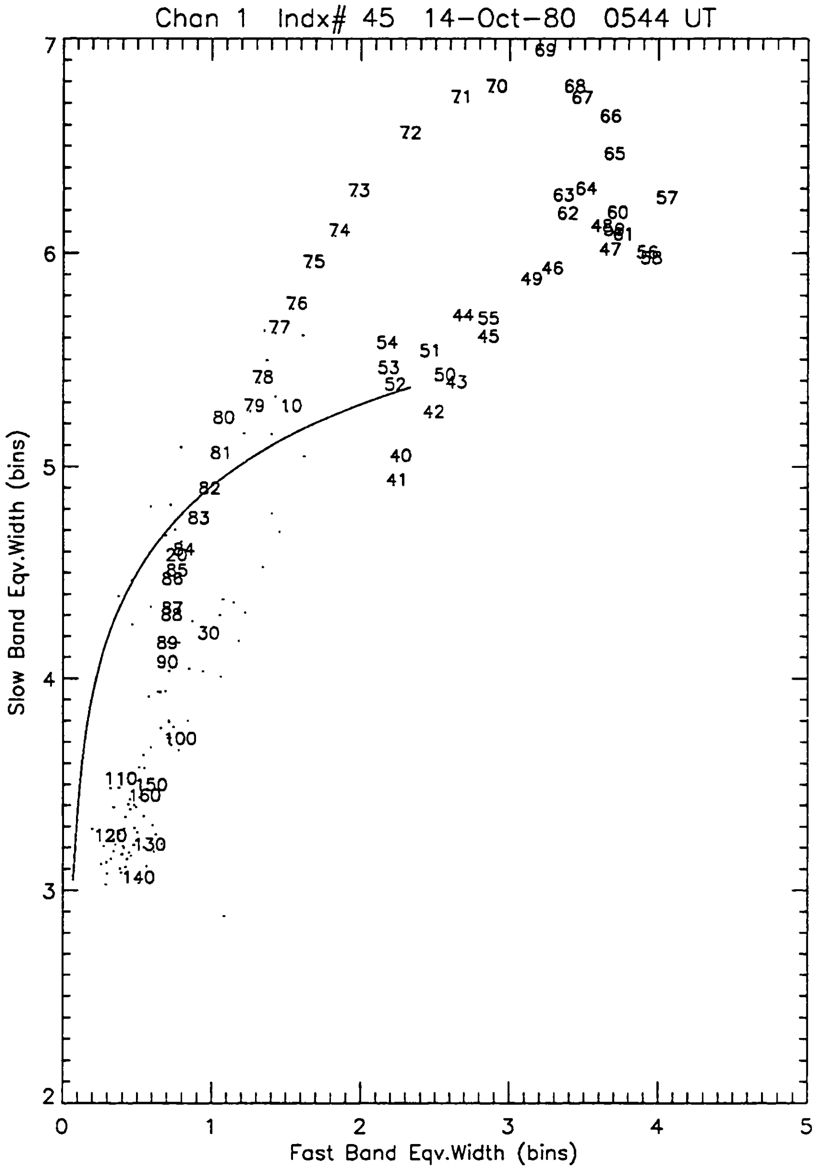

Figure 7.12: Line-width diagnostic plot - evolution of upflows in Channel 1
The line-width diagnostic plot can be used to monitor the evolution of upflows in a flare. The numbers indicate a time sequence: 40 - 0559UT, 50 - 0602UT, 60 - 0606UT, 70 - 0610UT, 80 - 0614UT, 90 - 0617UT, 100 - 0621UT, 110 - 0625UT, 120 - 0629UT, 130 - 0630UT, 140 - 0636UT, 150 - 0640UT, 160 - 0644 UT. Where the data points are crowded together, only selected points are numbered.

0

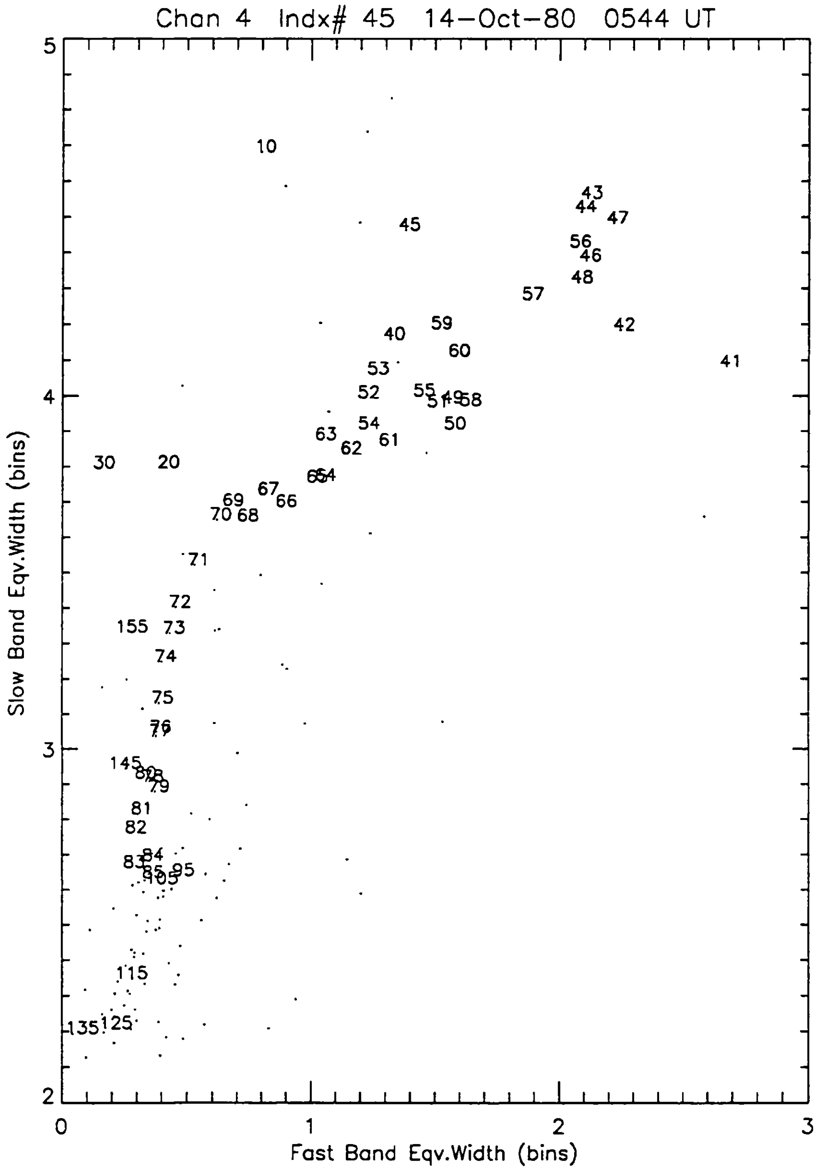

Figure 7.13: Line-width diagnostic plot - evolution of upflows in Channel 4

The line-width diagnostic plot can be used to monitor the evolution of upflows in a flare. The numbers indicate a time sequence: 40 - 0559UT, 50 - 0602UT, 60 - 0606UT, 70 - 0610UT, 80 - 0614UT, 90 - 0617UT, 100 - 0621UT, 110 - 0625UT, 120 - 0629UT, 130 - 0630UT, 140 - 0636UT, 150 - 0640UT, 160 - 0644 UT.

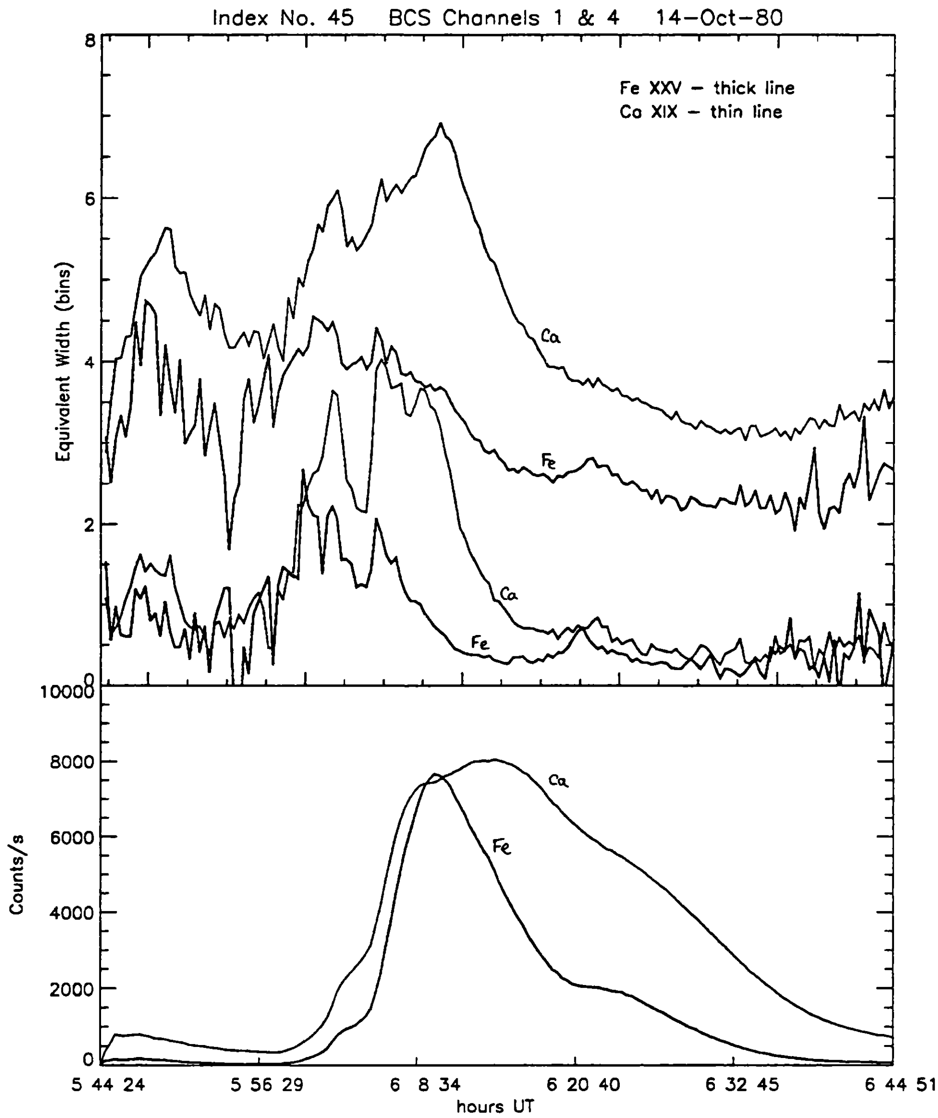

Figure 7.14: Line-width time plot - 14 October 1980
The evolution of upflows seen in the line-width diagnostic plot can be compared with the line-width time plot and with the flare lightcurve.

7.3.3 Derivation of an upflow velocity from the equivalent widths.

In Section 7.3.2 above, the time evolution of the upflows in a flare was described in *qualitative* terms. This section describes how a mean upflow velocity may be derived by using the line-width diagnostic diagram.

The synthesized "no upflows" curves plotted in Figures 7.12 and in 7.40 represent $W_{F,st}$ *vs.* $W_{S,st}$ (see Equation 7.3). The real data points, however, represent $(W_{F,st} + W_{S,st})$ *vs.* $(W_{F,up} + W_{S,up})$.

The essence of the problem is to find $W_{S,up}$ and $W_{F,up}$ by moving upwards and sideways respectively from the "no upflows" curve to meet the real data points. But in the absence of additional information there is no way of identifying the correct combination of $W_{S,up}$ and $W_{F,up}$ out of all the combinations that will connect any given real data point and the "no upflows" curve.

It becomes apparent that an assumption has to be made about the relationship between $W_{S,up}$ and $W_{F,up}$, for example that $W_{F,up} = 5\ W_{S,up}$. In other words a *distribution* of upflow velocities has to be assumed.

One particular distribution that may be assumed is that of a single Gaussian centered at some point in the blue wing of the resonance line. This special case is discussed in the next section.

7.3.4 Relation to component fitting methods.

The special case mentioned in the section above is in fact equivalent to the Gaussian component fitting methods used by other workers (see Section *7.2.1(a)*. Because of the currency of component fitting methods, their physical meaning is well understood. It is, therefore, worth explaining the correspondence between the equivalent width used in this analysis and the mean upflow velocities derived by component fitting methods. The velocity that other workers use to

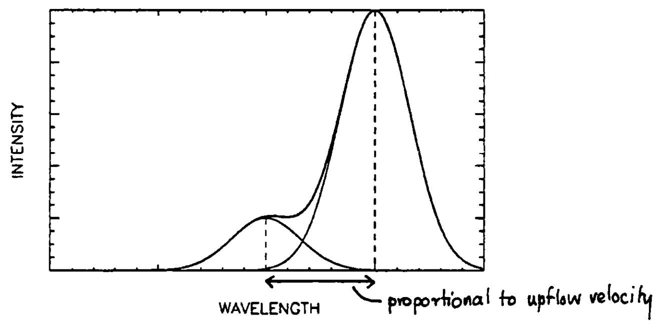

Figure 7.15: Mean upflow velocities correspond to the displacement of the "fast component" fitted to a line profile.

indicate the level of upflow activity in flares is the position of the peak of a "fast component" which is fitted to observed resonance line profiles in conjunction with a "stationary component". Figure 7.4 illustrates the fitting method used by these workers. Figure 7.15 shows how the upflow velocities quoted by other workers correspond to observed line profiles.

Component fitting methods yield a *single upflow velocity* on the assumption that the upflow line component has a Gaussian shape. Component-fitting methods, are however, not easy to use because of the number of free parameters involved in the fitting procedure. The Gaussian distribution itself has a variable width (spread of velocities) and a variable area (total counts), and the position of the entire distribution with respect to the line peak is a third variable.

Thus the problem lies in the mechanics of trying to achieve a good fit of synthesized line profiles to the observed line profiles. This problem may be sidestepped by using equivalent width analysis as an intermediary between the synthesized profiles and the observed profiles.

Equivalent widths may be derived from synthesized profiles and compared with the equivalent widths from observed data. It is relatively easy to manipulate synthesized profiles and produce equivalent width trends that roughly match the observed equivalent width trends derived from large samples of flare data . This combination of the component fitting method and equivalent width analysis is used in Section 7.3.5 to study the effect of flare position on observed plasma velocities.

Flare Index No.	Date	Time UT	Active Region No.	Coord-. inates	GOES class	Peak Equivalent Width (bins)			
						Slow Band		Fast Band	
						CaXIX	FeXXV	CaXIX	FeXXV
0	07 Apr 80	0108	2372	N10 E03	M4	6.4	5.3	2.8	1.8
2	08 Apr 80	0307	2372	N12 W13	M4	6.2	4.2	5.9	1.5
3	10 Apr 80	0922	2372	N12 W42	M4	6.8	4.4	3.6	2.0
5	30 Apr 80	2025	2396	S13 W90	M2.2	4.3	3.6	1.3	1.0
7	09 May 80	0715	2418	S21 W32	M7.2	5.0	3.9	2.7	1.6
8	21 May 80	2105	2456	S14 W15	X1.4	5.6	3.6	4.1	1.0
9	04 Jun 80	0911	2490	S13 E58	M4	5.0	3.3	-	-
10	13 Jun 80	2234	2502	N17 E11	-	6.0	-	2.7	-
11	21 Jun 80	0102	2528	S12 E17	M2	6.7	-	3.3	-
12	24 Jun 80	1524	2522	S29 W15	M1	5.3	5.1	2.8	-
13	25 Jun 80	1555	2522	S29 W28	M4.8	5.8	-	2.3	1.8
14	29 Jun 80	0238	2522	S27 W90	M3.6	5.1	3.3	1.0	0.8
15	29 Jun 80	1044	2522	S27 W90	M4.2	-	-	2.5	-
16	29 Jun 80	1826	2522	S20 W90	M4.2	5.1	3.5	1.5	1.1
17	01 Jul 80	1628	2544	S12 W38	X2.5	6.0	4.3	1.8	2.0
18	05 Jul 80	2245	2550	N28 W31	M8.9	5.2	4.7	1.6	1.5
21	12 Jul 80	1121	2562	S14 E56	M4.3	5.4	4.4	1.9	1.9
28	13 Jul 80	1434	2562	S10 E46	M2	5.5	-	1.1	-
30	13 Jul 80	1919	2562	S13 E50	C9.2	6.6	-	4.4	2.4
34	14 Jul 80	0827	2562	S13 E43	X1.1	5.5	3.9	1.6	1.1
39	23 Aug 80	2130	2629	N17 W52	-	5.9	4.4	3.9	0.5
40	24 Aug 80	1612	2629	N17 W52	-	6.2	-	3.2	-
45	14 Oct 80	1614	2725	S09 W07	X3.3	6.9	4.6	2.6	2.6
55	06 Nov 80	1728	2779	S09 E65	M4.2	5.8	4.6	2.2	1.4
60	07 Nov 80	1137	2779	S07 E56	M4	5.3	5.7	2.1	2.2
61	07 Nov 80	1535	2779	S07 E56	-	5.5	-	1.7	-
69	10 Nov 80	0812	2779	S12 E14	M1.4	6.7	-	6.4	-
83	18 Nov 80	1455	2779	S10 W90	-	6.0	5.7	4.6	4.4
88	26 Apr 84	0903	4474	S09 E34	M2.5	5.2	3.6	1.8	1.0
89	27 Apr 84	0540	4474	S10 E24	M2.3	5.6	-	2.6	-
96	02 May 84	1925	4474	S11 W58	M3.0	5.1	4.0	1.8	1.6
100	05 May 84	0107	4476	S11 W64	C4.7	5.3	-	2.4	-
101	05 May 84	1824	4474	S11 W90	M7.5	5.2	4.5	1.8	1.2
106	19 May 84	2155	4492	S10 E66	X4.1	9.6	4.5	9.3	1.4
107	20 May 84	0129	4492	S10 E64	M2.9	6.0	4.6	3.0	1.4
108	20 May 84	0301	4492	S13 E62	M4.6	4.8	3.5	1.5	1.9
110	20 May 84	0542	4492	S08 E57	M5.4	6.1	3.5	1.8	0.6
114	21 May 84	1747	4492	S06 E42	-	5.8	4.7	2.5	2.4
118	21 Jan 85	0353	4617	S10 W28	M2.2	6.2	5.2	3.3	1.9
120	23 Jan 85	0733	4617	S09 W35	M2.4	5.6	-	4.0	-

Table 7.1: Peak Equivalent Widths

This table is a subset of the complete flare sample listed in the Appendix.

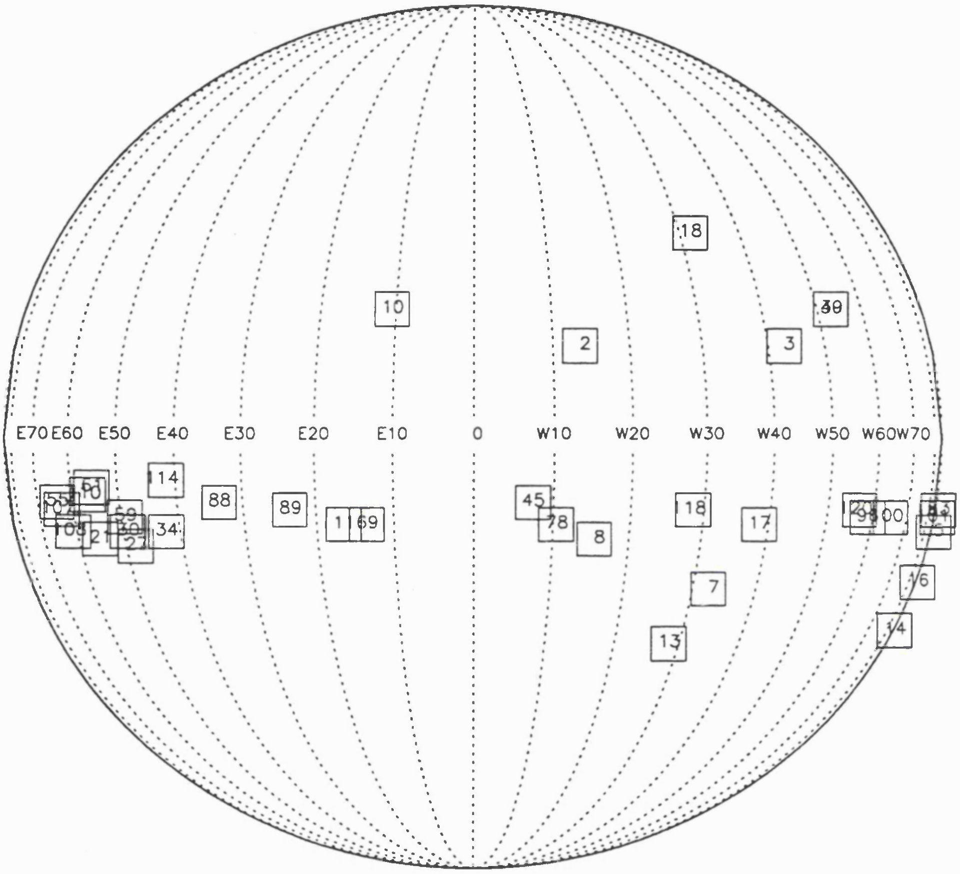

Figure 7.16: Positions of flares on the Sun's disc.
The positions of the flares listed in Table 7.1 are marked in this diagram. The numbers in the boxes correspond to the flare index number given in the first column of the table in the Appendix , of which Table 7.1 is a subset.

7.3.5 Variation of equivalent width with flare position.

The variation of the fast band equivalent width with flare position can be used to confirm that what is being measured in the fast band is indeed related to plasma upflows.

If flares possess radially directed upflows, the observed magnitude of the upflows would be expected to decrease with displacement from the centre of the Sun's disc, as the angle between the upflows and the line of sight increases.

The two graphs in Figures 7.21 and 7.27, show the variation of fast band equivalent width with displacement from the centre of the Sun's disc, for Channel 1 (Ca XIX) and Channel 4 (Fe XXV).

In contrast to the behaviour of the fast band equivalent width, the slow band equivalent width is expected to exhibit *no* dependence on the directionality of flare loops, because what is seen is the cumulative effect of randomly directed motion averaged over 10 to 20 seconds. The two graphs in 7.24 and 7.28, show how the maximum slow band equivalent width varies with displacement from the disc centre.

The trends exhibited by these graphs are discussed below, in Sections 7.3.5 (b), (c) and (d)

7.3.5 (a) Calculation of the projection effect.

The expected variation of a given unprojected upflow will follow the expression

$$V_{upflow,projected} = V_{upflow} cos(\alpha + d\alpha) cos(\theta + d\theta) \tag{7.4}$$

where α and θ are the longitude and latitude respectively and $d\alpha$ and $d\theta$ are the deviations from the normal to the Sun's surface.

The work of Berton and Sakurai (1985), though based on a study of *stable* coronal loops, does provide some idea of the range of loop inclinations that could exist. Using their results, it can be assumed that flare loops have a maximum inclination to the normal of 30° .

In order to demonstrate the effect that flare position has on the observed equivalent widths, it is necessary to assume some distribution of upflow velocities.

7.3.5 (b) A single fast upflow component

This is the obvious distribution to use, as it is commonly used in component-fitting methods. It consists of a dominant, un-shifted Gaussian stationary component and a single subsidiary, blueshifted Gaussian upflow component (similar to the distribution shown in Figure 7.15). This distribution has been simulated by combining a single Gaussian-shaped upflowing line component with the usual Gaussian shaped stationary line component, and the equivalent widths of the combined line profile measured while the value of the viewing angle is varied.

The effect of varying the viewing angle is to slide the upflowing component towards the centre of the stationary line component, as shown in the sequence of frames in Figure 7.20. On the limb, with the flare pointing at right angles to the line of sight, the upflowing component will be exactly superimposed on the stationary component.

The predicted variation has been plotted in Figures 7.22 and 7.25, alongside the observed data instead of being plotted over them. The reason for maintaining this distinction is that the synthesized variation has only been used to qualitatively establish that the fast band emission is from upflowing plasma. There are too many variables (mean velocity, intensity ratio and loop tilt angle) for each synthesized curve to permit a unique curve to be assigned to any given data point.

One obvious way of constraining the solutions would be to require that the right combination of upflow velocity, intensity ratio and loop tilt should reproduce both the fast band equivalent width *and* the slow band equivalent width for each flare.

In other words, for any given data point on Figure 7.21, the right combination of variables should produce a Figure 7.22-type curve that passes through it, *and* a Figure 7.25-type curve that passes through its companion data point on Figure 7.24.

7.3.5 (c) Fast and slow upflow components

The problem with the combination of the single fast upflow and a stationary component is that it does not reproduce the dependence of the slow band equivalent width on flare position. In fact, the effect of a single upflow component in a limb flare is to *increase* the slow band equivalent width, which is exactly the opposite of what is observed.

It is clear that a single fast upflow is not an adequate explanation of the result obtained in the slow band. It would seem that upflows with velocities of less than 200 km s^{-1} are required. This possibility was investigated by combining a stationary component, a fast upflow component and a number of slow upflow components, to produce the simulated profiles shown in Figure 7.29.

7.3.5(d) Channel 1: fast band

In confirmation of the assumption that this band of the blue wing mainly contains emission from upflowing plasma, the variation of the fast band equivalent width exhibits a drop-off towards the solar limb. The pattern of this decrease mimics that exhibited in Figure 7.22 by the synthesized line profiles with Gaussian upflow components (examples of which are shown in Figure 7.20).

Each synthesized curve, however, represents a particular combination of upflow velocity, intensity ratio to the stationary component, and loop tilt angle, and it is not possible to fix on a unique combination of values for these three variables to match any given data point.

This is why the synthesized curves have not been plotted over the observed data points in the customary fashion, but have instead been plotted alongside, to point out qualitative similarities without misleadingly establishing a direct correspondence.

7.3.5(e) Channel 1: slow band

In confirmation of the assumption that this band of the blue wing contains emission from mainly stationary plasma, the variation of the slow band equivalent width with flare position is very much less than that in the fast band. However, the plot in Figure 7.24, measured from the cooler plasma (CaXIX spectra), does show a decrease with distance from the disc centre, which contradicts the trend seen in the synthesized profiles in Figure 7.25.

The curves in Figure 7.26, which represent combinations of a single fast upflow component with several slow upflow components and a stationary component, are clearly much closer to the observed trends than the single upflow case.

In addition, the fast band equivalent width variation for the multiple upflows model follows the observed trend slightly more closely than does the single upflow model.

Either of these two differences on their own would not have been sufficient to sway the argument in favour of the multiple-upflow model: *what does it is the fact that the multiple upflow model simultaneously satisfies the fast band equivalent width variation and the slow band equivalent width variation.*

7.3.5(f) Channel 4: fast and slow bands

In both Channel 4 graphs (Figures 7.27 and 7.28), there are fewer flares represented than there are in the corresponding Channel 1 graphs (Figure 7.21 and 7.24), because the weaker emission in Channel 4 makes for a lower level of data quality than in Channel 1, forcing the exclusion of several flares. Fortunately, the Channel 4 data points are only more sparse, and remain as evenly distributed as in Channel 1, allowing conclusions to be drawn with just as much confidence.

The drop-off of fast band equivalent widths which was seen in Channel 1 (Figure 7.21) is also seen in Channel 4 (Figure 7.27), although the range of equivalent widths for the same group of flares is smaller (varying from 2.6 bins to 0.5 bins) than that in Channel 1 (varying from 4.1 bins to 1.0 bins).

The ratio between these ranges (= 2.1/3.1 = 0.68) is about the same as the ratio between the km per second binwidth[5] of Channels 4 and 1 (=0.64). Thus if the Channel 4 drop-off were multiplied by this ratio, it would be found that both Channels show the same equivalent width drop-off with flare longitude.

7.3.6 Temperature dependent differences

The Ca XIX resonance line (Channel 1) is mainly due to plasma with a mean temperature of about12 MK, while the Fe XXV resonance line is mainly due to plasma with a mean temperature of about17MK. Provided that the instrumental differences between these two channels are taken into account, a comparison of the data from Channel 1 with that from Channel 4 should give some indication of how the dynamical behaviour of the plasma depends on its temperature.

The frequency distribution plots in Figure 7.19 show the distribution of maximum equivalent widths achieved in the rise phase. The Channel 4 equivalent widths have been scaled up by a factor 1.6, which is the ratio of the km per second binwidth in Channel 1 to that in Channel 4.

The distribution of maximum fast band equivalent widths (shown in the upper half of Figure 7.19 is almost identical in both Channels. This means that plasma at around17 MK is not any more dynamically active than plasma which is 5 MK cooler.

The distribution of maximum slow band equivalent widths (shown in the lower half of Figure 7.19 is slightly more peaked for Channel 1 data. Both Channels have the same lower limit of 4 - 5 bins, but about a third of the flares have slow band equivalent widths greater than 7 bins. This means that in a third of the flares in this sample, hotter plasma is more turbulent, or that it dominates the slow upflows (if there are any).

7.3.7 Summary of line-width diagnostic plot behaviour.

Line profiles similar to the ones shown in Figure 7.20 were synthesized by combining symmetrically broadened Gaussian profiles with Gaussian upflow compo-

[5] km per second binwidth : dispersion measure expressed as a Doppler velocity gives 45 km s^{-1} for BCS Channel 4 and 28 km s^{-1} for Channel 1.

nents, and their line-width diagnostic diagrams plotted. By relating the known (simulated) plasma dynamics to the corresponding line-width diagnostic plots, it is possible to establish some rules for the interpretation of line-width diagnostic plots.

1. **A smooth curve coinciding with the "no upflows" curve:**
   indicates that the flare truly has no upflows.

2. **A smooth curve shifted above the "no upflows" curve:**
   this is caused by the resonance line peak shifting to the short wavelength side (blue wing) of the rest position, which usually results from relative movement between the spacecraft axis and the flare (the upper curve in Figure 7.17).

3. **A smooth curve shifted below the "no upflows" curve:**
   this is caused by the resonance line peak shifting to the short wavelength side (red wing) of the rest position, which could be due to a dominant upflow in the rise phase (the lower curve in Figure 7.17).

4. **Data points displaced far to the right of the main body of points:**
   this is caused by shortlived and fairly narrow upflow velocity distributions, i.e.,: upflowing surges of plasma.

5. **Data points clustered close to the "no upflows" curve with no discernible trend:**
   this is the effect of combining projected upflows with the symmetrically broadened component from stationary plasma, and is expected only in limb flares.

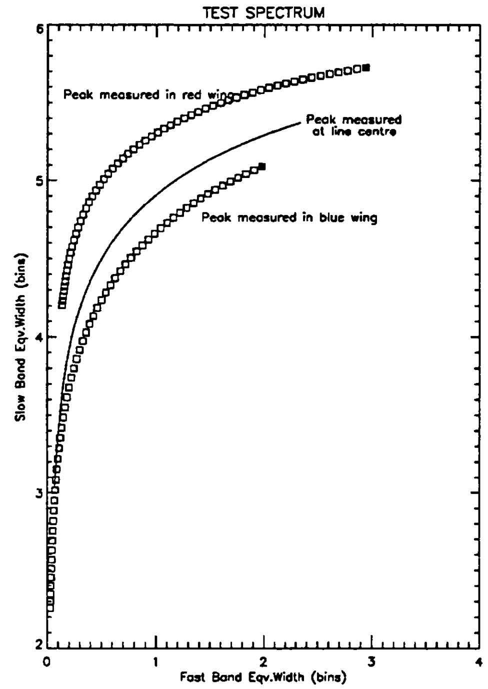

Figure 7.17: Line-width diagnostic plot: the effect of shifting the line peak relative to the rest line position
If the line peak intensity is measured at any point other than the true peak position, the line-width diagnostic curve will be shifted accordingly. This can be caused by (a) a true wavelength shift of the line centre, (b) relative movement of the flare position and the BCS *instrument axis which causes the line position to slide along the detector to a new position.*

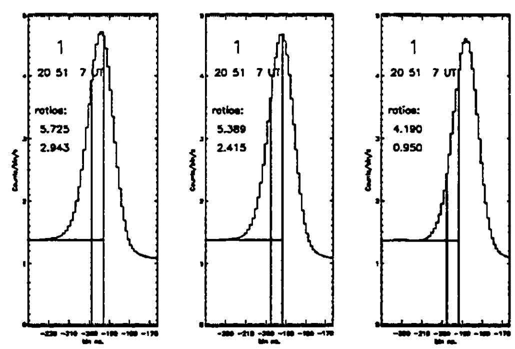

Figure 7.18: Shifting the line peak relative to the rest line position
The three profiles shown above show how the relative positions of the true line peak and the point at which the peak is measured affect the shapes of the line-width diagnostic curves shown in Figure 7.17.

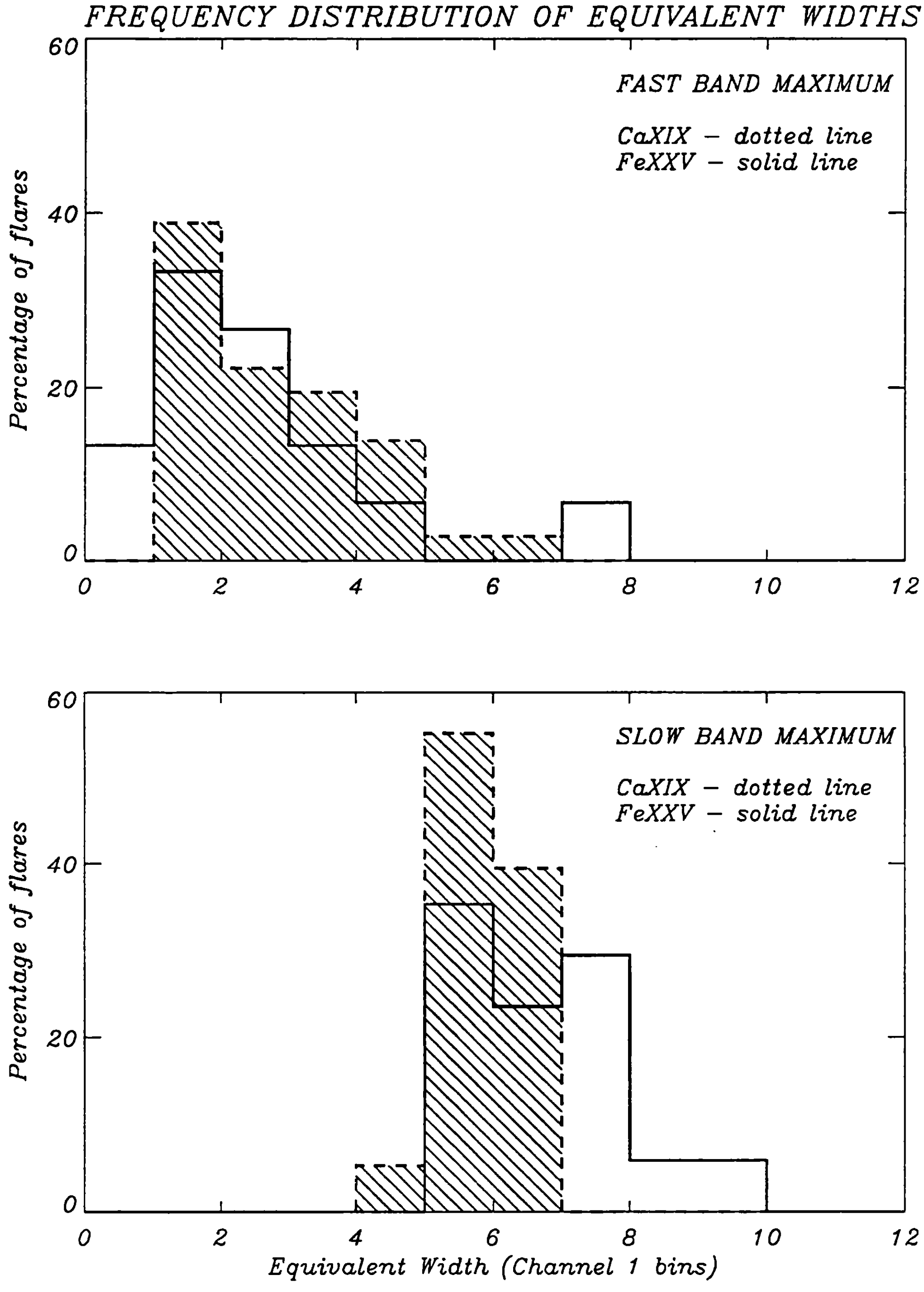

Figure 7.19: Temperature dependent differences.
Because Channels 1 and 4 of the BCS *are sensitive to plasmas of different temperatures, a comparison of the data from these two channels should show up any temperature dependent differences.*

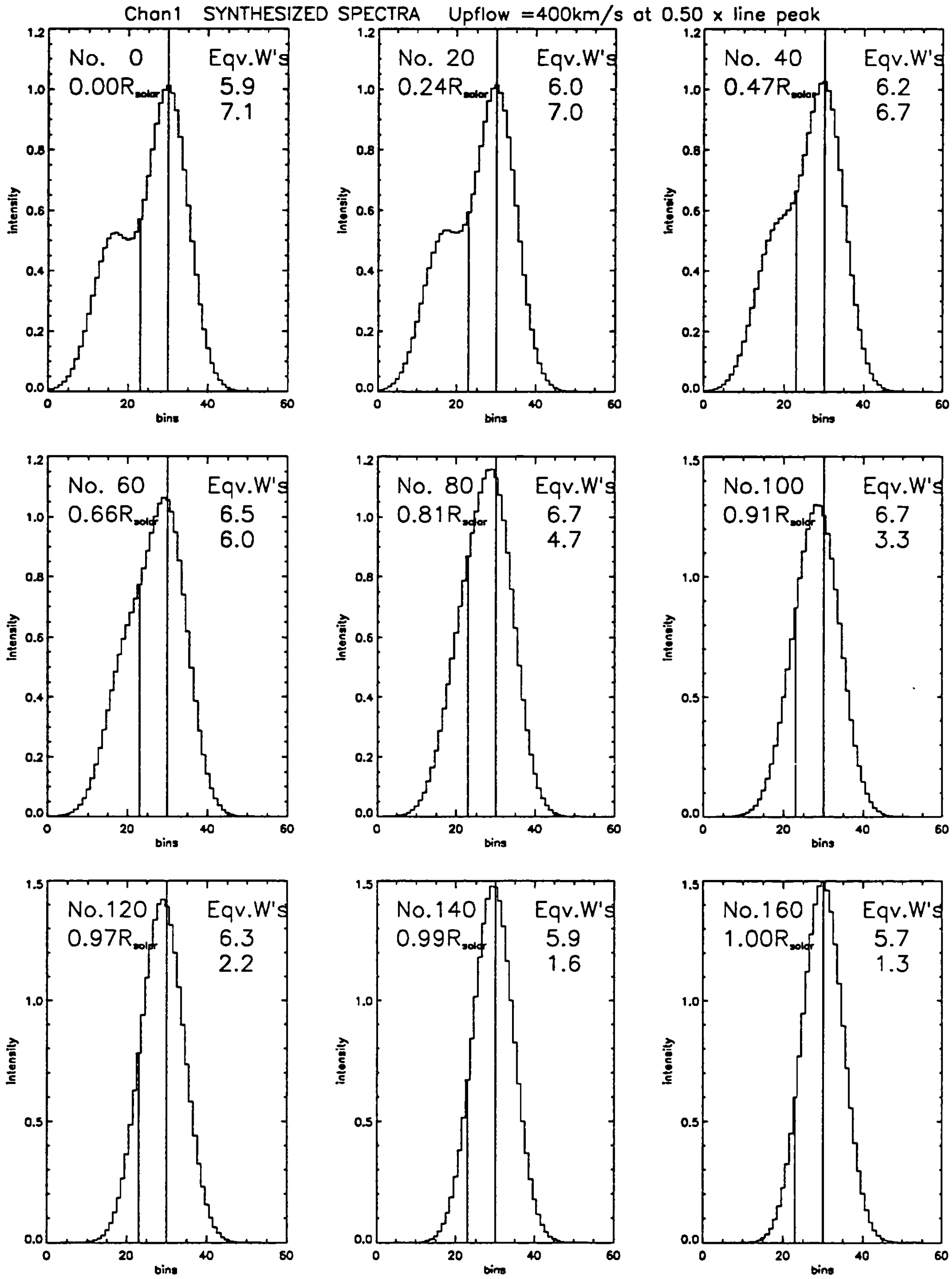

Figure 7.20: . Synthesized line profiles showing the effect of flare position on a Gaussian upflow component.
In this 180 frame simulation, a Gaussian line profile has been combined with a Gaussian upflow component of the same width and half the total intensity, the position of which varies as cos(longitude) cos(latitutude). The displacement of the flare from the disc centre is given as a fraction of the solar radius (R_{solar}), in the top left hand corner of each frame, below the frame number. The equivalent widths are given in the top right hand corner.

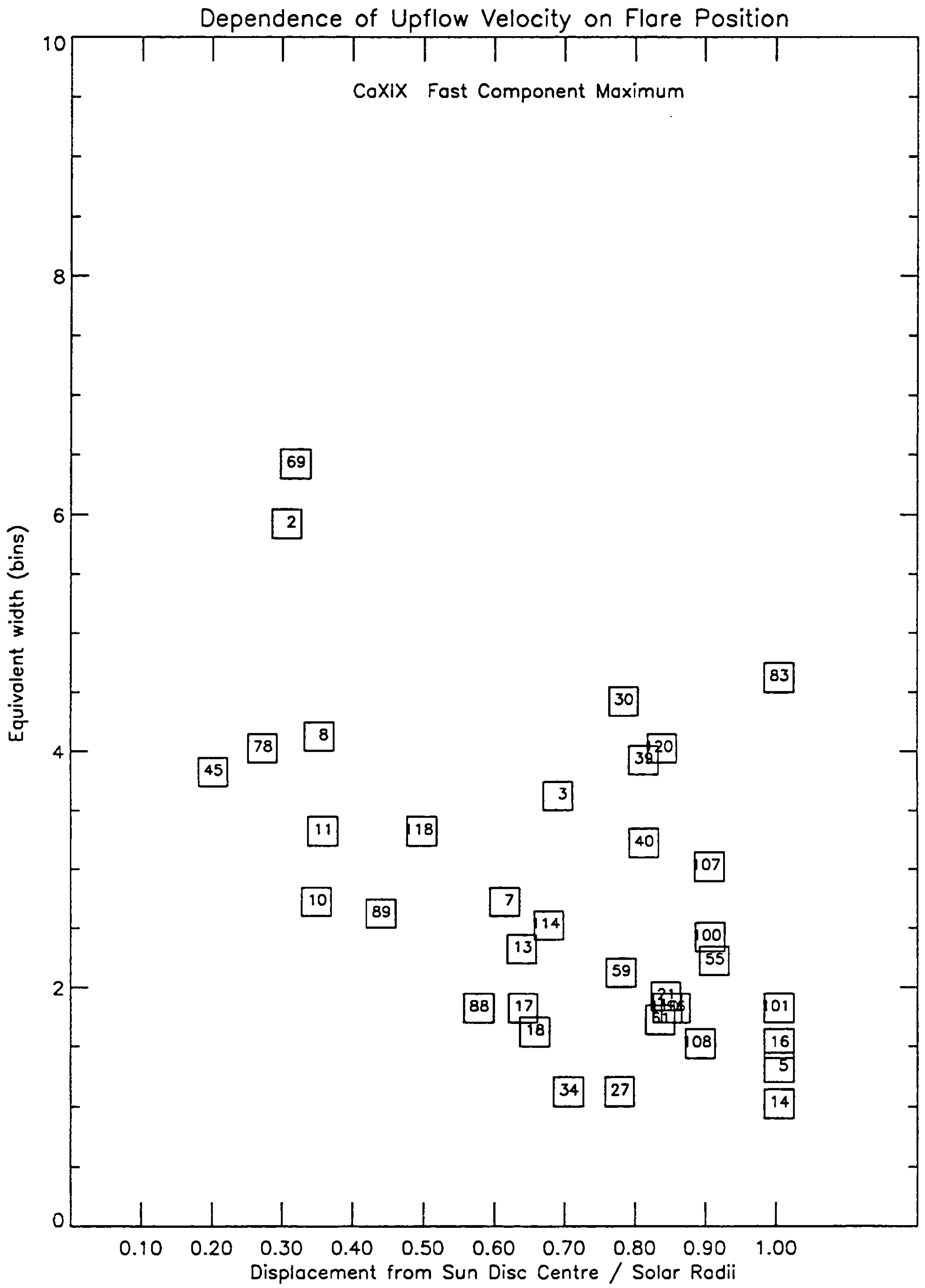

Figure 7.21: Variation of the equivalent width in the "fast band" with position on the Sun's disc as measured in the cooler component of the plasma seen by the *BCS*

There is a clear drop-off of the fast band equivalent width with position on the Sun's disc, which is matched quite well by the drop-off of the equivalent widths of synthesized line profiles (with upflows), shown in Figure 7.22 and 7.23.

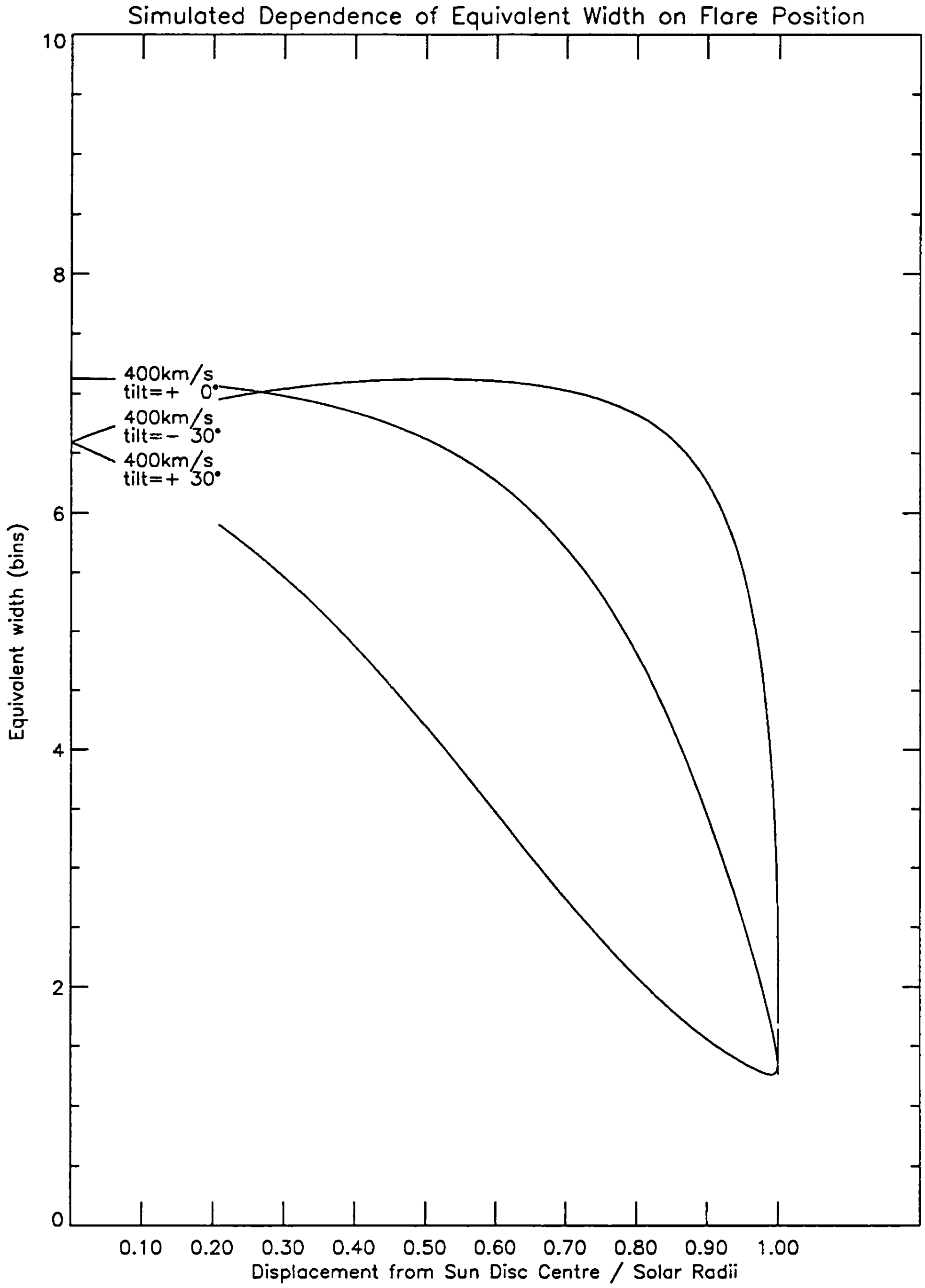

Figure 7.22: Simulated variation of the fast band equivalent width with position on the Sun's disc, as measured in Channel 1 of the *BCS*. *This is the expected fast band equivalent width variation for a a mainly stationary plasma combined with a single velocity upflow. (the velocity is marked on each curve, along with the loop tilt angle).*

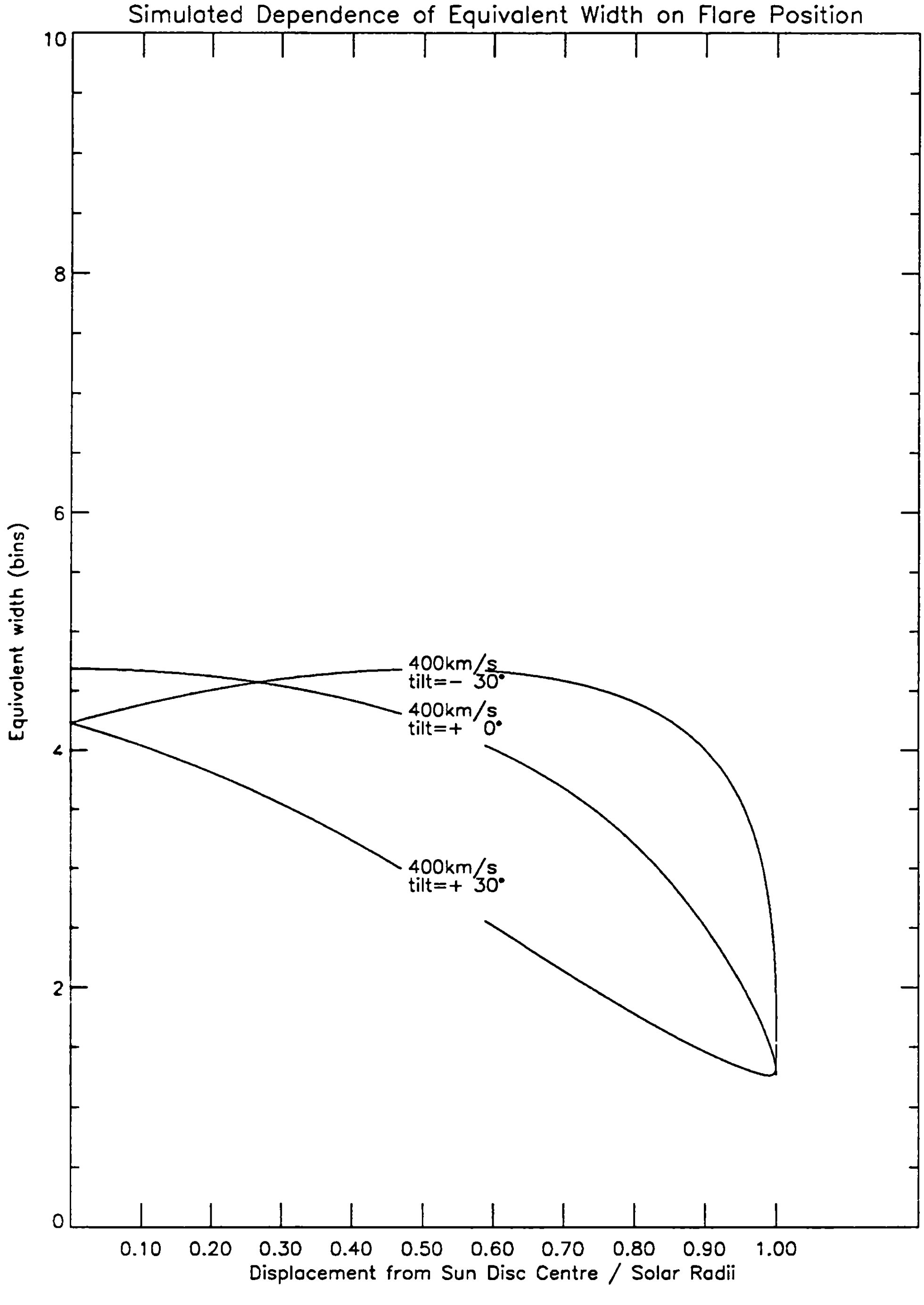

Figure 7.23: Simulated variation of the fast band equivalent width with position on the Sun's disc as measured in Channel 1 of the *BCS*. *This is the expected fast band equivalent width variation for a combination of a single fast upflow velocity component (the velocity of which is marked on each curve) and a number of slow upflow components.*

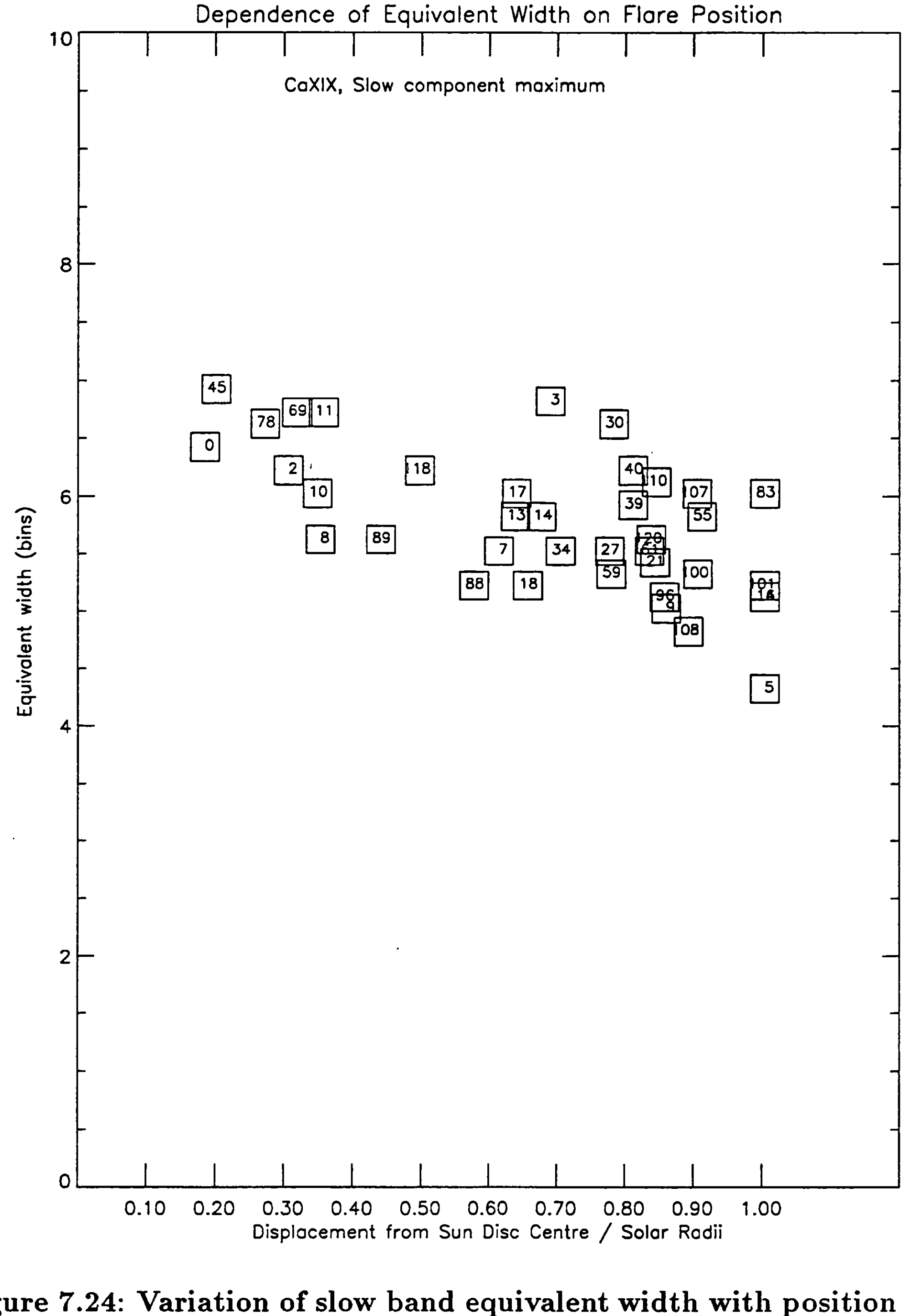

Figure 7.24: Variation of slow band equivalent width with position on the Sun's disc as measured in Channel 1 of the *BCS*.
In contrast with the fast band equivalent width, the slow band equivalent widths plotted here show a more uniform distribution across the Sun's disc. The data does show a slight drop-off towards the limb, which is in excess of that predicted for a single Gaussian upflow component, and which can only be due to a distribution of slow upflow velocities.

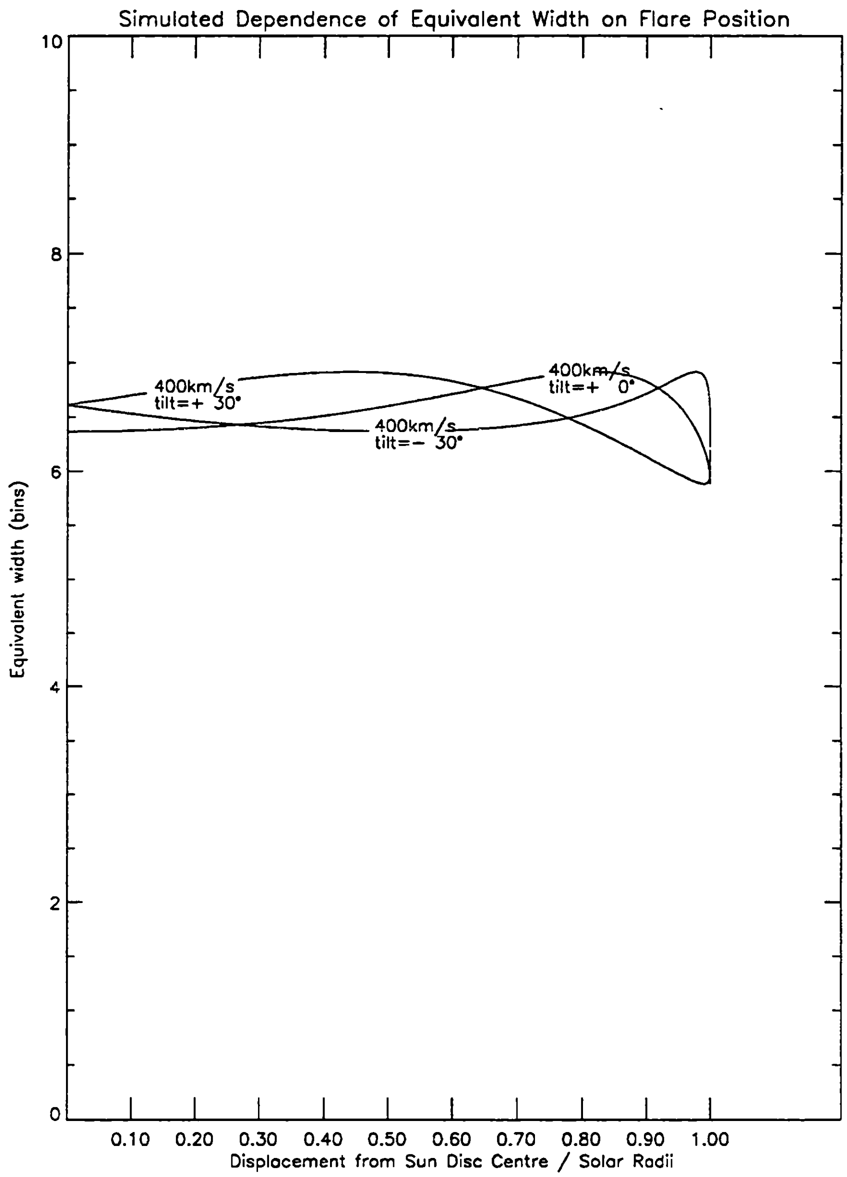

Figure 7.25: Simulated variation of slow band equivalent width with position on the Sun's disc as measured in Channel 1 of the *BCS*.
This is the expected slow band equivalent width variation for a stationary plasma combined with a single velocity upflow (the velocity of which is marked on the curve, along with the loop tilt angle).

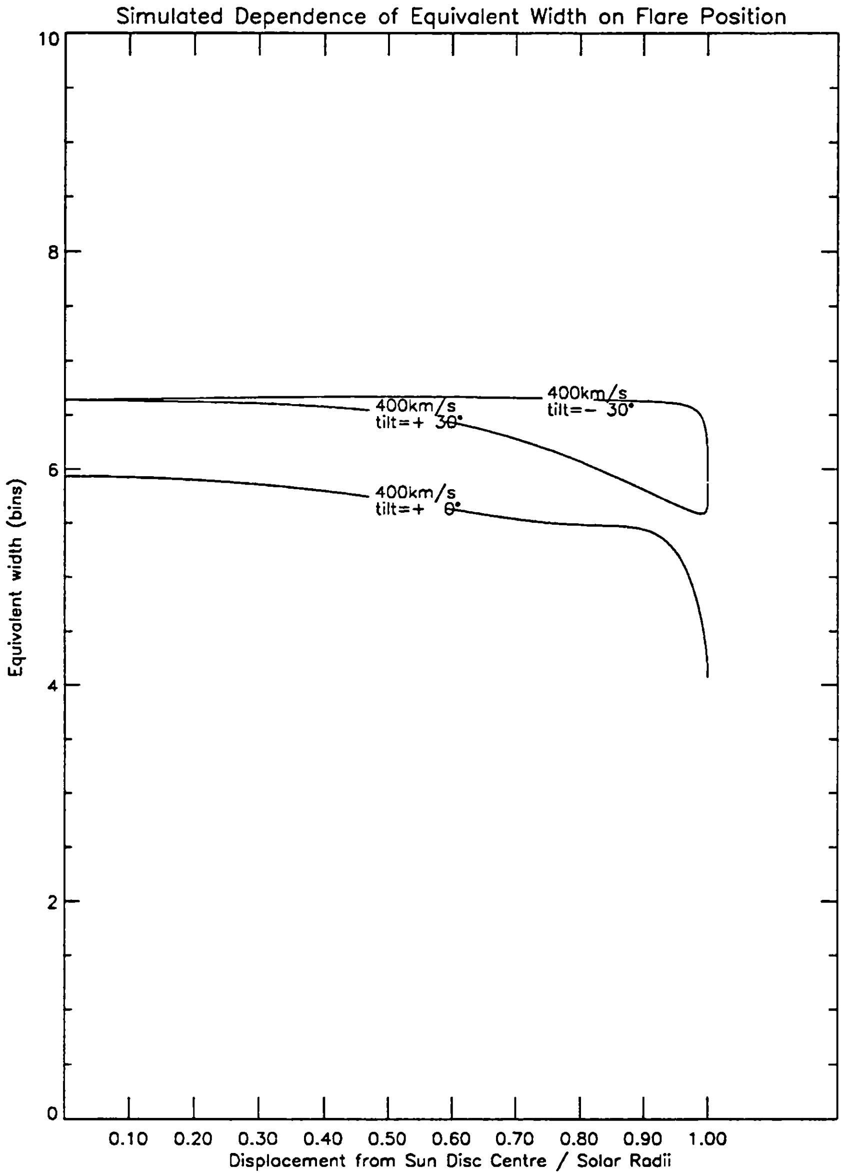

Figure 7.26: Dependence of the simulated slow band equivalent width with flare position, as seen in Channel 1.
This is the expected slow band equivalent width variation for a combination of a single fast Gaussian upflow component combined with a distribution of slow upflows.

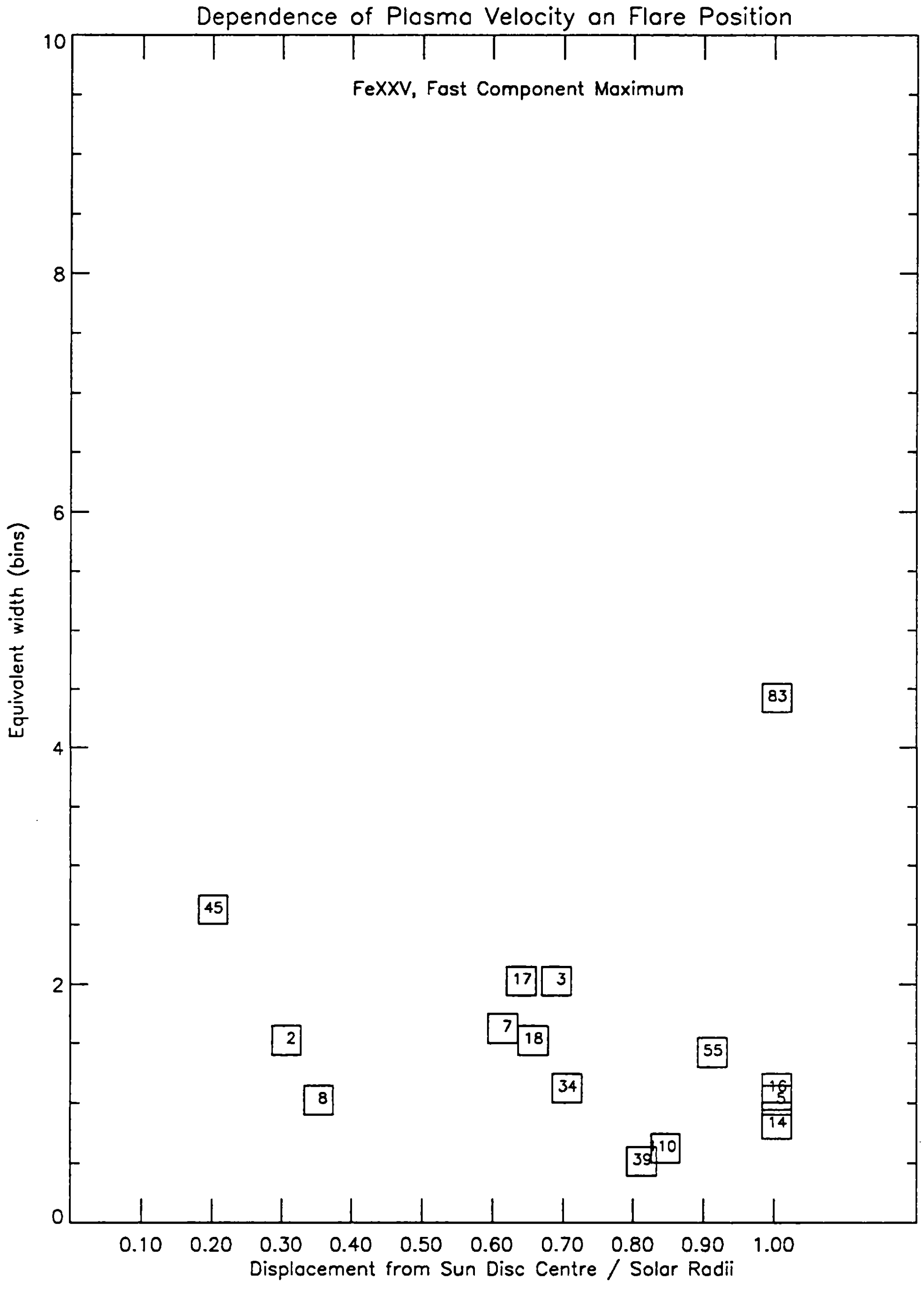

Figure 7.27: Variation of equivalent width in the "fast band" with position on the Sun's disc, as measured in Channel 4 of the *BCS*. *Because of the lower count rate in this channel, the number of flares represented in this plot is smaller than for CaXIX.*

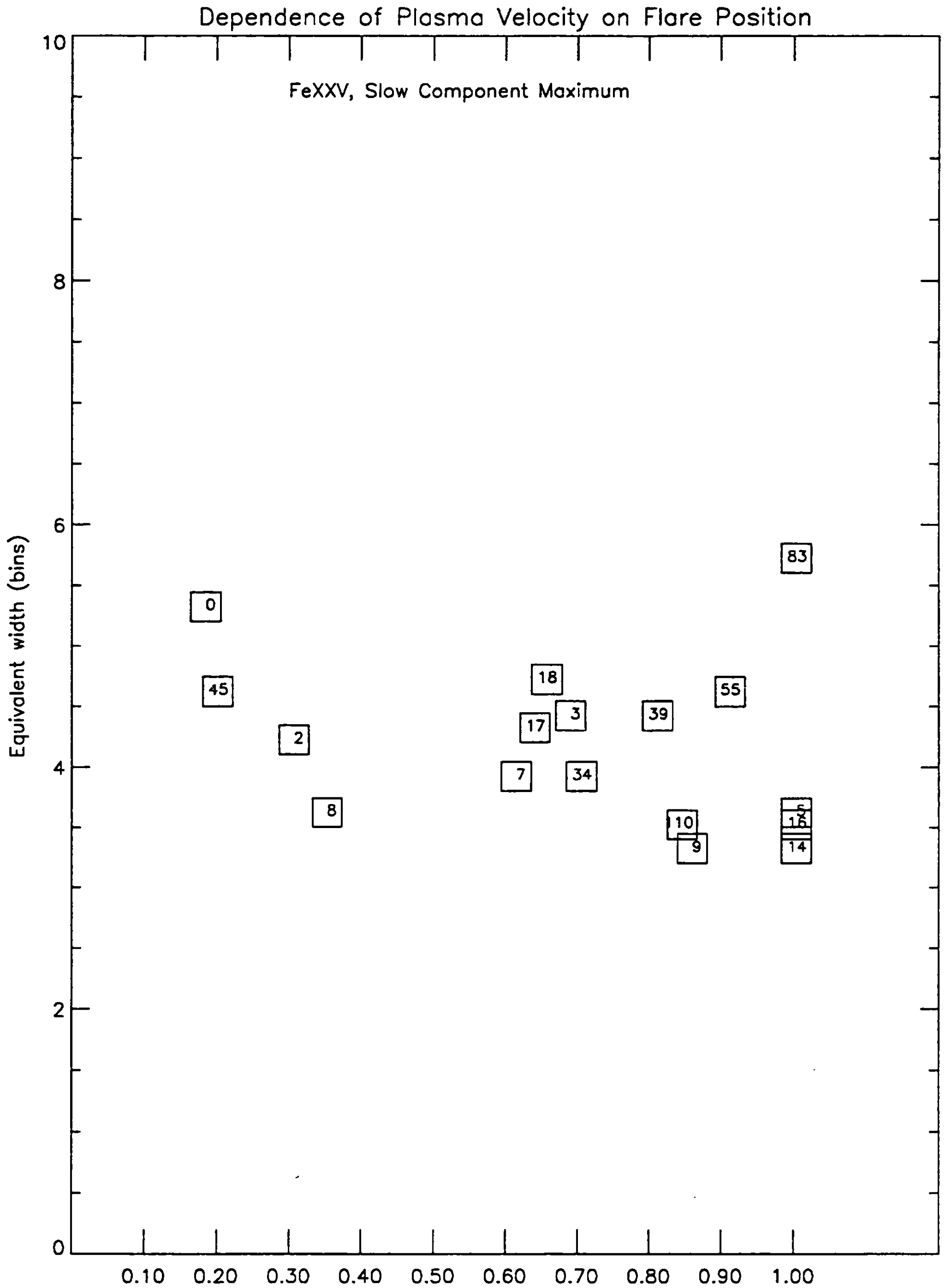

Figure 7.28: Variation of equivalent width in the "slow band" with position on the Sun's disc, as measured in Channel 4 of the ***BCS.*** *Because of the lower count rate in this channel, the number of flares represented in this plot is smaller than for CaXIX.*

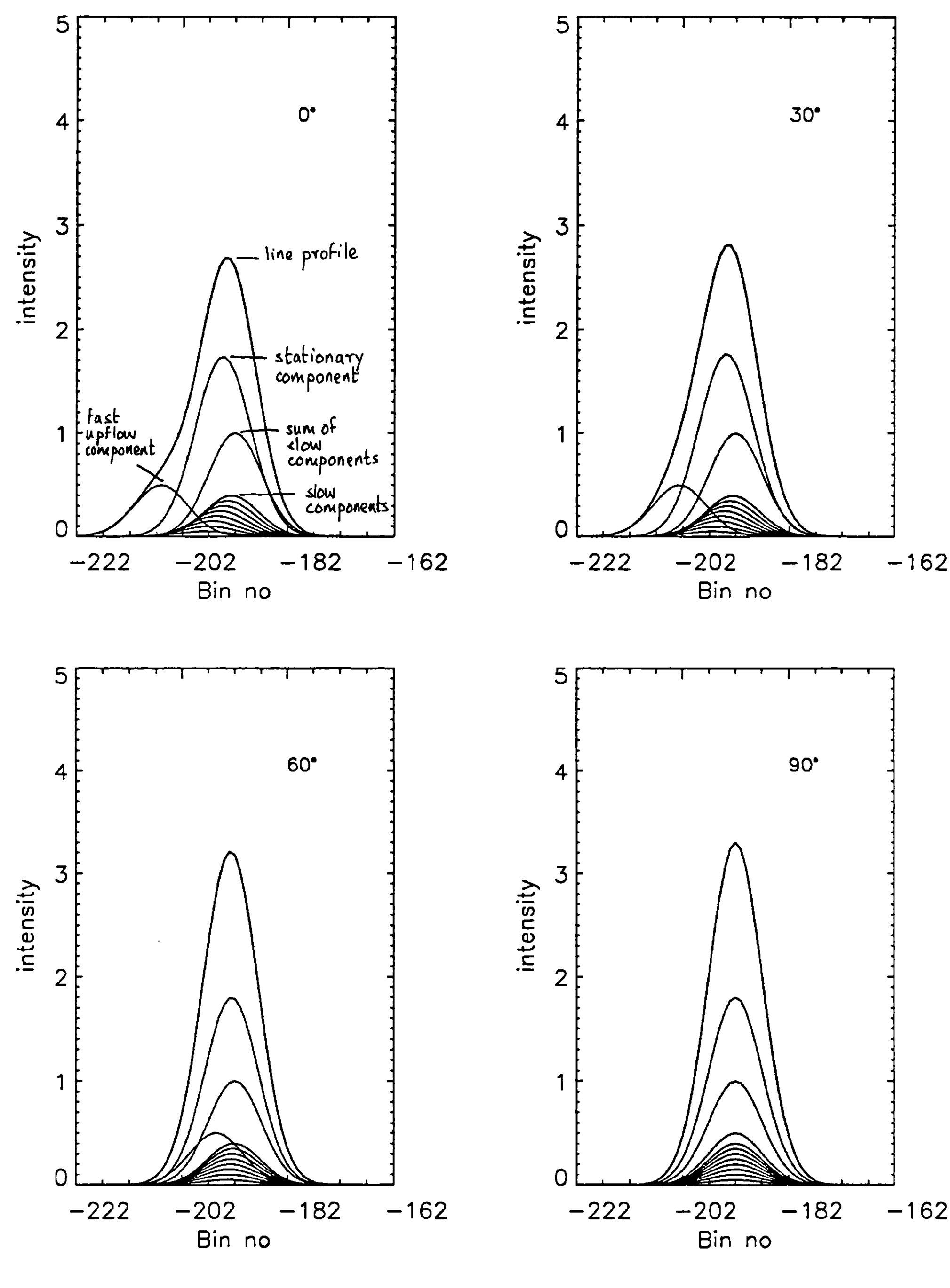

Figure 7.29: Simulated resonance line profiles composed of a stationary component, a fast upflow component and a distribution of slow upflows.
The frames in this figure show how the line profile varies with position on the Sun's disc (the flare longitude is given in the top right hand corner of each frame). The line-width diagnostic plot in Figure 7.23 was derived from such simulations.

7.3.8 Equivalent width behaviour in the flare sample.

In this section individual line-width diagnostic plots are discussed. It is expected that most flares will fall into one of four categories based on position on the Sun's disc and mean upflow velocity. They are:

(I) Disc flares with no upflows

(II) Disc flares with upflows

(III) Limb flares with no upflows

(IV) Limb flares with upflows

Type I : the 0820 UT flare on 14 July 1980

(Figure 7.30- 7.32)
It would be thought that if upflows are radially directed, it would not be possible to know whether a limb flare had upflows or not. The answer lies in the difference between the equivalent width behaviour of flares with upflows and those without upflows. Flares with no upflows follow the synthesized curve quite precisely, and this is true no matter what orientation the flare has to the line-of-sight. There will be no difference between the line-width diagnostic plots of a disc flare with no upflows and a limb flare with no upflows. (This is because they have contributions only from $W_{F,st}$ and $W_{S,st}$, which are not affected by viewing angle.)

Type II : the 0330 UT flare on 8 April 1980

(Figure 7.33- 7.35)
In the case of a disc flare with upflows, the effect of the upflows on the line-width diagnostic diagram is very marked. Fast upflows pull the data points horizontally to the right of the "no upflow" curve, and slow upflows pull the points vertically upwards. This flare exhibits very strong upflows which pulls the data points far into the right hand corner of the line-width diagnostic plot.

Type III-IV : the 1810 UT flare on 5 May 1984

(Figure 7.39- 7.41)
This flare occurs on the very edge of the limb, and the decay phase data points follow the "no upflows" curve quite closely. During the rise phase, however, there appears to be signs of weak upflows which cause the data points to be pulled slightly to the right of the "no upflows" curve. This also means that the flare loop would have been inclined towards the observer.

Type IV : the 0230 UT flare on 29 June 1980

(Figure 7.48- 7.49)
On the limb, however, upflows will not be seen, and the counts that would have fallen in the fast band for a disc flare now fall into the slow band. This increases the slow band equivalent width, causing the data points on the line-width diagnostic diagram to move vertically up from the "no upflows curve".

(This is because these flares have contributions from $W_{F,st}$ and $W_{S,st}$, as well as from $W_{F,up}$ and $W_{S,up}$. The former pair of equivalent widths are not affected by viewing angle, while the latter pair are, because they are measures of directed motion.)

This is exactly what is seen in the line-width diagnostic plots in Figures 7.31 and 7.48

The data shows that there is a difference between the line-width diagnostic plots of limb flares with upflows present, and those in which they are not.

7.3.9 Transfer of energy from upflows to stationary plasma

Some of the line-width diagnostic plots (eg:Figure 7.12) show that while the fast band equivalent width decreases, the slow band equivalent width increases so as to conserve the total equivalent width. This relationship exists for a few minutes after the fast band equivalent width reaches its peak, and it could indicate that a conversion of energy is taking place from fast upflows to non-thermal mass motion or turbulence.

A mechanism for the conversion of energy from directed flows into turbulence has been suggested by Bornmann (1987). In this paper the author tries to show that turbulence is itself an intermediary in the conversion of the kinetic energy of directed flows into thermal energy to heat flares. She invokes a *continuum* of eddies of different scales, which are driven by upflows at the largest scales, and which have their kinetic energy converted to thermal energy at the smallest scales. It is this continuum of eddies which is seen as turbulence. The continuous cascade of energy from eddies of one scale to eddies of the next smallest scale means that as soon as the driver (the upflows) is removed the turbulence begins to decay, and disappears altogether.

It is known that there is turbulence in quiet coronal loops and in flare loops both before and after the flare event, and that flare turbulence is seen as an enhancement of existing turbulence. It then becomes clear that in the line-width time plots, the stable minimum level reached by the slow band equivalent widths corresponds to the quiet turbulence level and that all values above this level must be either linked to the upflows or are due to post-rise-phase heating that is over and above the quiescent loop/active region heating.

7.3.10 Consequences for the flare models.

The most important result to emerge from this analysis is the fact that slow upflows are required to explain the behaviour of rise phase line profiles. Whatever mechanisms are proposed in rise phase models to explain fast upflows must be capable of explaining the slow upflows as well. In this section, the flare models introduced in Section 7.1 are revisited, to see how some of the predicted features stand up to being compared with observations.

7.3.10(a) Electron beam models

The basic flaw of the electron beam models is that in trying to satisfy the constraints imposed by hard X-ray emission, they fail to explain the observed soft X-ray emission patterns . Electron beam models predict extreme blueshifts in the rise phase, and in fact cannot account for the dominant stationary component. The identification of slowly moving upflows would mitigate this failing to some extent, if it were possible to show that electron heating could cause slow upflows as well as fast upflows. †

7.3.10(b) Thermal conduction models.

Thermal conduction models do not try to explain the higher energy emissions, but are more tailored to the soft X-ray component of the energy of flares. Antonucci *et al.*,. (1987) simulated two variations of this model, one in which the thermal heating was sited in the loop top, and the other with the heating sited in the footpoints. The predicted decay of upflow velocity and turbulent velocity for the loop-top heated model more closely resemble the fast band equivalent width measured here than does the decay predicted by the loop-footpoint heated model.

7.3.10(c) Alternative models.

The quasi-static electric field model proposed by Winglee *et al.*, (1991a,b) is found to have the most satisfactory relationship to observations to date, of any of the models proposed. In this model, the acceleration of ions across an electric field causes upflows, while short-scale transverse acceleration causes random mass-motion. This model allows for the existence of a dominant stationary

† Electron beam models are not ruled out entirely. However, the time resolution and sensitivity of *SMM-BCS* does set a limit on the duration and strength of the electron beam energisation.

component and would allow for the existence of slow upflows (which have been identified here) alongside fast upflows.

7.4 Summary

This analysis has shown how a very simple method of line-width measurement can be used to identify trends in the dynamic behaviour of flares. This simple method consists of estimating the amount of emission in two velocity bands, representing upflowing plasma and turbulent plasma respectively. These quantities are normalised to obtain an *equivalent width* for each velocity band. The relation between the equivalent widths in each band is found to be a quite sensitive measure of the dynamic state of the plasma.

The equivalent width analysis can be extended to a certain extent by simulating models of velocity distributions and subjecting them to the equivalent width analysis. The most likely velocity distributions can then be picked out by comparing the equivalent width behaviour of the simulated data with that of the observed data.

The main points that emerge from this this analysis are:

(1) The observed magnitude of upflow velocities depends on the flare position on the disk. This confirms that flare loops are mostly radially oriented, with possible deviations from the vertical of 30° .

(2) The equivalent widths in the slower velocity band have a dependence on flare position which, if it has to be explained in terms of a distribution of upflow velocities, can only be due to a continuous distribution of upflow velocities (probably a Maxwellian velocity distribution) with a mean velocity quite close to the rest position of the resonance line. This means that a substantial amount of the blue wing excess line broadening is due to slow upflows.

(3) A comparison of the equivalent width behaviour in the two *BCS* Channels shows that there is little difference between them. As this result is based on a sample of 40 flares which occurred over a period of 4 years, it can be taken to be fairly reliable. The physical significance of this is that the two *BCS* Channels are sensitive to plasmas of different temperatures, and the fact that they show no difference in dynamical behaviour means that plasma at these two temperatures behave in a similar way. That is to say, upflows are not dominated by plasma at the higher temperature, nor do they have a greater amount of cooler plasma, and the same may be said of the stationary plasma.

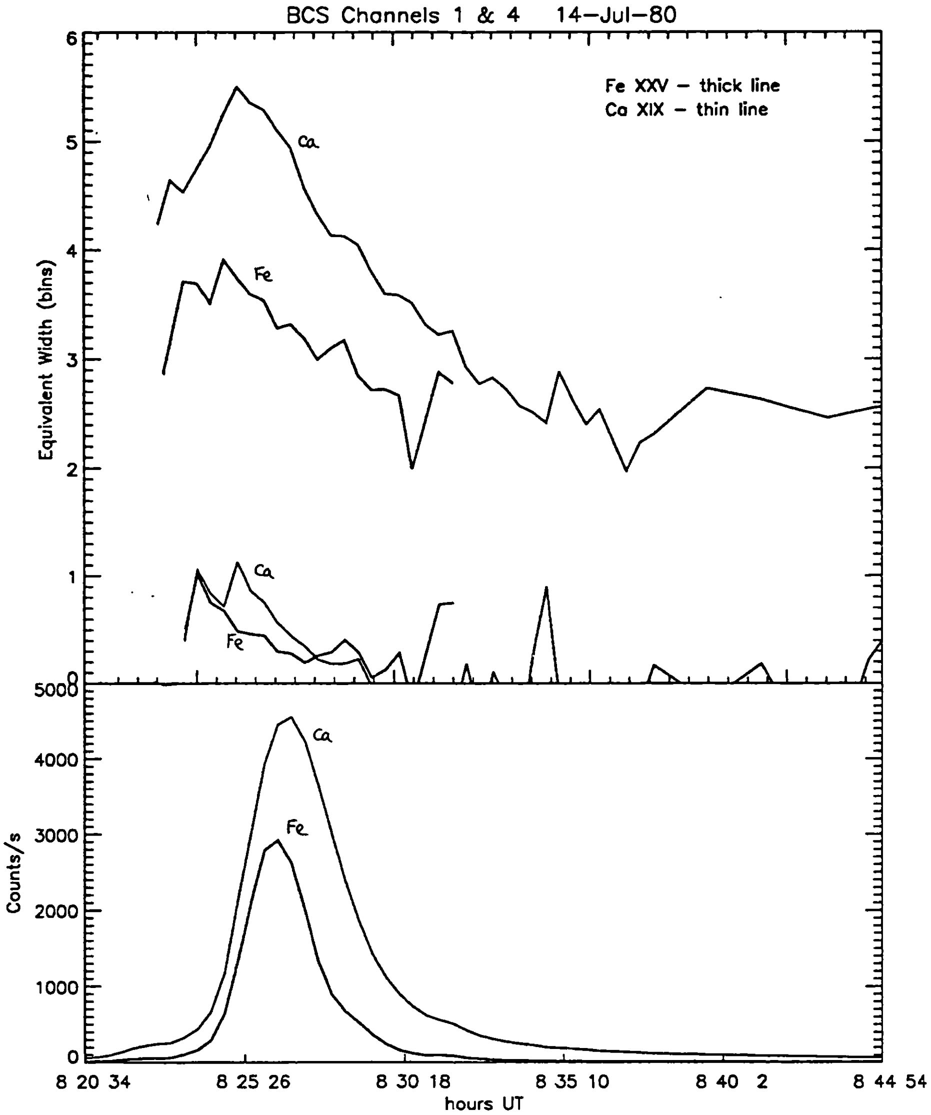

Figure 7.30: The line-width time plot for a disc flare with no upflows: the 0820 UT flare on 14 July 1980.
The variation of the equivalent widths for this flare are exactly as expected for a symmetrically broadened line. It is believed not to have any upflows whatsoever.

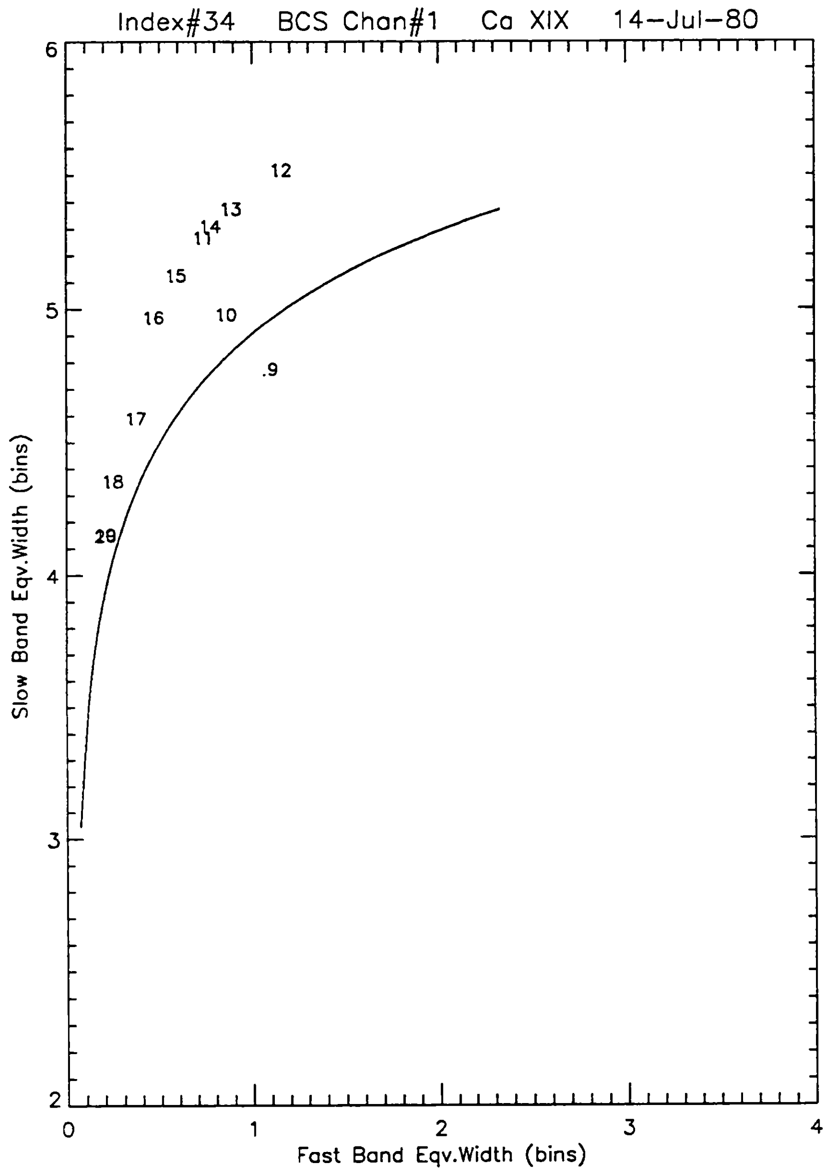

Figure 7.31: The line-width diagnostic plot for a disc flare with no upflows: the 0820 UT flare on 14 July 1980 as seen in *BCS* Channel 1.
The upward shift of the real data points from the "no upflows" curve is caused by the blueshift of the entire line profile during the rise phase of the flare. This behaviour has been illustrated in Figures 7.17 and 7.18. However, the line profiles for the 14 July 1980 flare are too symmetrical to allow the possibility of upflows. Therefore the shift of the line towards the red end of the spectrum later during the flare must be due to a drift of the spectrum (caused by the instrument pointing changing, or by misbehaving detector electronics).
The "no-upflows" curve, on the other hand, is measured from a synthesized Gaussian line profile. The height of this profile is always measured at the true line peak, and the resulting equivalent width plot (the "no-upflows" curve) does not suffer from the spurious vertical shift that the real data suffers from. This is why there is a mismatch between the "no-upflows" curve and the real data curve, even though this flare is known not have any upflows.

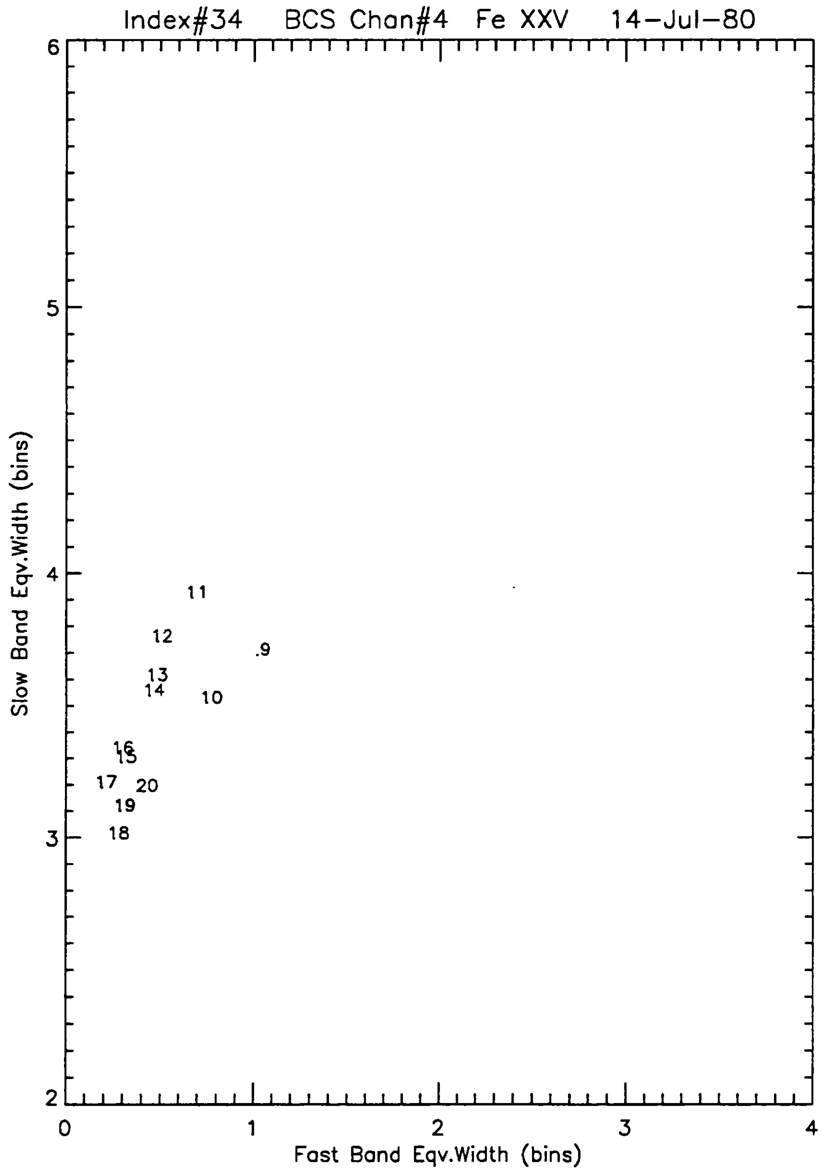

Figure 7.32: The line-width diagnostic plot for a disc flare with no upflows: the 0820 UT flare on 14 July 1980 as seen in *BCS* Channel 4.

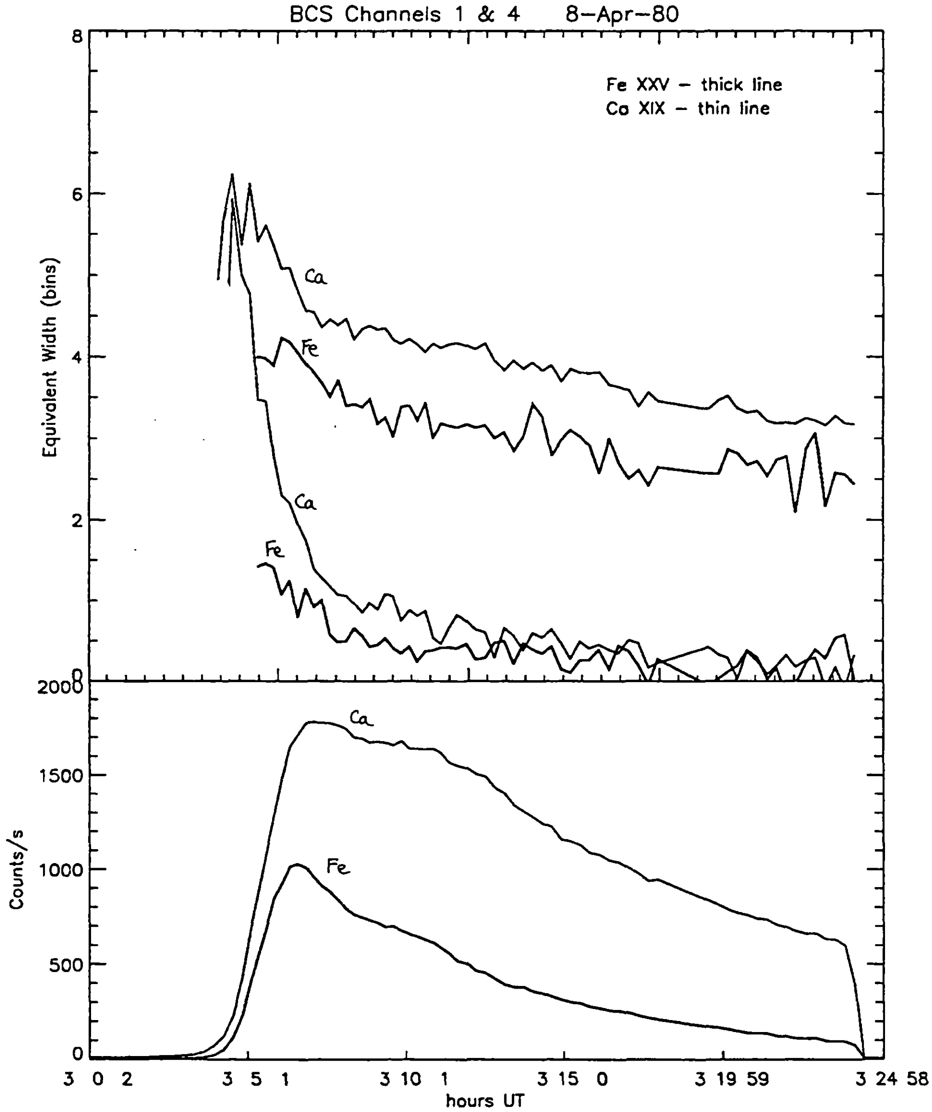

Figure 7.33: The line-width time plot for a disc flare with upflows: the 0300 UT flare on 8 April 1980.
The slow plasma emission decays more slowly than the emission from the fast plasma. This divergence is probably related to the energy input that persists after the rise phase, as is apparent from the bumpy lightcurve.

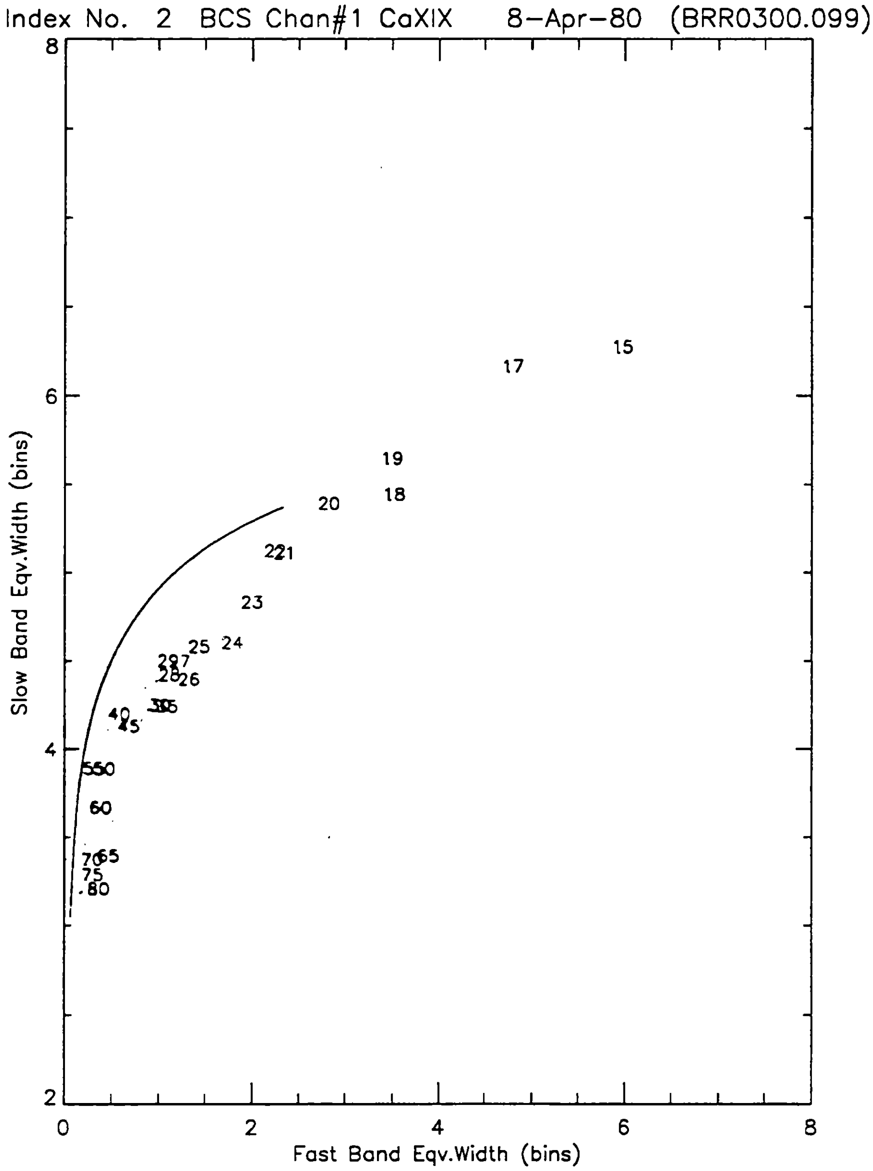

Figure 7.34: The line-width diagnostic plot for a disc flare with upflows: the 0300 UT flare on 8 April 1980.

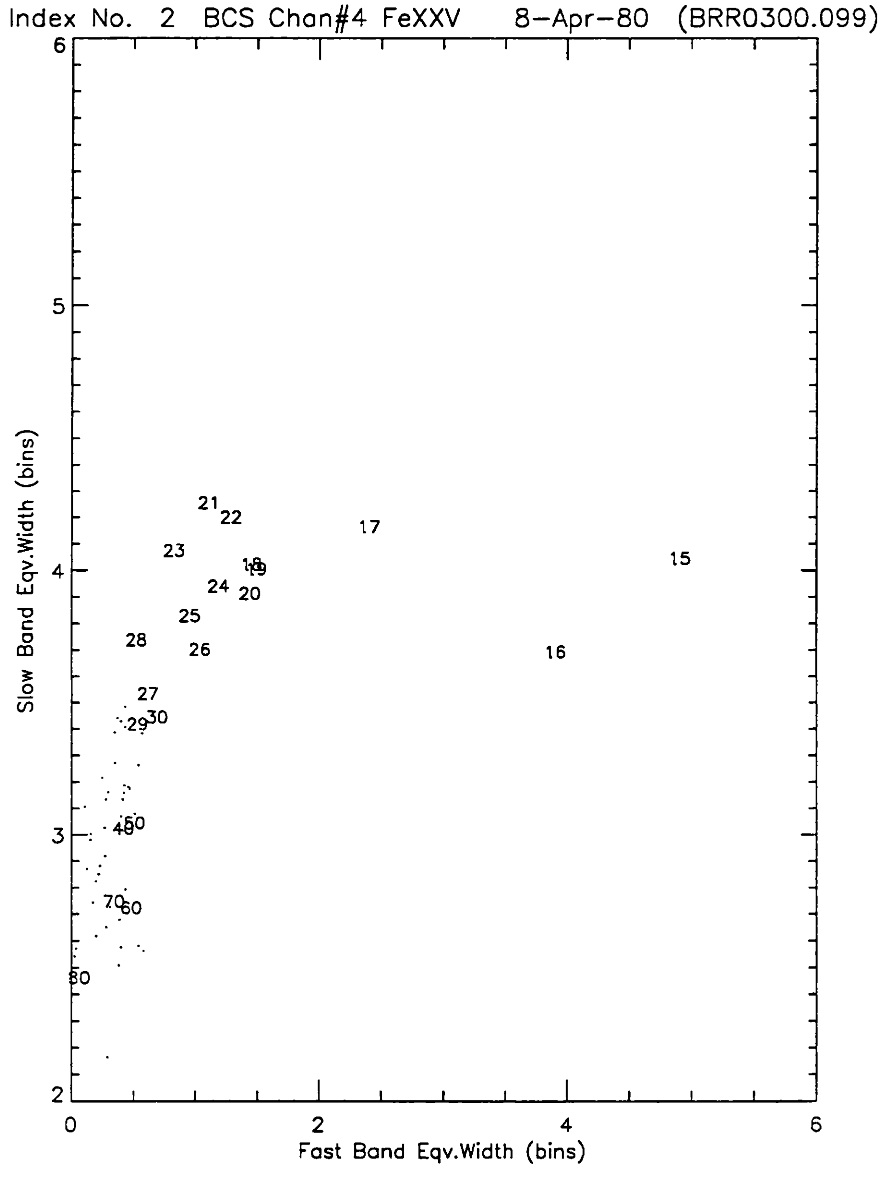

Figure 7.35: The line-width diagnostic plot for a disc flare with up-flows: the 0300 UT flare on 8 April 1980.

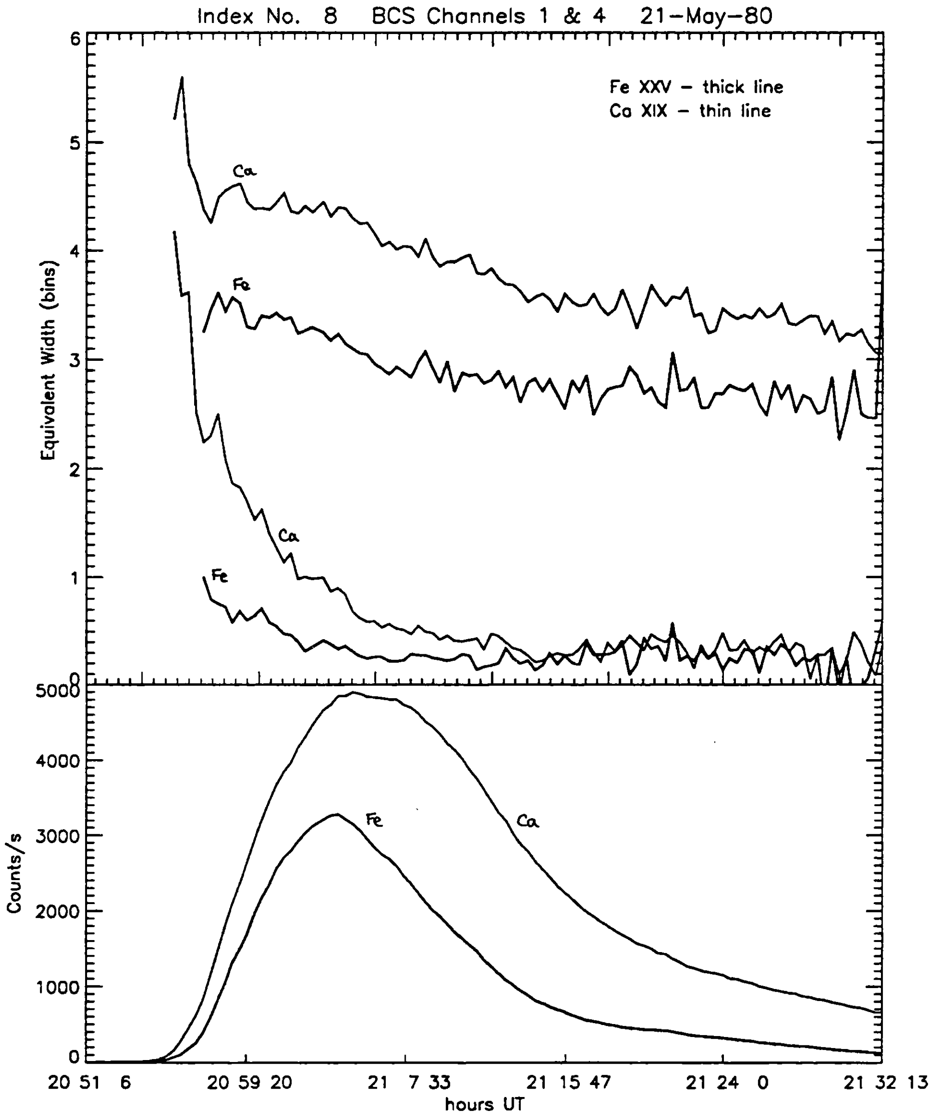

Figure 7.36: The line-width time plot for the 2051 UT flare on 21 May 1980.
The same flare was analysed by Fludra et al., (1990), who found that their turbulent velocities were proportional to the upflow velocity for about 3 minutes during the rise phase. In this plot, it is clear from the equivalent width measured from CaXIX spectra (thin line) that upflows and turbulence evolve together for at least the first 3 minutes. Because of low count rates, early FeXXV spectra have been excluded, but the parallel evolution of upflows and turbulence is still evident.

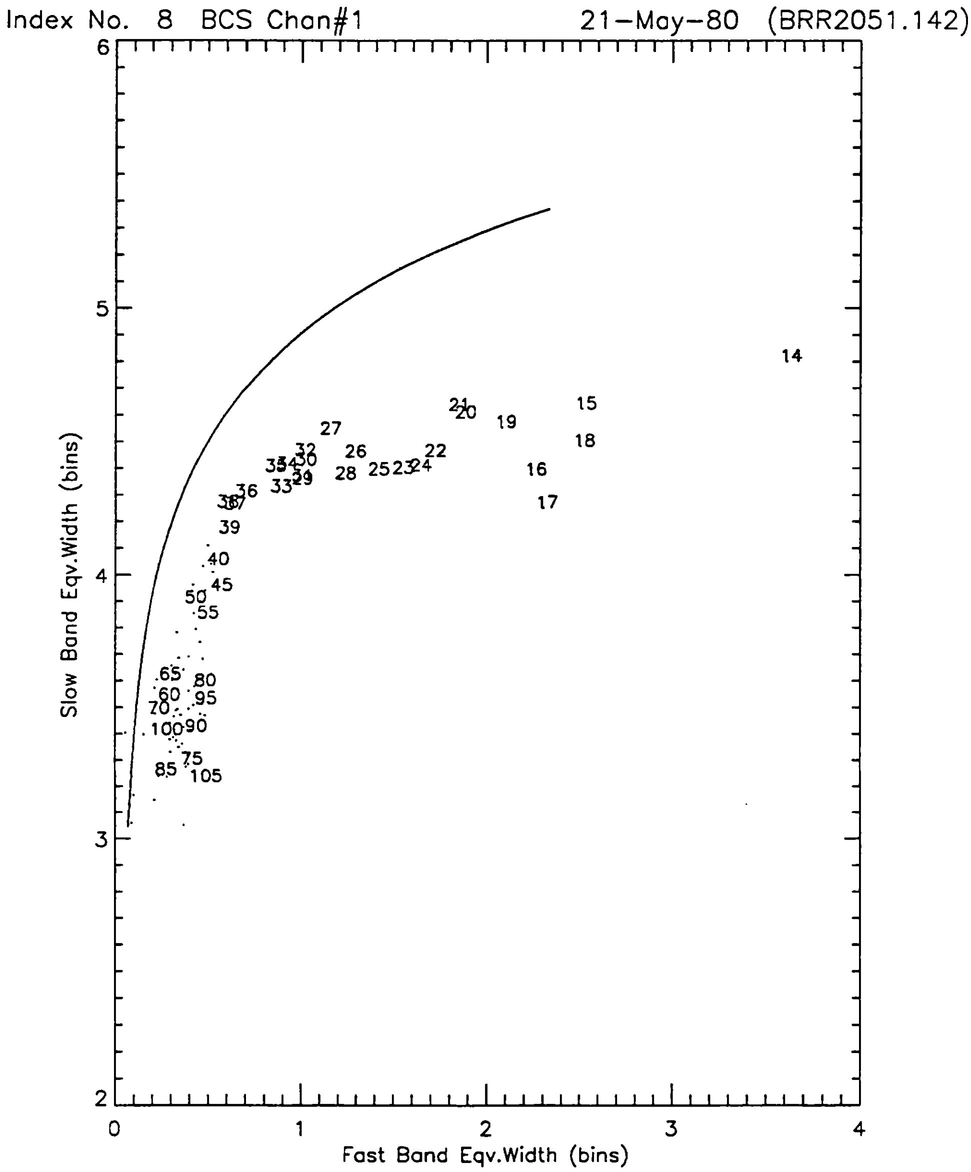

Figure 7.37: The line-width diagnostic plot for the 2051 UT flare on 21 May 1980 (as seen in Channel 1).

The same flare was analysed by Fludra et al., (1990), who found that their turbulent velocities were proportional to the upflow velocity for about 3 minutes during the rise phase.

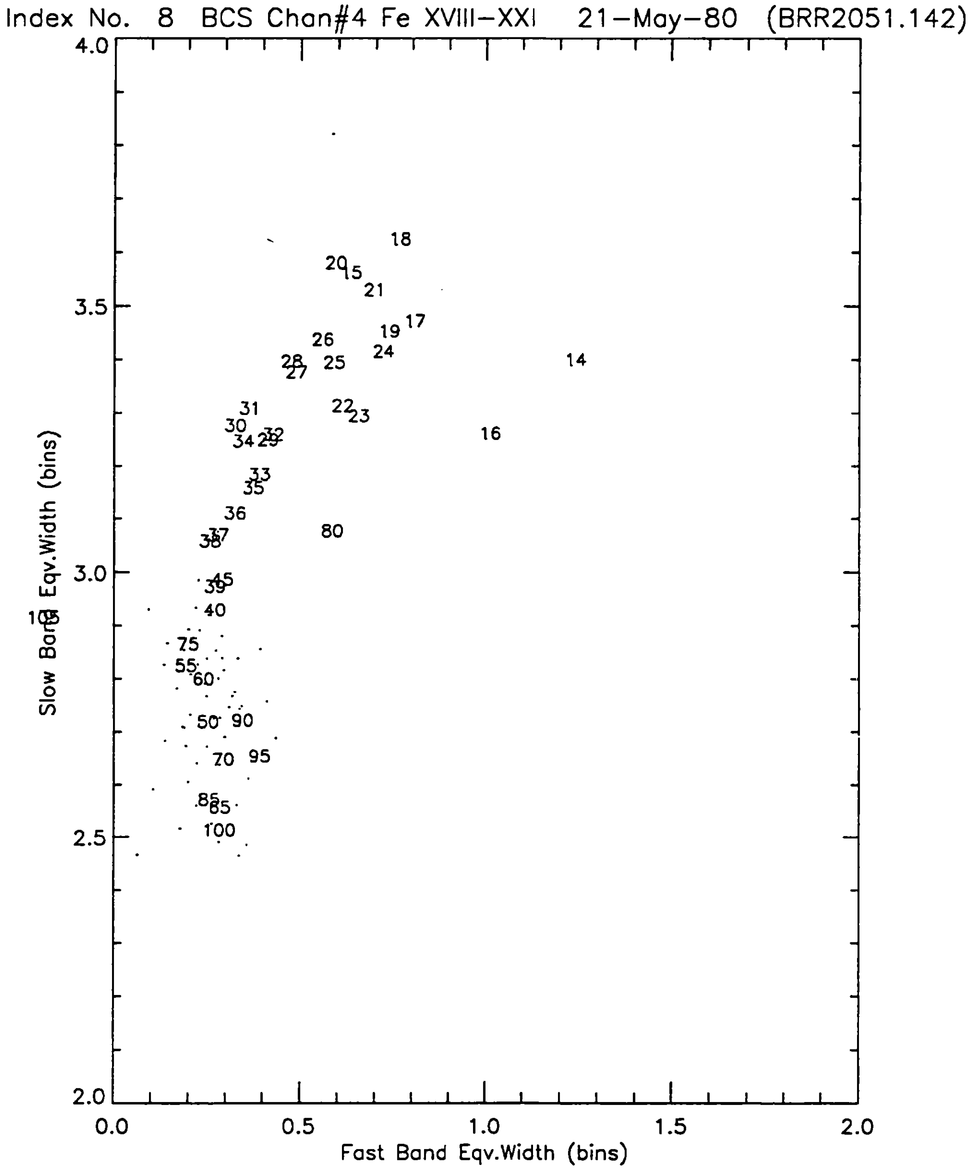

Figure 7.38: The line-width diagnostic plot for the 2051 UT flare on 21 May 1980 (as seen in Channel 4).

The same flare was analysed by Fludra et al., (1990), who found that their turbulent velocities were proportional to the upflow velocity for about 3 minutes during the rise phase.

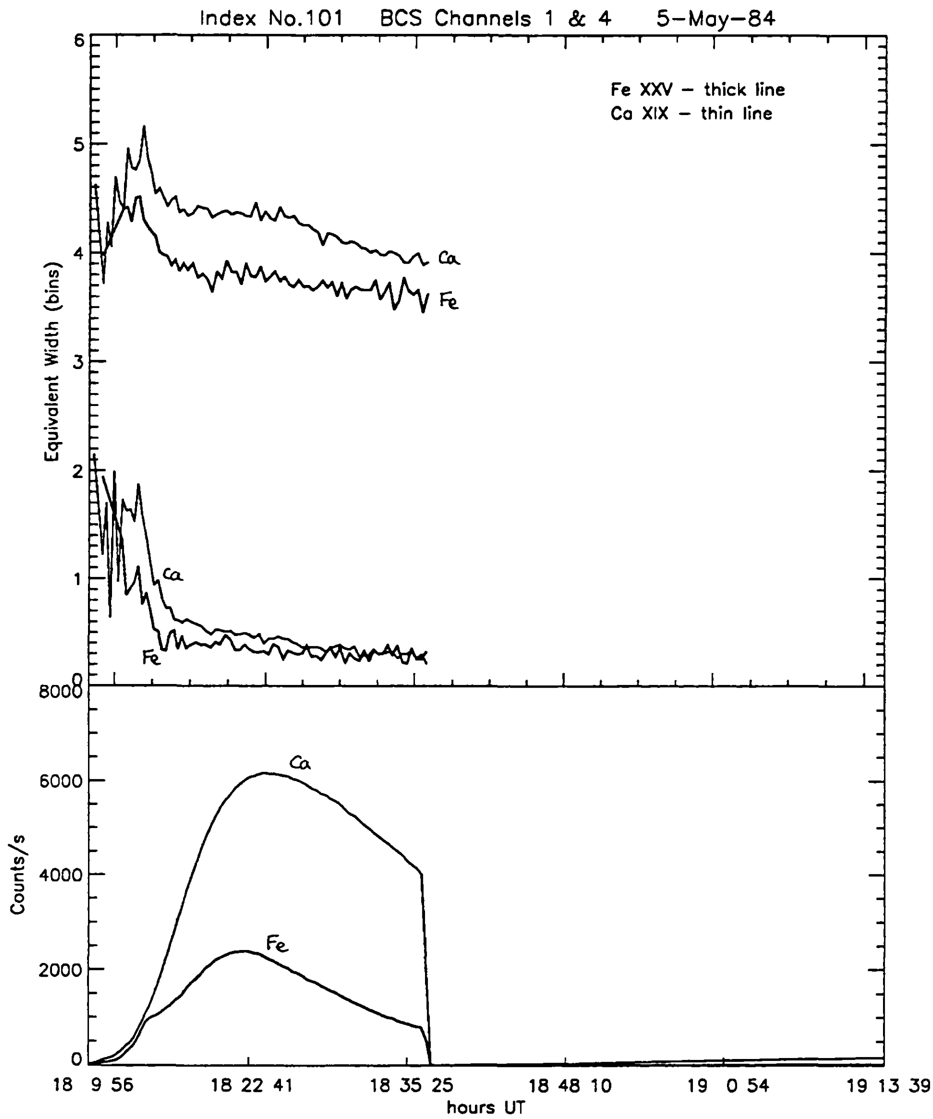

Figure 7.39: The line-width time plot of a limb flare with weak upflows: the 1810 UT flare on 5 May 1984.

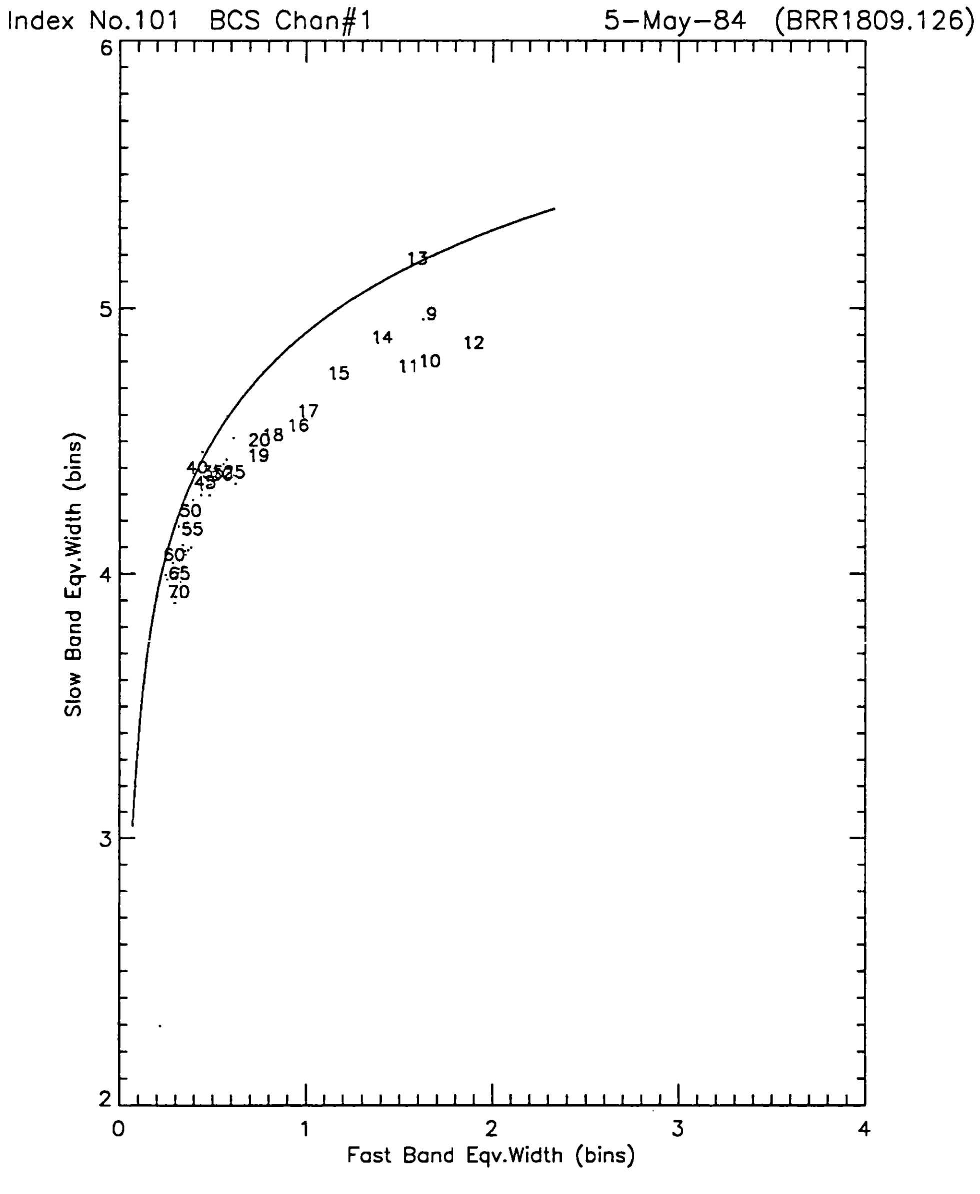

Figure 7.40: The line-width diagnostic plot of a limb flare with only weak upflows (seen in Channel 1):the 1810 UT flare on 5 May 1984.

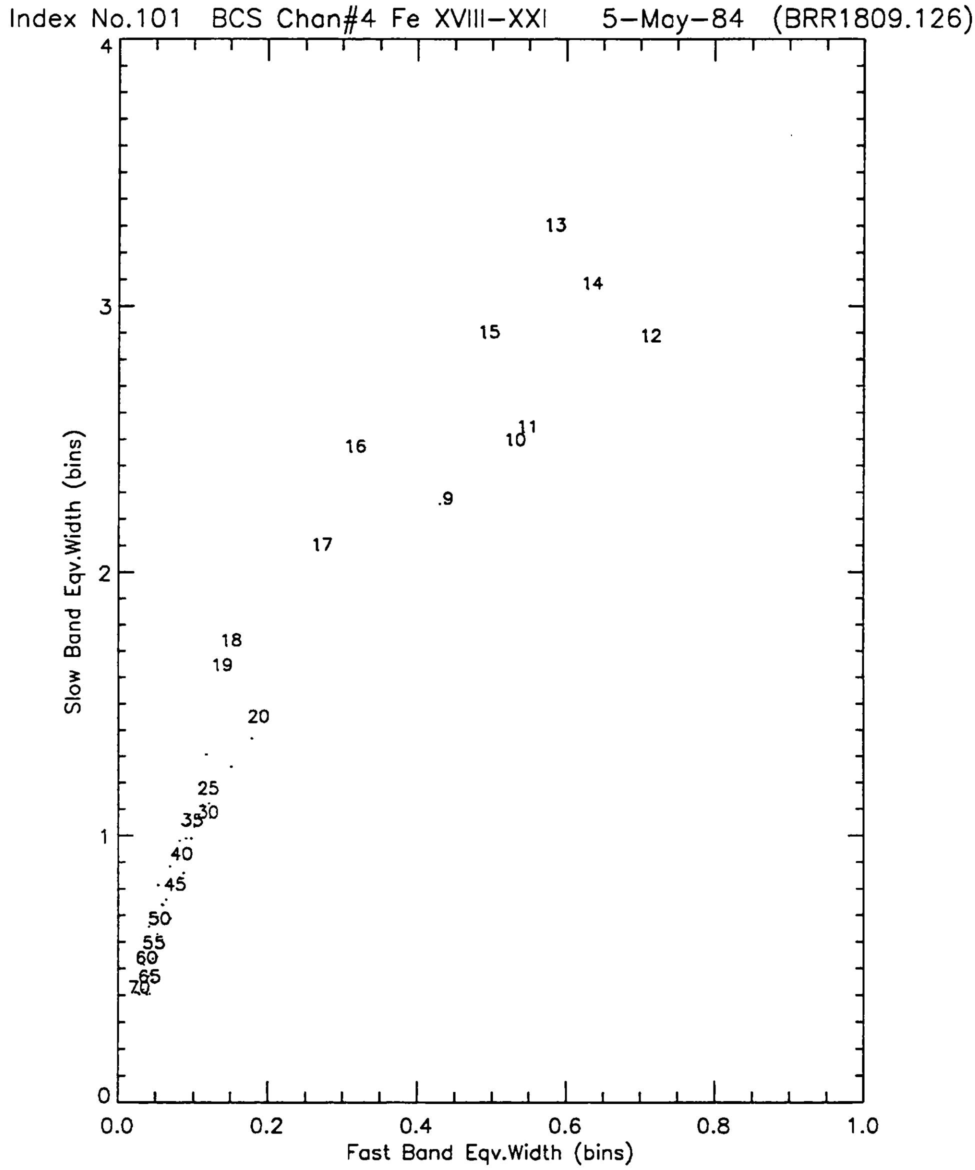

Figure 7.41: The line-width diagnostic plot of a limb flare with only weak upflows (seen in Channel 4): the 1810 UT flare on 5 May 1984.

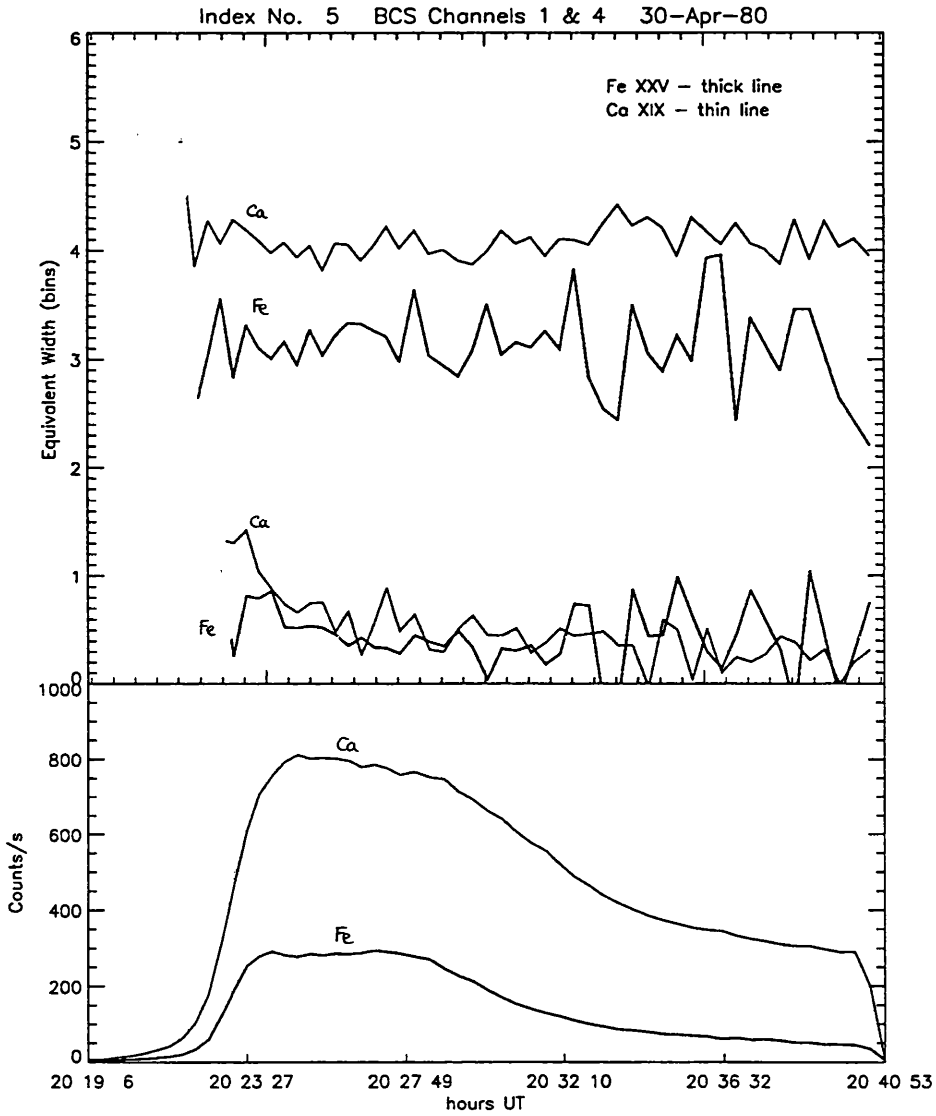

Figure 7.42: The line-width time plot of a limb flare with upflows: the 2019 UT flare on 30 April 1980.

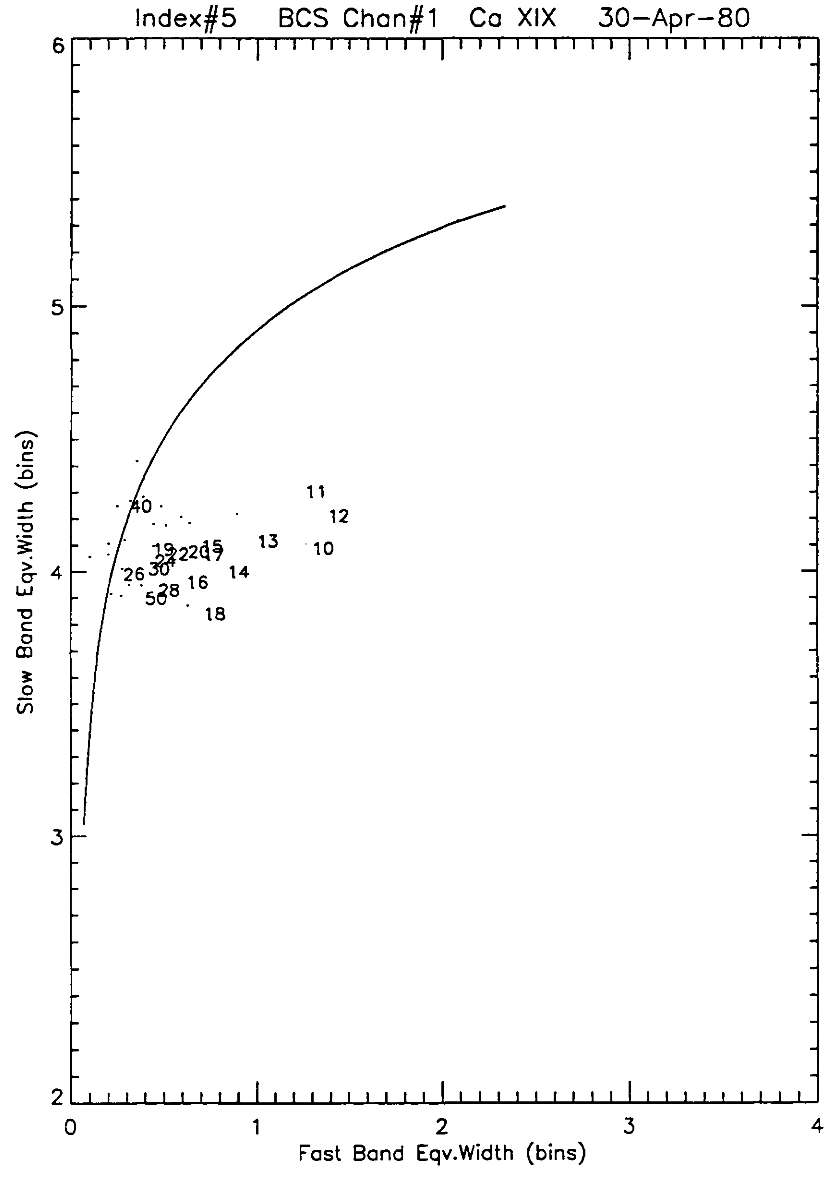

Figure 7.43: The line-width diagnostic plot of a limb flare with up-flows (seen in Channel 1): the 2019 UT flare on 30 April 1980.

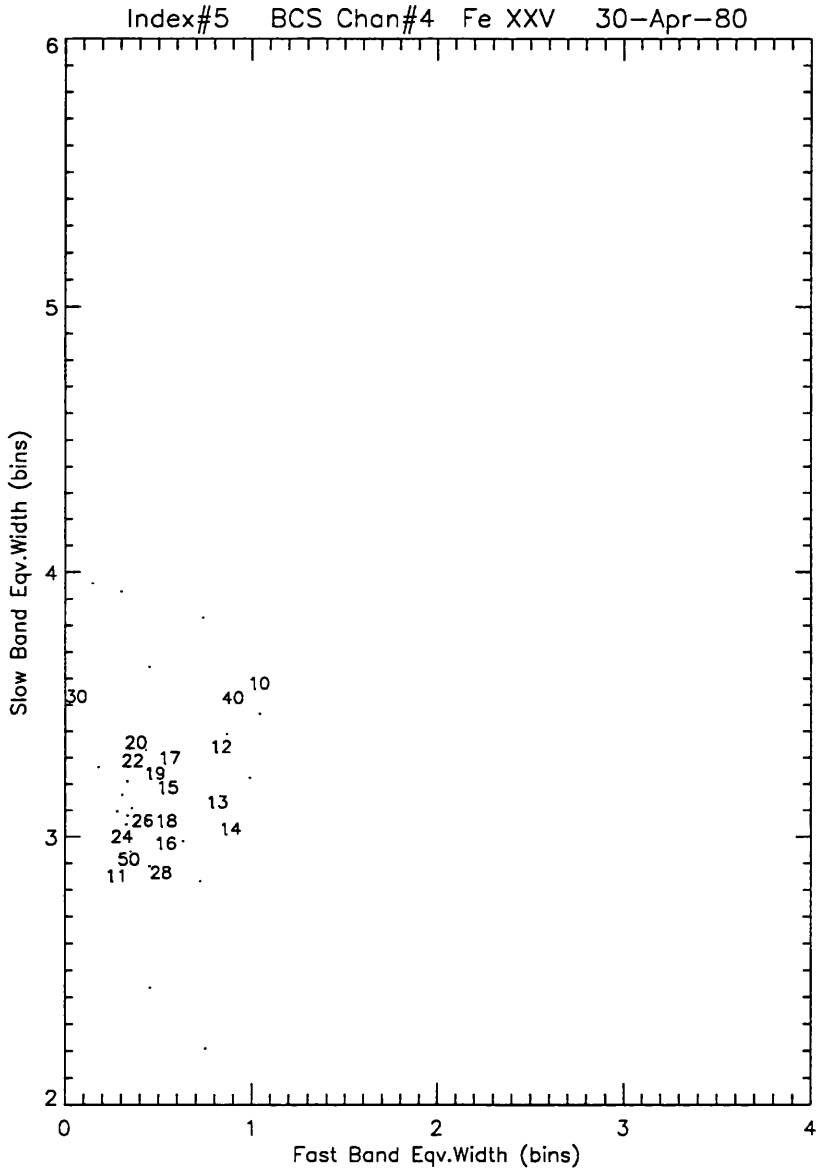

Figure 7.44: The line-width diagnostic plot of a limb flare with upflows (seen in Channel 4): the 2019 UT flare on 30 April 1980.

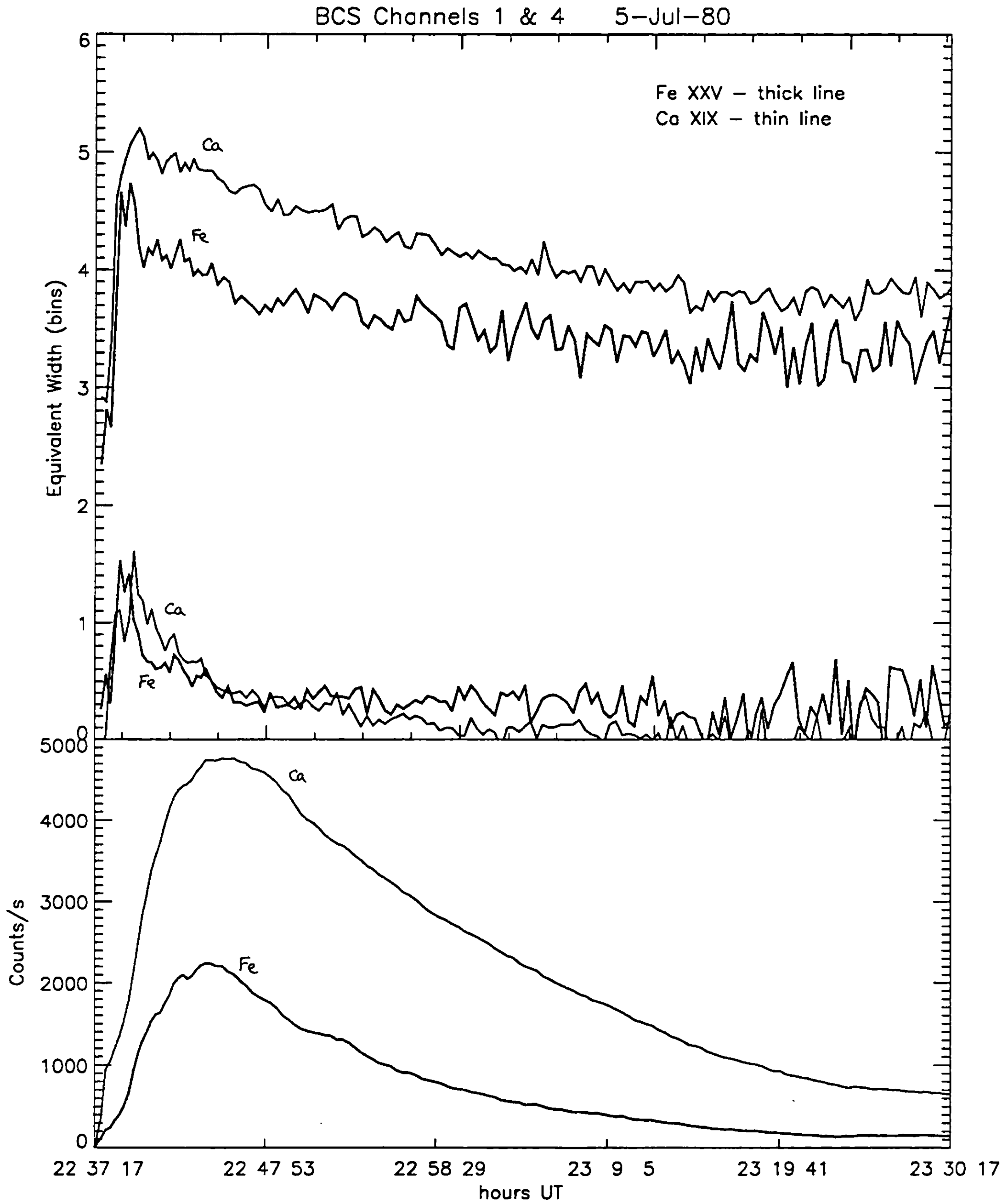

Figure 7.45: Line-width time plot: 5 July 1980
The ratio of the count rate in the blue wing of an emission line to that at the line centre gives an "equivalent width" which is a measure of the distribution of plasma velocities. The division of the wing into two bands enhances the sensitivity of this diagnostic. The equivalent width in the "fast band" reflects the amount of fast upflowing plasma, while the equivalent width derived from the "slow band" depends on the temperature and amount of random mass motion in the stationary plasma.

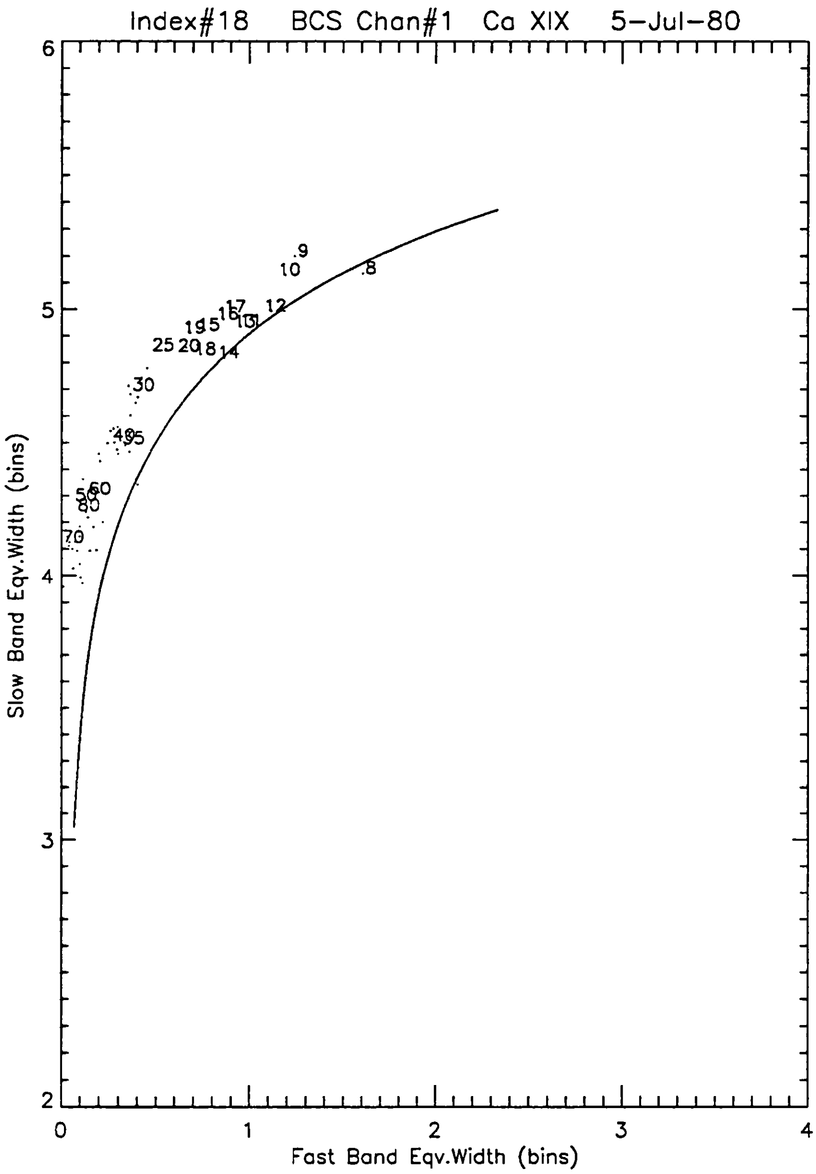

Figure 7.46: Line-width diagnostic plot for *BCS* Channel 1: 5 July 1980

This plot directly compares the equivalent widths in each of the velocity bands, which were plotted separately against time in the accompanying line-width time plot. The solid curve represents the variation expected from a flare with no upflows. The point at which it ends corresponds to the maximum observed width that a symmetrical resonance line (i.e.: no upflows) can have.

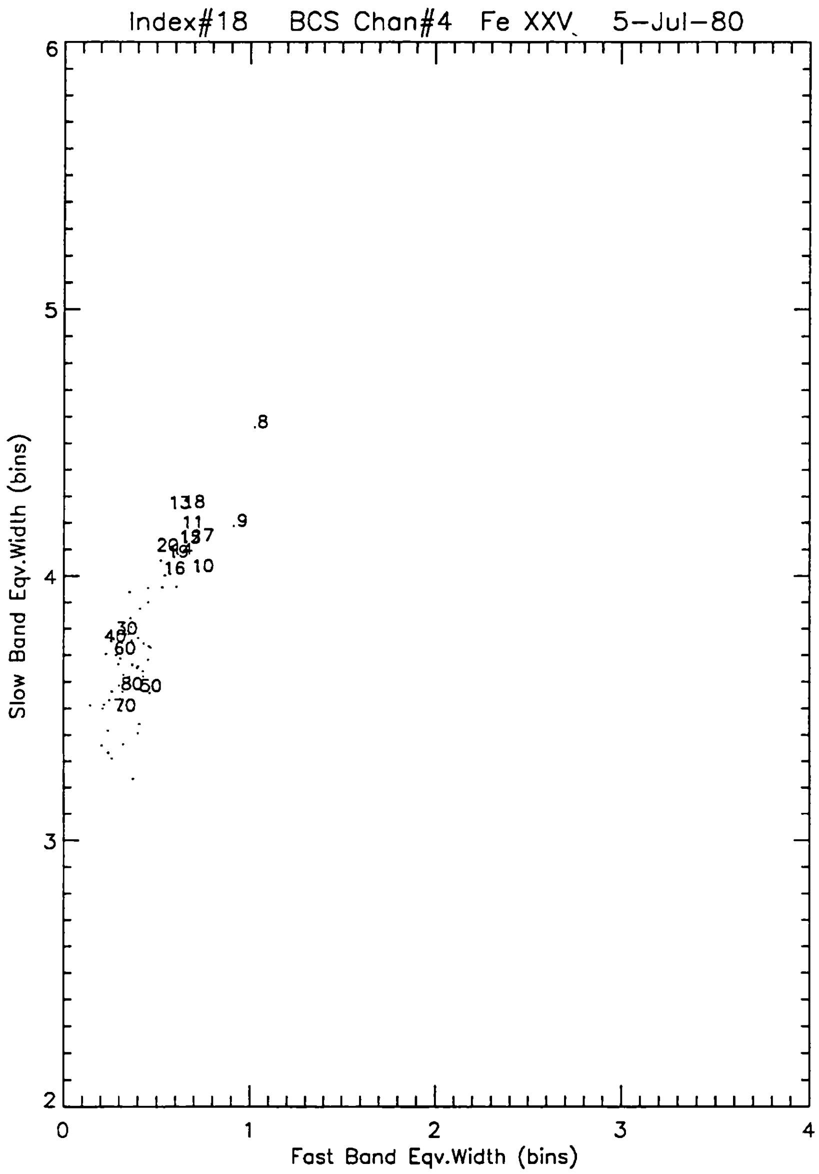

Figure 7.47: Line-width diagnostic plot for *BCS* Channel 4: 5 July 1980
This plot directly compares the equivalent widths in each of the velocity bands, which were plotted separately against time in the accompanying line-width time plot.

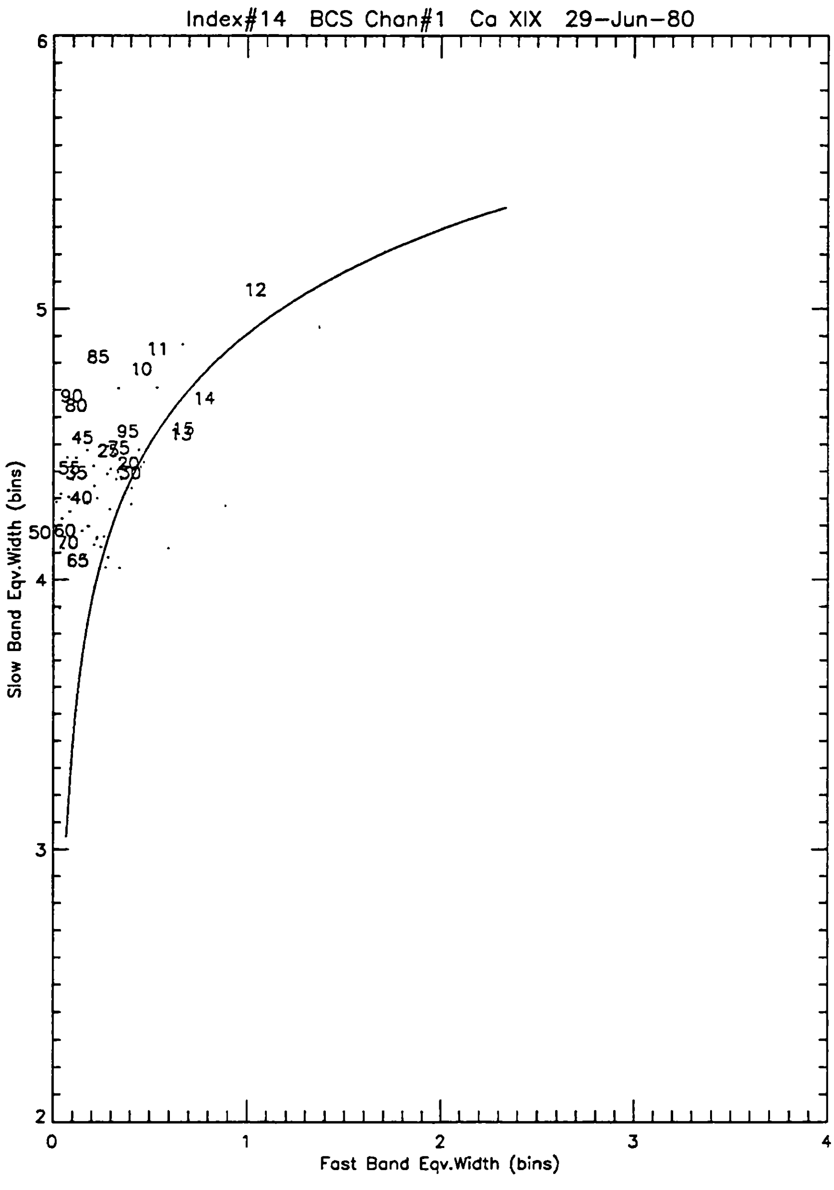

Figure 7.48: Line-width diagnostic plot for *BCS* Channel 4: 5 July 1980
This flare occurred on the limb.

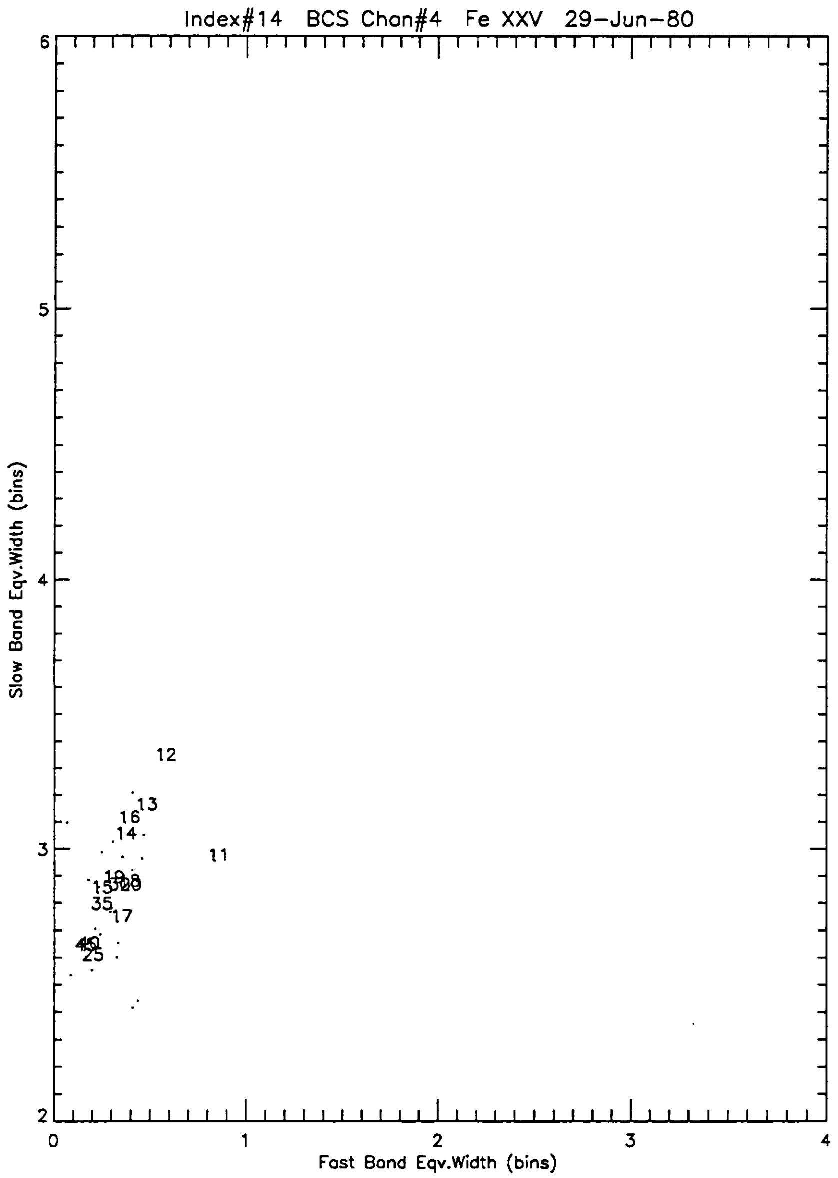

Figure 7.49: Line-width diagnostic plot for *BCS* Channel 4: 29 June 1980
This flare occurred on the limb.

CHAPTER 8

Conclusions

Measurements of the radius of curvature of the crystals in the *Bent Crystal Spectrometer (BCS)* are important for the interpretation of *BCS* spectra. When the *SMM* satellite was launched in 1981, an experiment was performed to measure the crystal curvature.

The experiment consisted of swinging the spacecraft in the east-west direction so that the spectra in each of the *BCS* channels slide across the respective crystal faces. This allows the crystal curvature to be measured at different points along the length of the crystal.

In Chapter 4, the results of this experiment were used to measure the curvature of the *BCS*'s Channel 1 crystal. Channel 1 was used to record the spectrum between 3.1Å and 3.5Å, the main features of which are the resonance line of the Ca XIX ion, and its satellite, known as the k-line. These two lines are diffracted from two different sites on the crystal face, placed about 9 cm apart.

The radius of curvature around the site of diffraction of the w-line was found to have increased from 550 cm in 1981 to between 620 cm and 630 cm in 1989 (an increase of 13%). At the site of the k-line, the radius of curvature increased from 620 cm to between 640 cm and 650 cm in 1989 (an increase of 4%). The 10 cm range of the measurements made in 1989 indicate the extent to which the crystal curvature varies around the diffraction site of the w- and k-lines. The gradual increase in the radius of curvature of the crystal could perhaps be due to the artificially deformed crystal gradually returning to its original, unstressed shape.

Shortly after the crystal curvature experiment was conducted, the *SMM* spacecraft was destroyed on re-entering the atmosphere, ruling out the possibility of continued monitoring of the crystal curvature. The method of measuring crystal curvature has been shown to be effective and reliable and it should be employed to monitor the crystal curvature of all future bent crystal spectrometers.

The *SMM-BCS*, like all bent crystal spectrometers, suffered from a line broadening effect that depended on the angular size of the source. Though this effect is already known to exist, previous workers have usually neglected it, or at best, have made rough estimates of its magnitude. Because the effect is size dependent, its magnitude may be measured if the source size can be measured independently.

This was done for the first time in Chapter 5, where *FCS* images have been used in conjunction with contemporaneous *BCS* spectra to measure the actual magnitude of this effect. It was found that the size dependent effect contributes 20 %, on average, to the total line width, and that the contribution is greatest when the turbulent velocity reaches a minimum during the decay phase.

A pattern is revealed in the behaviour of the non-thermal line broadening during the decay phase, whereby the rise phase turbulent velocities (100 - 200 km s^{-1}) rapidly decrease to a minimum point (30 - 50 km s^{-1}), after which there is a gradual increase to a more or less constant level that merges with the turbulent velocity levels known to exist in active regions.

A temperature dependence was also discovered, from a comparison of Ca XIX spectra from the *FCS* and the *BCS*. The *FCS* spectra yielded temperatures which were 25 % lower than *BCS* temperatures and resonance lines which were narrower than *BCS* resonance lines. In other words, hotter plasma is more turbulent, a result which is consistent with the findings of other workers.

It has been suggested that non-thermal line broadening is actually due to a superposition of line shifts due to upflows in radially directed loops, and that there is no need to invoke random mass motion to explain it. This hypothesis was tested by investigating the dependence of the corrected turbulent velocity on flare longitude. It was found that there is no such dependence. Moreover, if upflows were being projected in such a way as to cause symmetrically broadened lines, they would be required to have velocities far in excess of those that could reasonably exist in the decay phase.

The mechanical coupling of the magnetic field to the flare plasma permits the observed non-thermal line broadening to be used to constrain the amount of energy that can be provided by Alfvén waves to heat the corona. Alfvén waves propagating along field lines cause them to oscillate in a direction transverse to their length. The flare plasma is constrained to follow the motion of the field lines and this motion causes non-thermal line broadening. Thus the measured non-thermal line broadening can be used to determine the amplitude of the Alfvén waves, and hence determine the amount of energy that they carry. In

Chapter 5, decay phase non-thermal line widths were used to show that Alfvén waves could transport, typically, 3.2×10^8 erg cm^{-2} s^{-1} into the corona. Such calculations provide figures which may be compared with the energy requirements of flares in which there is decay phase heating, and it is suggested that this is done whenever evidence is found of decay phase heating.

A method for detecting the presence of decay phase heating was presented in Chapter 6. The basis of this method was to assume a rate of cooling that depends on flare geometry (roughly speaking, longer loops cool more slowly). This relationship was used to derive loop lengths from observed flare cooling rates. If these loop lengths were found to be greater than observed loop lengths, it was concluded that heating was present in the flare.

Again, the presence of an imaging instrument alongside a spectrometer aboard the *SMM* satellite was exploited: *FCS* images were used to estimate flare loop sizes, and *BCS* spectra were used to estimate flare cooling rates.

This method was applied to a sample of flares, several of which were found to have decay phase heating. However, comparisons of the results of this method with another more rigorous method appear to show that at least one of the flares for which no heating was found did show signs of heating when investigated by the other method.

What holds back the method presented in Chapter 6 is the lack of spatial resolution of the *FCS* images. It is hoped that future imaging instruments with higher resolving capabilities (such as the *Soft X-ray Telescope* aboard the *Yohkoh* satellite) will provide more fertile ground for the development of this method, the attractions of which are that it is relatively simple.

The dynamics of the rise phase was investigated in Chapter 7, for which purpose a line-width diagnostic method was developed. This method is very quick, simple to use and is a quite robust way of detecting the presence of upflows in flares. It is a useful complement to the commonly used component fitting method, which though very sensitive, suffers from the drawback of being time-intensive and rather delicate in application. The line-width diagnostic method was applied to a large sample of flares distributed across the disc, from which arose several results.

The most important of these results is the discovery that the presence of a substantial contribution from low velocity upflows (< 200 km s^{-1}) is required to explain the observed variation of line-width with flare position. This discovery has important consequences for line-profile analysis methods, notably component-fitting methods. In the past, these methods have been concentrated on identifying one or two fast-moving upflow components, but more recently, multiple component fits have been used. The results of Chapter 7 support this change in practice, and suggest that multiple component fits should incorporate upflows with velocities of less than 200 km s^{-1} .

The other results were the confirmation that flare loops are predominantly radially directed, and that upflows are not dominated either by hotter plasma or by cooler plasma, and probably have a distribution of temperatures similar to the stationary plasma.

The line-width diagnostic method is the ideal method to use when faced with a large sample of flares to investigate, as it can be speedily applied to the whole sample, and the results used to select a sub-set to which the more delicate component-fitting method may be applied. As the *Bragg Crystal Spectrometer* on *Yohkoh* has already observed almost two hundred flares, and looks like it will continue to do so even while the present solar maximum declines, the line-width diagnostic method should prove to be extremely useful in tackling an otherwise daunting data-reduction task.

Acknowledgements

I would like to thank my supervisor Professor Len Culhane and Dr. Andrzej Fludra for the guidance and help that they extended to me.

I acknowledge the receipt of a Studentship from the Science and Engineering Research Council, which supported me for two years of my studies.

Appendix
SMM Flares

This appendix contains a list of the major flares observed by the instruments aboard the *Solar Maximum Mission* (*SMM*) satellite between 1980 and 1989. Most of the flares were observed during the maximum year 1980, after which faults developed and were not put right until 1984, when observations resumed. In the subsequent years fewer and fewer flares were observed, partly because the Sun was passing through a period of minimum activity, and partly because the detectors were beginning to show their age (for example, the leakage of gas from the gas proportional detectors).

Flare Index No.	Date	Time UT	Active Region No.	Coord-. inates	GOES class
0	07 Apr 80	0108	2372	N10 E03	M4
1	07 Apr 80	0541	2372	N12 E01	M8
2	08 Apr 80	0307	2372	N12 W13	M4
3	10 Apr 80	0922	2372	N12 W42	M4
4	13 Apr 80	0408	2372	N10 W77	M1
5	30 Apr 80	2025	2396	S13 W90	M2.2
6	07 May 80	1457	2418	S22 W12	C7
7	09 May 80	0715	2418	S21 W32	M7.2
8	21 May 80	2105	2456	S14 W15	X1.4
9	04 Jun 80	0911	2490	S13 E58	M4
10	13 Jun 80	2234	2502	N17 E11	-
11	21 Jun 80	0102	2528	S12 E17	M2
12	24 Jun 80	1524	2522	S29 W15	M1
13	25 Jun 80	1555	2522	S29 W28	M4.8
14	29 Jun 80	0238	2522	S27 W90	M3.6
15	29 Jun 80	1044	2522	S27 W90	M4.2
16	29 Jun 80	1826	2522	S20 W90	M4.2
17	01 Jul 80	1628	2544	S12 W38	X2.5
18	05 Jul 80	2245	2550	N28 W31	M8.9
19	07 Jul 80	1153	2550	N26 W49	M2
20	11 Jul 80	2218	2562	S10 E70	M5.3
21	12 Jul 80	1121	2562	S14 E56	M4.3
22	12 Jul 80	1600	2562	S10 E60	M3.2
23	12 Jul 80	1738	2562	S09 E59	C7
24	12 Jul 80	1925	2562	S12 E60	C5
25	12 Jul 80	1933	2562	S14 E53	C4
26	13 Jul 80	0633	2562	S13 E48	C4
27	13 Jul 80	1434	2562	S15 E49	C6
28	13 Jul 80	1434	2562	S10 E46	M2
29	13 Jul 80	1803	2562	S09 E49	C6
30	13 Jul 80	1919	2562	S13 E50	C9.2

Flare Index No.	Date	Time UT	Active Region No.	Coord-. inates	GOES class
31	13 Jul 80	1922	2562	S13 E50	C9.2
32	13 Jul 80	1932	2562	S13 E50	C9.2
33	14 Jul 80	0152	2562	S10 E43	C4
34	14 Jul 80	0827	2562	S13 E43	X1.1
35	15 Jul 80	2248	2562	S15 E18	C4.4
36	17 Jul 80	0611	2562	S12 E06	M3.4
37	20 Jul 80	1926	2562	S19 W45	M1.4
38	21 Jul 80	0300	2562	S14 W60	M8
39	23 Aug 80	2130	2629	N17 W52	-
40	24 Aug 80	1612	2629	N17 W52	-
41	24 Aug 80	1635	2629	N17 W52	-
42	25 Aug 80	1305	2629	N18 W62	M1
43	31 Aug 80	1249	2646	N12 E28	-
44	31 Aug 80	1252	2646	N12 E28	M2.8
45	14 Oct 80	1614	2725	S09 W07	X3.3
46	20 Oct 80	1834	2744	S17 E45	M1.0
47	05 Nov 80	2229	2776	N11 E07	-
48	05 Nov 80	2234	2776	N10 E07	M4.0
49	06 Nov 80	1012	2776	S11 E71	C7
50	06 Nov 80	1125	2779	S13 E66	C7
51	06 Nov 80	1145	2779	S12 E66	C9
52	06 Nov 80	1236	2779	S09 E65	M3.1
53	06 Nov 80	1413	2779	S09 E65	M3.1
54	06 Nov 80	1526	2779	S09 E65	X1.2
55	06 Nov 80	1728	2779	S09 E65	M4.2
56	07 Nov 80	0447	2779	S11 E57	-
57	07 Nov 80	0458	2779	S11 E57	M2.5
58	07 Nov 80	0941	2779	S06 E59	M1.2
59	07 Nov 80	1137	2779	S11 E50	M1.0
60	07 Nov 80	1137	2779	S07 E56	M4
61	07 Nov 80	1535	2779	S07 E56	-
62	07 Nov 80	1537	2779	S07 E56	C7.6

Flare Index No.	Date	Time UT	Active Region No.	Coord-. inates	GOES class
63	07 Nov 80	1539	2779	S07 E56	C7.6
64	07 Nov 80	2230	2779	S10 E47	M1
65	08 Nov 80	1126	2779	S15 E43	C6.2
66	08 Nov 80	1619	2779	S08 E42	C4.9
67	09 Nov 80	0430	2779	S09 E36	M1
68	09 Nov 80	1721	2779	S11 E21	C5.3
69	10 Nov 80	0812	2779	S12 E14	M1.4
70	10 Nov 80	0937	2779	S15 E11	M1.5
71	11 Nov 80	0629	2779	S12 E06	M1.2
72	11 Nov 80	1032	2779	S12 E02	M3.6
73	11 Nov 80	1517	2779	S12 W01	M1
74	11 Nov 80	1554	2779	S12 W01	M2
75	12 Nov 80	0251	2779	S13 W06	M1.9
76	12 Nov 80	0810	2779	S12 W10	C8
77	12 Nov 80	0924	2779	S12 W10	C8
78	12 Nov 80	1106	2779	S12 W10	C8.6
79	12 Nov 80	1704	2779	S14 W11	M1.4
80	12 Nov 80	1737	2779	S13 W15	C7
81	12 Nov 80	2335	2779	S13 W18	M3
82	13 Nov 80	0103	2779	S11 W21	M9.4
83	18 Nov 80	1455	2779	S10 W90	M3.0
84	19 Nov 80	0544	2779	S10 W90	M6.0
85	22 Nov 80	0538	2793	N12 W02	C9.0
86	25 Apr 84	0022	4474	S12 E43	X10
87	25 Apr 84	0057	4474	S11 E42	-
88	26 Apr 84	0903	4474	S09 E34	M2.5
89	27 Apr 84	0540	4474	S10 E24	M2.3
90	29 Apr 84	0250	4474	S13 E12	C4.8
91	29 Apr 84	0744	4474	S17 E02	M1
92	30 Apr 84	0557	4474	S14 W34	M1.1
93	30 Apr 84	1213	4474	S12 W31	M2.3
94	01 May 84	0134	4474	S14 W32	M4.0

Flare Index No.	Date	Time UT	Active Region No.	Coord-. inates	GOES class
95	02 May 84	1617	4474	S14 W54	C7.9
96	02 May 84	1925	4474	S11 W58	M3.0
97	02 May 84	2023	4474	S11 W58	-
98	02 May 84	2058	4474	S11 W58	-
99	03 May 84	0318	4474	S12 W67	C7.1
100	05 May 84	0107	4476	S11 W64	C4.7
101	05 May 84	1824	4474	S11 W90	M7.5
102	06 May 84	0145	4481	N06 E83	C5
103	06 May 84	0823	4481	N07 E89	C3
104	06 May 84	1625	4481	N08 E89	C3.1
105	06 May 84	1904	4481	N05 E78	C3.8
106	19 May 84	2155	4492	S10 E66	X4.1
107	20 May 84	0129	4492	S10 E64	M2.9
108	20 May 84	0301	4492	S13 E62	M4.6
109	20 May 84	0302	4492	S13 E62	M4.6
110	20 May 84	0542	4492	S08 E57	M5.4
111	20 May 84	0620	4492	S08 E57	M5.4
112	20 May 84	2253	4492	S08 E52	X10
113	20 May 84	2311	4492	S06 E53	X10.1
114	21 May 84	1747	4492	S06 E42	-
115	21 May 84	1810	4492	S08 E42	C9.7
116	22 May 84	1501	4492	S09 E24	M6.3
117	20 Jan 85	2051	4617	S09 W24	M4.1
118	21 Jan 85	0353	4617	S10 W28	M2.2
119	21 Jan 85	1419	4617	S09 W35	M2.4
120	23 Jan 85	0733	4617	S09 W35	M2.4
121	23 Jan 85	0743	4617	S11 W58	M1.3
122	23 Jan 85	0752	4617	S11 W58	M1.3
123	24 Apr 85	0152	4647	N05 E26	C8.8
124	02 May 85	0819	4647	N03 W86	-
125	21 May 85	0955	4656	N05 E27	-
126	02 Jul 85	2126	4671	S14 E57	M4.5

Flare Index No.	Date	Time UT	Active Region No.	Coord-. inates	GOES class
127	07 Jul 85	0528	4671	S15 E00	C3.0
128	07 Jul 85	2028	4671	S15 W07	C2.7
129	09 Jul 85	0210	4671	S13 W25	-
130	13 Jul 85	0659	4671	S17 W86	C2.3
131	13 Jul 85	1321	4671	S17 W89	C2.0
132	26 Oct 85	0434	4698	N06 W58	M1.8
133	07 Feb 86	1056	4711	S11 W21	M5.2
134	19 Oct 86	0046	4750	N23 E62	M4.7
135	19 Oct 86	0141	4750	N23 E62	M4.7
136	24 Oct 86	1240	4750	N23 W03	C2.4
137	05 Apr 87	1937	4787	S29 E90	M1.1
138	06 Apr 87	0433	4787	S28 E86	C9.2
139	17 Apr 87	0238	4790	S30 W56	C1.9
140	18 Apr 87	1437	4790	S30 W74	–
141	18 Apr 87	1458	4790	S30 W75	C2.8
142	25 May 87	0343	4811	N30 W48	–
143	25 May 87	0348	4811	N30 W47	M1.3
144	25 May 87	1856	4811	N29 W56	C5.9
145	26 May 87	2000	4811	N28 W70	C8.1
146	26 May 87	2022	4811	N29 W73	–

References

1. Acton, L. W., Culhane, J. L., Gabriel, A. H., Bentley, R. D., Bowles, J A., Firth, J. G., Finch, M. L., Gilbreth, C. W., Guttridge, P., Hayes, R. W., Joki, E. G., Jones, B. B., Kent, B, J., Leibacher, J W., Nobles, R. A., Patrick, T J., Phillips, K. J. H., Rapley, C. G., Sheather, P. H., Sherman, J. C., Stark, J. P., Springer, L. A., Turner, R. F., and Wolfson, C. J. 1980 *Solar Physics*, **65**, 53-71: *The Soft X-ray Polychromator for the Solar Maximum Mission.*

2. Alexander, D., 1990 *Astr. Astrophys.*, **236**, L9 : *Soft X-ray line broadening in Solar flares.*

3. Alexander, D., and MacKinnon, A. L., 1993 *Solar Physics*, **144**, 155-168: *Alfvén turbulence and the time dependence of non-thermal line broadening in flares.*

4. Antonucci, E., 1990 *Solar Physics*, **121**, 31-60: *Solar flare spectral diagnosis: present and future.*

5. Antonucci, E., and Dennis, B. R., 1983 *Solar Physics*, **86**, 67-77: *Observation of chromospheric evaporation during the Solar Maximum Mission*

6. Antonucci, E., Dennis, B. R., Gabriel, A. H., and Simnett, G. M., 1985 *Solar Physics*, **96**, 129-142 : *Initial phase of chromospheric evaporation in a Solar flare.*

7. Antonucci, E., Dodero, M. A., Martin, R., 1990 *Astrophys. J. Suppl.*, **73**, 137-146 : *High-velocity evaporation during the impulsive phase of the 1984 April 24 flare.*

8. Antonucci, E., Dodero, M. A., Peres, G., Serio, S., and Rosner, R., 1987 *Astrophys. J.*, **322**, 522-543 : *Simulations of the CaXIX spectral emission from a flaring Solar coronal loop. I. Thermal case.*

9. Antonucci, E., Gabriel, A. H., Acton, L. W., Culhane, J. L., Doyle, J. G., Leibacher, J. W., Machado, M. E., Orwig, L. E., and Rapley, C. G., 1982, *Solar Physics*, **78**, 107-123: *Impulsive phase of flares in soft X-ray emission.*

10. Antonucci, E., Marocchi, D., Gabriel, A. H., Doschek, G. A., 1987 *Astr. Astrophys.*, **188**, 159: *Calcium ionization balance and argon/calcium abundance in Solar flares.*

11. Antonucci, E., Rosner, R., and Tsinganos, K., 1986 *Astrophys. J.*, **301**, 975-980: *On the magnetic field stochasticity and non-thermal line broadening in Solar flares.*

12. Berton, R., and Sakurai, T., 1985, *Solar Physics*, **96**, 93-111: *Stereoscopic determination of the three-dimensional geometry of coronal magnetic loops*

13. Bhatnagar, A., 1986 In *Solar Terrestrial Physics, Indo-US Workshop Proceedings, 1984*, eds., Kundu, M. R., Biswas, B., Reddy, B. M., and Ramadurai, S.,), publ., National Physical Laboratory, New Delhi, p.73-88: *Optical observations of solar flares.*

14. Bely-Dubau, F., Dubau, J., Faucher, P., Gabriel, A. H., Loulerge, M., Steenman-Clark, L., Volonté, S., Antonucci, E., and Rapley, C. G., 1982 *Mon. Not. R. astr. Soc.*, **201**, 1155-1169: *Dielectronic satellite spectra for highly-charged helium-like ions - VII. Calcium spectra - theory and comparison with SMM observations.*

15. Billings, D. E., 1966 *A Guide to the Solar Corona*, publ., Academic Press Inc., p158.

16. Bohlin, J. D., Frost, K. J., Burr, P. T., Guha, A. K., and Withbroe, G. L., 1980 *Solar Physics*, **65**, 5-14: *Solar Maximum Mission*

17. Bornmann, P. L., 1987, *Astrophys. J.*, **313**, 449-455: *Turbulence as a contributor to intermediate energy storage during Solar flares.*

18. Bornmann, P. L., and Strong, K. T., 1988 *Astrophys. J.*, **333**, 1014-1025 : *Two-component analysis of the decay of soft X-ray line emission during solar flares.*

19. Bruner, M. E., Crannell, C. J., Goetz, F., Magun. A., and McKenzie, D. L., 1988 *Astrophys. J.*, **334**, 494-509 : *Dynamic evolution of the source volumes of gradual and impulsive solar flare emissions.*

- Burgess, A., 1964 *Astrophys. J.*, **139**, 776.

20. Canfield, R. C., Zarro, D. M., Metcalf, T. R., and Lemen, J. R., 1990 *Astrophys. J.*, **348**, 333-340 : *Momentum balance in four Solar flares.*

21. Carrington, R. C., 1860 *Mon. Not. R. astr. Soc.*, **20**, 13: *Description of a Singular Appearance seen in the Sun on September 1, 1859.*

22. Cheng, C., Doschek, G. A., and Feldman, U., 1979 *Astrophys. J.*, **227**, 1037-1046: *The dynamical properties of the Solar corona from intensities and line widths of EUV forbidden lines of Si VIII, Fe XI and Fe XII.*

23. Chipman, E. G., 1981, *Astrophys. J.*, **244**, L113-L115: *The Solar Maximum Mission*

24. Christensen-Dalsgaard, J., 1992 Chapter 1 of *The Sun: A Laboratory for Astrophysics*, Proceedings of the NATO Advanced Study Institute held in Crieff, Scotland, 1991, eds., Schmelz, J. T., and Brown, J. C., publ., Kluwer Academic Publishers, p11-28: *The Structure and Evolution of the Sun.*

25. Craig, I. J. D., and Brown, J. C., 1976 *Astr. Astrophys.*, **49**, 239-250: *Fundamental Limitations of X-ray Spectra as Diagnostics of Plasma Temperature Structure.*

26. Craig, I. J. D., and McClymont, A. N., 1991 *Astrophys. J.*, **341**, L41-L44: *Dynamic magnetic reconnection at an X-type neutral point.*

27. Craig, I. J. D., McClymont, A. N., and Underwood, J. H., 1978 *Astr. Astrophys.*, **70**, 1-11 : *The temperature and density structure of active region coronal loops.*

28. Démoulin, P., van Driel-Gesztelyi, L., Schmeider, B., Hénoux, J. C., Csepura, G., and Hagyard, M. J., 1993, *Astr. Astrophys.*, **271**, 292-307 : *Evidence for magnetic reconnection in solar flares.*

29. Doschek, G. A., 1990 *Astrophys. J. Suppl.*, **73**, 117-130 : *Soft X-ray spectroscopy of solar flares: An overview.*

30. Doschek, G. A., and Feldman, U., 1987 *Astrophys. J.*, **313**, 883-892 : *The temperature of solar flares determined from X-ray spectral line ratios.*

31. Doschek, G. A., Feldman, U., Kreplin, R. W., and Cohen, L., 1980, *Astrophys. J.*, **239**, 725-737 : *High-resolution X-ray spectra of solar flares. III. General spectral porperties of X1 - X5 type flares.*

32. Doschek, G. A., Kreplin, R. W., and Feldman, U. 1979 *Astrophys. J. (Letters)*, **233**, L157: *High resolution Solar flare X-ray spectra.*

33. Doyle, J. G., and Bentley, R. D., 1986 *Astr. Astrophys.*, **155**, 278-282: *Broadening of soft X-ray lines during the impulsive phase of solar flares: Random or directed mass motions?*

34. Emslie, A. G., 1992 Chapter 23 of *The Sun: A Laboratory for Astrophysics*, Proceedings of the NATO Advanced Study Institute held in Crieff, Scotland, 1991, eds., Schmelz, J. T., and Brown, J. C., publ., Kluwer Academic Publishers, p465-474: *Overview of Solar Flares.*

35. Emslie, A. G., and Alexander, D., 1987 *Solar Physics*, **110**, 295-303: *Soft x-ray line profiles in the impulsive phase of electron-heated solar flares.*

36. Fisher, G. H., Canfield, R. C., and McClymont, A. N., 1984 *Astrophys. J.*, **281**, L79-L82: *Chromospheric evaporation velocities in Solar flares.*

37. Fisher, G. H., Canfield, R. C., and McClymont, A. N., 1985(a) *Astrophys. J.*, **289**, 414-424 : *Flare loop radiative hydrodynamics. V. Response to the thick-target heating.*

38. Fisher, G. H., Canfield, R. C., and McClymont, A. N., 1985(b) *Astrophys. J.*, **289**, 425-433 : *Flare loop radiative hydrodynamics. VI. Chromospheric evaporation due to heating by non-thermal electrons.*

39. Fisher, G. H., Canfield, R. C., and McClymont, A. N., 1985(c) *Astrophys. J.*, **289**, 434-441 : *Flare loop radiative hydrodynamics. VII. Dynamics of the thick-target heated chromosphere.*

40. Fludra, A., Lemen, J. R., Jakimiec, J., Bentley, R.D., and Sylwester , J., 1989 *Astrophys. J.*, **344**, 991-1003: *Turbulent and directed plasma motions in solar flares.*

41. Fludra, A., and Sylwester, J., 1986 *Solar Physics*, **105**, 323-337: *Comparison of three methods used for caluclation of the differential emission measure.*

42. Gabriel, A. H., 1972 *Mon. Not. R. astr. Soc.*,**160**, 99-119: *Dielectronic satellite spectra for highly-charged helium-like ion lines.*

43. Gabriel, A. H., 1992 Chapter 13 of *The Sun: A Laboratory for Astrophysics*, Proceedings of the NATO Advanced Study Institute held in Crieff, Scotland, 1991, eds., Schmelz, J. T., and Brown, J. C., publ., Kluwer Academic Publishers, p277-296: *The Solar Corona.*

44. Gaunt, J. A., 1930 *Phil. Trans.*, **229**, 163-204: *V. Continuous absorption*

45. Hiei, E., and Widing, K. G., 1979 *Solar Physics*, **61**, 407-417: *A single loop of 21 January 1974 flare*

46. Hodgson, R., 1860 *Mon. Not. R. astr. Soc.*, **20**, 15-16: *On a curious Appearance seen in the Sun.*

47. Hollweg, J. V., 1984 *Astrophys. J.*, **277**, 392: *Resonances of Coronal Loops.*

48. Jakimiec, J., and Fludra, A., 1991 *Adv. Space Res.*, **Vol 11, No 5**, 99: *Investigation of turbulent kernels in Solar flares.*

49. Jakimiec, J., Sylwester, B., Sylwester, J., Lemen, J. R., Mewe, R., Bentley, R. D., Peres, G., Serio, S., Schrijver, J., 1986 *Adv. Space Res.*, **6**, 237.

50. Jakimiec, J., Sylwester, B., Sylwester, J., Serio, S., Peres, G., and Reale, F., 1992 *Astr. Astrophys.*, **253**, 269-276 : *Dynamics of flaring loops. II. Flare evolution in the density-temperature diagram.*

51. Karpen, J. T., Doschek, G. A., and Seely, J. F., 1986 *Astrophys. J.*, **306**, 327-339: *High-resolution X-ray spectra of Solar flares VIII. Mass upflows in the large flare of 1980 November 7.*

52. Kundu, M. R., and Woodgate, B., (eds.) 1986 *Energetic Phenomena on the Sun*, The Solar Maximum Mission Flare Wokshop Proceedings, publ., NASA.

53. Li, P., Emslie, A. G., and Mariska, J. T., 1989 *Astrophys. J.*, **341**, 1075 - 1081: *Soft X-ray diagnostics of electron-heated solar flare atmospheres.*

54. Livi, S. H., Martin, S., Wang, H., Ai, G., 1989 *Solar Physics*, **121**, 197-214: *The association of flares to cancelling magnetic features on the Sun.*

55. MacNeice, P., McWhirter, R. W. P., Spicer, D. S., and Burgess, A., 1984 *Solar Physics*, **90**, 357-382 : *A numerical model of a Solar flare based on electron beam heating of the chromosphere.*

56. McClements, K. G., and Alexander, D., 1989 *Solar Physics*, **123**, 161-175: *Observations of the CaXIX resonance line during the impulsive phase of solar flares.*

57. McClements, K. G., Harrison, R. A., and Alexander, D., 1991 *Solar Physics*, **123**, 161: *The detection of wave activity in the Solar corona using UV line spectra.*

58. Nagai, F., and Emslie, A. G., *Astrophys. J.*, **279**, 896-908 : *Gas dynamics in the impulsive phase of Solar flares. I. Thick-target heating by non-thermal electrons.*

59. Neupert, W. M., 1968 *Astrophys. J.*, **153**, L59-L63: *Comparison of solar x-ray line emission with microwave emission during flares.*

60. Pallavacini, R., Peres, G., Serio, S., Vaiana, G., Acton, L., Leibacher, J., and Rosner, R., 1983 *Astrophys. J.*, **279**, 270- : *Closed coronal structures. V. Gasdynamics models of flaring loops and comparisons with SMM observations.*

61. Pallavacini, R., Serio, S., and Vaiana, G. S., 1977 *Astrophys. J.*, **216**, 108-122: *A survey of soft X-ray limb flare images: the relation between their structure in the corona and other physical parameters.*

62. Parmar, A., 1981 *Ph.D. Thesis*, University College London: *Studies of X-ray Emission from Hercules X-1 OAO1653-40 and X-ray Spectroscopy of Solar Flares.*

63. Parker, E. N., 1989 *Solar Physics*,**121**, 271-288: *Solar and stellar magnetic fields and atmospheric structures: theory.*

64. Peres, G., Rosner, R., Serio, S., Vaiana, G. S., 1982 *Astrophys. J.*, **252**, 791-799: *Coronal closed structures. IV. Hydrodynamic stability and response to heating perturbations.*

65. Rapley, C. G., Culhane, J. L., Acton, L. W., Catura, J. W., Joki, E. G., Bakke, J. C., 1977 *Rev. Sci. Instrum.*, **48**, 9, 1123-1130: *Bent crystal spectrometer for solar X-ray spectroscopy*

66. Raymond, J. C., Cox, D. P., Smith, B. W., 1976 *Astrophys. J.*, **204**, 290-292: *Radiative cooling of a low-density plasma*

67. Rosner, R., Tucker, W. H., and Vaiana, G. S., 1978 *Astrophys. J.*, **220**, 643-665 : *Dynamics of the quiescent solar corona.*

68. Saba, J. L. R., and Strong, K. T., 1991 *Astrophys. J.*, **375**, 789-799: *Coronal dynamics of a quiescent active region.*

69. Saba, J. L. R., and Strong, K. T., 1992 , **preprint**, : *Active region mass motions observed in soft X-ray lines.*

70. Smith, H. J., and Smith, E. V. P., 1963 *Solar Flares*, publ., Macmillan.

71. Serio, S., Reale, F., Jakimiec, J., Sylwester, B., and Sylwester, J., 1991 *Astr. Astrophys.*, **241**, 197-202 : *Dynamics of flaring loops. I. Thermodynamic decay scaling laws.*

72. Sturrock, P. A., (ed.) 1980 *Solar Flares*, publ., Colarado Associated University Press

73. Švestka, Z., 1989 *Solar Physics*, **121**, 399-417: *Solar flares: the gradual phase.*

74. Sylwester, B., Sylwester, J., Serio, S., Reale, F., Bentley, R. D., and Fludra, F., 1993 *Astr. Astrophys.*, **267**, 586-594: *Dynamics of flaring loops. III. Interpretation of flare evolution in the emission measure-temperature diagram.*

75. Sylwester, J., Schrijver, J., and Mewe, R., 1980 *Solar Physics*, **67**, 285-309: *Multitemperature analysis of solar X-ray line emission.*

76. Tanaka, K., Watanabe, T., Nishi, K., and Akita, K., 1982 *Astrophys. J. (Letters)*, **254**, L59: *High resolution Solar flare X-ray spectra obtained with rotating spectrometers on the Hinotori satellite.*

77. Tanaka, K., and Zirin, H., 1985 *Astrophys. J.*, **299**, 1036-1046 : *The great flare of 1982 June 6.*

78. Tandberg-Hanssen, E., and Emslie, A. G., 1988 *The Physics of Solar Flares*, publ., Cambridge University Press.

79. van den Oord, G. H. J., and Mewe, R., 1989 *Astr. Astrophys.*, **213**, 245-260: *The X-ray flare and the quiescent emission from Algol as detected by EXOSAT.*

80. van Regemorter, H., 1962 *Astrophys. J.*, **136**, 906-915: *Rate of collisional excitation in stellar atmospheres.*

81. Watanabe, T., 1990 *Solar Physics*, **126**, 351. *Plasma motions in the flare of 1982 June 6 (X12).*

82. Winglee, R. M., Kiplinger, A. L., Zarro, D. M., Dulk, G. A., and Lemen, J.R., 1991 *Astrophys. J.*, **375**, 366-381: *Interrelation of soft and hard x-ray emissions during solar flares. I. Observations.*

83. Winglee, Dulk, G. A., Bornmann, P. L., and Brown, J. C., 1991 *Astrophys. J.*, **375**, 366-381: *Interrelation of soft and hard x-ray emissions during solar flares. II. Simulation model.*

84. Withbroe, G. L., 1975 *Solar Physics*,**45**, 301-317: *The analysis of XUV emission lines.*

85. Zarro, D. M., Canfield, R. C., Strong, K. T., and Metcalf, T. R., 1988 *Astrophys. J.*, **324**, 582-589: *Explosive plasma flows in a Solar flare.*